Design of a Helium-6 Production Target for the iThemba LABS Radioactive-Ion Beam Facility

by

LANCE GARTH DAVIS

A thesis presented in partial fulfilment of the requirements for the Degree of Master of Science (MSc) in the Department of Physics, University of the Western Cape.

Supervisor:
Dr. R.A. Bark (iThemba LABS)
Co-supervisor:
Prof. J.N. Orce (University of the Western Cape)

Date: September 2018

ABSTRACT

It is well known, that there is a severe lack of information available pertaining to neutron rich nuclei, specifically of those nuclei with mass numbers ≥ 60. These neutron rich nuclei are not easy to access in current experimental facilities or be produced with sufficient yield to allow for it to be studied. In order to expand our understanding of nuclear physics by studying the properties and characteristics of these nuclei, the development of new facilities producing Radioactive-ion Beams (RIBs) is required. The applications for RIBs are wide, allowing for deeper investigations into the properties of nuclei, their interactions and the manner in which they were formed in the early universe. Additionally, there are various interdisciplinary fields such as medicine, biology and material science in which RIBs can be utilized as a driving mechanism for new research and technological innovation.

The iThemba Laboratory for Accelerator Based Sciences (iThemba LABS), South Africa, has proposed a new facility for the production and acceleration of radioactive-ion beams (RIBs). The RIB Project is to be developed in sequential phases and would produce a range of neutron-rich isotopes for low-energy materials science and nuclear physics research. Of specific interest, is the production of the Helium-6 isotope (^{6}He), for its potential applications in various areas of nuclear physics research.

The aim of this research work was to design, model and optimise a RIB production target capable of producing high intensity ^{6}He beams, guided by the characteristics of the primary proton beam available for use at iThemba LABS. This research work/design study is however limited, due to the absence of experimentally measured and verified ^{6}He cross section data for proton induced reactions on the proposed target materials (Graphite and Boron Carbide). However, best-estimate approaches were adopted through the use of validated computer codes. Additionally, all ^{6}He yield results are presented as in-target yields, as this study did not cover the diffusion (isotope release) efficiency of the target systems in question.

Three RIB production targets types were investigated using Graphite, Boron Carbide and Beryllium Oxide as potential target materials. Following numerous optimisation processes, a Boron Carbide RIB target was converged upon, proving to be suitable for the production of high intensity ^{6}He beams at iThemba LABS, by meeting the material thermal and mechanical limiting criteria for operation. This target system was found to produce an in-target ^{6}He yield rate of 2 ~ 3 x 10^{11} ^{6}He/s, considered sufficient for experimental application at iThemba LABS.

DECLARATION

I declare that "*Design of a Helium-6 production target for the iThemba LABS Radioactive-ion Beam facility"* is my own work, that it has not been submitted for any degree for examination at any other university, and that all the sources I have used or quoted have been indicated and acknowledge through complete reference**.**

Full name: **Lance Garth Davis**

Date: **September 2018**

Signature:

ACKNOWLEDGEMENTS

Firstly, I would like to extend my utmost thanks to my supervisor, Dr. Bark, for the extensive guidance and support throughout this research work. Your critical reviews and assessments were of infinite value, and has truly enhanced my approach to the scientific method.

To my co-supervisor, Prof. Orce, thank-you for the administrative support and review comments, I truly appreciate it.

I would like to thank the SPES project team at INFN (Legnaro, Italy) and specifically Alberto Monetti, for the fruitful technical exchange during my visit in 2015, as well as the subsequent assistance with the ANSYS code implementation.

To my sister, Tracey-Lee, thank-you for your grammatical reviews and suggestions during the writing of this thesis.

To my mother, I cannot thank-you enough for your support and encouragement during and prior to, the completion of this thesis. My success is a result of a lifetime of your unwavering support - I truly appreciate all you have done for me.

Last, but most definitely not least, to my wife, Amy, these few words will never be enough, but thank-you for your support, patience, love and encouragement. My determination is a direct result of your constant support, and thus, I could not have done this without you.

DEDICATION

Dedicated to my daughters, Amelia Rayne and Emily Winter.

‘One's mind, once stretched by a new idea, never regains its original dimensions.’

(O. W. Holmes)

TABLE OF CONTENTS

LIST OF FIGURES

LIST OF TABLES

LIST OF ABBREVIATIONS

ABBREVIATION	DESCRIPTION
FEA	Finite Element Analysis
FEM	Finite Element Model
FWHM	Full Width at Half Maximum
INFN	Instituto Nazionale di Fisica Nucleare
ISOL	Isotope On-Line Separation
iTL	IThemba Laboratory for Accelerator Based Sciences
RIB	Radioactive-ion beam
SPES	Selective Production of Exotic Species
SMN	Minimum result value
SMX	Maximum result value

GLOSSARY

TERM	DESCRIPTION
Adsorption	A material surface phenomenon of solid materials to attract particles/molecules with which they are in contact with, to their surface. This attraction of a particle is referred to adsorption and the release of a particle adsorbed to the surface is referred to as desorption
Binding Energy	The amount of energy required to remove all protons and neutrons from the nucleus, given by the mass difference between the nucleus and the sum of the free nucleons constituting the nucleus
Diffusion	the process in which particles move from an area of high concentration to an area of low concentration
Effusion	the process in which particle moves through a ‘hole/opening’ smaller than itself, from an area of high concentration to an area of low concentration
Isobar	Nuclides with the same mass number, but with different proton and neutron numbers
Isotope	Nuclides of the same element, with different numbers of neutrons, are referred to as isotopes
Nucleon	Proton or neutron

Nuclide	A nuclide refers to a particular atom or nucleus with a specific number of protons and neutrons. A nuclide can either be stable or unstable (radioactive).
Radionuclide	An unstable/radioactive nuclide

CHAPTER 1: INTRODUCTION

1.1 The Nuclear chart and valley of stability

The Nuclear Landscape Chart (also known as the Segré chart) can be viewed as a summary of what we have and have not yet discovered about nuclei within the driplines, which mark the regime of unbound nuclei. With reference to figure 1-1 below, the chart represents the stable nuclear species which are plotted as black squares, as a function of atomic (proton) number (Z) and neutron number (N). For each proton number there are generally one or more stable nuclei, or isotopes, each containing a different number of neutrons [Won98]. The chemical properties of an element are characterised by the electrons orbiting outside the nucleus in addition to the number of protons inside the nucleus. It is generally found that the chemical properties of different isotopes are rather similar to each other. Their nuclear properties, however, are significantly different as a result of their differing neutron numbers [Won98].

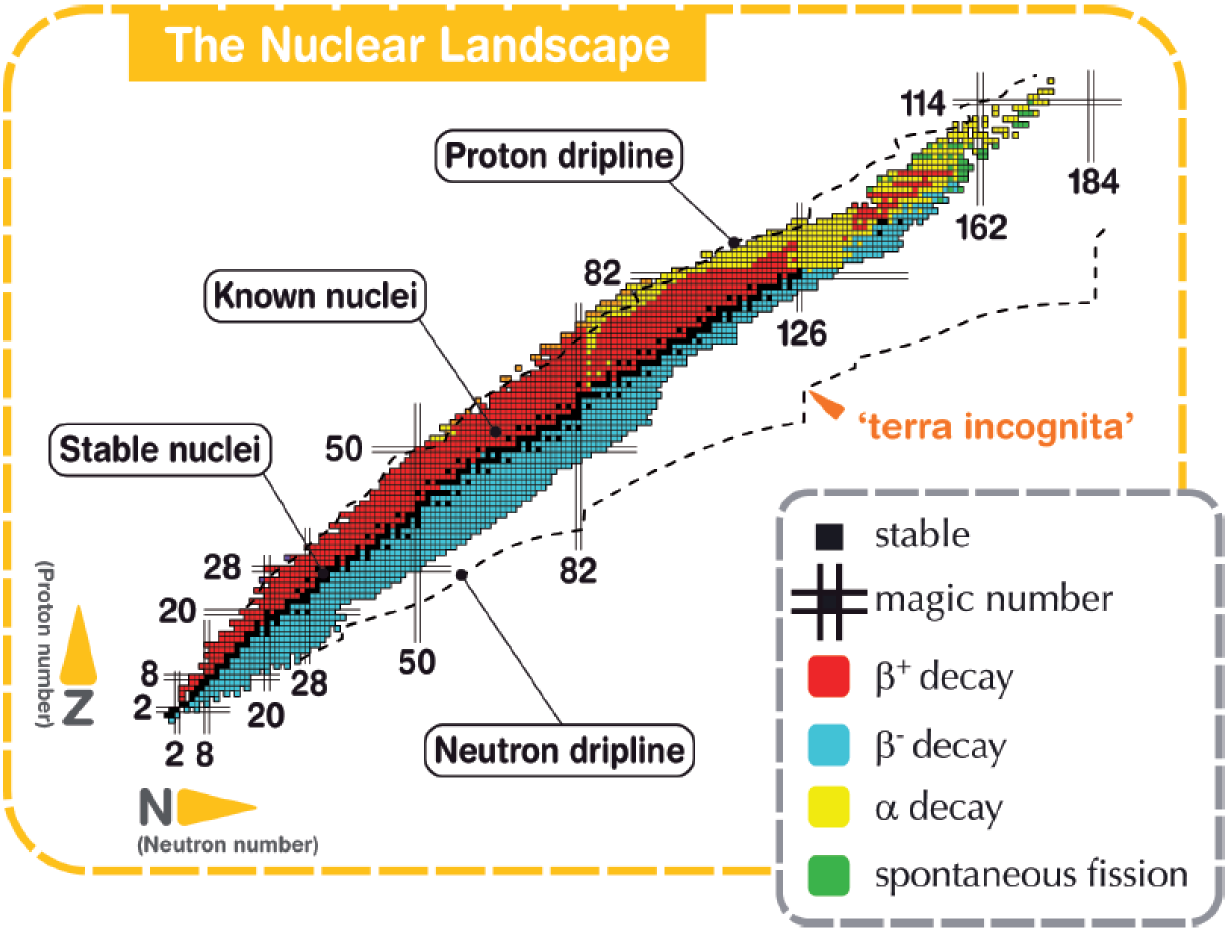

Figure 1-1: The Nuclear Chart [Eur18].

For light stable nuclei ($N + Z = A < 40$), a generic approximation of $N = Z$ can be made. An example of this approximation can be made by observing nuclei with mass number, $A = 4$. Here, it can be noted that the only stable nucleus ($^{4}_{2}\mathrm{He}$) with $A = 4$, also referred to as the α-particle, contains two protons and two neutrons ($Z = N = 2$). However, the $A = 4$ nuclei containing three protons, ^{4}Li ($Z = 3, N = 1$) and three neutrons ^{4}H ($Z = 1, N = 3$) are both known to be highly unstable.

The collection of black squares along the diagonal of the nuclear chart (figure 1-1) is referred to as the *valley of beta stability*. Where a nuclear species is considered stable if it is long enough lived to be found on Earth [Gel01].

Additionally, the nuclear chart shows estimates of the proton and neutron drip lines, which are the points at which another proton or neutron can no longer be added and bound to a nucleus. Thus far, the most progress in establishing the limits of nuclear existence has been made around the proton drip-line, which separates nuclei into “bound” and “unbound” with respect to proton emission from their ground states. This is to say, the nuclide at which the addition of another proton results in the nuclear ground state becoming energetically unstable to the emission of a proton [Gel01]. The neutron drip-line can be defined in an analogous way [deA14]. The neutron drip-line is located much further away from the valley of stability as opposed to the corresponding proton drip-line, due to the lack of electrical repulsion between neutrons. The exact location of the neutron drip-line is, however, still largely undefined, as the experimental data currently available only accounts for nuclei with masses up to around 30. To obtain a more exact description of the neutron drip-line, another significant factor for investigation is the density dependence of the effective interaction between nucleons in nuclei of exotic N/Z ratios [deA16]. It is predicted, from current research, that changes in nuclear density and size in nuclei with increasing N/Z ratios would result in different nuclear symmetries and new modes of excitation. An example of this prediction was found in light nuclei, such as ^{6}He, where a halo structure has been identified (this is discussed in further detail in section 1.2.1).

As all the nuclear species found between the drip-lines and the valley of beta-stability, which represent the large majority of nuclei, are unstable and hence radioactive, studying these nuclear species present significant challenges.

1.2 Studying Radioactive Nuclei

In order to overcome the present restriction of being limited to studying nuclei close to the valley of beta stability, or neutron deficient nuclei, new techniques are required to probe/investigate the before mentioned radioactive nuclear species, with the most prevalent method being that of Radioactive-ion Beams (RIBs). RIBs allow for the study of nuclear processes currently inaccessible with stable projectile-target combinations. RIBs make it possible to examine reactions important in expanding our knowledge about the structure of the nucleus and the nucleosynthesis processes responsible for heavy element formation in the relevant stellar processes driving such activities in the universe [Zha01]. The recent development and production of beams of unstable ions has stimulated the research of nuclear structure and reactions for exotic nuclei in previously unexplored regions of the nuclear chart, especially on the neutron-rich side [deA14] [Ber04]. As mentioned in the preceding section, the nuclear chart defines two lines, the proton and neutron drip lines, which could be considered a measuring gauge for our current knowledge of nuclei. Since the neutron drip-line is considered undefined, it is a significant area of focus in current research.

The applications for RIBs are wide, allowing for deeper investigations into the properties of nuclei, their interactions and the manner in which they were formed in the early universe. Additionally, there are various interdisciplinary fields such as astronomy, medicine, biology and material science in which RIBs can be utilized as a driving mechanism for new research and technological innovation. A few of the areas in which RIBs can be applied are discussed briefly in the sub-sections to follow.

1.2.1 Nuclear Physics – RIB application

In order to understand the characteristics of a nucleus, it is necessary to have an insight into its structure, by being able to determine the arrangement of the nucleons contained within the nucleus. Various areas of nuclear physics research such as nuclear structure (of specific interest in this work, as it relates to halo nuclei), limits of nuclear stability, clustering in nuclei and neutron skins, could and would draw great benefit from the advancements and availability of intense radioactive-ion beams.

Halo nuclei:

The field of halo nuclei has provided for much excitement and initiated a large body of research since its initial discovery in 1985 at the Lawrence Berkeley Laboratory [Tan85a] [Tan85b].

Further work conducted by Hansen and Jonson produced a paper on the subject two years later, thereby first coining the term "*halo*" nuclei [Han87]. It is worth mentioning, especially in relation to this thesis work, that the first '*halo nucleus'* to be produced in the laboratory was ^{6}He, as early as 1936, by impinging a neutron beam onto a ^{9}Be target.

To conceptualise the concept of halo nuclei, a good place to start is with the following mathematical expression describing the energy required to separate a neutron from a nucleus (E_s) [Bar13]:

$$E_s \approx -\lambda(-\Delta_n)$$

where λ is the Fermi level, described as a measure of the shell level spacings and Δ_n is the neutron pairing gap, described as a measure of the strength of the residual pairing interactions.

It is well understood that in nuclei near the drip-line, the separation energy of the last nucleon(s) becomes extremely small ($E_s \approx 0$) [Bar13] [Tan96]. In stable nuclei, the separation energy is commonly 6-8 mega electronvolt (MeV), however, many dripline nuclei have either one or two nucleon separation energies that are less than 1 MeV. The neutron density distribution in these loosely bound nuclei exhibit an extremely long tail, known as the neutron halo. This neutron density of the halo, although very low, has significant effects on the cross section of the nuclei and leads to new properties in these nuclei [Tan96]. An example of these new deviating properties is the size of the nucleus in these halo nuclei, such as that of ^{11}Li which has a significantly large nucleus [Jen04] [Tan85b], comparable in size to the much heavier nucleus ^{208}Pb, as graphically depicted in figure 1-2 below. The three most studied halo nuclei are ^{6}He, ^{11}Li and ^{11}Be (although others such as ^{14}Be and ^{15}C have been confirmed), all of which are neutron halo systems and are close to the neutron dripline at the limits of stability [Al04].

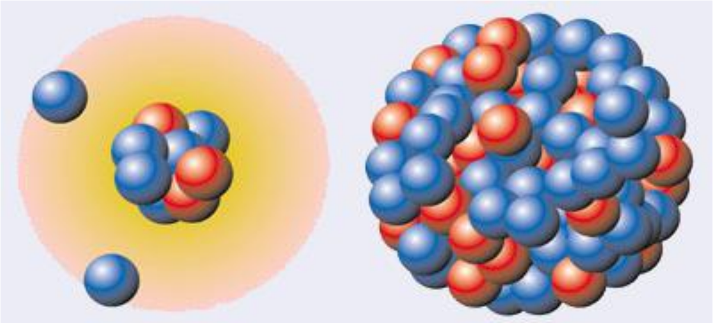

Figure 1-2: Comparative size of ^{11}Li (left) and ^{208}Pb (right). The large size of ^{11}Li can be seen to be attributed to the large volume occupied by its two-neutron halo [Lun04].

Due to the short-lived nature of halo nuclei, they need to be studied using RIBs, by which they are formed and subsequently used to initiate nuclear reactions for experimentation purposes [Al04].

Neutron skin:

When the Z and N numbers in a nucleus are similar, their distributions throughout the nucleus are also similar, that is to say, their radii are approximately equal. However, when there is a large excess of neutrons relative to protons, significant differences are noted. This significant excess of neutrons, generally noted in heavy nuclei with a neutron rich outer-layer, results in what is known as a "neutron skin" [Bar13].

This neutron skin formation is as a result of neutrons extending further in radius as opposed to the protons of the given nuclei. Understanding how these nucleon distributions differ from nuclide to nuclide would provide insight into the complex interactions which hold nuclei together, and by extension, insight into more exotic structures such as neutron stars [Tar14]. RIB facilities, producing neutron rich nuclei, can be used to study the properties of neutron skins.

Clustering in nuclei:

The traditional description of the nucleus describes it as a central structure in which there is a roughly homogenous distribution of protons and neutrons. However, it is now predicted, with theoretical models, that certain nuclei behave like molecules composed of clusters of protons and neutrons [Ebr12]. Clustering is a recurrent phenomenon observed in light neutron rich nuclei as well as halo nuclei [Bec11], such as ^{6}He and ^{11}Li [Mar01].

Clustering in nuclei is significant when considering the states in nuclei that lie close to their cluster decay threshold (Q-value for separating the nucleus into its separate cluster constituents). A rather well-known example of clustering in nuclei is the *Hoyle State*, which is understood to be a cluster of three α-particles at an energy of 7.654 MeV, which is just above the triple-alpha threshold energy of 7.275 MeV [Coo57]. This state was first predicted by British astronomer Fred Hoyle in 1954 to account for the abundance of carbon in the universe [Fre10]. This led to the understanding of carbon synthesis in stellar environments, which occurs through a triple-alpha process, whereby two α-particles first fuse momentarily to form an unstable, but relatively long lived ^{8}Be nucleus, with a resonance capable of combining with another α-particle to form ^{12}C [Epe13] [Fre10]. The bulk of the carbon (^{12}C) present in the universe is produced through this process and drives the process of oxygen (^{16}O) production by capturing an additional α-particle, resulting in a ^{12}C : ^{16}O abundance ratio of ~ 1 : 2 [Cso01].

The production of an appreciable amount of carbon is a necessity for carbon-based life in the universe, in addition to the production of oxygen, as no spontaneous development of carbon-based life would be possible without water (H_2O) [Cso01].

Light-ion neutron-rich beams, produced in RIB facilities, can be used to populate cluster states in inelastic reactions, allowing for interesting and extensive research related to clustering in nuclei. An example of this would be the use of ^{6,8}He beams to probe the molecular states involving neutron-rich helium isotopes in ^{12}Be, ^{22}O and ^{26}Ne [Bar13].

1.2.2 Nuclear Astrophysics – RIB application

Most nuclear reaction sequences which play a pivotal role in our understanding of the cosmos occur under extreme astrophysical conditions (i.e. high temperatures and pressures) and involve short-lived, rare isotopes, which in recent years have been unattainable in laboratory scale experiments [Facility for Rare Isotope Beams [FRIB12]]. As a result, stellar explosions and nucleosynthesis processes, which can be generalised as the production of '*new*' atomic nuclei on a cosmic scale from pre-existing protons and neutrons, are poorly understood. The current astronomical observations used to examine these processes, such as large optical telescopes, UV, X-ray and Gamma-ray observations, neutrino detection, meteoritic abundances, cosmic rays and most recently gravitational waves [Abb16], cannot be fully exploited and, in some cases, remain unexplained [FRIB12]. The recent astronomical observations made with these methods have however added depth to the mystery pertaining to the origin of elements heavier than iron $(Z = 26)$. On the one side, observations of old (metal-poor) stars in the Galaxy, conducted with the largest available telescopes, have shown a robust pattern of abundances of elements heavier than tin $(Z = 50)$ that agrees with that of the solar system [FRIB12]. On the contrary, significant differences between the observations and solar abundances are seen for elements between iron and tin. The physical processes that result in these abundances in the early history of the Galaxy are challenging to explain within the boundaries of our current understanding of astrophysical phenomena [FRIB12]. Realistic models of core collapse supernovae (explosions of massive stars in which most of the nuclei found in the Universe are produced and disseminated [Jan07]) fail to reproduce the hydro-dynamical conditions required to robustly create heavy rapid neutron capture process ("r-process") elements $(Z > 56)$. In addition, neutron star mergers are currently considered too infrequent to produce sufficient abundances of heavy elements early in the history of the Galaxy [FRIB12]. The overarching issue is that the significant uncertainties in the properties of short-lived nuclei induce ambiguity to a direct comparison of the wealth of new observations and realistic astrophysical models/simulations.

The current research and development in the field of RIBs, specifically the production of short-lived isotopes of sufficient intensity, could thus address most of the fundamental nuclear physics required for refining our understanding of stellar explosions and the origin of the elements in the Universe.

1.2.3 Solid State Physics – RIB application

Radioactive atoms have been applied in solid state physics research for many years. Well established, classical nuclear techniques such as Mössbauer spectroscopy, Beta Nuclear Magnetic resonance (β-NMR) and emission channelling have now been extended by new tracer techniques such as radioactive deep level transient spectroscopy, capacitance voltage measurements and photoluminescence spectroscopy [For99]. These new tracer techniques arise as a result of the usage of radioactive nuclei and are applied to study defects and/or impurities in metals, semiconductors and superconductors [For99]. The radiotracers for diffusion studies, in general, rely on measuring the amount of radiation as a function of specific parameters. RIBs are therefore a powerful diagnostic tool for providing detailed information on materials in the solid state research arena [Cor13].

1.3 Basics of RIB production

Two complimentary techniques exist for the production of RIBs – Isotope Separation Online (ISOL) and In-flight fragmentation. ISOL facilities allow for high quality, low emittance beams of lower energy and generally higher yields near stability, whereas In-flight facilities are suited for high energy beams of very-short-lived species [Lax14]. In the ISOL method, radioactive species are produced through nuclear reactions occurring from the interaction of a primary beam and target material, with the resulting reaction products being produced within the target material. Similarly, radioactive species are produced through the same process in the in-flight fragmentation method, however, the produced reaction products are ejected (“fly out”) from the target material. Another common aspect shared by these RIB production techniques, is that the nuclei of interest are transported from their place of production to a well-shielded experimental set-up [Blu13], where further research can be conducted with or on these nuclei.

The four main properties of importance in the production sequence of RIBs at any RIB facility, are production rate, efficiency, selectivity and delay time. These properties can be expanded upon as follows:

- ***Production rate*** **–** For any RIB facility, the highest production rate of the nuclei of interest will be strived for. In order to achieve the highest possible production rate of a particular nuclide, factors such as reaction cross section (σ), target material density, primary beam type, current and energy have to be optimised through the selection of the beam-target combination [Blu13]. This optimisation requires the establishment of the correct balance between the highest possible beam intensity of the impinging beam and the maximum power deposition which the target system can cope with.

- ***Efficiency*** **–** The processes undergone by the reaction products (nuclei of interest) during the transport phase (i.e. place of production to experimental set-up) such as ionisation, acceleration, and purification, have to be done at the highest transmission efficiency possible, to ensure a high quality, intense RIB for experimentation.

- ***Selectivity*** **–** Since a significant quantity of unwanted species (reaction products which are not of interest in a given experiment) are produced in the nuclear reaction taking place between the impinging primary beam and target material, a selective separation process should be used to reduce these unwanted species and the primary beam, from the nuclei of interest to be used for experimentation.

- ***Delay time*** **–** As the produced exotic nuclei of interest have very short half-lives, the losses as a result of radioactive decay between the moment of production and the delivery to the experimental set-up should be kept to a minimum [Blu13].

The ISOL RIB production technique is now discussed in further detail, as this is the proposed RIB production technique to be developed and used at iThemba LABS.

ISOL is a multi-step method, which produces isotopes through nuclear reactions occurring as a result of a highly energetic beam (e.g. protons) interacting with a thick target material [Ego16]. The target is heated so that the reaction products are vaporised and diffuse out of the target. They subsequently move towards an ion source where they are ionised and extracted as an ion beam. The ion beam is then transported through an electromagnetic device which separates the ions by mass, before being injected into a second accelerator which increases the energy of the ions to the required levels for experimentation [Gel01]. It should be noted that non-accelerated ion beams exiting the separator could be used for beta-decay experiments/studies.

RIB production facilities using the ISOL Technique generally consist of four primary components, namely:

1. Primary accelerator / Primary beam delivery
2. Target system, including extraction and ionisation systems
3. Mass and isotope separators
4. Post-accelerator

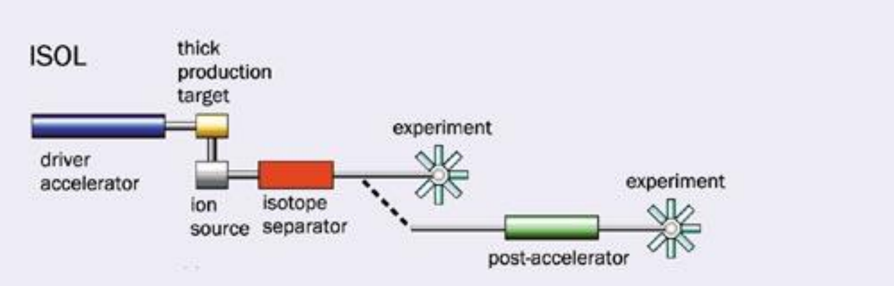

Figure 1-3: ISOL RIB Production schematic [Har04].

These primary components constituting a complete ISOL facility are discussed briefly, as follows:

- **<u>Primary accelerator:</u>**
  A cyclotron or linear accelerator (LINAC) could be used as a primary accelerator, or driver, which is tasked with delivering the primary beam to the target system. This is general done through the injection of proton or low energy ionised atoms into the accelerator, which subsequently accelerates the injected particles to the required energy and the required beam current [Ros14].

- **<u>Target System:</u>**
  The primary beam with desired energy and current is delivered to the front-end of the target system, where it impinges the RIB production target, producing radioactive isotopes as a result of nuclear reactions. The radioactive isotopes produced constitute the secondary beam.

Two classes/types of target exist, namely direct targets and two-step or convertor targets. In the case of a direct target, the primary beam impinges on the target producing radioactive isotopes. In the case of a two-step or convertor, the leading target is used to convert a beam of protons into a flux of neutrons, which is subsequently directed onto the target which induces the nuclear reactions, producing radioactive isotopes.

- **Ion Source:**
  The produced radioactive isotopes migrate through a transfer line to an ion source. In order to limit the ‘sticking’ of atoms to the transfer-line internal walls, the line is kept at a high temperature, to assist the migration process. Depending of the experimental requirements, different types of ionisation sources (e.g. plasma ion-source, surface ion-source) could be used [Van06], in which singly-charged positive or negative ions are produced from the radioactive isotopes.

- **Mass and isotope separators:**
  In order to chemically and isobarically purify the complex of radioactive isotopes produced, highly efficient electromagnetic mass separators are crucial to select and purify the desired nuclei.

- **Post-accelerator:**
  Following the mass separation process, the now “purified” beam, consisting of the desired radioactive isotope, is subsequently injected into the accelerator. This process is referred to as post-acceleration. The resultant purified, energetic beam of radioactive-ions is then sent to the experimental set-up(s) where it can be used for a multitude of applications or as desired by the user.

1.4 iThemba LABS RIB Project

The iThemba Laboratory for Accelerator Sciences (iTL) in South Africa, is a multidisciplinary research facility which provides accelerator-based facilities for physical, biomedical, material sciences, as well as the production of radioisotopes. iThemba LABS currently operates a number of accelerators, with the biggest of these accelerators being the Separated-Sector Cyclotron (SSC). The SSC is a variable energy machine, capable of producing proton beams up to about 200 MeV, a variety of heavy ion beams and polarised protons, at energy sufficient to probe the structure of sub-atomic matter [Con16]. Currently, the SSC is shared between several disciplines/departments within iThemba LABS, including nuclear physics research, radioisotope production, medical physics, neutron dosimetry, etc.

The proposed iThemba LABS RIB production facility was recently named the South African Isotope facility (SAIF). SAIF will consist of two phases, the first being the Accelerator Centre for Exotic Isotopes, comprising the Low-Energy Radioactive-Ion Beam (LERIB) project and a new cyclotron for commercial radionuclide production. The second phase is the Accelerator Centre for Exotic Beams (ACE Beams) project, implementing post acceleration [Bar18].

The RIB demonstrator/test facility, currently under construction, would be upgraded to become the Low-Energy RIB (LERIB) facility [Bar18]. LERIB represents a collection of collaboration efforts between iThemba LABS and *Istituto Nazionale di Fisica Nucleare* (INFN) in Legnaro (Italy).

The acquisition and installation of a dedicated 70 MeV H-minus cyclotron, to be procured from either Best Cyclotron Systems Inc. (BCSI) or Ion Beam Applications (IBA) [Bar18], for the iThemba LABS radioisotope production programme, would allow the current iThemba LABS SSC to be exclusively used on the LERIB project and stable beam experiments. LERIB will make use of the high intensity 66 MeV proton beam from the SSC to produce neutron-rich isotopes, expanding the range of available beams at iThemba LABS. It is envisaged that the second phase will allow for the acceleration of low-energy RIBs using a post accelerator, which will be capable of accelerating radioactive beams from the LERIB project to an initial energy of approximately 5 MeV per nucleon [Con16]. Full use of the existing building infrastructure will be made to establish the independent radioisotope production facility (SAIF). The 70 MeV H-minus cyclotron will be installed in the currently under-utilised neutron therapy vault [Con16], while the proton therapy vault and the third redundant vault will house a number of isotope production target stations. Therefore, the isotope production target station will be completely decoupled from the SSC [Bar18]. The layout of the iThemba LABS Accelerator Centre for Exotic Isotopes project is shown in figure 1-4 below.

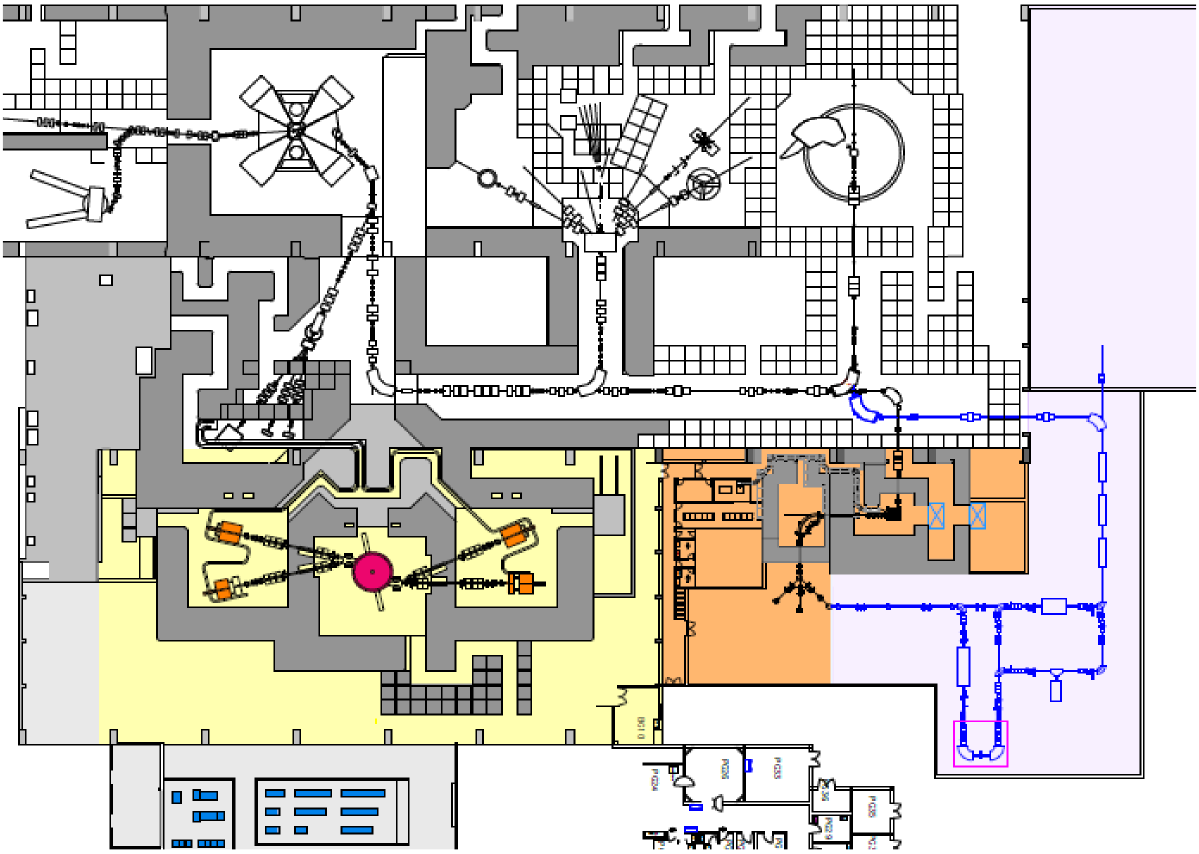

Figure 1-4: Layout of the ACE Isotopes project. New 70 MeV cyclotron and new radioisotope bombardment stations (yellow). The SSC (top left) providing a 66 MeV proton beam to the LERIB facility (orange) which will supply low-energy RIBs for post-acceleration in the ACE Beams facility (purple). Adapted from [Bar18]

1.5 iThemba LABS and INFN collaboration

Since the inception phase of the proposed iThemba LABS RIB project, the intention has been to draw on past international experience through collaborative efforts. The iThemba LABS RIB project is similar to the Selective Production of Exotic Species (SPES) project, currently under construction at INFN, and plans to make use of a 70 MeV proton beam at an intensity of 200 µA the primary beam [Bar13], with the primary goal of producing intense ‘exotic’ radioactive-ion beams. The SPES facility will be making use of a 40 MeV proton beam with an intensity of 200 µA as the primary beam, with an upgrade to 70 MeV at an intensity of 750 µA envisaged for the future. A Memorandum of Understanding (MoU) has been drawn up between iThemba LABS and the INFN laboratory to test their SPES target system at iThemba LABS, due to iThemba’s availability of high power proton beams [Bar13]. Furthermore, the MoU provided the protocol for various technical exchanges between iThemba LABS and INFN, as it relates to RIB target design, construction and testing.

Similar to the iThemba LABS RIB project, SPES will be operating using the ISOL methodology, in which a primary beam provided by a driver accelerator induces nuclear reactions in a thick target. A direct, uranium carbide (UCx) target will be used in SPES, expected to produce up to 42 elements (mainly neutron rich) at a production rate of 10^{13} fissions per second. The reaction products/isotopes are extracted from the target via thermal processes due to the high operating temperature (2000 - 2300ºC) of the target-ion source system [deA14]. The isotopes are sequentially ionised and extracted by means of an ion source, then isotopically separated and further ionised to produce an 'exotic' radioactive-ion beam. The produced RIB is finally injected into a post-accelerator for delivery to the experimental setup.

The iThemba LABS target design and modelling process is largely similar to that of the INFN SPES process, in terms of design methodology, technical considerations during target modelling and the computer codes employed for calculations and analysis.

1.6 iThemba LABS RIB Target design study

The target design and modelling process, illustrated in figure 1-5 below, is conducted in an iterative manner to achieve two objectives, namely, maximizing the product yield obtained from the beam-target interaction (reactions) and ensuring the target is operated within the material's thermal and mechanical (thermo-mechanical) thresholds/limits.

The process starts by defining the beam parameters and target material specifications, with the latter informing the specification of the target geometry. The beam-target interaction is then computed using computer codes capable of simulating various nuclear reactions and the energy transfer mechanisms (power deposition onto target materials) accompanying these reactions. This simulation produces two outputs, the first being the yield results, which could be further optimised by adjusting the target geometry specifications, and secondly, the power deposition output data which are subsequently used to simulate the thermo-mechanical effects occurring within the target system. The analysis of the results obtained from the simulation of the thermo-mechanical effects is then compared against the thermo-mechanical thresholds of the target system materials, to ensure the target design is fit for purpose. A favourable (optimised) balance between the highest attainable yield and acceptable thermal-mechanical results is then used to inform the final target design.

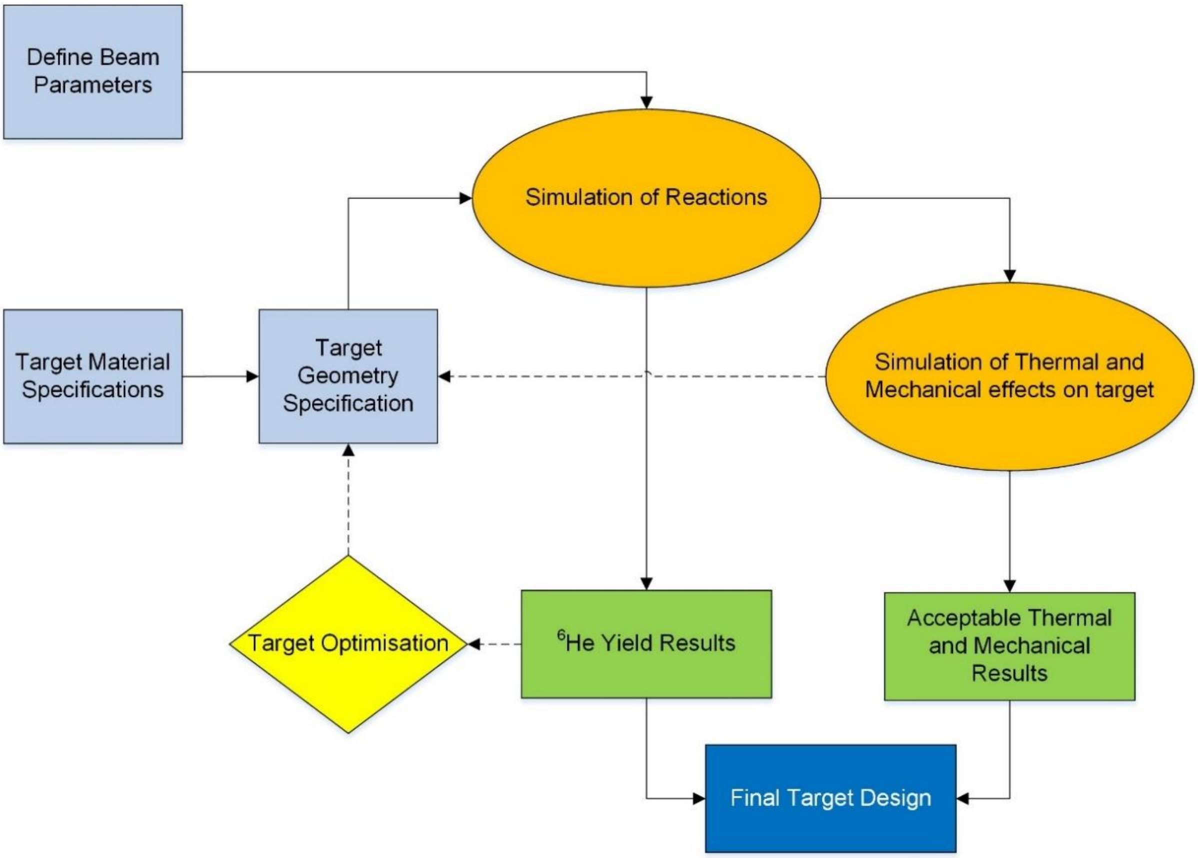

Figure 1-5: RIB target design and modelling process.

The initial target geometry used as a generic target system, was adopted from the SPES target design, and used as a starting point for the design and optimisation of the iThemba LABS RIB target.

As is the case in the SPES target system design, the target canister, coupled to a resistive heater and ion source, is to be housed inside a larger vacuum chamber. The vacuum chamber contains an integrated water cooling circuit and secondary beam dump. The primary beam (indicated as PPB in figure 1-6) enters the target canister resulting in the production of nuclides, which are subsequent ionised and extracted from the target canister, as discussed in the previous section. It should be noted that the specific design and thermo-mechanical analysis for the SPES adapted vacuum chamber to be used for the proposed iThemba LABS RIB target configuration, was not covered in this work.

The target canister contains a number of target discs, arranged sequentially along the proton beam path and positioned inside the target canister, as illustrated in figure 1-7. The discs are optimally spaced to allow the heat generated (during operation) in the target discs to be dissipated (via thermal radiation). The back end of the target canister contains a number of beam dumps, with sufficient thickness to ensure the primary beam is stopped within the target system. Two thin ‘windows’ are located at the proton beam entry point of the target canister in order to prevent the unwanted emission of nuclear fragments. Due to the high operating temperature (> 2000 °C) required for efficient release of radioisotopes, and the fact that the energy provided by impinging proton beam is not sufficient to maintain the target system above 2000 °C, an additional heating source is required. This requirement is met by attaching an external resistive heater to the target canister, which assists in the heating of the target and subsequent control/maintenance of optimal temperature.

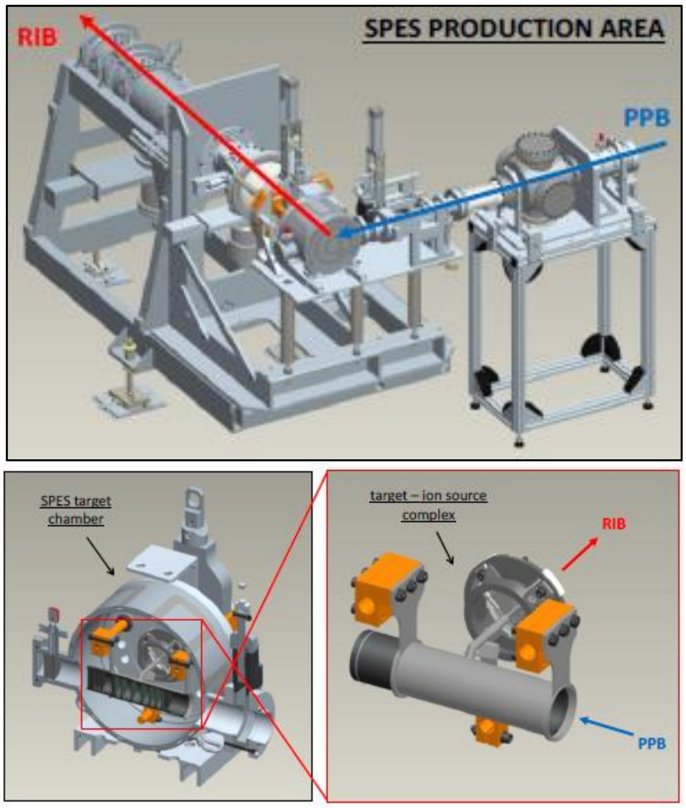

Figure 1-6: SPES target system design and layout. [Cor13].

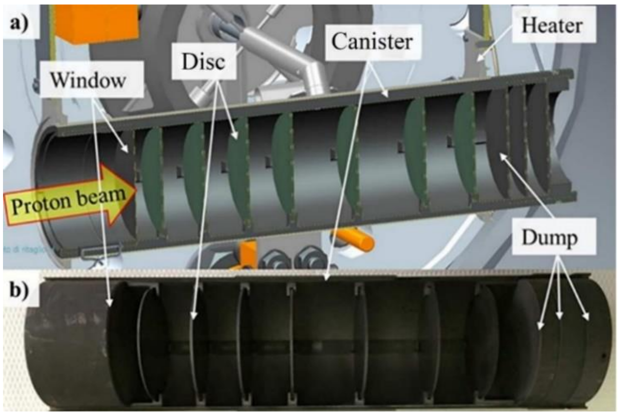

Figure 1-7: Generic target layout as shown by SPES prototype. Adapted from [Mon15].

In 2014, iThemba LABS and INFN conducted a successful collaborative online experiment to test a high-power Silicon Carbide (SiC) prototype target [Mon16]. This test confirmed the ability of finite element method (FEM) calculations to simulate temperature and mechanical stress profiles of the production target under realistic operating conditions [Bar18]. During this test a 66 MeV proton beam with 60 µA intensity, was injected into the target assembly comprising of 13 thin SiC discs housed in a graphite canister. SiC was chosen as a target material for this test due to its relatively low post-irradiation residual activity with the proton beam. The design of the SiC target used in the online test, is similar in its layout of core components (canister, discs and beam dumps) as that of the INFN SPES target and proposed iThemba LABS RIB target, discussed in this work.

During the 2014 online SiC test, it was possible to monitor the temperature of the first SiC disc, target canister and target beam dump. The measured temperatures of the SiC disc, canister and beam dump were compared against the simulated FEM computer model temperatures. The experimentally measured and FEM temperatures were found to be in good agreement, with the relative differences in temperature values between measured and FEM being 4.3%, 1.6% and 3.4%, for the first SiC disc, canister and beam dump [Mon16], respectively. These results thus served as confirmation of the validity of the FEM model to be used for thermal and mechanical stress analysis in the RIB design and modelling process.

1.7 Helium-6 User request

Resulting from the establishment of the iThemba LABS RIB project, a user request (by Prof. P. Papka) for a high intensity Helium-6 (^{6}He) beam was made for nuclear physics research, more specifically nuclear structure studies. Precision measurements of nuclear structure in very neutron-rich nuclei, of which ^{6}He is the lightest, is of specific interest as it allows for investigations of aspects related to the nuclear configuration and nucleon interactions that are less prevalent in nuclei closer to stability [Mue07]. Additionally, access to intense ^{6}He beams would open a plethora of additional nuclear physics research areas, such as low density nuclear interactions, asymmetric nucleus, shells for high-isospin interactions and collective motions of low density nuclear matter [Tan96], to name a few.

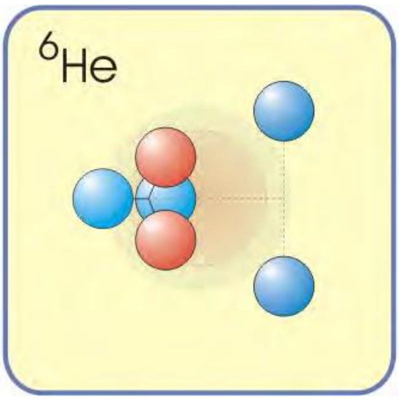

Figure 1-8: Illustration of ^{6}He configuration. Blue spheres – neutrons, Red spheres – protons, with the two outlying, "orbiting" neutrons representing the "halo". Adapted from [Lu13].

The ^{6}He nucleus is unstable with respect to beta-decay, but with a measured half-life of 807 ms [Kne12], is considered to be sufficiently long to achieve production and acceleration via the Isotope On-Line Separation (ISOL) method.

This research works aims to design, model and optimise a radioactive-ion beam production target capable of producing high intensity ^{6}He beams, based on the characteristics of the primary proton beam available for use at iThemba LABS.

1.8 Review of past, present and proposed ^{6}He production facilities

The first documented case of ^{6}He being produced for nuclear physics research purposes was in the early 1990^{s}, through a collaboration between the Belgian universities of Louvain-la-Neuve, Brussels and Leuven [Huy11]. The collaboration project, called the Radioactive Ion Beam project, was housed at university of Louvain-la-Neuve. The Louvain-la-Neuve facility made use of a dual cyclotron providing 30 MeV proton beams at an intensity of 300 µA (9 kW beam power) [Ols93]. Louvain-la-Neuve produced ^{6}He at a maximum intensity of 1.2 x 10^{6} ^{6}He/s (post accelerated) using the 9 kW proton beam impinging a lithium floride (LiF) target [Loi96]. The RIB facility at Louvain-la-Neuve was closed in 2009.

Currently the TRIUMF-ISAC facility in Canada and GANIL-SPIRAL1 facility in France have the capability to produce ^{6}He beams at sufficient intensities for experimentation. The TRIUMF-ISAC facility is currently capable of producing ^{6}He at an intensity of ~ 5.0 x 10^{7} ^{6}He/s using a 32.5 kW proton beam impinging a silicon carbide (SiC) target [TRI18]. GANIL-SPIRAL1 makes use of a 2.5 kW ^{13}C primary beam impinging a ^{12}C target, capable of producing ^{6}He beams at an intensity of 2.0 x 10^{8} ^{6}He/s [GAN16]. The GANIL facility is in the process of upgrading the capacity for radioactive ion beam production, through the proposed SPIRAL-2 facility. GANIL-SPIRAL2 is predicted to be capable of producing ^{6}He at an intensity of ~ 4.0 x 10^{11} ^{6}He/s through the use of 200 kW deuteron (^{2}H) beam impinging a two-step target constituting a rotating carbon converter and beryllium oxide target [Sai10].

Facilities such as CERN-ISOLDE (Switzerland) and SOREQ-SARAF (Israel) have also proposed target designs for high intensity ^{6}He production, for future implementation at these facilities. CERN-ISOLDE plans to make use of a two-step target containing a tungsten convertor and beryllium oxide target, impinged by a 100 kW proton beam predicted to be capable of producing ~ 2.0 x 10^{13} ^{6}He/s. Similar to that of SPIRAL2, the SOREQ-SARAF facility plans to use a deuteron beam with a power of 80 KW impinging a two-step target consisting of a lithium (Li) convertor and beryllium oxide target, which is predicted to yield ^{6}He at an intensity of ~ 2.0 x 10^{13} ^{6}He/s [Sai10].

The challenge for iThemba LABS is to design a target capable of ^{6}He production at appreciable intensities (> 10^{10} ^{6}He/s), comparable or better than the current ^{6}He production rates obtained by operational facilities.

1.9 iThemba LABS RIB Target design process

Initial design and modelling work conducted on the RIB target system for use at iThemba LABS, results of which are presented in this work, focused on graphite as the suitable target material. Graphite was chosen as a natural starting point, as it has been relatively well investigated and modelled by the INFN SPES project team, and therefore the design of the graphite target was used as a means to calibrate/validate the computer models to be used during the design of the iThemba LABS RIB target to that of the experimentally verified SPES computer models. From the outset of this research work, it was well known that boron carbide (B_4C) was a more beneficial target material, as a result of its higher ^{6}He yield, which was verified by preliminary target yield results obtained from the computer code used to simulate reactions. An order of magnitude increase in ^{6}He production was observed from simulation results when using boron carbide as opposed to graphite as the target material. Further optimisation, using the design and modelling process shown in figure 1-5 above, was then conducted for the boron carbide RIB target. Lastly, a two-step RIB target using Beryllium Oxide (BeO) was partially evaluated as an alternative high ^{6}He yielding target, as Beryllium was known (from literature) to be a good material for the production of neutron rich light nuclei. However, the modelling and design process could not be completed on this target, due to the lack of critical material specification information required to conduct feasible thermo-mechanical simulations.

This work presents the technical aspects (of both the physics and engineering fields) investigated and analysed within the target design process, resulting in the design of an optimised RIB target to produce high ^{6}He yields at iThemba LABS.

CHAPTER 2: TARGET DESIGN METHODOLOGY

2.1 Designing the RIB target

When selecting a RIB production target, it is important to optimize the primary beam and target combination with respect to the highest achievable production cross-section and the lowest quantity of undesired nuclei (contaminants) [Van06]. The production of isotopes will be dependent on the nuclear reactions occurring when the primary beam and target material interact. The class of reaction(s) could be direct, compound, spallation and/or fission reactions (these reactions are described in detail in section 2.2.1). Additionally, consideration should be given to the use of a target material that can withstand the highest possible beam currents, within its operational safety envelope. The following section deals with the factors to be considered when selecting a RIB production target, and the system characteristics which influence these factors.

2.1.1 Isotope production in the RIB target

A major objective for any ISOL facility is maximizing the RIB intensity, which can be analytically described by the following equation:

$$I = \emptyset . \sigma . N_{target} . \epsilon_{Diff} . \epsilon_{Eff} . \epsilon_{Ion} . \epsilon_{MS} \ ,$$

where I is the intensity of the radioactive-ion beam, $\emptyset$ the primary beam intensity, σ the production reaction cross section and N_{target} the number of target atoms per surface area. The reaction cross section is an energy dependent measure of the probability that a nuclear reaction will occur during the interaction between the primary beam and the target, and can be expressed as follows:

$$P_{reaction} = n . x . \sigma \ ,$$

where $P_{reaction}$ is the reaction probability per beam particle, n the number of target atoms per unit volume, x the target thickness and σ the reaction cross section (usually expressed in cm^2 or barns, 1 barn = 10^{-24} cm^2).

The efficiency terms are denoted as follows: ϵ_{Diff} is the efficiency for the radioactive atoms of interest to migrate out of the target material (diffusion), ϵ_{Eff} is the efficiency for the transfer of these atoms (from the target material) through the transfer line (effusion), ϵ_{Ion} is the efficiency of ionisation and ϵ_{MS} is the efficiency of mass separation.

The losses as a result of decay are included in the individual efficiencies, ϵ, which are dependent on the speed of release and transport and the lifetime of the isotope under consideration [Kös03]. Selectivity of separation is another important parameter to be considered, as the use of a less selective method would result in a higher isobaric background. This higher isobaric background would require the collection of more data in order to obtain a significant signal above the background for an exotic isotope [Kös03]. The accuracy of the modelling of these processes is crucial for predicting the radioactive-ion beam yield, and in addition, for the study of target optimisation.

Optimising the radioactive-ion beam yield can prove to be rather complex, as all the optimisation factors are interdependent. It is noted for example, that increasing the number of target atoms impinged by the primary beam by means of increasing the target length would be theoretically possible if the primary beam energy is high enough to provide sufficient penetration range. However, the increase in target length, would result in longer release time of the product nuclei and could thus reduce the radioactive-ion beam yield, unless changes to the target geometry (such as splitting the target into a number of wafers/discs with the same total effective ‘increased’ target length) is made to counteract the increased release time. The radioactive-ion beam yield is thus strongly dependent of the exact target geometry and the interplay between the effusion and diffusion processes [Kös03]. Therefore, the optimisation of target size and geometry needs to be done individually, in a somewhat iterative manner.

2.1.2 RIB target requirements

In addition to the material’s reaction cross section and isotope release efficiency (geometric consideration) as discussed in the preceding sections, the following target material properties are desirable [Bro96] for the production of light neutron rich isotopes (^{6}He) at a RIB production facility:

- High melting/sublimation point
- High thermal conductivity
- Chemically inert – minimal corrosion

- Radiation damage resistance
- Target material composition – minimal impurities
- Material availability and cost

The thickness of the production target is chosen in order to maximize the production rate, more specifically the desired yield. The production target is often of sufficient thickness to stop the impinging primary beam delivered from the accelerator. The beam power deposited into the target results in a temperature increase of the target material, and introduces thermo-mechanical stresses. The target lifetime is thus determined by the time in which the target is able to operate under these thermo-mechanical conditions, before failing due to cracking, sintering or evaporation. In order for a target to be considered useful, a target lifetime of at least a few weeks is usually required [Str04], although not always achieved.

2.1.3 RIB target modelling – Computer simulations

The RIB production target design can be divided into two phases/categories, starting with the modelling and analysis of the production reactions occurring during the primary beam-production target interaction and secondly, modelling of the energy transfer and material effects occurring in the target system as a result of the production reactions taking place. Due to the statistical nature of the processes involved in production reactions and the complex numerical solutions required to analyse the mechanical and thermal effects on the target materials resulting from the production reactions, computer simulations are used to model and analyse these complex multi-variable problems. These computer simulations allow for the solutions of large equation sets within the user defined physical boundaries (i.e. target material properties, target geometry, primary beam properties, etc.). The following aspects of RIB target design are modelled/analysed/solved using computer simulations:

- **Nuclear reactions and decay processes** occurring during the interaction of the primary beam and target - provide details regarding the species and their quantities produced in this interaction.
- **Energy transfer mechanisms** during the primary beam and target material interaction – provide details regarding the energy deposited into the target by the primary beam and energy released as a result of the nuclear reactions occurring during the interaction.

- **Thermal and mechanical analysis** of target system materials – provides details regarding the thermal and mechanical effects undergone by the materials in the target system as a result of the energies imparted on it during operation.
- **Release of reaction products –** provide details regarding the rate at which reaction products are released from the target system.

The computer simulated aspects listed above, except that of the release of reaction products, are employed in this research work and will be described in further detail in the remainder of this chapter.

2.2 Nuclear Physics Aspects

The two most important nuclear physics aspects as it relates to the modelling of a RIB target, is that of nuclear reactions and nuclear decay. The ability to accurately predict and model, by means of computer simulations, the nuclear reactions taking place during the beam-target material interaction and the subsequent nuclear decay processes undergone by the produced radioactive nuclides, is a key criterion in RIB target design. These aspects (nuclear reactions and nuclear decay), relevant to the experimental energy range (< 100 MeV) considered in this work, are discussed in the sub-sections to follow.

2.2.1 Nuclear reactions

A ‘*nuclear reaction’* occurs when a particle (e.g. proton, neutron) strikes a nucleus, resulting in an interaction between particles. Depending on the energy of the incoming particle, different types of reactions, also known as reaction channels, could occur. A simple reaction is generally written as follows [Kra88]:

$$A + a \rightarrow B + b \; .$$

Or more concisely:

$$A(a, b)B \; ,$$

where A is the target nucleus, a the incident particle, B the residual nucleus and b the ejectile.

In the production of RIBs, the most commonly employed reaction channels/types are direct, compound, spallation and fragmentation reactions. Although not all of these reaction types are relevant to this research work (e.g. compound reactions), they are briefly elaborated on below.

Compound reactions

A compound reaction is a two-step process in which the incident particle (a) and target nucleus (A) merge, forming an intermediate 'compound nucleus' (C^*) before de-exciting by releasing one or more particles through evaporation. Compound reactions generally occur in a time period < 10^{-16} seconds. The most common final state is one in which two classes of final products are formed, the evaporated (ejected) particles (b) plus the residual nuclides (B), as follows [Ber04]:

$$\boldsymbol{A + a \rightarrow C^* \rightarrow B + b} \, .$$

Direct reactions

A direct reaction is a reaction in which the incident particle probes the nucleus and in doing so, proceeds directly from an initial state to a final state without the formation of an intermediate compound nucleus. Direct reactions generally occur with incident particle energy > 20 MeV/A and in a time period in the order of 10^{-22} seconds, considered 'fast' when compared to compound reactions [Ber04]. There are various types of direct reactions, described as follows [Ber04] [Kra88]:

- **Elastic scattering:** In elastic scattering reactions the target nucleus remains unchanged and in its ground state.
- **Inelastic scattering:** In inelastic scattering reactions the target nucleus is left in an excited energy state.
- **Transfer reactions:** In a transfer reaction, the transfer (or rearrangement) of nucleons between the target nucleus and incident particle occurs. There are two sub-groups of transfer reactions:
  - **Stripping** – a nucleon (or nucleons) is transferred from the incident particle to the target nucleus
  - **Pickup –** a nucleon (or nucleons) is transferred from the target nucleus to the incident particle (which becomes the ejectile)

- **Knock-out reaction:** In a knock-out reaction the incident (a) and ejectile (b) is the same, but the reaction causes another nucleon to be ejected from the target nucleus, separately.
- **Break-up reactions:** In a breakup reaction one or more particles are emitted from the target nucleus after interaction with the incident particle. The incident particle is not always present in the final reaction state.

Fission reactions

The fission reaction/process was discovered in the late 1930s, shortly after James Chadwick's prolific discovery of the neutron in 1932. Subsequent to the discovery of the neutron, it was soon realised that *thermal* neutrons could induce splitting of the nucleus. The fission reaction, by means of neutron induced nucleus splitting would from this point on, go on to be one of the most significant industrialised nuclear processes on Earth. Fission reactions are more applicable to the production of heavy neutron rich nuclei and are generally not prevalent in the production of light neutron rich nuclei, such as ^{6}He (considered in this work).

Fission reactions are classified into two groups, spontaneous fission and induced fission. Spontaneous fission occurs when an unstable nucleus splits up in order to attain a more stable state and in doing so, releases energy, fission fragments and particles. Induced fission occurs when a material is bombarded by particles such as protons or neutrons, resulting in a release of energy, fission fragments and particles [Gar16].

Spallation reactions

Spallation is a nuclear reaction in which a light projectile, such as a proton or neutron with kinetic energy ranging from several tens of MeV to several GeV, interacts with a heavy nucleus (production target) and results in the emission of a large number of hadrons (mostly neutrons) or reaction fragments [Krá10]. The two most important aspects in spallation reactions are spallation products (residual nuclei) and spallation neutrons. Spallation reactions occur in two stages, namely intra-nuclear cascade (INC) and de-excitation.

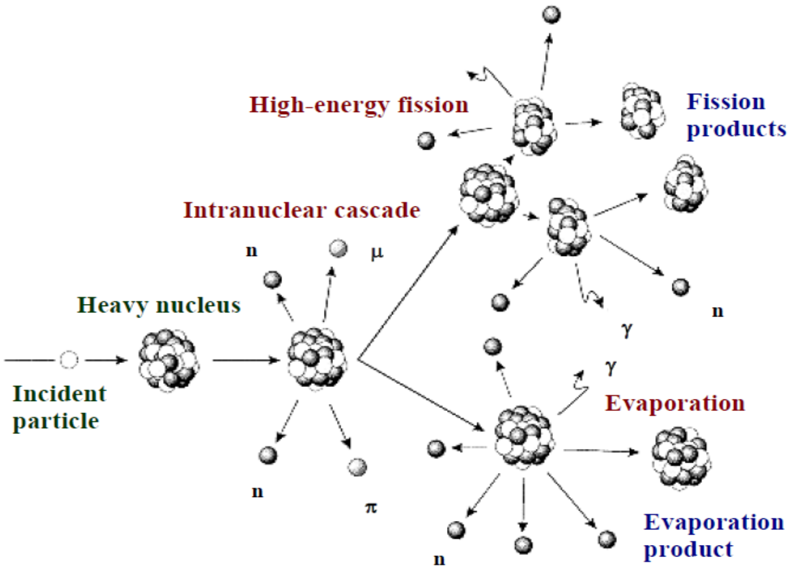

Figure 2-1: Spallation reaction scheme [Krá10].

The intra-nuclear cascade is a fast and direct stage, approximated to occur within 10^{-22} seconds. The incoming light projectile (i.e. proton) distributes its kinetic energy to the nucleons in the target material by elastic collisions, which results in a cascade of nucleon-nucleon collisions [Pfü12]. These fast proceeding nucleon-nucleon interactions lead to the ejection of some of the nucleons from the nucleus as well as to the excitation of the residual nucleus [Mon05], as depicted in figure 2-1, above. The subsequent de-excitation of the residual nucleus proceeds via two stages, namely evaporation and fission. The residual nucleus reduces its energy by isotropic evaporation of neutrons or light nuclei, such as alphas, helions, deuterium, tritium, with energies up to ≈ 40 MeV [Mon05]. In the second de-excitation process, fission, the residual nucleus is split into two fragments of different masses. When the excitation energy of the nucleus becomes less than the binding energy, typically around 8 MeV, the nucleus does not have enough energy to emit neutrons and thus de-excites via gamma emission [Krá10]. At the end of the de-excitation stage, the resulting nucleus is usually radioactive and will undergo nuclear decay until it reaches a stable state.

The above mentioned processes deposit heat in the target material, primarily from ionisation energy loss of the incoming projectile, as well as the kinetic energy of the nuclear collision interactions.

2.2.2 Nuclear Decay processes

As discussed in section 1.1, nuclei far from the valley of beta stability, characterised by their excess or shortage of neutrons, are unstable and therefore radioactive. The radioactive nuclei decay to a stable state by emitting different particles or electromagnetic radiation, dependent on the nature of the given nucleus. These nuclear decay mechanisms are therefore responsible for the transmutation of reaction products produced in the RIB system. Before elaborating on these decay mechanisms, an interlinking concept, known as half-life is worth discussing in sufficient detail.

The half-life is the measure of how quickly an unstable nucleus (radioactive) will decay. Half-lives can range from a fraction of a second to billions of years, as represented in figure 2-2 below. The radioactive half-life for a radioisotope is essentially a measure of the probability of the given nucleus to decay/disintegrate [Nav17]. The half-life of a radioisotope is independent of the physical state, temperature, pressure and any other external influence. Radioactive decay is a statistical process which is dependent on the instability of the particular radioisotope, but which for any given nucleus in a sample is completely unpredictable [Nav17]. Half-life can be mathematically expressed by starting with what is known as the decay constant (λ), given as follows:

$$dN = -\lambda . N . dt \, .$$

Rearranging:

$$\lambda = \frac{(dN/dt)}{N} ,$$

where N is the number of radioactive nuclei present at time t. The right hand side of the above equation is the probability per unit time for the decay of an atom. Integrating the equation above leads to the exponential law of radioactive decay, expressed as:

$$N(t) = N_0 e^{-\lambda t} ,$$

where N_0 is the original number of nuclei present at $t = 0$. The half-life $(t_{1/2})$ of a nuclide can now be expressed, as the time required for half of the original number of nuclei to decay, thus $N = N_0/2$. Solving the above equation:

$$t_{1/2} = \frac{\ln(2)}{\lambda}.$$

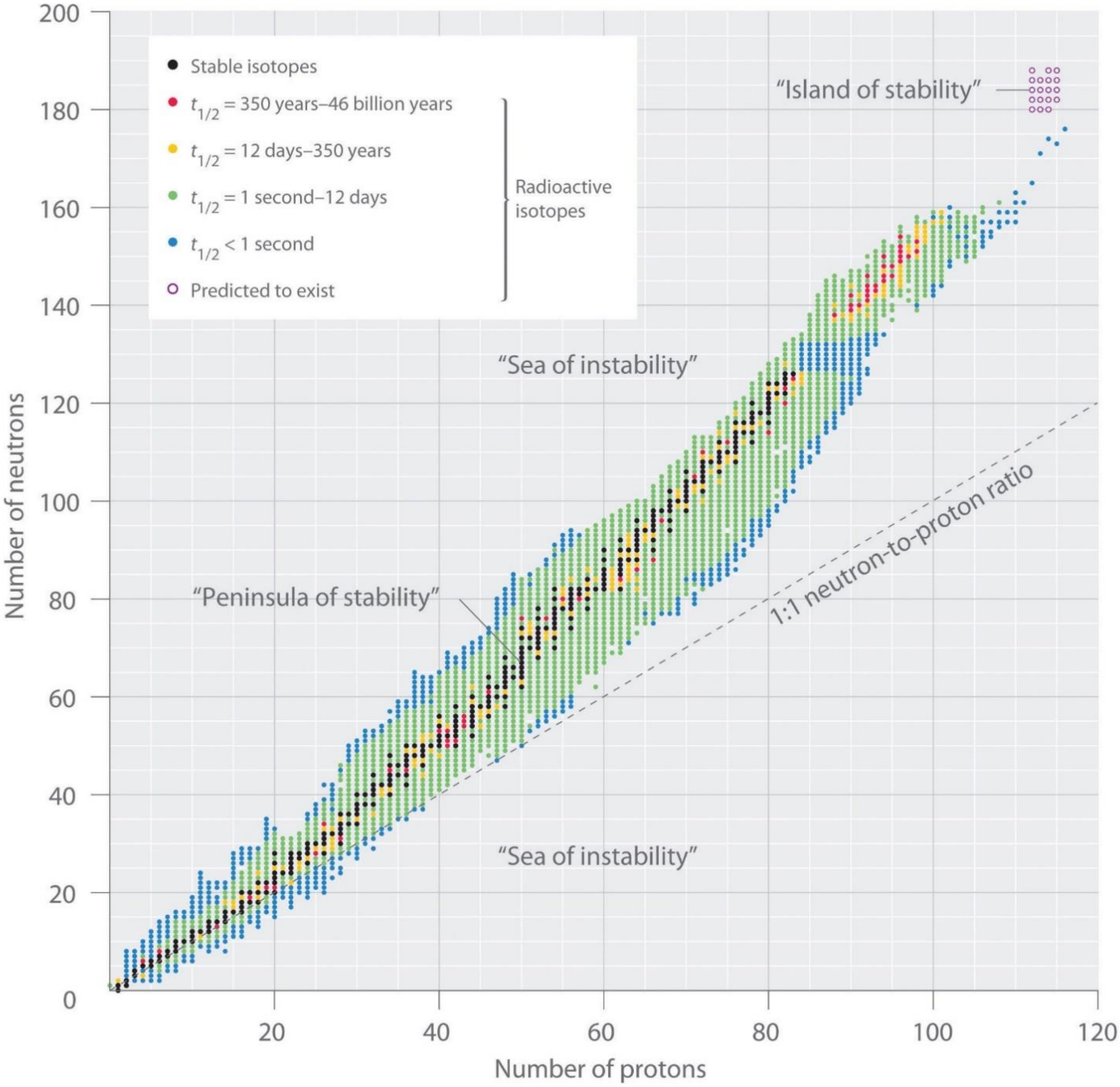

Figure 2-2: Chart of nuclei exhibiting the vast half-life range of radioactive nuclei [Sil07].

There are generally four types of decay mechanisms which can occur, described as follows:

- **Alpha Decay**:

  Alpha decay generally occurs in elements with a proton number, $Z > 83$, and is characterised by the emission of an alpha particle, or more descriptively, a helium nucleus (^{4}He) containing 2 protons and 2 neutrons. An example of such a decay process/reaction is shown as follows:

$$^{263}_{106}\mathrm{Sg} \rightarrow \ ^{259}_{104}\mathrm{Rf} + \ ^{4}_{2}\mathrm{He}$$

- **Beta Decay and Electron capture**:

  Beta decay can occur by three modes, namely beta-minus (β^-) decay, beta-plus (β^+) decay and electron capture. Beta-minus decay is the process in which a neutron is converted into a proton, accompanied by the emission of an electron (β^- particle) and an antineutrino ($\bar{\nu}$). Beta-minus decay thus results in Z being increased by 1 and A remaining constant. Beta-minus decay is specific to neutron-rich nuclei, and by undergoing this process of removing excess neutrons, the resultant nuclei moves closer to the valley of beta-stability [Fri81]. An example of the β^- decay process is shown as follows:

$$\mathrm{n} \rightarrow p^+ + \beta^- + \bar{\nu}$$

  In contrast, β^+ decay, is the process in which a proton is converted to a neutron, accompanied by the emission of a positron (β^+ particle) and a neutrino (ν). Beta-plus decay thus results in Z being reduced by 1 and A remaining constant. Beta-plus decay is specific to neutron-deficient nuclei, and by undergoing this process of neutron addition, the resultant nuclei move closer to the valley of beta-stability. An example of the beta-plus decay process is shown as follows:

$$\mathrm{p}^+ \rightarrow \mathrm{n} + \beta^+ + \nu$$

  Electron capture is the competing reaction/process of the β^+ decay, and has the same net effect on the atom in question, with Z being reduced by 1 and A remaining constant. Electron capture proceeds when an orbital electron of a given nucleus is captured by a proton in the said nucleus, resulting in the emission of a neutrino (ν) [Che12].

- **Gamma ray emission**:

  Decay via gamma-ray emission differs from the other 3 decay mechanisms as it does not result in a change in proton number (Z) or mass number (A) of the nucleus undergoing this type of decay. When a nucleus undergoes alpha or beta decay, a newly formed nucleus is produced, referred to as the ‘daughter nucleus’. Since this daughter nucleus is usually in an excited state, it emits its excess energy through electromagnetic radiation, also known as gamma rays, in order to reach a stable state. An example of the gamma-ray emission process is shown as follows:

$$^{137}_{56}\mathrm{Ba} \rightarrow \ ^{137}_{56}\mathrm{Ba} + \ \gamma$$

- **Spontaneous fission:**

  Spontaneous fission is the phenomenon in which a heavy nucleus spontaneously breaks apart, forming two large fragments accompanied by neutron emission [Fri81]. An example of the spontaneous fission process is shown as follows:

$$^{254}_{98}\mathrm{Cf} \rightarrow \ ^{118}_{46}\mathrm{Pd} + \ ^{132}_{52}\mathrm{Te} + 4^{1}_{0}\mathrm{n}$$

2.3 Energy Transfer Mechanisms

A key aspect of RIB target design is the modelling and analysis of the energy transfer mechanisms occurring during operation. This analysis is conducted by means of computer simulations, which can provide detailed information regarding the energy deposited into the target by the primary beam during the beam-target interaction.

The stopping power of a material is defined as the rate at which a given particle loses energy per unit path length when impinging on the material [Ros14]. The mathematical derivation of this stopping power is known as the *Bethe-Bloch* formula, and is expressed as follows [Ros14]:

$$-\frac{dE}{dx} = \left(\frac{Ze^2}{4\pi\varepsilon_0}\right)^2 \frac{4\pi Z\rho N_A}{Amv^2}\left[\ln\left(\frac{2mv^2}{I}\right) - \ln(1-\ \beta^2) - \beta^2\right],$$

where Ze is the particle’s electronic charge, m the mass of an electron, N_A Avogadro’s number, A and Z the atomic mass number and proton number respectively, ρ the density of the stopping material and $v = \beta c$ the velocity of the ion. Most light particles are stripped of their electrons when moving through matter and, hence, the charge of the impinging light particle can be considered equal to Ze. The quantity, $I,$ is the energy required to ionise an atom in the material and is considered as an empirical parameter used as $I \approx 11\,Z\,\mathrm{eV}$

[Ros14]. The stopping range for materials is commonly expressed in units of energy loss per mass per unit area (i.e. MeV.mg^{-1}.cm^{2}), which is obtained by dividing the stopping power, $-dE/dx$, by the density of the material [Ros14].

It should be noted that two types of stopping, namely electronic and nuclear, are present when a projectile impinges a target material. Electronic stopping occurs as a result of the collisions between the impinging particle and the electrons of the target material and leads to excitation and ionisation of target atoms as well as energy loss of the impinging particle. In contrast, nuclear stopping is a result of the elastic collisions between the impinging particles and target material's nuclei [Bos11]. The total stopping power of a material is given as the sum of the electronic and nuclear stopping power. For interactions involving a light particle impinging a heavy target, the nuclear stopping power is considered negligible in comparison to the electronic stopping powers, with the nuclear stopping power increasing the heavier the impinging particle is. Additionally, at high primary/impinging particle velocities (typically > keV), electronic stopping is the dominant stopping mechanism [Yos16]. Figure 2-3 below illustrates the total, electronic and nuclear stopping power of a proton impinging on graphite. From figure 2-3 it is noted that the contribution of the nuclear stopping power to the total stopping power is negligible, as it is numerous orders of magnitude lower than that of the electronic stopping power across the depicted energy range (keV to GeV), with the contribution decreasing with an increase in proton energy. Since this research work only considers high energy (> MeV) light particles (protons) impinging heavy targets, the total stopping power is considered to be that of the material's electronic stopping power.

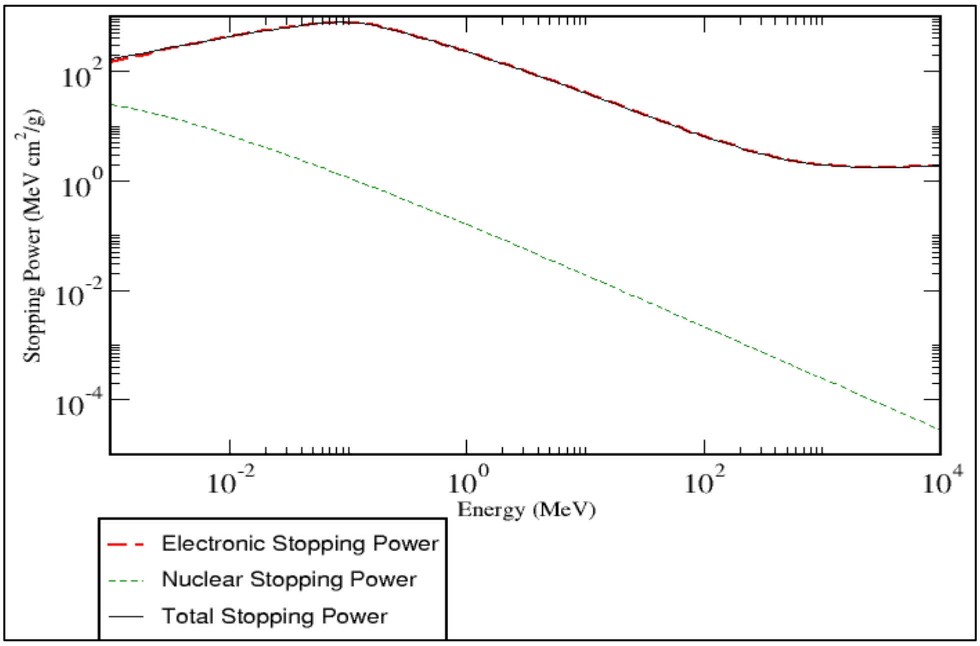

Figure 2-3: Stopping power of protons in graphite (ρ = 1.7 g/cm^3). Adapted from source [Sel93].

Additionally, when an incident particle travels through the material, ionising atoms and depositing energy along its path, a maximum peak in stopping power is noted just before the particle comes to rest (kinetic energy ~ 0) [Bro16]. This maximum peak in stopping power is known as the Bragg peak, discovered by British physicist Sir William Henry Bragg in 1903.

The Bragg peak occurs as a result of the interaction cross section increasing as the charged particle's energy decreases. The energy lost by charged particles is inversely proportional to the square of their velocity, due to greater time spent in the negative electron field when the particle velocity is low and hence the peak occurs just before the particle comes to rest [Nuc17]. Slight variations in the Bragg curve for a given material with the same incident particles and initial energy could be noted as a result of what is known as *straggling*. The straggling effect is due to the fact that microscopic interactions involving any specific particle will have some measure of random variation as a result of the statistical nature of the energy loss process which consists of a large number of individual collisions [Nuc17]. Figure 2-4 below, illustrates the typical profile of a Bragg curve.

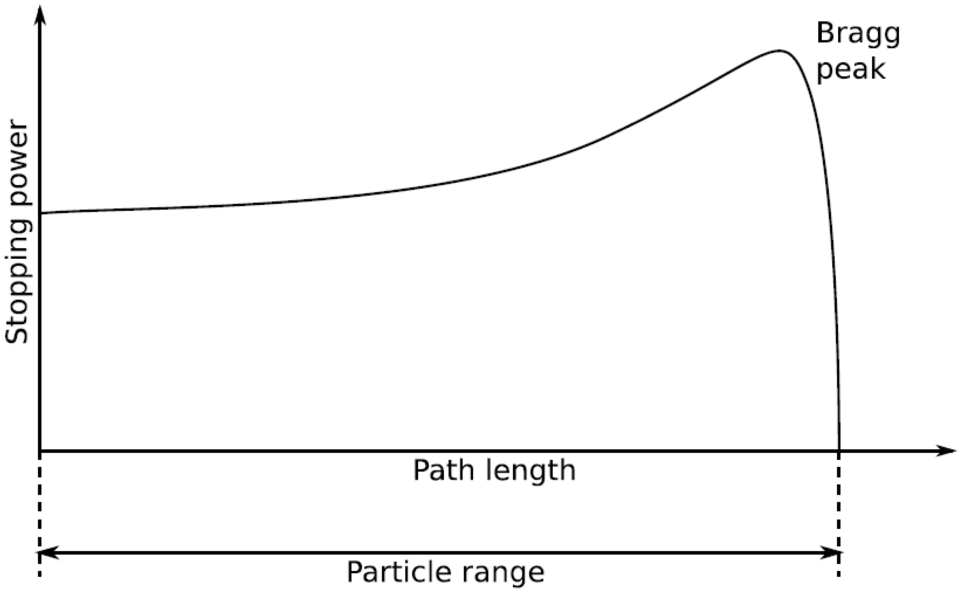

Figure 2-4: Generic illustration of a Bragg curve, with Bragg peak towards the end of the particle range [Ros14].

In this research work, the computer code/software, SRIM, was employed to calculate the stopping powers of the proposed RIB target materials. SRIM, *Stopping and Range of Ions in Matter*, is a widely applied collection of software packages which is able to calculate many features of the transport of ions in matter. SRIM allows for quick calculations which produce tables of stopping powers, range and straggling distributions for any ion at any energy in any elemental target [Zie10].

2.4 Solving the RIB Physics problem – FLUKA

FLUKA (*FLUktuierende KAskade*), is described as a general purpose tool for calculations of particle transport and interaction with matter [Fer05]. The original FLUKA code was written in the 1960s for the purpose of designing shielding systems in high energy proton beam accelerators. Over the years, FLUKA was gradually developed to cover a large variety of applications, which include neutrino physics, cosmic ray physics, calorimetry, radiation protection, activation studies and many more [Wür16]. FLUKA is an ideal tool for modelling, analysing and solving the nuclear physics aspects of RIB target design as discussed in sections 2.2 and 2.3 above.

In this research work, FLUKA is used to simulate the various nuclear reactions occurring during the primary beam and RIB target interaction as well as to provide an indication of the residual nuclide yields to be expected from these reactions, based on the experimental parameters provided. Additionally, FLUKA is used to calculate the energy deposition of the primary beam in the target material, which is subsequently used (in engineering software packages, to be discussed in section 2.5) to model and analyse the thermal and mechanical (thermo-mechanical) loads undergone by the RIB target system materials during operation.

Some of the key aspects of FLUKA are briefly discussed in the sub-sections to follow.

2.4.1 Monte Carlo method

The FLUKA software package employs the Monte Carlo simulation method to predict the outcomes of various physics models, with given input parameters, and provides results/outputs with a minimal set of free parameters fixed for all energy/target/projectile combinations. FLUKA is able to simulate, to a high degree of accuracy, the interaction and propagation in matter of about 60 different particles (neutrinos, neutrons, hadrons, photons, electrons, etc.), for a vast array of ‘particle dependent’ energy ranges [Wür16].

The Monte Carlo (MC) method can be defined as a class of computational algorithms which makes use of repeated random sampling to compute results [Rub16]. These algorithms are constructed from insight into a given physical system described by natural laws and numerical methods in the form of differential equations. The algorithm is then coded into a computer program and executed to produce results, in the form of desired output parameters of the physical system. The coding of algorithms containing the MC method (repeated random sampling) is therefore referred to as a Monte Carlo simulation (and/or simulation code).

MC simulation can therefore be considered as a methodical way of conducting a “what-if analysis”, using mathematical models [Ray08]. These mathematical models rely on a number of input parameters, which produce one or more outputs, when processed through the mathematical formulas in the model [Ray08], as depicted in figure 2-5, below.

Figure 2-5: Mathematical model process flow diagram [Ray08].

In MC simulation, the statistical distribution to be used as a source for each of the input parameters is identified. Random samples are then drawn from each distribution, representing the values of the input variables. For each set of input parameters, a set of output parameters is produced. The value of each output parameter is thus one outcome scenario in the simulation run [Ray08].

2.4.2 FLUKA – Code aspects

PEANUT Model

In FLUKA, nuclear reactions below 1 GeV are computed using the PEANUT model. The PEANUT (**P**re-**E**quilibrium **A**pproach to **NU**clear **T**hermalisation) model accounts for the following nuclear processes: intranuclear cascades (INC), pre-equilibrium emission, evaporation and de-excitation [Fas03].

Within the Intranuclear cascade (INC) component of the PEANUT model, relativistic kinematics are applied, with accurate conservation of energy and momentum, with the inclusion of the recoil energy and momentum of the residual nucleus. All particles are transported along paths which are subject to the shape of the Coulomb and nuclear potentials, allowing for refraction and reflection at the nuclear surface to be accounted for and the Coulomb effects to be accurately described [Fas94].

Particle Transport

Within the confines of four assumptions – (1) particles travel in straight paths with no energy losses between collision points, (2) particles undergo a collision per unit distance with probability $P(t)$, (3) the transition time between entering and leaving a collision is negligible, and (4) the particle transport being simulated is linear [Car75], a generic description of the particle transport mechanism occurring during FLUKA simulation can be given as follows:

Considering a particle in Cartesian coordinates, with its origin being (x, y, z) and direction of flight specified by direction cosines as (u, v, w). The new position of this particle after travelling a distance k would thus be $(x', y', z') = (x, y, z) + k(u, v, w)$. The free distance travelled, k, is a function of the material the particle interacts with, the type of particle and the energy of the particle [Car75].

Once the particle has travelled it's free path, the collision takes place which results in a variety of interactions with various particles of the target material. FLUKA is designed to solve transport problems consisting of shared regions. The material properties within each region are uniform in order to make the data storage traceable. The region's boundaries are specified by one or more quadratic surfaces of the general form:

$$Ax^2 + By^2 + Cz^2 + Dxy + Eyz + Fzx + Gx + Hy + Jz + K = 0 \ ,$$

where $A, B, C, \dots., K$ are constants [Car75]. For a simple surface, such as a plane, sphere, or cylinder, several of these coefficients are zero, and FLUKA thus treats these as special cases of the more general equation in order to save computation time.

Estimators and "Scoring" process

Any result produced in a Monte Carlo calculation is obtained by summing up the contributions to the "score" or "tally" of a user defined detector. A detector is the Monte Carlo equivalent of a measurement device. In FLUKA, each detector, also referred to as an estimator, is designed to estimate one or more radiometric quantities, with the final score/tally being a statistical estimation of the average value of the corresponding population [Fer05]. As in experimental measurements, it is possible to compute a standard deviation by running several independent computations.

2.4.3 FLUKA – Input file and simulation properties

In FLUKA, the framework and conditions for simulation are defined in a user developed input file. These input files consist of a various number of ‘commands’ (also referred to as ‘options’), with each command containing one or more ‘lines’ (also referred to as ‘cards’). In addition to the FLUKA commands, the input files may contain the description of the geometry of the experimental set-up to be simulated. The detail of this geometric description is provided by means of specific geometry ‘command cards’ [Fer05].

The typical, generic layout of a FLUKA input file could be described as follows:

- Simulation title
- Description of experimental geometry
- Definition of experimental material
    - When using user-defined material and/or material properties
- Material assignments
    - Regions of the experimental geometry are to be assigned a specific material
- Definition of particle source
    - Including particle type, initial position, travel path, distribution profile, energy (momentum)
- Definition of detectors
    - Various detectors (estimators) can be defined, corresponding to different quantities and to different algorithms used to estimate them.
- Definition of optional problem settings
    - Settings such as energy cut-offs, step size, physical effects not simulated by default, particles not to be transported
- Initialization of the random number sequence
    - Mandatory for the estimation of the statistical errors
- Starting signal and number of requested histories

One of the most important aspects to define accurately are the characteristics of the primary particle beam. The parameters of the particle beam are defined in the cards “BEAM” and “BEAMPOS”. In “BEAM” the particle beam type (proton, neutron, deuteron, etc.) and energy (momentum) are defined, whereas the beam’s starting co-ordinates and direction are defined in the “BEAMPOS” card. These two cards can also be used to define particle beams having angular or momentum distributions (i.e. Gaussian or rectangular), as is the case in this thesis work (discussed in section 2.6.1.1). The “PART-THR” card defines the transport cut-off energy for hadrons (e.g. protons), muons and neutrinos. In order to override the standard FLUKA defaults for some physics processes, the “PHYSICS” card is used. As applied in this research work, the “PHYSICS” card in set to activate ‘new evaporation with heavy fragmentation’, allowing for the modelling of the evaporation process of fragments up to mass number, $A = 24$, which is critical for the calculation of residual nuclei.

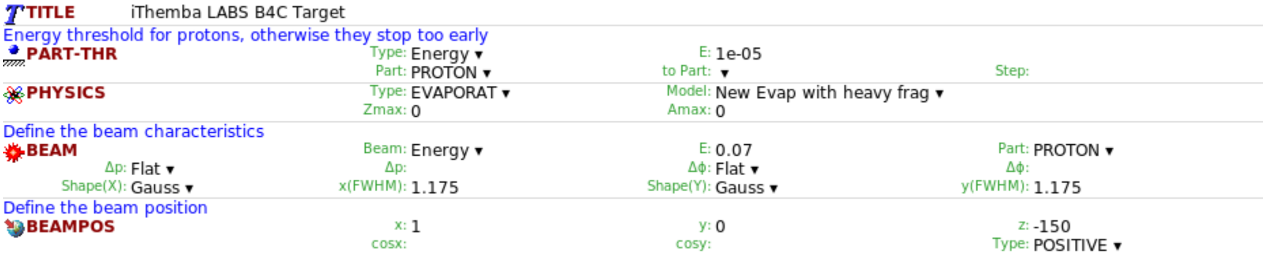

```
TITLE          iThemba LABS B4C Target
Energy threshold for protons, otherwise they stop too early
PART-THR                          Type: Energy ▾                E: 1e-05
                                  Part: PROTON ▾          to Part:  ▾                       Step:
PHYSICS                           Type: EVAPORAT ▾          Model: New Evap with heavy frag ▾
                                  Zmax: 0                    Amax: 0
Define the beam characteristics
BEAM                              Beam: Energy ▾                E: 0.07                     Part: PROTON ▾
              Δp: Flat ▾            Δp:                        Δϕ: Flat ▾                     Δϕ:
        Shape(X): Gauss ▾     x(FWHM): 1.175          Shape(Y): Gauss ▾                y(FWHM): 1.175
Define the beam position
BEAMPOS                              x: 1                       y: 0                           z: -150
                                  cosx:                      cosy:                          Type: POSITIVE ▾
```

Figure 2-6: Example of FLUKA “BEAM” and “BEAMPOS” cards.

FLUKA can handle both elemental and compound materials, the cards “MATERIAL” and “COMPOUND” are used to define these, respectively. The “ASSIGNMA” card, assigns the material or compound to a given region in the geometry. Two predefined ‘materials’ in FLUKA are worth mentioning due to their extensive use in FLUKA simulations, these are “BLCKHOLE” and “VACUUM”. Where the predefined “BLCKHOLE” is a material with infinite absorbance and “VACUUM” is a material with no absorbance.

Using the “RANDOMIZ” card, random number sequences can be generated, allowing several simulation jobs to run in parallel. The card “START” allows the user to set the number of primaries/particles to be simulated upon execution of the simulation.

2.4.4 FLUKA – Outputs

The outputs obtained from FLUKA are all explicitly requested by user defined scoring options (also referred to as scoring ‘cards’), as no default detector(s) are available. There are different input options corresponding to different types of detectors. The detectors/scoring cards relevant to this thesis work are briefly discussed in the sub-sections to follow.

<u>USRBIN</u>

Similar quantities can be scored in a uniform spatial mesh which is independent of geometry, called a “binning”, by means of FLUKA defined scoring card, USRBIN. There are several binning types, namely, Cartesian, 2D-cylindrical, 3D-cylindrical and more complex phase space structures. It is possible to use USRBIN to score dose, particle density and fluence distributions [Fer05]. USRBIN results are displayed as colour plots, with each colour corresponding to a pre-defined range of values.

USRBDX

The scoring card USRBDX calculates fluence averaged over the boundary between two geometry regions (e.g. across the surface of a material). It is therefore a boundary crossing estimator, scoring fluence as the surface density of cross particles weighted with the secant of the angle between the trajectory and normal to the boundary at the crossing point [Fer05]. The USRBDX results obtained can account (on user request) for particles crossing the boundary from either side or from one side only, and are in the form of double-differential energy and angular spectra.

USRYIELD

The scoring card USRYIELD is a multi-purpose estimator option, which can score several different double-differential quantities. The most common application of this card is for scoring the energy-angle double differential yield of particles escaping from a target, with the angle being with respect to a fixed directions [Fer05]. Energy and angle can be replaced by many other variables, such as momentum and rapidity.

RESNUCLEi

Scoring the production of residual nuclei can be conducted with the scoring card RESNUCLEi. The results obtained are provided through the scoring of residual nuclei after inelastic hadronic interactions and may include nuclei produced in low-energy $(E < 20\,MeV)$ neutron interactions, provided the corresponding information is available in the neutron cross-section library for the material of interest [Fer05].

2.5 Release of reaction products from a RIB target

Another significant physical factor for a RIB production target is its ability to release the desired nuclides at a rate that is faster or comparable to the radioactive decay rate of the desired nuclei. Three release processes, namely diffusion, adsorption and effusion, are to be considered during target design and are all strongly temperature dependent [Str04]. The targets are thus operated at the highest possible temperature (often in excess of 2000 ^{0} C), within its thermo-mechanical restrictions. In order to fully capitalize on the favourable effect of high temperature target operation, short diffusion paths within the target are generally required. Short diffusion paths, achieved by the use of thin fibre, powder or high voidage material structures, assist in minimizing losses due to radioactive decay during the period in which the nuclei diffuses from the target material matrix. In addition, an open material structure is favourable, allowing the desired nuclei to diffuse out of the target material matrix and into a collection chamber from which it can be extracted for further use in the RIB production process (ion-source, post-acceleration).

Once radioactive nuclei are generated within the target matrix, they migrate (diffusion process) with a given direction and speed, directly related to the operating temperature and microstructure of the target material. Once the nuclei migrate to the surface of the target material, certain nuclei would typically move in the surrounding target system volume (target canister), undergoing several collisions, before migrating through a transfer line (effusion process) directly connected to the target system, to reach the ion source. The term ‘release time’, is used to describe the time elapsed between the moment a given nucleus is produced to the moment this nucleus is extracted from the ion source. The release time is dependent on the diffusion from the target material, desorption (adsorption process) from the material surface and the effusion to the ion source exit [Van06]. During operation, collisions between the produced nuclei and the target system’s internal components (often called ‘sticking’), can have an increasing effect on the release time. Additionally, the release time could be increased by chemical reactions and re-diffusion inside the target material. Re-diffusion is generally uncommon, as target systems are typically operated at temperatures high enough to ensure that re-diffusion does not occur [Cor13].

For the case of “thin” target materials (e.g. discs/wafers), the thickness of the target is significantly smaller than its other dimensions. Diffusion is therefore only considered in the direction perpendicular to the surface of the foil. The diffusion process can be analytically described by means of Fick’s second law of diffusion, as follows [Ego16]:

$$\frac{\partial C(\vec{x},t)}{\partial t} = \nabla.\left(D(\vec{x})\nabla C(\vec{x},t)\right).$$

Accounting only for the perpendicular component (x), the above equation can be further simplified to:

$$\frac{\partial C(x,t)}{\partial t} = \frac{\partial}{\partial x}\left[(D(\vec{x})\frac{\partial C(x,t)}{dx}\right],$$

where D is the diffusion coefficient of the diffusing species/nuclei in the material and C the concentration profile of the species/nuclei. The Arrhenius law is used to describe the temperature dependence of the diffusion coefficient, shown as follows [Ego16]:

$$D = D_0 exp\left[-\frac{\Delta H}{RT}\right],$$

where T is the absolute temperature, ΔH the activation enthalpy of diffusion and R the universal gas constant. The above equation shows that the diffusion coefficient increases with increasing temperature, and it is for this reason that ISOL targets are required to be operated at high temperature.

In order to model/simulate the release of ^{6}He from the RIB targets proposed in this work, the use of RIBO (Radioactive-ion Beam Optimizer), a Monte Carlo code which is able to track the paths of point-like objects (namely atoms or photons) moving within solid (and even moving) boundaries [San05], was considered. RIBO was developed under the EURISOL (European Isotope Separation Online) project, with the intent of simulating the main phenomena involved in isotope extraction and ion beam formation, namely, diffusion, effusion, ionization, and ion transport. However, private communication with the INFN SPES project leader indicated that based on user experience, the RIBO code has proven to be unreliable and thus the use of RIBO was not advised.

Therefore, the release of reaction products was not simulated due to the unavailability of reliable computer codes for this application, coupled with the lack of information in literature pertaining to diffusion coefficients of ^{6}He diffusing from the target materials considered in this work (i.e. graphite, boron carbide and beryllium oxide). The release of ^{6}He from these target materials, thus requires experimental measurement for future refinement of this RIB target design study.

It should be noted however, that study was conducted by Stora et al. [Sto12] at CERN-ISOLDE in 2012, in which the release efficiency of ^{6}He from a two-step target, with tungsten (W) as the convertor and beryllium oxide (BeO) as the target material, was investigated. The extraction efficiency from the hot BeO target was measured in the temperature range from 700 to 1400 °C. This study found that 82% of the ^{6}He produced in-target was extracted at 1400 °C.

Although this study does not have direct application/bearing on this research work, it provides confidence that an appreciable quantity of ^{6}He can be extracted from solid targets at high temperatures.

Although the isotope release has not been calculated/simulated in this research work, the principles applied for reduction in release times, namely, high temperature target operation and low target material thickness, are taken into account during the RIB target design process.

2.6 Engineering Fundamentals of Materials

In order to link the before mentioned physics aspects related to the energy transfer mechanisms present during RIB target operation and the material engineering aspects (both mechanical and thermal) of the RIB target, the following concepts (in the sub-sections to follow) require a detailed description.

2.6.1 Mechanical Properties of materials

The mechanical properties of materials are dependent on the composition and microstructure of the specific material. The strength and ductility of a given material are directly related to material composition, mechanisms of bonding, defects and crystal structures. The following sections provide a review of the fundamental mechanical properties of materials and their behaviour under applied loads.

2.6.1.1 Stress and Strain

Stress is considered as the intensity of force, measured in terms of force per unit area of the surface upon which it acts [Ask11] [Roy08]. Three categories of stress exists, namely tensile, compressive and shear stresses. Tensile and compressive stresses are considered normal stresses, where a normal stress arises when the force applied acts perpendicular to the area of interest. Tension causes elongation in the direction of the applied force, whereas compression causes shortening. A shear stress results when the applied force acts in a direction parallel to the area of interest [Ask11].

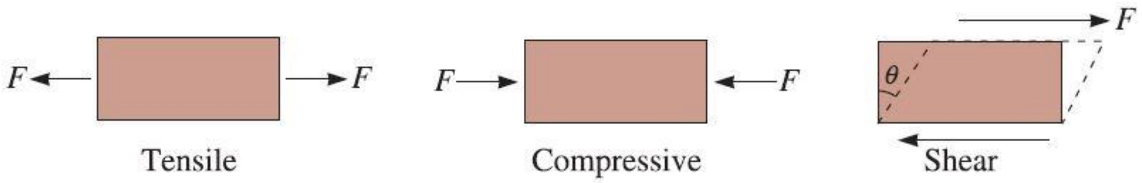

Figure 2-7: Schematic of Stress types [Ask11].

Strain is defined as the change in dimension per unit length [Ask11]. Elastic strain is defined as strain which is completely recoverable from an applied stress. The strain is said to be elastic if it develops as soon as the force is applied, remains for the period during which the load/force is applied, and is recovered when the force is removed.

Strain in the direction of the applied load is referred to as the normal strain, expressed as follows:

$$\epsilon_y = \frac{\delta_y}{L}.$$

The above equation defines the normal strain as the ratio of elongation/stretching to original length. Normal strain, ϵ_y, is therefore a dimensionless quantity.

2.6.1.2 Elastic and Plastic deformation

Deformations are quantifiable in terms of normal and shear strain. The effect of cumulative strains in a material component is a deformation, such as a stretch, bend or twist [Dow12]. It is worth noting that specific functionalities can be harnessed as a result of material deformations, such as the compression and stretching of a spring. Deformation which appears rapidly upon application of stress (loading) can be classified as either elastic deformation or plastic deformation [Dow12].

In cases where only elastic deformation is present, stress (σ) and strain (ε) are usually proportional, as shown in figure 2-8. In a case of axial loading, the constant of proportionality is known as the modulus of elasticity, E, which is further expanded upon in section 2.6.1.3.

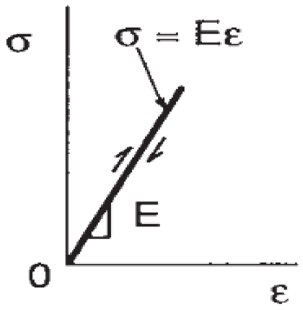

Figure 2-8: Example of elastic deformation as a result of axial loading [Dow12].

Plastic deformation in a material is known as the plastic strain, in this case, when the stress/load is removed, the material does not return to its original shape (i.e. the change is permanent). Materials that are capable of sustaining large amounts of plastic deformation are said to exhibit *ductile* behaviour, whereas materials that fail/fracture with relatively low amounts of plastic deformation are said to exhibit *brittle* behaviour [Dow12].

2.6.1.3 Young's Modulus

Young's modulus, also referred to as the modulus of elasticity (E), is one of the most important mechanical properties of a material. In order to completely describe how this modulus is obtained, the concepts of stiffness and strength should be defined and distinguished.

Stiffness is a measure of the load required to induce a given deformation (elastic or plastic) in a material, whereas *Strength* refers to a given material's resistance to failure by fracture or excessive deformation [Roy08]. The stiffness of a material can be approximated with the use of Hooke's Law, in which an applied load (P) is linearly related to its resulting deformation (δ). Hooke's Law is algebraically expressed as:

$$P = k\delta \,,$$

where $\boldsymbol{k}$ is a constant of proportionality called the stiffness with units of N/m, which is a function of the material's properties and shape.

In order to adjust the stiffness (*k*) to be solely a function of the material, the load (*P*) is normalised by the use of tensile stress. Furthermore, the deformation δ can be normalised by noting that an applied load spans the material uniformly, so that a reasonable measure of "stretching" is deformation per unit length [Roy08], expressed as follows:

$$\varepsilon = \frac{\delta}{L_o},$$

where L_o is the original length and ε a dimensionless measure of stretching called strain.

Using these more general measures of load per unit area and displacement per unit length, Hooke's Law thus becomes:

$$\frac{P}{A_o} = E\frac{\delta}{L_o}.$$

Or, further simplified to:

$$\sigma = E\varepsilon\,,$$

where the constant of proportionality E, is known as *Young's modulus (modulus of elasticity)* and has the same units as stress, "Pa".

2.6.1.4 Poisson's Ratio

Poisson's ratio, ν, relates the longitudinal elastic deformation produced by a compressive stress to a lateral deformation occurring simultaneously [Ask11], as follows:

$$\nu = \frac{-e_{lateral}}{e_{longitudinal}}.$$

The above equation can generally be described as the effect of a positive (tensile) strain in one direction contributing a negative (compressive) strain in the opposite direction [Roy08]. Poisson's ratio is a dimensionless parameter which provides a significant insight into the nature of the material.

Brittle materials have lower Poisson's ratio, and generally as the flexibility of materials are increased its Poisson's ratio increases. The attribute of a material to contract laterally as it is extended longitudinally is proportional to its molecular mobility [Roy08], where molecular mobility can be defined as the measure of freedom of movement of the molecules in a given material. The Poisson's ratio is also linked to the compressibility of a given material. The bulk modulus or modulus of compressibility, K, is the ratio of the hydrostatic pressure, p, required for a unit relative decrease in volume, $\Delta V/V$, and is expressed as follows [Roy08]:

$$K = \frac{-p}{(\Delta V/V)},$$

where the negative sign indicates that a compressive pressure induces a negative volume change [Roy08].

For isotropic materials, i.e. materials which have identical properties in all directions, the bulk modulus is related to the elastic modulus (Young's Modulus) and the Poisson's ratio, as follows [Roy08]:

$$K = \frac{E}{3(1-2v)}.$$

2.6.1.5 Material yielding and Von-Mises Stress criterion

Following work conducted by French mathematicians Poncelet and Saint-Venant in the mid-1800s on fracture mechanics of ductile materials, which was further expanded by Maxwell in 1865, the distortion-energy theory was developed. The distortion-energy theory was premised from the observation that ductile materials stressed hydrostatically exhibited yield strengths largely in excess of the values produced by rudimentary tension tests [Jon09]. It was therefore suggested that the yielding of a material was related to the angular distortion of the stressed element, as opposed to yielding being a simple tensile or compressive phenomenon. The modern distortion-energy theory for ductile materials is now summarised as, "*Yielding occurs when the distortion strain energy per unit volume reaches or exceeds the distortion strain energy per unit volume for yield in simple tension or compression of the same material*" [Jon09]. This phenomenon was further refined by Polish engineer Huber in 1904 and formalised by Austrian mathematician von Mises in 1913 [Bou86].

The theoretical strength of a material is defined as the stress required to break the atomic bonds and separate the atoms. It could be shown, as a rough rule of thumb, that the theoretical strength of a given material can be approximated as one-third of that material's Young's Modulus $(E/3)$ [And05]. However, it has been observed that most materials fail at 1%, or even 0.1% of their theoretical strength value. This discrepancy between theoretical strength and actual strength of materials can be attributed to the mechanisms by which materials fail. Failure (yielding) in ductile materials occurs as a result of sliding between atoms, and not the separation of atoms. Therefore, the yielding stress required for ductile materials is significantly less than that of the stress/energy required to separate the atoms of the material. In brittle materials, the material failure still occurs as a result of separation of atoms, however, the high value of stress/energy is provided by localised stress concentration caused by pre-existing flaws (i.e. cracks) in the material. The stress concentration factors can range in the order of 100 to 1000, therefore the stress applied to the material is amplified significantly due to the presence of flaws and is thus sufficient to separate the atoms of the material. When this process becomes unstable, brittle failure of the material occurs and the material separates over a large area.

Von-Mises (VM) Stress is defined as an effective or equivalent stress at which yielding is predicted to occur in ductile materials. Von-Mises stress is mathematically derived using principal stresses on principal axes σ_1,σ_2 and σ_3.

Using principal axes, the 'state of stress' at a point can be described in terms of the principal stresses σ_1,σ_2 and σ_3 into the sum of two states, namely (a) the state of hydrostatic stress due to the stress σ_{av} acting in each of the principal axis directions which only induces a volume change, and (b) the state of deviatoric stress (stress component containing unequal principal stresses) causing angular distortion without inducing a volume change. Where σ_{av} is mathematically defined as follows [Jon09]:

$$\sigma_{av} = \frac{\sigma_1 + \sigma_2 + \sigma_3}{3}.$$

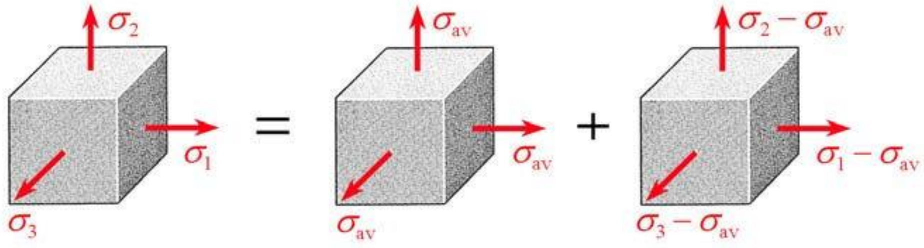

(a) (b) (c)

Figure 2-9: State of stress illustration, where (a) indicates the 'state of stress, (b) indicates the state of hydrostatic stress and (c) indicates the state of deviatoric stress [Jon09].

As discussed in section 2.5.1.3 above, in a simple tension test, Hooke's law can be derived and is given as follows:

$$\sigma = E.\varepsilon\,.$$

Therefore, the strain energy per unit volume for simple tension is given as follows [Jon09]:

$$u = \int_0^{\varepsilon} \sigma.d\varepsilon = \int_0^{\varepsilon} E.\varepsilon.d\varepsilon = \frac{1}{2}\,E.\varepsilon^2 = \frac{1}{2}\varepsilon.\sigma$$

For the state of stress depicted in figure 2-9 (a), the total strain energy per unit volume is:

$$u = \frac{1}{2}(\varepsilon_1\sigma_1 + \varepsilon_2\sigma_2 + \varepsilon_3\sigma_3),$$

where:

$$\varepsilon_1 = \frac{1}{E}(\sigma_1 - v(\sigma_2 + \sigma_3))$$

$$\varepsilon_2 = \frac{1}{E}(\sigma_2 - v(\sigma_3 + \sigma_1))$$

$$\varepsilon_3 = \frac{1}{E}(\sigma_3 - v(\sigma_1 + \sigma_2))$$

In which v is the Poison's ratio. By substitution using the above equations, the total strain energy can be obtained as follows:

$$u = \frac{1}{2E}[\sigma_1^2 + \sigma_2^2 + \sigma_3^2 - 2v(\sigma_1\sigma_2 + \sigma_2\sigma_3 + \sigma_3\sigma_1)]\,.$$

By setting $\sigma_1 = \sigma_2 = \sigma_3 = \sigma_{av}$ and applying it to the equation above, the strain energy associated with hydrostatic loading (volume change only), u_v, is obtained [Jon09]:

$$u_v = \frac{1 - 2v}{6E}[\sigma_1^2 + \sigma_2^2 + \sigma_3^2 - 2(\sigma_1\sigma_2 + \sigma_2\sigma_3 + \sigma_3\sigma_1)]\,.$$

The distortion energy per unit volume is therefore the difference between the two equations above:

$$u_d = u - u_v$$

$$u_d = \frac{1+v}{3E}\left[\frac{(\sigma_1-\sigma_2)^2+(\sigma_2-\sigma_3)^2+(\sigma_3-\sigma_1)^2}{2}\right].$$

It should be noted that no distortion exists in hydrostatic state of stress, as $u_d = 0$ if $\sigma_1 = \sigma_2 = \sigma_3$.

For a simple tensile test of a ductile material, the conditions would be $\sigma_1 = S_y$ and $\sigma_2 = \sigma_3 = 0$, where S_y is the yield stress in tension for the material [Jon09]. The distortion energy equation above, then reduces to:

$$u_{dy} = \frac{1+v}{3E}S_y^2$$

From the before mentioned distortion-energy theory, yield is predicted to occur if the value of u_d equals or exceeds the value of u_{dy}. This is to say, yielding occurs when the following condition is met:

$$\left[\frac{(\sigma_1-\sigma_2)^2+(\sigma_2-\sigma_3)^2+(\sigma_3-\sigma_1)^2}{2}\right] \geq S_y\,.$$

Therefore, the left side of the above equation represents an equivalent or effective stress at which yielding of any ductile material is predicted to occur. This stress is known as the *von Mises stress* and is denoted as $\boldsymbol{\sigma_{vm}}$ in this thesis work.

$$\sigma_{vm} = \frac{1}{\sqrt{2}}[(\sigma_1-\sigma_2)^2+(\sigma_2-\sigma_3)^2+(\sigma_3-\sigma_1)^2]^{0.5}\,.$$

Material manufacturers and industrial users often quote the *Elastic limit* (also referred to as the yield strength) of materials, which is the maximum stress a material can withstand before the onset of permanent deformation. It can thus be used as a design criteria when considering a certain material for a given application, whereby the user verifies that the von Mises stress does not exceed the elastic limit of that material.

In the material science and mechanical engineering industries, components are analysed digitally through the use of computer codes, by method of finite element analysis (FEA). Linear-elastic behaviour is usually assumed and graphical representations of the magnitude of the von Mises Stress are produced. This allows for the visualisation of any region on the component which would exceed its yield strength during the assumed load to be applied and is therefore an invaluable assessment tool for the user.

2.6.2 Thermal Properties of materials

The term “thermal property” can be generically described as the response of a given material to the application of heat. When proposing the use of a specific material for a given practical application, the three thermal properties that are often critical during material selection are thermal expansion, thermal conductivity and heat capacity (specific heat). The following section provides a review of the fundamental thermal properties of materials and their behaviour subsequent to the application of thermal energy/heat.

2.6.2.1 Thermal Expansion

Thermal expansion, also known as the coefficient of linear thermal expansion is a property of a material that is indicative of the extent of expansion a material undergoes upon heating. Most solid materials expand upon heating and contract when cooled. The bond between a pair of atoms of a solid material behaves as a “linear-elastic spring” when the relative distance between the atoms is small [Cve02]. However, when the distance between the atoms is larger, the before mentioned “spring” acts in a nonlinear manner. The bonds are said to be anharmonic, as the bonds become stiffer when the atoms are pushed together and less stiff when pulled apart. The thermal vibration of atoms involves significant large displacements, as the temperature is increased, the anharmonicity of the bonds pushes the atoms apart, increasing their mean displacement [Cve02]. This effect is measured by the linear expansion coefficient as is represented by the following equation [Cve02]:

$$\alpha = \left(\frac{1}{l}\right)\frac{dl}{dT},$$

where α is the coefficient of linear expansion with units (1/°C), l a linear dimension of the material and T the temperature.

2.6.2.2 Specific Heat

When a material is heated, it absorbs energy which is signified with an increase in temperature of the material [Cal12]. The property of a material to absorb heat from an external source, is known as heat capacity or specific heat, and represents the amount of energy required to produce a unit temperature increase. Heat capacity, C, can be expressed mathematically with the following equation [Cal12]:

$$C = \frac{dQ}{dT},$$

where dQ is the energy required to produce a dT temperature change.

Heat capacity and specific heat are differentiated by their units, where heat capacity has units *per mole of material* (i.e. J/mol.K) and specific heat has units *per unit mass* (J/kg.K). Heat capacity is measured by two methods. The first method entails the measurement of a material's heat capacity while maintaining a constant volume of sample material, which is denoted as C_v. In contrast, the second method entails the measurement of heat capacity of a sample material under a constant external pressure, denoted as C_p [Cal12].

In solid materials the principal method of thermal energy absorption is via the increase in vibrational energy of the atoms [Cal12]. These atoms are in a state of constant high frequency vibration, with adjacent atoms coupled by virtue of atomic bonding. Coordinated vibrations produce traveling lattice waves, which could be considered as elastic waves, having short wavelengths and very high frequencies, which propagate through the crystal at the speed of sound [Cal12]. Vibrational thermal energy of a solid material are constituted by a series of these elastic waves, with various distributions and frequencies, and it is these waves which allow for the transport of energy during thermal conduction.

Another method of thermal energy absorption which adds to the heat capacity of a solid material is the electronic contribution of free electrons, which are electrons freed from filled orbitals to empty states above Fermi energy [Cal12]. Fermi energy can be briefly defined as the highest occupied energy level of a material at a temperature of absolute zero (0 K) [Ait17] [Sin01]. Free electrons within the solid material absorb energy by increasing their kinetic energy [Cal12]. It should be noted however, that the electronic contribution of free electrons to overall energy absorption is relatively insignificant, except at temperatures near absolute zero.

2.6.2.3 Thermal Conductivity

The natural phenomenon by which heat is transferred from a high to low temperature region of a material or substance is known as thermal conduction [Cal12]. Thus, the property of a material to transfer heat is referred to as thermal conductivity. Thermal conductivity, k, can be expressed mathematically with the following equation [Cal12]:

$$q = -k\frac{dT}{dx},$$

where q is the heat flux per unit time per unit area, with units W/m^2. k is the thermal conductivity with units W/m.K and dt/dx the temperature gradient through the conducting material/substance. It should be noted that the area considered for heat flux, refers to the area which is perpendicular to the direction of heat flow.

As this thesis will be dealing with both high purity metals and ceramic materials, it is worth noting how other material properties influence the thermal conductivity of the given material.

In high purity metals, the free electron mechanism of heat transfer (as discussed in section 2.6.2.2) is largely more efficient than the vibrational contribution (lattice waves), as the electrons are not as easily scattered as the vibrational waves and have higher velocities [Cal12]. Generally, metals are very good conductors of thermal energy due to the relatively large numbers of free electrons available to participate in thermal conduction. Thermal conductivities of the common metals generally range between about 20 and 400 W/m.K [Cal12].

Ceramic materials could be considered ‘thermal insulators’ as they do not contain large numbers of free electrons, and hence vibrational waves are the primary mechanism for thermal conduction in ceramic materials. Starting at relatively low temperatures (i.e. 0 – 1400 °C), the scattering of vibrational waves becomes more pronounced with an increase in temperature, and therefore the thermal conductivities of ceramic materials normally reduces as the temperature increases. At higher temperatures (> 1500 °C), the thermal conductivity of the ceramic material begins to increase, as a result of radiant heat transfer in which significant quantities of infrared radiant heat is transported through the material. The efficiency of the radiant heat transfer increases with temperature [Cal12]. The effect of temperature on the thermal conductivity of ceramic materials is graphically represented in figure 2-10, below:

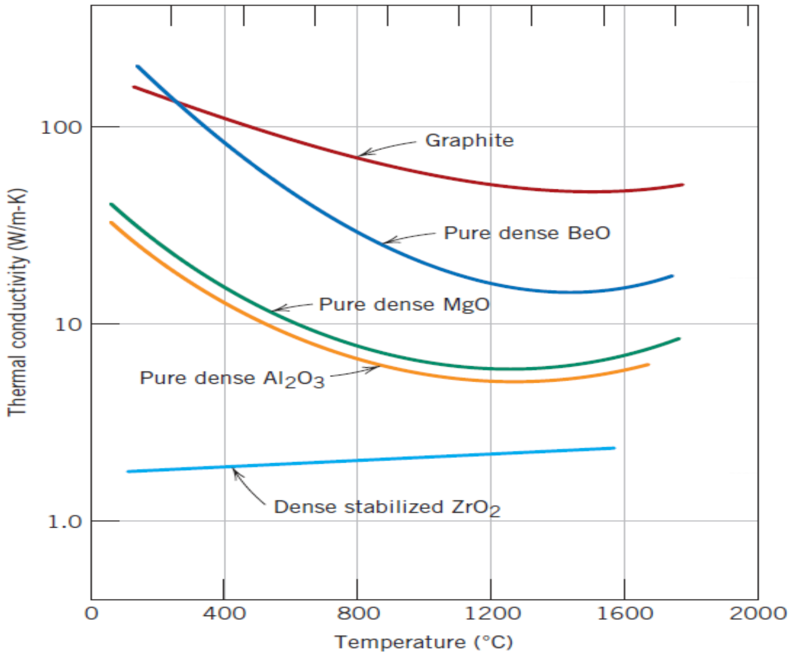

Figure 2-10: Effect of temperature on the thermal conductivity of various ceramic materials [Cal12].

Porosity in a ceramic material has a significant effect on the material's thermal conductivity, as increasing the volume of pores will generally induce a reduction in thermal conductivity. This reduction in thermal conductivity with increasing pore volume is a result of poor heat transfer across the stagnant air contained within the pores of the material. Furthermore, no heat transfer by means of conduction occurs within a vacuum, as the thermal conductivity of a vacuum is essentially zero, and heat is only transferred via the black body radiation mechanism [Bae10] (discussed in section 2.6.2.5 to follow).

2.6.2.4 Thermal Stress

Thermal stress can be defined as stress induced in a material as a result of changes in temperature [Cal12]. When selecting a material for a specific application, it is of utmost importance to understand the nature of thermal stresses the material will undergo, as these stresses could lead to fracturing or plastic deformation of the material.

In general, for an isotropic material which is not restrained in any manner, when a uniform temperature gradient is applied (heating or cooling), the expansion or contraction of the material will be stress free. However, in the event that the material is restrained, say by rigid supports, thermal stresses would be introduced. The magnitude of these thermal stresses, σ_T, resulting from a temperature change of T_i to T_f can be expressed mathematically as follows:

$$\sigma_T = E\alpha(T_i - T_f)\,,$$

where E is the Young's modulus and α the coefficient of thermal expansion of the given material. T_i and T_f are the initial and final temperatures, respectively.

When a solid material is heated or cooled, the internal temperature distribution is dependent on the size, shape and thermal conductivity of the material, as well as the rate at which the heating/cooling is occurring. Upon heating, the exterior of the material would be hotter and hence, would have expanded more than the interior regions of the material. Compressive stresses are thus induced at the exterior of the material, which are balanced by the tensile stresses in the interior [Cal12] [Bro86]. This exterior-interior stress mechanism is reversed for rapid cooling, such that the surface of the material is placed in a state of tension (contraction) [Bro86].

Ductile metals are alleviated from thermally induced stress by means of plastic deformation, which is to say, the metal retains the deformed shape (expansion or contraction) resulting from the applied thermal stress.

Ceramic materials, which are generally non-ductile, carry an increased possibility of brittle fracture from thermally induced stresses. Rapid cooling of a brittle material has a higher likelihood of inflicting thermal shock than heating, since the induced exterior/surface stresses are tensile [Mal13], which increases the probability of crack formation and propagation from the material's surface flaws [Cal12] [Dim08]. The capacity of a material to withstand failure resulting from thermal stresses is referred to as the material's thermal shock resistance (TSR) [Cal12]. The resistance to thermal shock of a ceramic material depends on the magnitude of the temperature gradient [Mal13] as well as the mechanical and thermal properties of the material. Ceramic materials having high fracture strengths (σ_f), high thermal conductivities (k), low moduli of elasticity (E) and low coefficients of thermal expansion (α), would have greater thermal shock resistance [Cal12] [Lu98]. The thermal shock resistance, TSR, of a material can be approximated as follows [Cal12]:

$$TSR = \frac{\sigma_f k\,(1-\nu)}{E\alpha}.$$

In addition to modification of the thermal and mechanical properties of the material, thermal shock could be reduced or even prevented by altering the material's operating conditions to a degree that heating and cooling rates are reduced and temperature gradients across the material are minimized.

2.6.2.5 Thermal Radiation and Emissivity

In order to discuss the material property, emissivity, the concept of thermal radiation is required for conceptualisation. Thermal radiation refers to the method of heat transfer through the emission of energy by means of electromagnetic radiation, with the intensity of this energy flux emitted being dependent on the temperature of the body and the characteristics of its surface [Lie13]. This energy emission is as a result of the thermal motions (kinetic energy of constituent particles in a material) at a microscopic level in atoms and molecules [Sie71]. Thermal radiation, as opposed to other forms of heat transfer, namely, conduction and convection, does not require any media through which to transfer energy/heat (i.e. thermal radiation can occur in a vacuum). The total amount of radiative energy emitted isotropically from a surface is known as emissive power $(E_{\lambda,b})$. The magnitude of the emissive power is dependent on wavelength (λ), temperature (T) and a surface property termed emissivity (ε). The emissive power, $E_{\lambda,b}$, of a black body surface is given by Planck's law as follows:

$$E_{b,\lambda} = \frac{c_1}{\lambda^5[e^{(C_2/\lambda T)} - 1]},$$

where c_1 and c_2 are radiation constants, also referred to as Planck function constants.

The total emissive power E_b of a black body (perfect emitter) is given by the Stefan-Boltzmann law, expressed as follows [Sie71]:

$$E_b = \int_0^{\infty} E_{\lambda,b} d\lambda \,.$$

Integration of the above equation, yields:

$$E_b = \sigma_B T^4 \,,$$

where σ_B is the Stefan-Boltzmann constant (5.67 x 10^{-8} W/m^2.K) and T the temperature in Kelvin (K).

All objects at temperatures above absolute zero ($0\ K$) emit thermal radiation. However, for any specific wavelength and temperature the amount of thermal radiation emitted is dependent on the emissivity of the surface of the object in question. Emissivity (ε) of a material surface or body is generally defined as the ratio of the radiation emitted by the surface (E_s) to the maximum possible radiation emittance, from a perfect emitter known as a 'black body' at the same temperature, expressed as follows:

$$\varepsilon = \frac{E_s}{E_b}.$$

Emissivity is a dimensionless number ranging from 0 (perfect reflector) to 1 (perfect emitter). Additionally, the emissivity of a surface does not only depend on the type of material in question, but also the nature and geometry of the surface.

2.6.3 Finite Element Analysis

Engineering problems can generally be considered as mathematical models of physical situations; whereby mathematical models refer to differential equations, derived from the application of fundamental laws of nature to a system, linked to a set of boundary and initial conditions. Under a given set of conditions, the exact solutions of these differential equations provide a detailed description of the behavior of a system. The behavior of a system in any given engineering problem is influenced by two sets of parameters, namely: (1) parameters providing information regarding natural (physical) characteristics (i.e. viscosity, thermal conductivity, specific heat capacity), and (2) parameters inducing disturbances in a system (i.e. temperature gradients, pressure gradients, moments) [Moa99].

A large number of engineering problems exist, for which an exact solution cannot be obtained. This could be as a result of the nature/complexity of the differential equations governing the system, and/or the difficulties presented when dealing with the boundary or initial conditions linked to the differential equations [Moa99]. In order to overcome these difficulties, numerical approximations are used to approximate exact solutions at discrete points, referred to as nodes. Two common classes of numerical approximation methods exist; finite difference methods (FDM), and finite element methods (FEM). Using finite difference methods, the differential equations are written for each node, and the derivatives are replaced by difference equations, which results in a set of simultaneous linear equations [Moa99]. Finite difference methods (FDM) are generally only useful for simple engineering problems, as this method becomes difficult to apply to problems containing complex geometries or boundary conditions. Alternatively, the finite element method (FEM) creates a system of algebraic equations by use of integral formulations. The system's solution region is divided into small parts referred to as elements, and an approximate continuous function is assumed to represent the solution of each element [Bha05] [Moa99]. The complete solution is then generated by assembling the individual solutions of the elements. The finite element method (FEM) is the preferred approximation method for solving engineering problems containing complex geometries, boundary conditions, and material characteristics.

The finite element procedure reduces the basic unknowns or field variables (i.e. displacements, velocities, temperatures) of a given engineering problem to a finite number by dividing the solution region into small parts referred to as elements. The unknown field variables are then expressed in terms of assumed approximating functions (Interpolating/Shape functions) within each element [Bha05]. The approximating functions are defined in terms of field variables of specified points called nodes (also referred to as key points), therefore the unknowns are the field variables of the nodes [Bha05].

Owing to the complexity and multi-variable nature of analysing the resultant thermal and mechanical loads imparted on the RIB target system during operation, the FEM method is thus the ideal tool for modelling, analysing and solving the engineering aspects relating to the RIB target, as discussed in sections 2.6.1 and 2.6.2 above.

2.6.3.1 Finite Element solution procedure

The finite element method solution procedure can be summarized in the following main steps [Nik09]:

1. ***Discretizing*****:** The first step is the dividing of the solution region into finite elements (a process known as discretizing), typically generated by a pre-processor program within the FEM software (discussed in section 2.7). A mesh is defined at this point which consists of arrays of nodal coordinates and their associated element connections.
2. ***Selection of interpolation functions*****:** Interpolation functions are used to interpolate the field variables over the element. Typically, polynomials are assigned as interpolation functions. The degree of the polynomial depends on the number of nodes assigned to the element.

3. ***Assigning element properties***: The matrix equation for the finite element should be established, which would relate the nodal values of the unknown function to other parameters. This task is done using numerical methods.
4. ***Assemble the element equations:*** In order to find the global equation system for the complete solution of the region of interest, all the element equation must be assembled. This is to say, the local element equations used for discretization should be combined to develop the global element equation. Boundary conditions are imposed on the global element equation at this point (before solution of the equation).
5. ***Solution of the global equation system:*** The finite element global equation system is solved using either direct of iterative methods (depending on the complexity of the problem). The nodal values of the unknown function are produced as the result of the solution.

2.6.3.2 Finite Element calculation method

As discussed in the preceding sections, finite element analysis involves solving of differential equations under various conditions such as boundary or initial conditions leading to the understanding of the physical phenomena and ability to predict future physical phenomena [Sto11] (i.e. material failure, plastic deformation, etc.). Obtaining exact solutions for a set of differential equations is generally challenging. Numerical methods can be adopted to obtain approximate solutions for these differential equations, these are referred to as 'discrete analysis' methods. By using these methods of discrete analysis, differential equations can be reduced to simultaneous linear algebraic equations and then solved numerically [Sto11]. If the physical formulation of the problem is known as a differential equation then the most popular method of its finite element formulation is the Galerkin method [Nik09].

The Galerkin method can be described using a simple one-dimensional example of finite element formulation. Consider the following equation to be solved numerically [Nik09]:

$$a\frac{d^2u}{dx^2} + b = 0, \quad (0 \le x \le 2L)$$

$$Boundary\ Conditions: u(0) = 0, \quad a\frac{du}{dx}(2L) = R\,,$$

where u is an unknown solution.

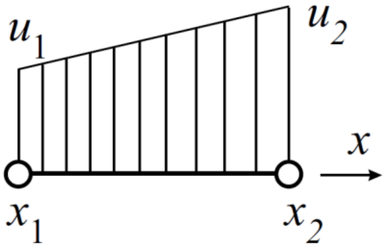

Figure 2-11: One-dimensional, 2 node line element with function interpolation inside element [Nik09].

The line element presented in figure 2-11 above, has two nodes, x_1 and x_2, and approximation of the function $u(x)$ can be done as follows [Nik09]:

$$u = N_1 u_1 + N_2 u_2 = [N]\{u\},$$

where functions $N_i(x)$ are the following piecewise linear functions and are called shape functions of the nodal point "i" [Sto11]:

$$N_1 = 1 - \frac{x - x_1}{x_2 - x_1}.$$

$$N_2 = \frac{x - x_1}{x_2 - x_1}.$$

which are used for interpolation of the function $u(x)$ using its nodal values. Nodal values u_1 and u_2 are unknowns which should be determined from the discrete global equation system. Substituting u expressed through its shape functions and nodal values, into the differential equation, results in the following:

$$a\frac{d^2}{dx^2}[N]\{u\} + b = Z,$$

where Z is a nonzero residual as a result of the approximation of a function inside a finite element. The Galerkin method is used to minimise the residual (Z) by multiplying terms of the above equation by shape functions, integrating them over the element and equating to zero [Nik09]:

$$\int_{x_1}^{x_2}[N]^T a\frac{d^2}{dx^2}[N]\{u\}dx + \int_{x_1}^{x_2}[N]^T b dx = 0.$$

Finally, in solving the finite element, a set of simultaneous algebraic equations for unknown variable of $u(x)$ at the i^{th} nodal point u_i and those of its derivatives $du/dx, (du/dx)_i$ are derived by integrating the above equation using the integration by parts method/procedure and then accounting for the boundary conditions [Sto11]. Simultaneous equations of this nature can easily be solved using the computational power of computers, through FEM software packages.

2.7 ANSYS® Software Package

ANSYS® [ANS15] is one of the most commonplace software packages in industry, used for finite element analysis and design. ANSYS is a general-purpose program, allowing for a wide variety of finite element analysis in numerous industries, such as aerospace, railway, electronics, automobile, power generation, civil construction and biomechanics, to name a few. The term “general purpose”, also refers to the multiple engineering disciplines, in which the ANSYS software suite is used, such as structural, mechanical, electrical, thermal and fluid [Bar01]. ANSYS Mechanical, is a sub-component of the complete ANSYS software package which employs FEM to solve mechanical and thermal engineering problems. ANSYS Mechanical is thus an ideal tool for modelling, analysing and solving the mechanical and thermal engineering aspects of the RIB target design, as discussed in section 2.6, above.The ANSYS mechanical software package, version 16.2, was used, and is discussed in this thesis work.

The general ANSYS Mechanical analysis process can be sub-divided into three main steps, as follows:

1. Pre-processing
2. Solution
3. Post-processing

These process steps above, are discussed in further detail in the sub-sections to follow.

2.7.1 Pre-processing

Pre-processing can be considered as the process of defining the engineering problem. The process of conceptualisation is initiated by constructing the geometry of the structure or component. The construction of the problem geometry starts with defining the keypoints/lines/areas/volumes, which serves as the ‘anchor points’ for defining the element type to which material properties (i.e. density, thermal conductivity, modulus of elasticity, etc.) are assigned. At this point, the geometrical framework of the structure/component is well defined, it is then further refined by meshing the geometry (elements) in order to allow for a more accurate final solution.

ANSYS allows for two methods of model geometry generation, namely solid modeling and direct generation. With solid modeling, the geometrical shape of the structure/component is described within ANSYS, and the program then automatically meshes the geometry with nodes and elements [Sto11]. The shape and size of the elements generated by ANSYS can be further manually edited/controlled. In contrast, with the direct generation method, the location of each node and the connection to each element is manually defined within ANSYS [Sto11], or imported from compatible software packages.

2.7.2 Solution

The solution stage of the ANSYS simulations consist of assigning loads, applying boundary conditions and running the solution.

A load is an external force applied to a structure/component, directly related to the function or constraint of this structure/component during use. Some common examples of loads applied to systems modeled using FEA are pressure loads on surfaces, body forces such as gravity and thermal loads on bodies, to name a few. The application of loads distorts the physical structure and thereby creates stress in it. ANSYS divides loads into six categories, namely, Degree-of-Freedom (DOF) constraints, forces, surface loads, body loads, inertia loads and couples field loads [Sto11]. These loads are either applied on the solid model (i.e. keypoints, lines, areas) or the finite element model (nodes and elements). There are two important terms in ANSYS, to be clarified when dealing with loads, these are the load step and sub-step. A load step is a configuration of loads for which the solution is obtained and a sub-step is an incremental step (also known as time-steps) taken within a load step [Sto11].

Boundary conditions are used to constrain portions/structure of the model to remain fixed or to shift by a prescribed or “allowable” amount. Boundary conditions are thus the limits/conditions in which the model may deviate from its original/initial structure, during and/or after the application of stress inducing loads.

Once the loads/boundary conditions are defined and integrated into the governing equations of the model, these equations are then assembled into mathematical matrix form to be solved numerically. The assembly of this mathematical matrix is dependent on the model's element types, material properties and loads/boundary conditions, as well as the type of analysis to be conducted. Two type of analysis are generally performed, depending of the required output required, these analysis are referred to as static (steady-state) or dynamic (transient) analysis.

Static or steady-state analysis can be generically described as the state that is established after a certain time/period has elapsed in the system. Whereas dynamic or transient analysis is the state between the beginning of the event (i.e. application of a load/boundary condition) and the steady state.

2.7.3 Post-processing

Post-processing is the stage at which the results of the solution is reviewed. ANSYS contains two post-processing mechanisms, labelled as POST1 and POST26.

POST1 is a general post-processor which allows for the review of results at one sub-step (time step) over the complete model or portion thereof [Sto11]. POST1 can produce contour displays, deformed shapes and tabular data listings for the review and interpretation of analysis results [Sto11]. Additionally, POST1 offers functionalities such as error estimation, calculations using results and path operations.

POST26 is a time history post-processor which can be used to review simulation results at specific points in the model over all time steps. Additionally, POST26 can be used to obtain graphical plots of specific result evolutions over time as well as tabular data listings [Sto11].

2.8 FLUKA and ANSYS integration

By coupling particle cascade simulations conducted in FLUKA with subsequent Finite Element thermo-mechanical calculations in ANSYS, a reliable means of analysing practical engineering problems related to the design and construction of RIB targets and associated system components can be developed. The integration of these software packages was used to study, model, design and optimize the RIB targets in this research work.

The following process flow diagram, figure 2-12, describes the FLUKA and ANSYS integration process employed during the RIB target design and optimisation. The components of the process are further described, under corresponding heading titles, in the section to follow.

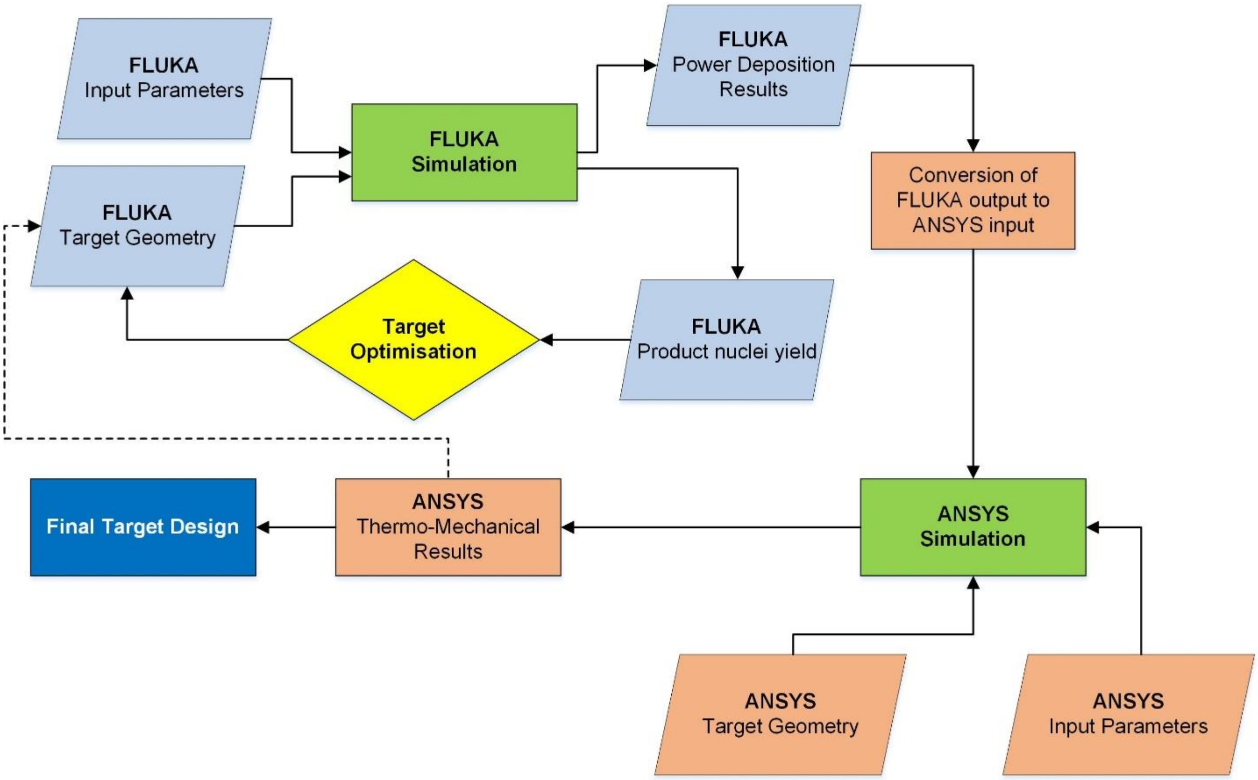

Figure 2-12: Target design and optimisation algorithm.

2.8.1 FLUKA Simulation

When modelling a simulation to test a proposed target design, there are various key physical parameters that are required to define the experimental simulation setup. The FLUKA simulation was conducted with the following primary beam and geometric input parameters, in order to obtain a model as close as possible to real experimental values. Additionally, the accuracy of these initial parameters are paramount, as this has a direct influence on the ^{6}He yield and power deposition results, with the latter informing the final thermo-mechanical analysis, which will be discussed in section 2.8.2 to follow.

2.8.1.1 FLUKA Input Parameters

As the iThemba LABS cyclotron is expected to deliver a proton beam at 70 MeV, this value was used as the primary proton beam energy for the simulation.

From studies conducted at INFN [Mon15], the use of a flat beam profile versus that of a wobbled Gaussian beam with fixed standard deviation was investigated. It was found that the use of a wobbler coupled to the cyclotron, which rotates the primary beam, allows for a more uniform power deposition along the radial axis of the target [Mon15], as seen in figure 2-13 below. This allows for safer and longer target operation, as the reduced power deposition at the center of the target (r = 0 mm) ensures a reduction in thermally induced material stress, and by extension stress related target failure. As a result of these studies, the primary proton beam is modelled with a Gaussian profile of 11.7 mm FWHM in both the x and y axes, in the FLUKA simulation.

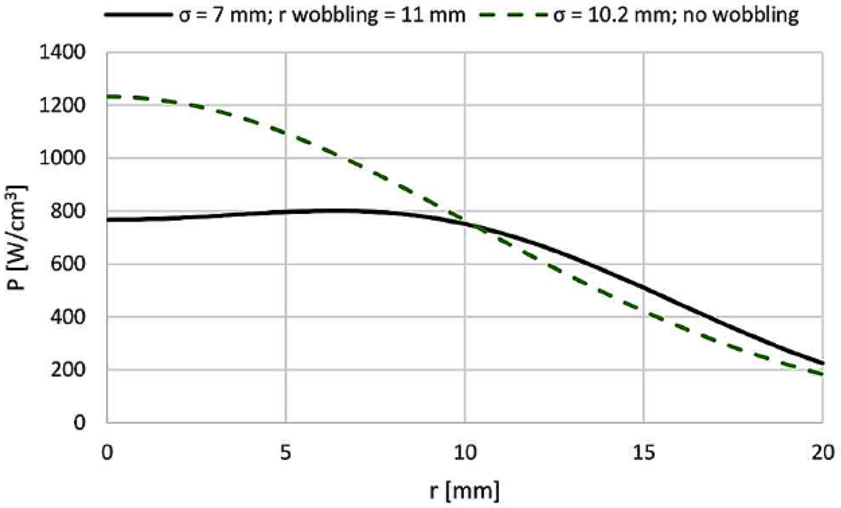

Figure 2-13: Power density distribution along the radial axis of target disc, for beam with and without wobbler [Mon15].

The beam properties for simulation are defined under the BEAM card in FLUKA. The PHYSICS model referred to as ‘Evaporation’ with ‘Heavy fragmentation’ was used, as this simulation configuration produces the most accurate results for residual nuclei production or fragmentation [Fer05].

2.8.1.2 FLUKA Target Geometry

The FLUKA target geometry, is a retrofit of the SPES RIB target developed at INFN as mentioned in Chapter 1. The SPES target however, consists of 7 aligned UC_x discs in a cylindrical container, with a 4 layer beam dump at the end of the disc array. During the RIB target adaption and subsequent optimisation phase, the general sub-component layout of the SPES design was maintained, but featured differing target configurations, in terms of number of target material discs, target material, canister length, beam dump thickness, etc. These adaptions to the SPES design were due to the fact that the primary beam power to be used at the iThemba LABS RIB production facility is significantly higher (70 MeV) than that of SPES demonstrator, which is operating with a beam of 40 MeV, in addition to the fact that the specific nuclide of interest in this research work is ^{6}He.

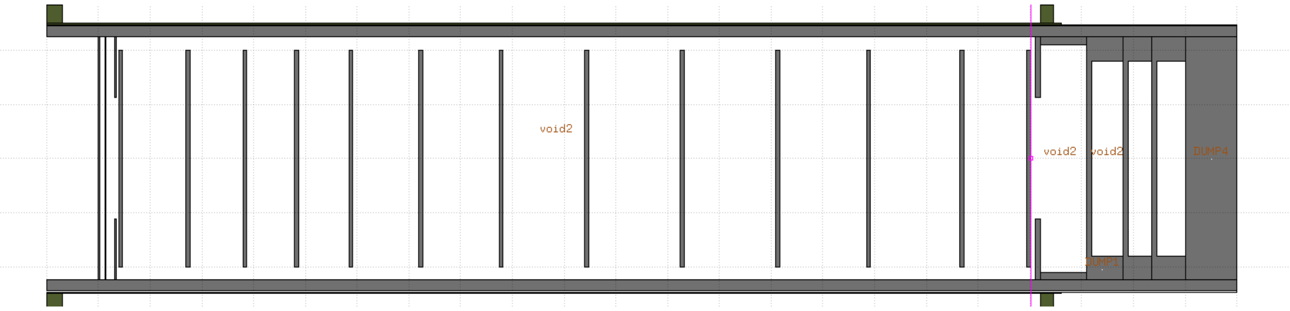

Figure 2-14: Example of adapted SPES RIB target design for iThemba LABS.

Target optimisation studies were conducted by adjusting the following parameters:

- Target material type
- Target disc thickness
- Spacing between target discs
- Beam dump thickness and spacing

2.8.1.3 FLUKA Yield of Product Nuclei

The key component of the target design is to obtain/produce the largest quantity possible of the required nuclide (^{6}He). The type and quantity of the nuclides produced by the impingement of the primary proton beam on the target material can be obtained by means of scoring with FLUKA's integrated scoring card, RESNUCLEi. FLUKA defines the function of the RESNUCLEi scoring card as "*scores residual nuclei produced in inelastic interactions on a region basis*" [Fer05].

The nuclide yield results were used as the cornerstone for target optimisation, with the primary aim of obtaining higher ^{6}He yields.

2.8.1.4 FLUKA Power Deposition Calculation

The energy deposited by the primary beam into the target system can be analysed using FLUKA's integrating scoring card, USRBIN. The function of the USRBIN scoring card is defined as "*scores distributions of several quantities in a regular spatial structure (binning detector) independent from the geometry scores distribution*" [Fer05]. Thus, by using the

USRBIN card it is possible to score/analyse the distribution of energy throughout the target system.

Use is made of 1D binning with cylindrical coordinates, in order to model the energy deposited of the target disc surfaces along the radius of the discs. By employing symmetry, it is possible to produce a complete energy deposition for each target disc, this process is illustrated by figure 2-15, below.

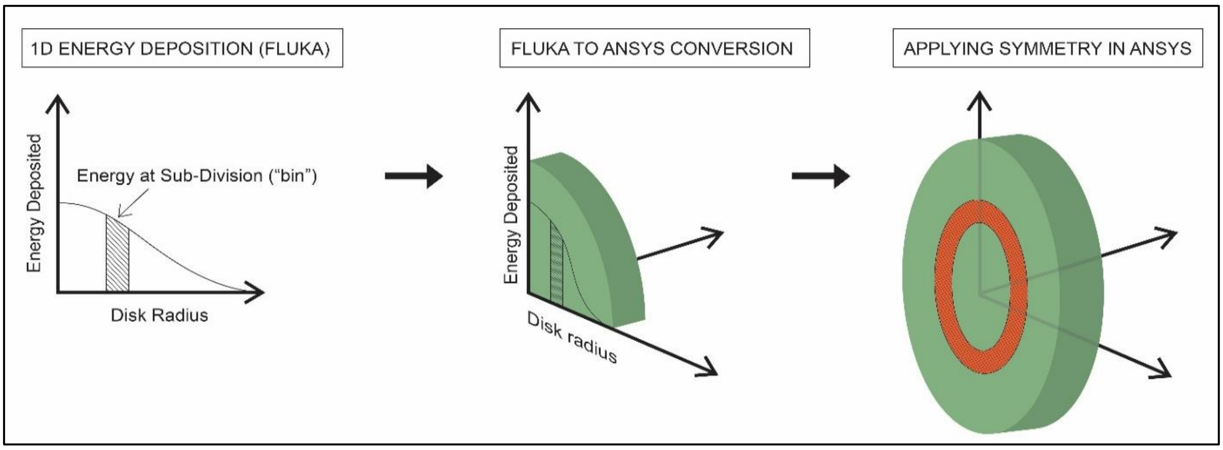

Figure 2-15: Conversion process of FLUKA output energy deposition data to ANSYS energy deposition input data.

The FLUKA output data are then converted to ANSYS input data, which provide the thermal load applied to each disc, during the ANSYS thermo-mechanical analysis.

2.8.2 ANSYS® Simulation

In order to accurately model the RIB target system for operation, the parameters selected for use during the thermo-mechanical analysis is of utmost importance, as the accuracy and quality of results provided by ANSYS is only as good as the accuracy of the detailed mechanical model, material data files and applied loads and boundary conditions.

2.8.2.1 ANSYS Target Geometry and Solution setup

As previously mentioned in section 2.7.1, the starting point to developing the ANSYS model is 'Pre-processing', which is the process of defining the engineering problem. The RIB target geometry model was constructed using the 'direct generation' method, in which the nodes/key-point are user-defined and meshed together to form solid volumes (elements). These key-points provide the spatial co-ordinates of the sub-divided elements of a given component in the target system, and collectively describe the dimensions of the elements/components (i.e. disc thickness, disc spacing, target chamber thickness, etc.). The RIB target system was split into separate components/elements for easier load and boundary condition application. These components were the target canister, target dump canister, target discs, beam dumps, screens, windows and heater. It is important to note that the geometry defined in ANSYS is the same as the geometric definition used in FLUKA to simulate the interaction of the primary proton beam with the RIB target.

The material properties of each of these components were provided by means of user-defined ANSYS material data files. These data files, which are further discussed in chapter 3 to follow, were validated against experimental data for the given materials, obtained from literature.

In order to analyse the effect of a long term load, which is to say, during stable operation of the RIB target system, a transient structural analysis was used in ANSYS. By definition, a transient analysis involves loads that are a function of time (i.e. heat generation in target discs due to impinging proton beam) and hence this type of analysis is used to determine the dynamic response of a structure under the action of any general time-dependent loads. With this type of analysis, time scale of the loading is such that the inertia or damping effects are accounted for, as opposed to a static analysis. For all simulations conducted in ANSYS, the simulation was run until the default ANSYS convergence criteria was achieved, in order to ensure accurate representation of the dynamic behavior of the RIB target system materials under continuous load.

2.8.2.2 ANSYS Loads and Boundary Conditions

Following from section 2.8.1.4 above, the power deposition results extracted as an output from FLUKA on completion of the simulation of the primary proton beam interaction with the RIB target, was converted into input loads for simulation in ANSYS.

In ANSYS, the power deposition results obtained from FLUKA for the RIB components - discs, dumps, screens and windows, were applied as input loads in terms of power density (W/m^3). This was done by fragmenting the power density values as sub-divisions along the component's radius, and then employing the use of symmetry to provide a complete 2π power density profile for the given component.

2.8.2.2 ANSYS Post-processing - Thermo-Mechanical results

As discussed and described in section 2.7.3 above, the post-processor used in ANSYS on completion of simulation was POST1. This allowed for the generation of contour plots (both nodal and elemental solutions) of the body temperature results and von Mises (VM) stress results for the completion time evolution of the solutions (simulation).

These contour plots allowed for user-analysis of the final solution results at various points in the RIB target system. Most importantly, during the target optimisation phase, this information allowed for the identification of potential problem areas (i.e. over-stress on components, exceeding of material thermal thresholds) and informed the steps to be taken to correct or enhance the RIB target's capabilities.

The final thermo-mechanical results for the proposed RIB target design, to be shown and discussed in Chapter 3, are presented by means of ANSYS contour plots.

CHAPTER 3: TARGET MATERIAL EVALUATION

The following chapter evaluates the proposed target materials, Graphite and Boron Carbide, used in the RIB target designs conducted in this research work. The rationale for choosing these materials has been covered in section 1.6. The material evaluation assesses and employs information obtained from literature as well as commercial material manufacturers, in order to obtain sufficiently accurate mechanical and thermal characteristics for the materials evaluated in this work.

3.1 Graphite

Graphite, is one of two naturally occurring forms of solid carbon, with the other being diamond. The distinguishing atomic factor which differentiates graphite and diamond from one another, is the mechanisms with which their carbon atoms bond within their atomic structure [She01]. In diamond, the atomic structure is cubic with each carbon atom covalently bonded to four other carbon atoms to form a tetrahedron. In graphite, the structure is said to be hexagonal with only three of the four valence electrons of carbon forming covalent bonds with adjacent carbon atoms. The fourth electron resonates between the valence bond structures [She01].

For this research study and material application, isostatic graphite, also referred to as *isomolded graphite* was considered. Isomolded graphite is produced using a technique known as Cold Isostatic Pressing (CIP). CIP is a common manufacturing process used for the consolidation of metal and ceramic powders. Around 100% of theoretical density for metals and 95% theoretical density for ceramic powders can be achieved with this method. CIP makes use of a liquid media, such as water or an oil, to apply pressure to the powder [Ekl16]. The powder is contained in a mold that does not change shape, but preserves the shape from the mold and ensures none of the liquid media penetrates into the powder. This process is conducted at typical pressure ranges of 100 – 600 MPa, which enables the voids in the powder to be smaller or eliminated, through the high compaction forces that will likely result in ceramic powders crumbling so that the density increases and the end-product is the “green compact” (unsintered ceramic item) that can be handled, machined and sintered, where sintering is the process of compacting a solid material (i.e. ceramic) by heat or pressure without melting it [Ekl16].

The greatest advantage of the CIP process is that it produces a final ceramic product/material with uniform properties is all directions (isotropic). Additionally, the CIP process produces ceramics with improved thermal and mechanical properties [XRD17], such as:

- Good Thermal Stability
- Low thermal expansion coefficients
- Excellent thermal and electric conductivity coefficients

3.1.1 Graphite – Sublimation point

When proposing and developing a RIB target system, one of the most important parameters to be considered is the melting/sublimation point of the given target/component materials. To this end, literature sources were consulted to obtain thermal limits for graphite operating under RIB target operation conditions (i.e. high temperature and vacuum). Various literature and commercial manufacturer sources quote the graphite sublimation temperature in vacuum to be in the range of 2000 – 2400 °C.

A study conducted in the early 2000s by *Thieberger* [Thi00] and *Haines* [Hai02], at The Brookhaven National Laboratory (BNL), America, investigated the upper limits for sublimation from hot carbon target in a vacuum and in gasses. This study was conducted as part of the BNL Muon Collider Project, to examine the possible carbon target life-time limitations due to sublimation in vacuum conditions. This study evaluated the mass loss the carbon would undergo during continuous operation at high temperature and high vacuum, and concluded a safe/feasible continuous operating temperature of 2365 °C [Thi00]. The carbon mass loss rate results obtained during this study at temperatures above 2100 °C and approximate vacuum of 10^{-3} - 10^{-4}, are shown in figure 3-1 below. These results indicated a stable mass loss rate of approximately 0.0011 g/hr in the operating temperature range of 2120 to 2135 °C. A sharp increase in mass loss rate is noted beyond 2135 °C up to a maximum measured mass loss rate of 0.0092 g/hr at 2227 °C. Although these results are insightful, they cannot be directly used to make inferences on the proposed graphite components (target and beam dumps) in this research work as the exact geometry and graphite type proposed in this work is not accounted for. Additionally, it should be noted that these results do not consider the re-condensation of evaporated/sublimated carbon.

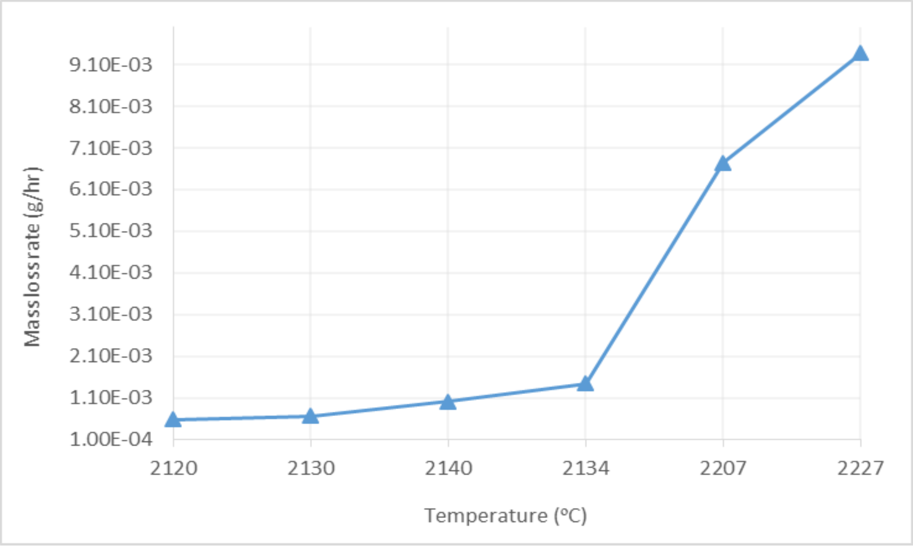

Figure 3-1: Measured mass loss rates for carbon sublimation test in high vacuum. Adapted from [Thi00].

For this design study, taking into account the manufacturer, literature and experimental sources, as discussed above, a safe operational temperature of 2300 °C for graphite was adopted during RIB target design.

3.1.2 Graphite – Density

Generally, in graphite, the physical and mechanical properties of the material improve as the density increases. The theoretical density of graphite is said to be 2.26 g/cm^3, however, commercially produced graphite rarely exceeds 80 % of this theoretical value due to natural voids and pores in the material structure. Additionally, the density of graphite is known to be temperature dependent, with the density increasing with an increase in temperature, this increase however, is rather insignificant below 2000 °C [She01].

In order to obtain a density specification value for commercially available graphite, manufacturer data sheets and material specifications were reviewed. Grade AJT isomolded graphite was considered, as it has been an industry standard for many years, which can be machined to precise tolerances and fine surfaces finishes.

Using the Grade AJT graphite specification [Gra09], a density value of 1.76 g/cm^3 was used during simulation (FLUKA and ANSYS) for graphite throughout the operating temperature range. No significant density change was assumed since the material is not expected to undergo a phase change during operation and would not be operated far above 2000 °C.

3.1.3 Graphite – Thermal conductivity

In order to obtain a realistic thermal conductivity data for graphite at RIB target operating temperature ranges, a study conducted by *Taylor & Groot* in 1978 [Tay78] at the Properties Research Laboratory in Indiana, America, was employed for reference. This study analysed the thermal properties (thermal conductivity, specific heat and electrical resistivity) for two samples of POCO AXM 5Q graphite of differing densities. Fig 3-2 below, shows the results obtained during this study for the thermal conductivity of graphite in the temperature range 400 to 2400 °C. The two samples tested, indicated as sample 3A1 and 3A2 had densities of 1.742 g/cm^3 and 1.834 g/cm^3, respectively. As described in the preceding section (6.4.1.3), a graphite density value of 1.760 g/cm^3 was used during simulations (FLUKA and ANSYS). Therefore, interpolated thermal conductivity values corresponding to a graphite density of 1.76 g/cm^3 were taken as a best approximation and included into the ANSYS material data file as such.

From figure 3-2 it can be seen that the difference in thermal conductivity for the two samples of differing density is marginal. The thermal conductivity decreases in an exponential fashion with increasing temperature, and stabilizes in the range of 36 to 38 W/m.K beyond 2200 °C.

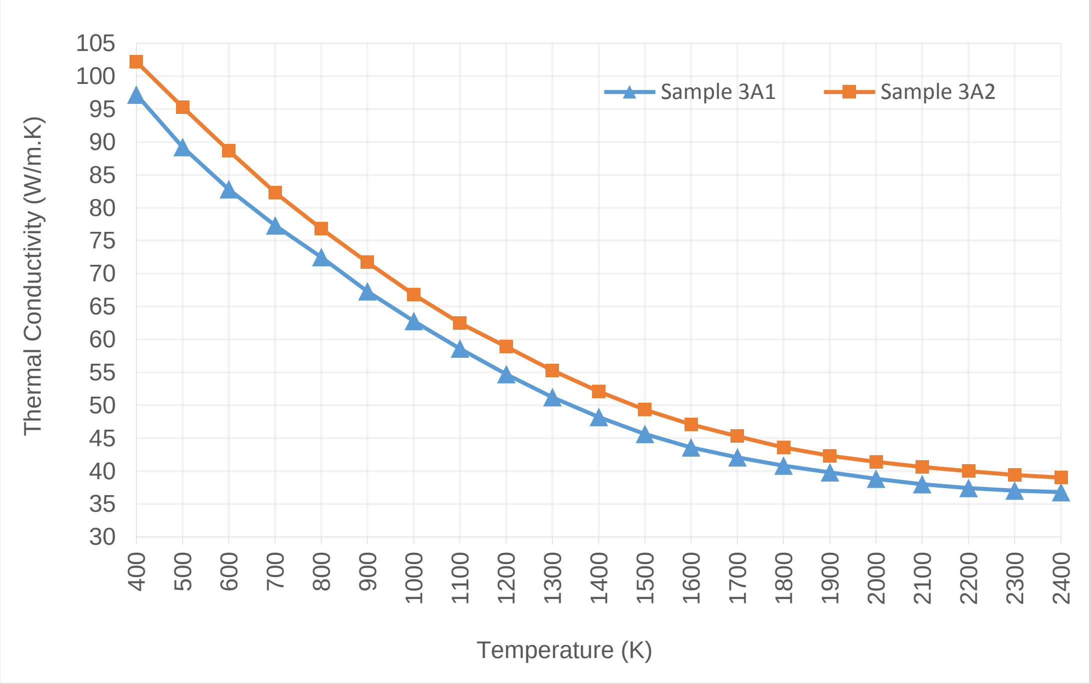

Figure 3-2: Thermal conductivity of two graphite samples of differing densities (ρ). Sample 3A1 (ρ = 1.742 g/cm^3) and Sample 3A2 (ρ = 1.834 g/cm^3). Adapted and developed from [Tay78].

3.1.4 Graphite – Coefficient of Thermal expansion

Data relating to the thermal expansion characteristics of graphite was obtained in a comprehensive study conducted in 1977, by *Touloukian, et al.* [Tou77], published under the Thermophysical Properties Research Centre (TPRC) data series. This study considered the before mentioned Grade AJT isomolded graphite, and provides the results obtained for coefficient of thermal expansion in the temperature range, 293 to 2600 K, as depicted in figure 3-3. As expected, the thermal expansion coefficients increase in a linear manner with an increase in temperature, as a result of widening gaps between the atoms in the material as it receives energy/heat. This thermal expansion data set was considered to be the most comprehensive of the data found in current literature, and is therefore used in the ANSYS material data file for graphite.

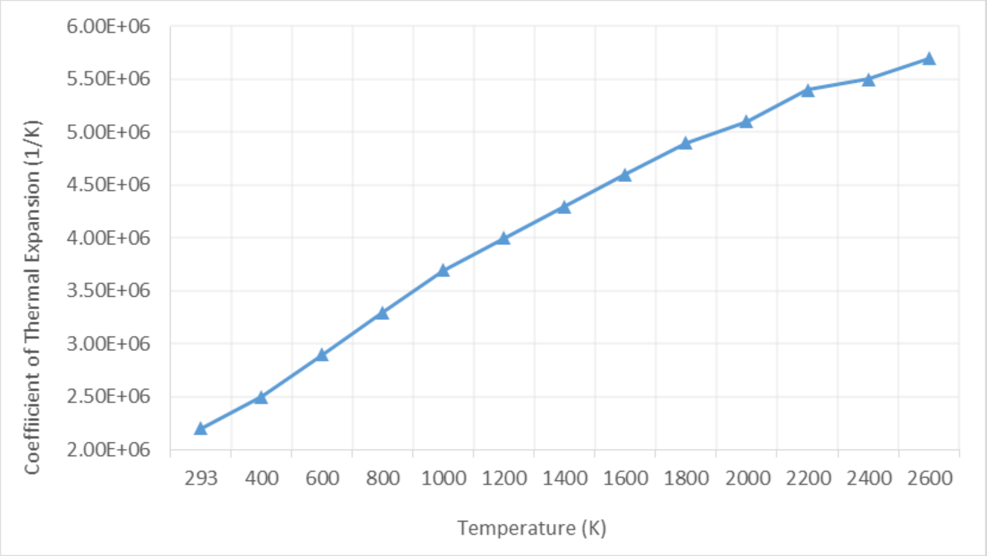

Figure 3-3: Coefficient of thermal expansion vs. temperature for isomolded graphite. Adapted and developed from [Tou77].

3.1.5 Graphite – Young's Modulus

In order to obtain realistic/measured Young's modulus (modulus of elasticity) data for graphite at RIB target operating temperature ranges, a study conducted by *Marlowe* in 1970 [Mar70] at the General Electrical Nucleonics Laboratory, America, under a NASA contract, was employed for reference. In this study, three grades of graphite were tested up to 2000 °C, to evaluate the effect of increasing temperature on the Young's and shear modulus of these materials. One of these grades of graphite was ATJS with a similar density to the grade AJT proposed for simulation in this research work. The Young's modulus results obtained in this study, for AJTS graphite heated from room temperature to 2000 °C, where adapted through unit conversion (psi to Pa) and presented in figure 3-4, below.

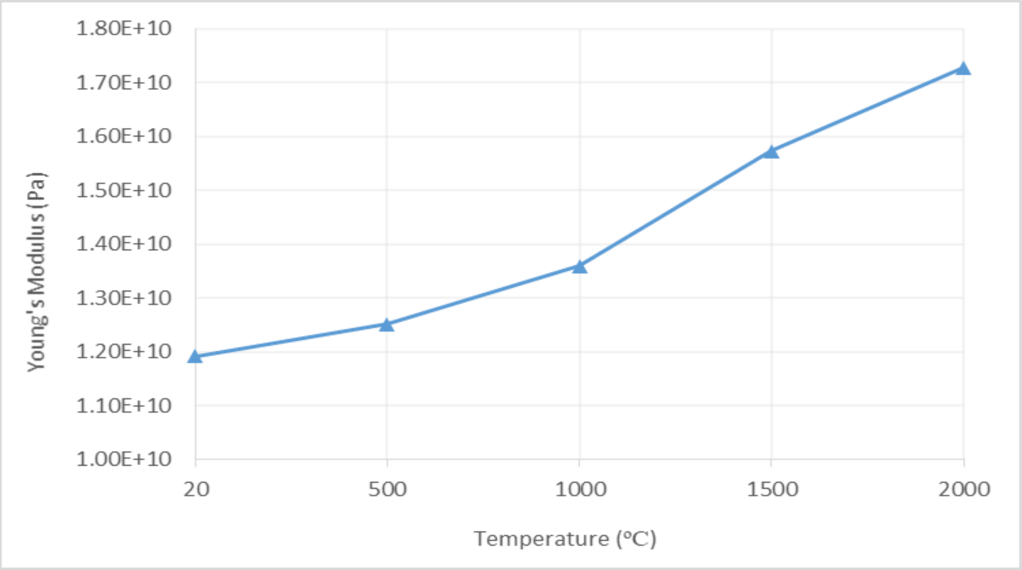

Figure 3-4: Young's Modulus vs. temperature for isomolded graphite. Adapted and developed from [Mar70].

3.1.6 Graphite – Poisson's ratio

No comprehensive literature could be found, examining the effects of high temperature and low pressure (vacuum) on the Poisson's ratio of isomolded graphite. Commercial manufacture's technical data sheets indicate the Poisson's ratio graphite to be approximately 0.3. This value corresponds to measurements taken in a study conducted by Sun & Yoon in 1988 [Sun88], in which the Poisson's ratio of graphite was found in the region of 0.31 across the temperature range of 0 to 200 °C. The value of 0.3 was used during simulation as a "best estimate" value for this parameter, and included as such as a constant value across the complete operational temperature range in the ANSYS material data file.

3.1.7 Graphite – Specific heat

In order to obtain a realistic specific heat capacity data for graphite at RIB target operating temperature ranges, a study conducted by *Taylor & Groot* in 1978 [Tay78] at the Properties Research Laboratory in Indiana, America, was employed for reference. This study analysed the thermal properties (thermal conductivity, specific heat and electrical resistivity) for two samples of POCO AXM 5Q graphite of differing densities. Figure 3-5 below, shows the results obtained during this study for related to the specific heat of graphite in the temperature range

300 to 2400 °C. The two samples tested, sample 3A1 and 3A2, had densities of 1.742 g/cm^3 and *1.834* g/cm^3, respectively. As described in the preceding section (3.1.2), a graphite density value of 1.76 g/cm^3 was used/assumed during simulations (FLUKA and ANSYS). Therefore, interpolated specific heat values corresponding to a graphite density of 1.760 g/cm^3 were taken as a best approximation and included into the ANSYS material data file as such.

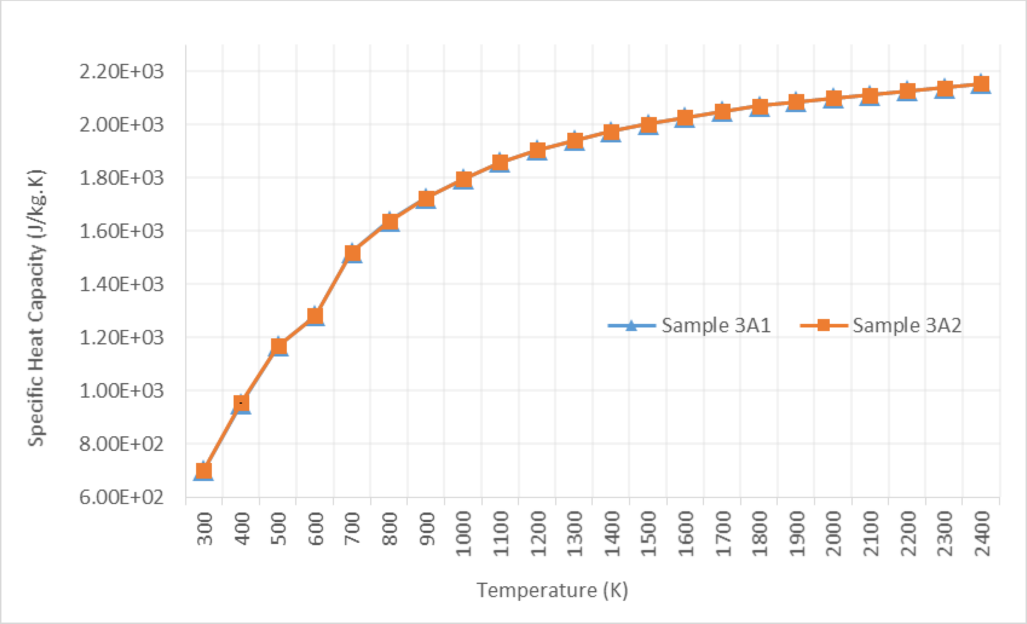

Figure 3-5: Specific Heat capacity of two graphite samples of differing densities (ρ). Sample 3A1 (ρ = 1.742 g/cm^3) and Sample 3A2 (ρ = 1.834 g/cm^3). Adapted and developed from [Tay78].

From figure 3-5 it can be seen that the specific heat capacity of graphite increases is a somewhat linear manner from 300 to 700 °C and thereafter flatten outs between 2.0E+3 and 2.2E+3 J/kg.K beyond 1400 °C.

3.1.8 Graphite – Electrical Resistivity

In order to obtain a realistic electrical resistivity data for graphite at RIB target operating temperature ranges, the study conducted by *Taylor & Groot* in 1978 [Tay78] at the Properties Research Laboratory in Indiana, America, was again employed for reference. Figure 3-6 below, shows the results obtained during this study for related to the electrical resistivity of graphite in the temperature range 300 to 2400 °C. As described in the preceding section (5.4.1.3), a graphite density value of 1.760 g/cm^3 was used/assumed during simulations (FLUKA and ANSYS). Therefore, interpolated electrical resistivity values corresponding to a graphite density of 1.760 g/cm^3 were taken as a best approximation and included into the ANSYS material data file as such.

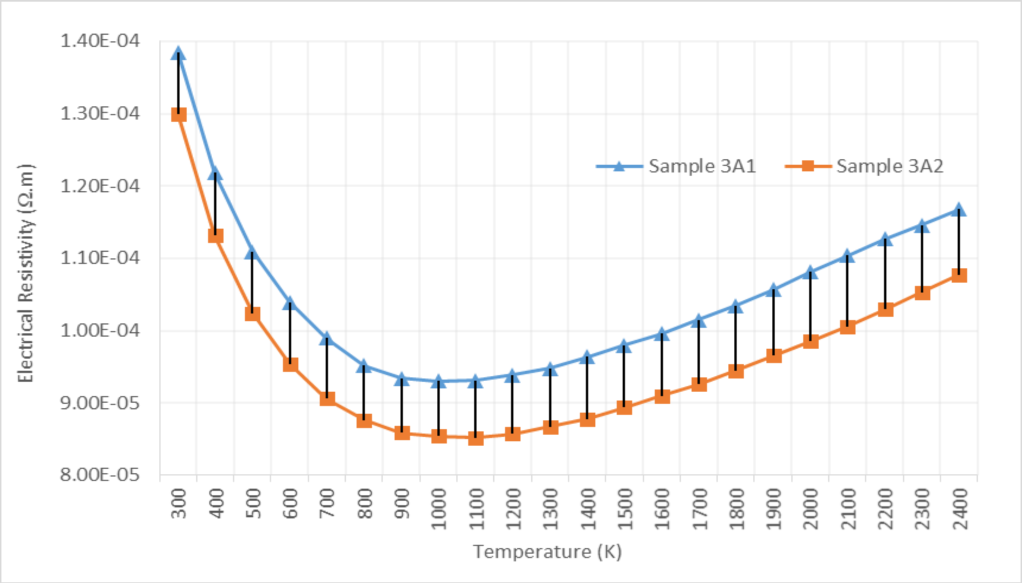

Figure 3-6: Electrical resistivity of two graphite samples of differing densities (ρ). Sample 3A1 (ρ = 1.742 g/cm^3) and Sample 3A2 (ρ = 1.834 g/cm^3). Adapted and developed from [Tay78].

3.1.9 Graphite – Emissivity

Emissivity measurements for Graphite, under the SPES project framework at INFN, Italy, were conducted in 2008 by *Biasetto, et al.* [Bia08]. This experimental study was employed for reference of realistic graphite emissivity values in the range of 1000 to 2000 °C under high vacuum (10^{-4} Pa) conditions.

In this experiment, four grades of isomolded graphite were used, namely *EDM200*, *AF5*, *EDM3* and *CL 2114*, which only differ in grain size, but other than that are no less similar to the Grade AJT isomolded graphite mentioned in the preceding sections.

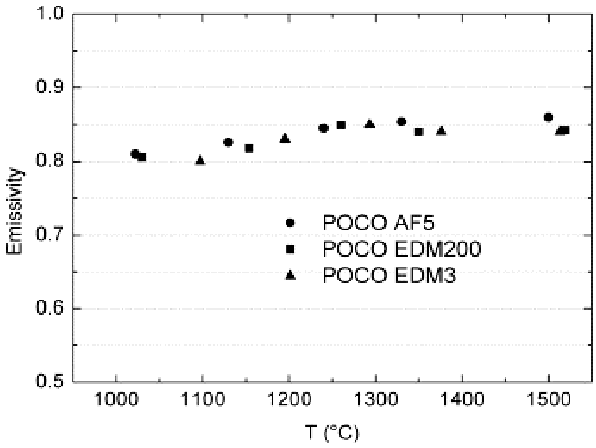

Figure 3-7: Measured emissivity values for isomolded graphite of varying grain size, *d* (in *µm*). POCO AF 5 (*d* < *1*), POCO EDM200 (*d* > *5*), POCO EDM3 (*1* < *d* < *5*) [Bia08].

From figure 3-7 above, it can be seen that the experimental study found the emissivity of graphite (for three of the four grades) to be between 0.8 and 0.9 in the temperature range of 1000 to 1500 ºC. A further test, conducted on graphite grade CL 2114, which sought to compare the emissivity values of polished and unpolished samples of this graphite grade in the temperature range 1000 to 2000 ºC was done. These results, shown in figure 3-8 below, for the unpolished graphite samples, were well in agreement with the three previously tested graphite grades, showing emissivity values ranging from 0.8 to 0.9 in this temperature range. Additionally, the effect of surface roughness is shown to be significant, as reducing the surface roughness of the graphite sample, yielding significantly lower emissivity values.

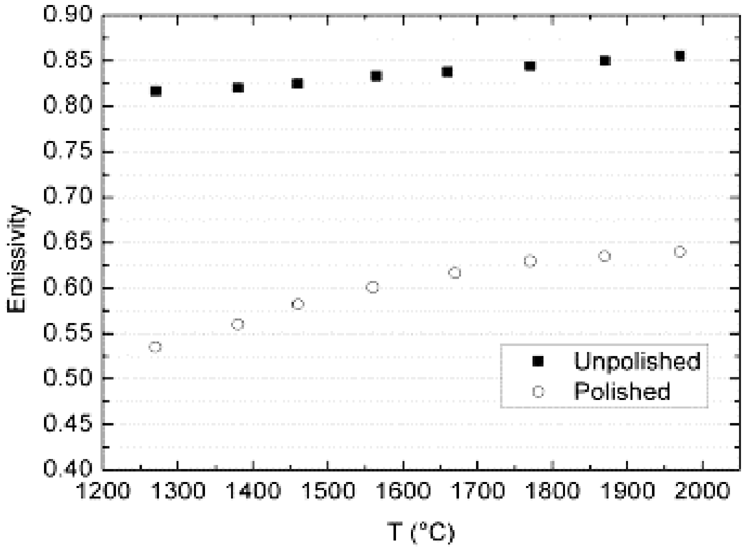

Figure 3-8: Measured emissivity values for 'polished' and 'unpolished' isomolded graphite grade CL 2114 [Bia08].

The results obtained from this study, which provided realistic emissivity values at the RIB target operating conditions found to be in the range of 0.8 to 0.9, were used in the ANSYS material data file for thermo-mechanical simulations.

3.1.10 Graphite – Elastic limit

Due to absence of commercial or literature references relating to the elastic limit of graphite, the best estimate elastic limit (yield strength) value for graphite was assumed to be 200 MPa (same value as used by INFN SPES). This value was considered as the limiting mechanical stress value in the target design process.

3.2 Boron Carbide

Boron carbide was discovered in the 19th century as a by-product of a reaction involving metal borides [Sur10]. In recent years, boron carbide has become the material of choice for various engineering applications, due to its unique combination of properties. Boron carbide is used in refractory applications for its high melting point and thermal stability [Dom11]. Industries such as abrasive and ballistic manufacturing and development, employ boron carbide for its high abrasion resistance, high hardness and low density. Furthermore, boron carbide is extensively used in nuclear applications, specifically in boiling water nuclear reactors, for its neutron absorption properties.

Although information on the crystalline structure of boron carbide is available in the literature, largely obtained from diffraction measurements, the exact site occupancies of the boron and carbon atoms are still under investigation. The difficulty in distinguishing the atomic configuration is a result of carbon and boron's similar electronic and nuclear scattering cross sections (^{12}C and ^{11}B isotopes). By means of crystal symmetry considerations, two configurations for stable boron carbide have initially been proposed, (i) B_4C and (ii) $B_{13}C_2$. However, it is widely accepted that carbon rich B_4C ($B_{12}C_3$) is the stoichiometrically stable state of boron carbide [Dom11].

The current commercial method of boron carbide production is known as *carbothermic reduction*, which involves carbon reduction of boric acid (H_3BO_3) and boron trioxide (B_2O_3). The reaction process/step proceeds in three stages, as follows [Sur10]:

Upon heating, boric acid (H_3BO_3) coverts to B_2O_3 with the release of water

- *Stage 1:* $4\ H_3BO_3 \rightarrow 2\ B_2O_3 + 6\ H_2O$

B_2O_3 is reduced by the addition of carbon monoxide (CO) at temperatures above 1400 °C

- *Stage 2:* $B_2O_3 + 3\ CO \rightarrow 2\ B + 3\ CO_2$

Boron and carbon are reacted at furnace temperatures in excess of 2000 °C, enhancing the overall rate of reaction, as this reaction is highly endothermic.

- *Stage 3:* $4\ B + C \rightarrow B_4C$

Boron carbide is proposed as a suitable target for the iThemba LABS RIB facility, due to its favorable ^{6}He cross section and material properties. These favorable material properties for iThemba LABS RIB application are as follows:

- Good thermal properties - thermal conductivity, coefficient of thermal expansion
- High melting point
- Low density
- Optimal mechanical properties – Poisson’s ratio, Young’s Modulus
- Chemical inert nature at high operating temperature

For this thesis work, various literary and commercial sources were used to obtain measured or in some cases, best approximations, for the thermal and mechanical properties of B_4C. Due to the lack of studies relating to the use of B_4C in systems operating at high temperature and high vacuum, some extrapolation and estimation was required for modelling of the material properties. These material properties were used to compile material data input files for use in ANSYS. The material properties of B_4C are evaluated in the sub-sections to follow.

3.2.1 Boron Carbide – Melting point

When proposing and developing a RIB target, one of the most important parameters to be considered in the melting/sublimation point of the given target material. For boron carbide, of high carbon content (i.e. B_4C), various phase diagrams are available in the literature which indicate a phase transition (sublimation) of B_4C at 2450 ^oC under atmospheric pressure (see figure 3-9, below). It should be noted however, that these sublimation/melting point temperatures for B_4C do not account for the low pressure (vacuum) conditions to which the target would be subjected to during operation in the RIB target system.

Due to the lack of literature available related to the melting point of B_4C under low pressure (high vacuum) condition, commercial B_4C manufacturers were contacted for information on this matter. The Kurt J. Lesker Company® provided a B_4C melting point temperature range [Kur17] of approximately 2500 - 2580 ^oC at a pressure of 10^{-4} Pa (RIB target system pressure). Although this temperature value is higher than the melting point temperature for B_4C under atmospheric conditions, a conservative approach was taken and the B_4C target limiting temperature (melting point) was set at 2400 ^oC for this target design.

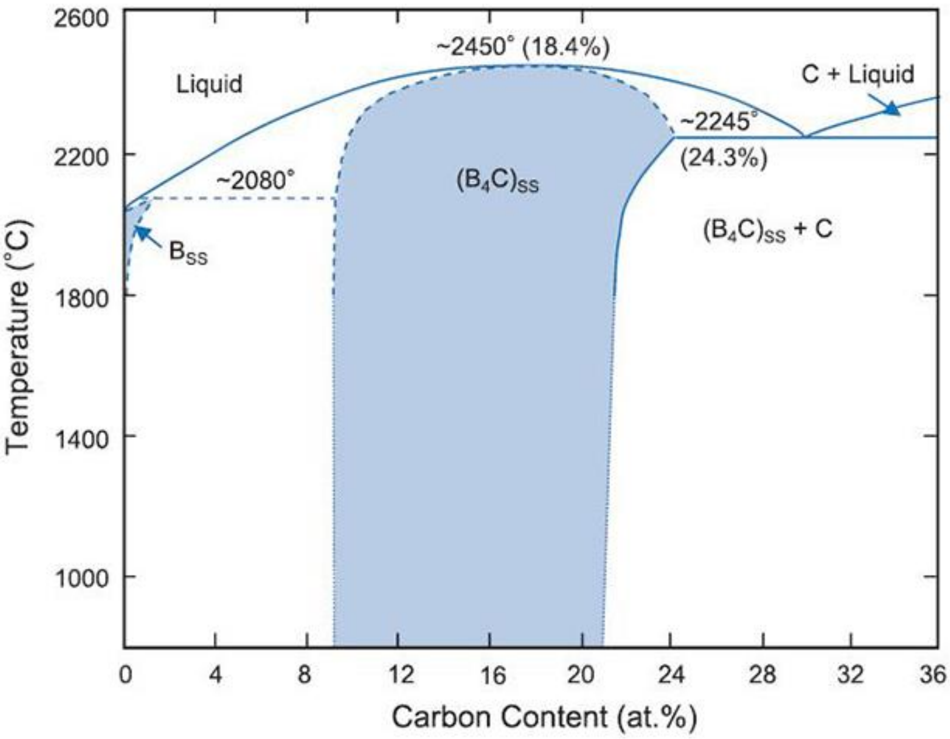

Figure 3-9: Phase diagrams for varying grades/compositions of boron carbide [Dom11].

3.2.2 Boron Carbide – Thermal conductivity

In order to obtain a realistic thermal conductivity for Boron Carbide at varying temperatures, a study conducted by *Wood & Zoltan* in 1985 [Woo85] , was employed for reference. This study found that thermal conductivities of boron carbides (samples of varying compositions were tested) at high temperature, are moderately low (0.1 – 0.01 W/m.K at 1000 K). Boron carbide of the highest carbon concentration, B_4C (20% carbon, 80% boron), exhibited the highest thermal conductivity between the tested boron carbides, as well as the most significant decrease due to increasing temperature [Woo85]. This relatively high thermal conductivity value of B_4C is characteristic of the lattice thermal conductivity of the crystal, suggesting that at the high carbon concentration, carbon atoms occupy all available sites, and therefore the thermal transport is that of a well ordered crystal. In contrast, at lower carbon concentrations, the carbon atoms only occupy a fraction of the available locations in the crystal structure, and thus the thermal transport through this defect structure resembles that of a disordered material [Woo85]. Therefore, it can be concluded that the carbon content and the impurity levels of the manufactured boron carbide, would have a significant impact on the thermal transport of the material, and therefore its thermal conductivity.

Although this study only measured the thermal conductivity of boron carbide up to approximately 1700 ºC, the “best-estimate” for values up to 2200 ºC using extrapolation were used. This adapted thermal conductivity data set was imported into the B_4C ANSYS material file for simulation

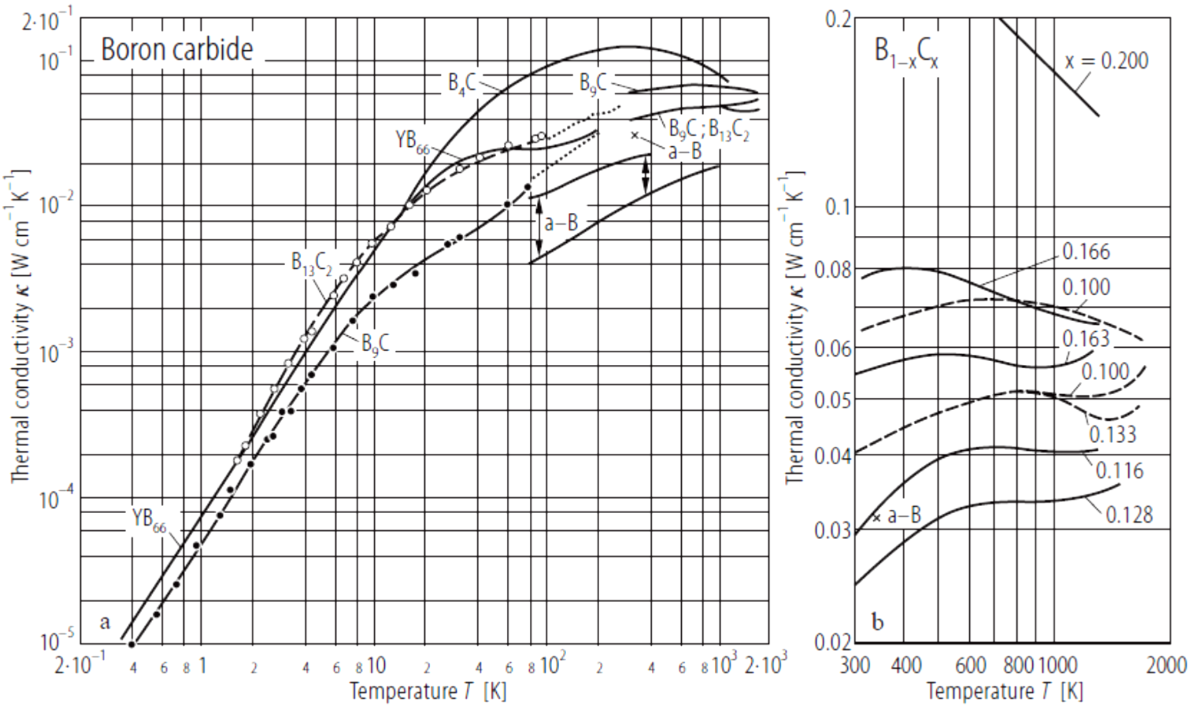

Figure 3-10: Experimentally obtained thermal conductivity values of various grades of boron carbide for temperature range 0 to 1800 ºC [Woo85]

3.2.3 Boron Carbide – Coefficient of Thermal expansion

In order to obtain a realistic, best approximation values for the thermal expansion of Boron Carbide, a study published by *Michaux, et al.* [Mic07] in 2007, in which the thermal expansion of various ceramic materials was studied, was employed for reference. In this studies, two marginally varying grades of boron carbide were tested, denoted as B_4C (1) and B_4C (2). These grades differed as a result of different manufacturing processes used to produce the boron carbide.

During the thermal expansion test, the boron carbide behaved as would be expected from a ceramic material upon heat application, by expanding. Figure 3-11 below, indicates the thermal expansion values obtained during this experiment, from these two grades of boron carbide between the temperature range 0 to 1200 ºC.

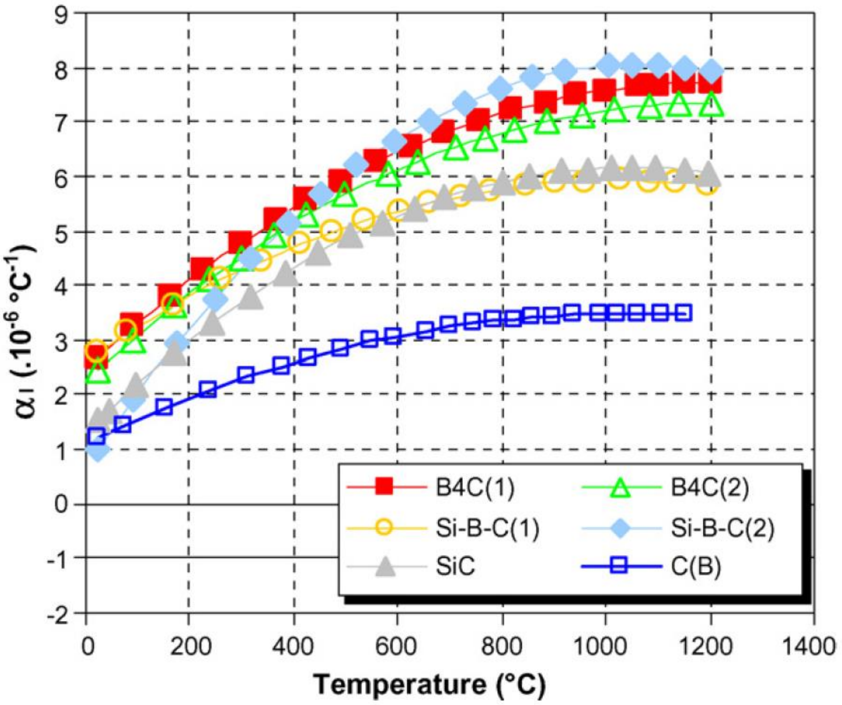

Figure 3-11: Experimentally obtained thermal expansion coefficient values of various ceramic materials (including Boron Carbide) for temperature range 0 – 1200 °C [Mic07].

These thermal expansion values were averaged between the two grades of boron carbide, and used as an input in the ANSYS material data file, for the range 0 – 1200 °C. Best estimate values, by means of extrapolation were used for temperatures above 1200 °C.

3.2.4 Boron Carbide – Young's Modulus

The same study used for reference of thermal expansion data, published by *Michaux et al.* [Mic07] in 2007, was consulted for information related to the modulus of elasticity (Young's Modulus) of B_4C upon heating. This study found that the modulus of elasticity of B_4C decreases in a constant manner with an increase in temperature, as shown in figure 3-12 below [Mic07]. This observation is stated to be as a result of the progressive weakening of the intra-chemical bonds of the B_4C material.

These Young's modulus values were averaged between the two grades of boron carbide, $B_4C(1)$ and $B_4C(2)$, and used as an input in the ANSYS material data file, for the range 0 – 1200 °C. Best estimate values, by means of extrapolation were used for temperatures above 1200 °C.

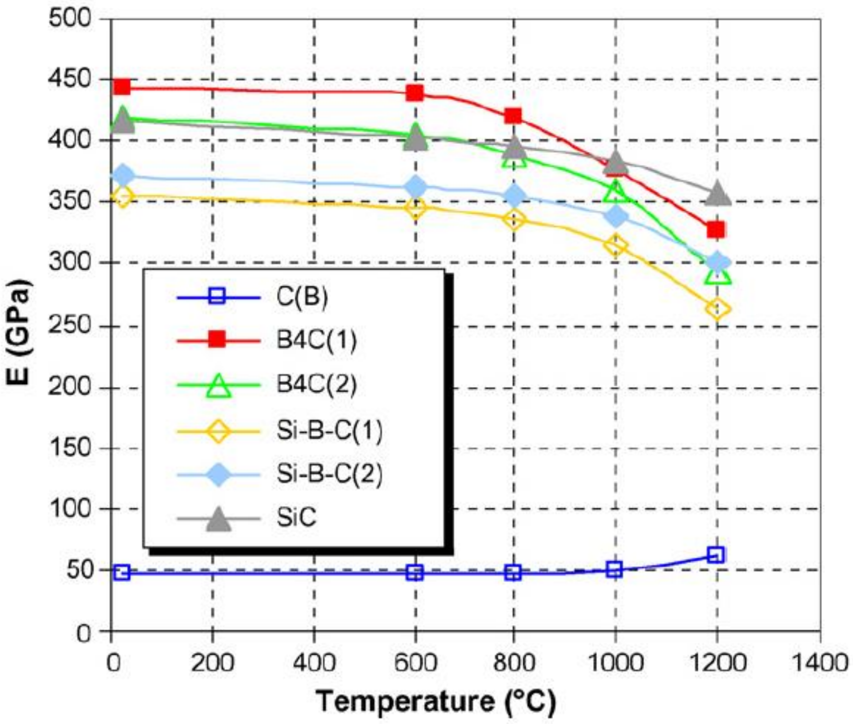

Figure 3-12: Experimentally obtained elastic modulus of various ceramic materials (including Boron Carbide) for temperature range 0 – 1200 ºC [Mic07].

3.2.5 Boron Carbide – Density

In order to ensure a realistic density value for B_4C, various manufacturers of commercially produced B_4C were contacted for reference. The quoted density values for 20% carbon containing B_4C ranged between 2.30 and 2.52 g/cm^3 [AZo01] [Kur17] [Ted14]. Using these manufacturer inputs, a density value of 2.50 g/cm^3 was used during simulation (FLUKA and ANSYS) for B_4C throughout the operating temperature range. No significant density change was assumed since the material is not expected to undergo a phase change during operation.

3.2.6 Boron Carbide – Poisson's ratio

No literature could be found, examining the effects of high temperature and low pressure (vacuum) on the Poisson's ratio of boron carbide. It is well documented, in the literature [Dom11] and commercial manufacture technical data sheets [AZo01] [Pan17], that the Poisson's ratio of high carbon containing boron carbide, B_4C, is approximately 0.2. This value was used during simulation as a best estimate value for this parameter, and included as such as a constant value across the complete operational temperature range in the ANSYS material data file.

3.2.7 Boron Carbide – Specific heat

A review study conducted by the *International Atomic Energy Agency (IAEA)* in 1997 [Cle97], evaluating experimental results of the thermal properties of boron carbide, was used for reference for realistic values of boron carbide's specific heat through the RIB target operational temperature range. This study considered experimental results of 10 boron carbide samples with densities ranging from 2.38 to 2.50 g/cm^3. These results are presented in figure 3-13 below, with the code numbers E000xxxx indicating the various boron carbide samples considered.

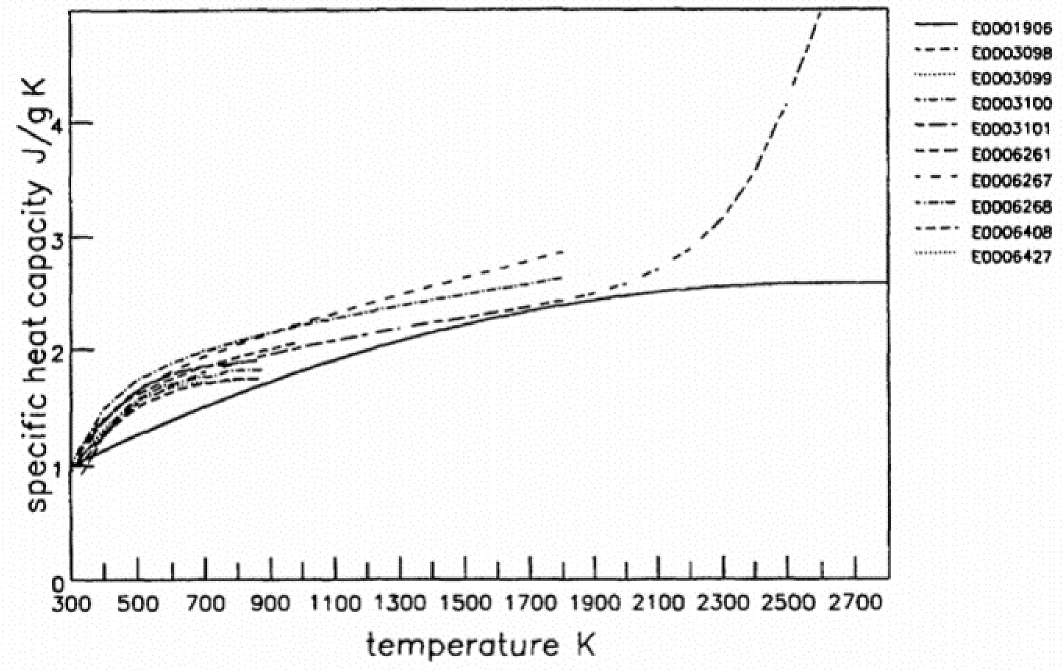

Figure 3-13: Specific heat capacity of various boron carbide samples, with densities ranging from 2.38 to 2.50 g/cm^3, for temperature range 0 – 2700 °C [Cle97].

From the results shown in figure 3-13, the boron sample *E0001906* was considered relevant for the purposes of this research work, as its density value was the same (2.50 g/cm^3) as the boron carbide sample proposed for use. From these results, it is noted that the specific heat of boron carbide increases in a somewhat linear fashion between the temperature range 0 – 1100 °C, and then begins to flatten out as it approaches 2000 °C and beyond. This data set represents a realistic analysis of the specific heat profile of boron carbide at the RIB operating temperature range, and was thus used in the ANSYS material file for boron carbide.

3.2.8 Boron Carbide – Electrical Resistivity

In order to obtain realistic electrical resistivity data for boron carbide at RIB target operating temperature ranges, a study conducted by *Lee et al.* in 1992 [Lee92], was employed for reference. In this study, the electric resistivity of approximately 20% carbon containing boron carbide was measured. The measured results, for the temperature range 750 to 3000 K are presented in figure 3-14 below. It should be noted however, that this study measured the electrical resistivity of thin film boron carbide, and does not provide an indication of the density of the boron carbide that was tested. Therefore, these results are considered a "best approximation" for electrical resistivity data as it relates to this research work. This data set was used in the ANSYS material file for boron carbide.

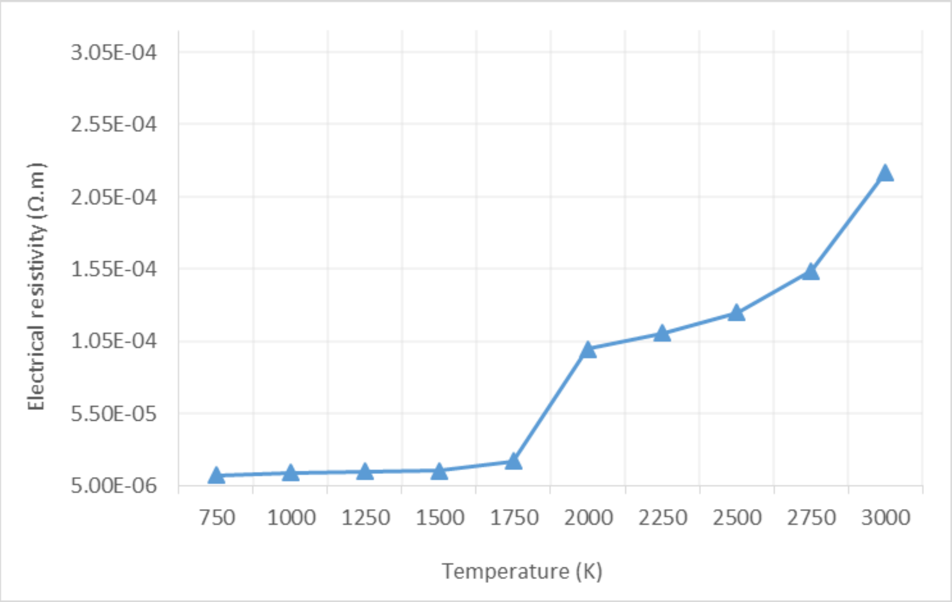

Figure 3-14: Electrical resistivity of thin film, 20% carbon containing boron carbide. Adapted and developed from [Lee92].

3.2.9 Boron Carbide – Emissivity

In order to obtain a realistic and most accurate emissivity value for Boron Carbide, a study conducted [Kam92] in 1991 in which the heat transfer between boron carbide fuel pellets and control rod cladding in a Fast breeder reactor was experimental evaluated, was employed for reference. In this study, it was found that the emissivity of boron carbide decreases with increasing temperature, up to approximately 300 ^{o}C, and thereafter exhibits a constant emissivity of 0.85 [Kam92]. Relatively high emissivity values are noted below 100 ^{o}C, which is attributed to the reflection of incident energy from the surroundings. The results of this experimental evaluation are provided in figure 3-15, below.

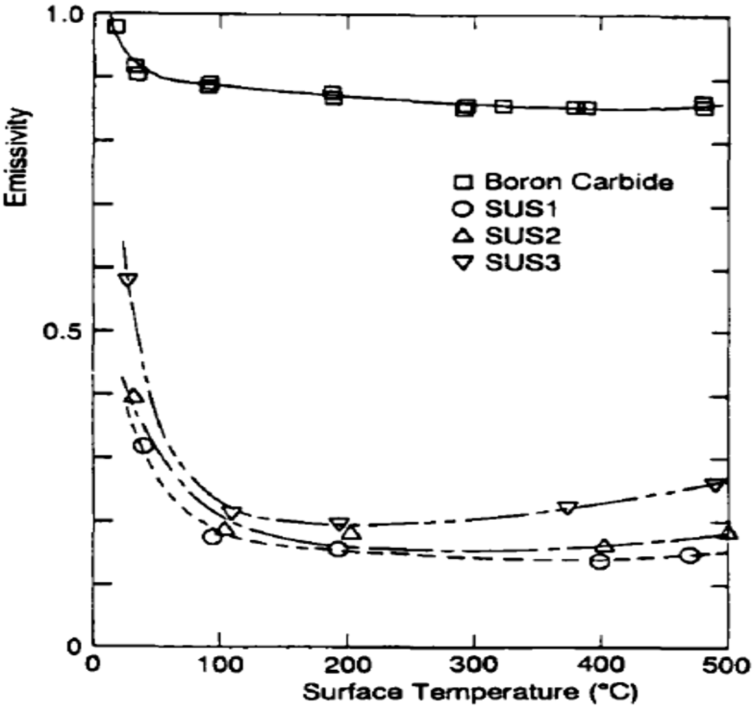

Figure 3-15: Emissivity of Boron Carbide. Adapted from [Kam92].

This data set was used for the emissivity values in the ANSYS material file for Boron Carbide, with a constant emissivity value of 0.85 used for operating temperatures above 500 ^{o}C.

3.2.10 Boron Carbide – Elastic limit

The best estimate elastic limit (yield strength) value for boron carbide was found to be 260 MPa, as referenced by material manufacturer, AZO Materials [AZo01]. This value was considered as the limiting mechanical stress value in the target design process.

CHAPTER 4: SIMULATIONS

During the iThemba LABS RIB target design and optimisation process, numerous target configurations of differing target materials, geometries and thicknesses, were tested and simulated. A number of these target configurations and their accompanying simulation results are presented in this chapter.

4.1 Graphite Targets

As discussed in chapter 1, graphite was considered a suitable target material for use in an adapted SPES target configuration, due to its well defined and referenced thermal and mechanical properties. Furthermore, the design of the SPES adapted graphite target was considered a departure point for further RIB target design and a means of providing assurance of the accuracy of the computer codes and simulations applied during the design process.

4.1.1 Graphite Targets – Design and optimisation

As previously mentioned, during the RIB target design the main aim was to produce the highest possible quantity of ^{6}He within the engineering constraints (thermal and mechanical limits) of the target material and associated target system components. The ^{6}He yield obtained from the target can be optimised by adjusting the following parameters: target disc thicknesses and the number of target discs. However, these two parameters have direct and significant influence on the following aspects: the release time of ^{6}He from the target disc, the spacing between discs and the thermo-mechanical stresses exerted on the target discs.

Increasing the target disc thickness would result in:

- An increase in the ^{6}He release time from the target material, which, due to the short half-life of ^{6}He (807 ms), would result in a reduction of extractable ^{6}He from the target system.
- An increase in power deposited by the primary beam into the target disc, resulting in increased thermo-mechanical stresses on the target discs

Additionally, increasing the number of target discs (assuming a fixed target canister length) would result in:

- An increase in thermo-mechanical stresses on the target discs due to the increased contribution of thermal radiation between the target discs
- An increase in the time taken for the ^{6}He to migrate from the target discs to the transfer line, used to extract the ^{6}He from the target system. This increased delay would thus reduce the quantity of extractable ^{6}He for post-acceleration

It is therefore important to find an optimal balance between these parameters, to ensure effective and reliable operation of the RIB target. In order to balance these parameters, the following aspects were considered:

- The proton energy range at which the proton-graphite reaction cross section is highest
- The stopping power and projected range of protons in graphite

In order to gain insight into the reaction cross section for the ^{12}C(p,x)^{6}He reaction (where *x* in the reaction is classified as one or more “unknown” secondary particles), a study conducted in 1970 by Davids, et al. [Dav70], was employed for reference. In this study, a thin graphite target (65.0 – 80.0 µg/cm^{2} average thickness) was impinged by a primary proton beam at various energies within the 28 - 40 MeV range and the collective reaction cross sections of mass (A=6) particles ^{6}He and ^{6}Li measured. A FLUKA simulation was conducted to validate the PEANUT (*Pre-Equilibrium Approach to NUclear Thermalisation*) model employed by FLUKA to compute hadron-nucleus interactions, against that of the experimental cross section data obtained from the *Davids* study. The FLUKA simulation was conducted using the experimental parameters defined in the *Davids* study, with the graphite target thickness being averaged to a value of 72.5 µg/cm^{2}. The FLUKA in-target yield results for ^{6}He and ^{6}Li at the varying experimental proton beam energies were summed and converted to a reaction cross section value. A comparison of the reaction cross section data from the *Davids* study and the FLUKA simulation for the reactions ^{12}C(p,x)^{6}He + ^{12}C(p,x)^{6}Li*,* is shown in figure 4-1 below.

From figure 4-1, is can be seen that the FLUKA simulation results are well in agreement with that of the experimentally measured cross section data in the 28 – 40 MeV energy range. It should be noted that ~ 99 % of combined ^{6}He and ^{6}Li in-target yield value obtained from FLUKA is that of ^{6}Li and therefore the apparent correlation with experimental data from the Davids study, cannot be considered as a measure of FLUKA’s accuracy in simulating in-target ^{6}He yields. However, this data validation, although limited, is considered to provide additional confidence in the application of FLUKA for this research work.

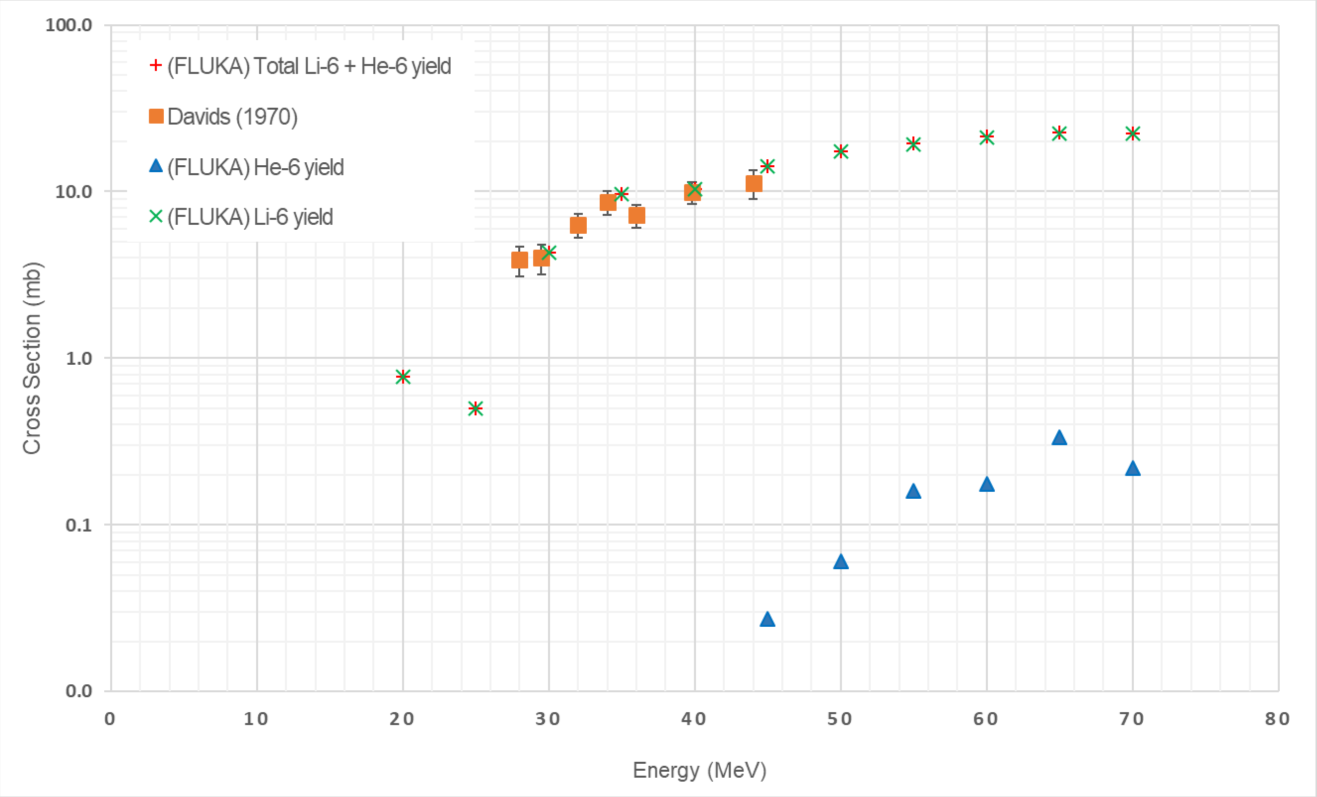

Figure 4-1: Reaction cross section data obtained from FLUKA simulation and Davids, et al. [Dav70] study for the $^{12}C(p,x)^{6}He$ + $^{12}C(p,x)^{6}Li$ reactions. Note: Error bars smaller than data points.

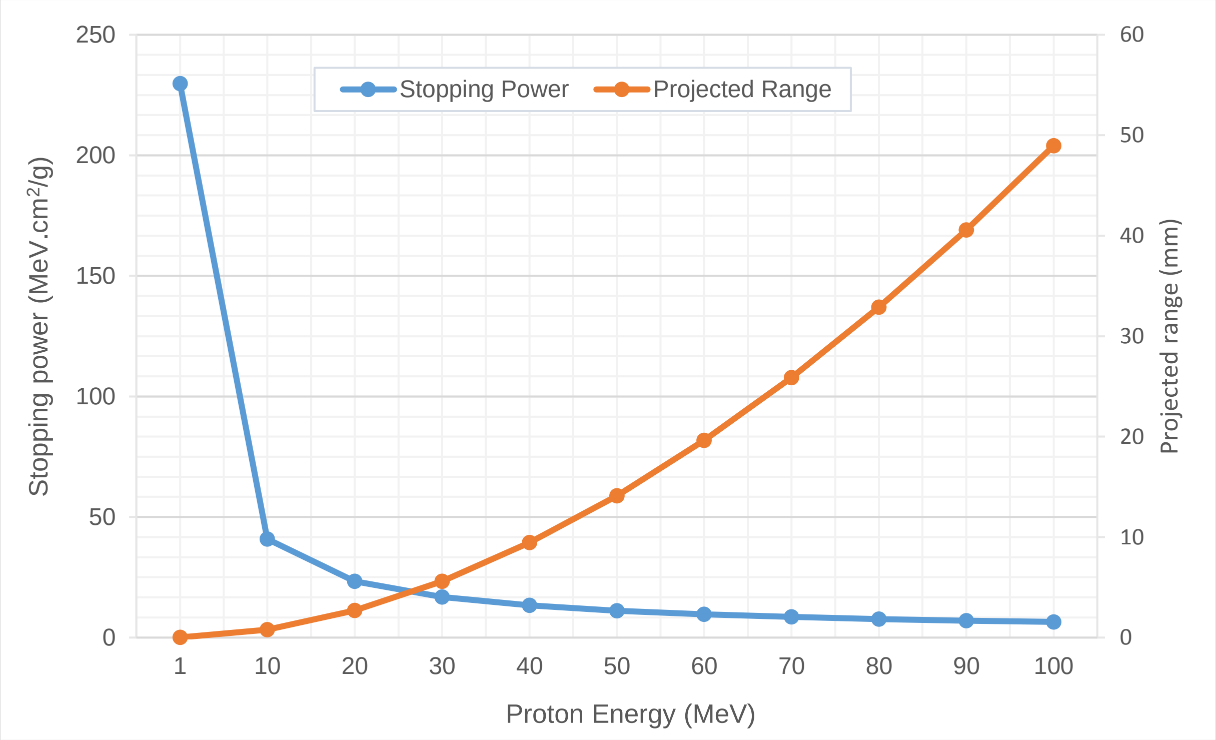

Figure 4-2: Stopping power and proton range in graphite. Extracted from SRIM [Zie10].

The stopping power and proton range in graphite, presented in figure 4-2 above was obtained from the SRIM software package. From figure 4-2, it can be seen that the effective length of graphite (ρ = 1.760 g/cm^3) required to stop 70 MeV protons is 25.9 mm. The graphite beam dump has an effective length of 13 mm, retained from the SPES design, and is an operational safety requirement as the primary proton beam deposits a maximum amount of energy (Bragg peak) at the end of its range, as a result of lower energy protons interacting with graphite, as shown by the sharp increase in stopping power below 10 MeV, in figure 4-2. The other contributions to the effective length of graphite in the target system is that of the two windows and screen at the entry of the target, the screen prior to the beam dump and the beam dump containing 4 graphite dumps at the backend of the target system. The use of graphite screens, in the form of an annulus, was introduced during the SPES target design at INFN, as it was shown to reduce the thermal and mechanical stresses on the first and last target discs at the front and back of the target system, respectively. Accounting for the contribution of the beam dump and neglecting the graphite windows (negligible thickness) and screens (due to its shape being that of an annulus), an effective minimum length of 12.9 mm graphite, is thus required to ensure the beam is stopped within the target system.

In order to meet the effective minimum length of 12.9 mm graphite, it was decided as an initial target design consideration to make use of thirteen (13) 1.1 mm graphite discs, thus providing an effective target discs length of 14.3 mm (~ 10% safety margin) and effective target system graphite length of 27.3 mm, enough to ensure that the primary proton beam would be stopped within the target system. This target system is hereafter referred to as configuration 1. Since the SPES prototype target layout was used, the following target parameters were maintained from the SPES design:

- Disc radius - 20 mm
- Target canister: Length - 230 mm, inner radius – 22.5 mm, outer radius – 24.5 mm
- Graphite windows at target entry: Thickness – 0.2 mm, radius – 22.4 mm
- Graphite screen (1) at target entry: Thickness – 0.3 mm, inner radius – 11.25 mm, outer radius – 20 mm
- Graphite screen (2) at beam dump entry: Thickness – 1 mm inner radius – 11.25 mm, outer radius – 20 mm
- Four beam dumps at the end of target: Beam dump 1, 2 and 3 thickness – 1 mm, Beam dump 4 thickness – 10 mm

Figure 4-3 below illustrates the layout of configuration 1, as simulated in FLUKA, with 13 1.1 mm graphite discs evenly spaced at 13.4 mm apart.

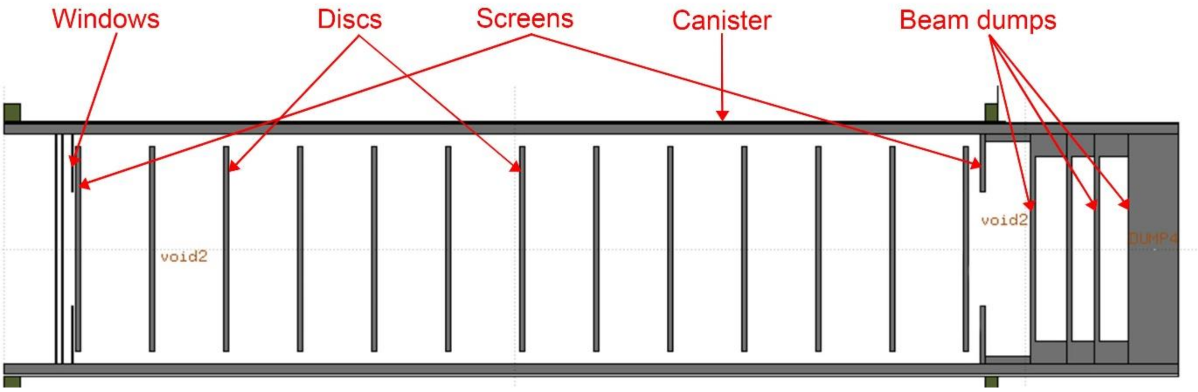

Figure 4-3: Configuration 1 target system layout, as simulated in FLUKA.

The in-target ^{6}He yield results for configuration 1, per 1.1 mm graphite target disc, is shown in figure 4-4, below

It should be noted that all ^{6}He yield results presented in this work are considered as in-target yields with a typical in-target average ^{6}He yield error of ± 1-5 % given by FLUKA.

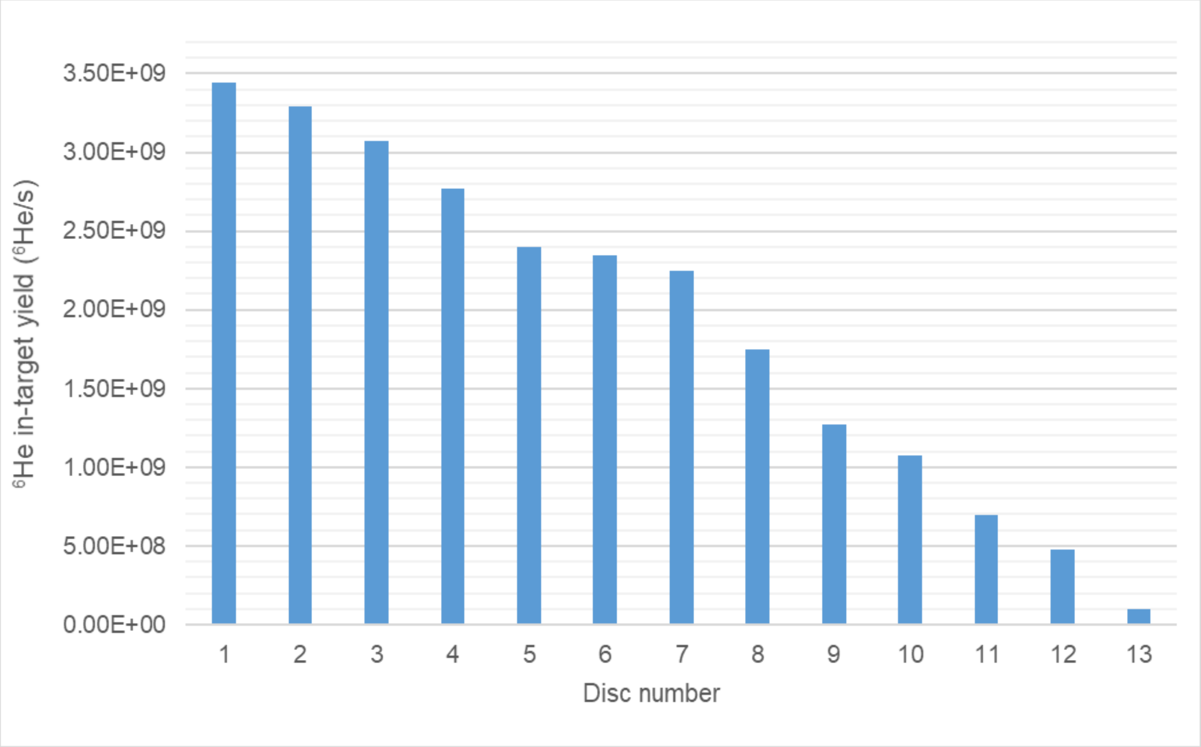

Figure 4-4: Configuration 1 - In-target ^{6}He yield results, per 1.1 mm graphite target disc.

The FLUKA simulated total ^{6}He yield obtained from configuration 1, was found to be **2.49 x 10^{10} ^{6}He/s** for a 70 MeV, 200 µA primary proton beam. From the results shown in figure 4-4 above, it can be seen that the highest yield occurs in disc 1, which is to be expected as the primary beam has undergone minimal beam energy losses in this front region of the target system. Disc 2 to 12 shows a gradual decrease in in-target ^{6}He yield, with a significant drop in ^{6}He yield at disc 13. The gradual decrease in ^{6}He yield throughout the length of the target system can be attributed to reduction in reaction cross section due to reducing proton energies as the protons move through the target system.

In order to verify the reproducibility of ^{6}He yield result obtained from FLUKA for the simulation of configuration 1, a second configuration (denoted configuration 2) was simulated with the same 13 1.1 mm discs at variable spacing between discs. Since the effective graphite target disc length is the same in both configuration 1 and 2, it was expected that the ^{6}He yield results would be the same, as the primary beam is modelled as a collimated beam (i.e. no beam spreading). The ^{6}He yield comparison between configuration 1 and 2, per graphite target disc, is shown in figure 4-5 below. From figure 4-5 it can be seen that the scoring of residual nuclei in the FLUKA simulation can be considered reproducible as the two yield results are within the 5% error, with configuration 1 and 2 providing a total ^{6}He yield of **2.49 x 10^{10} ^{6}He/s** and **2.41 x 10^{10} ^{6}He/s**, respectively.

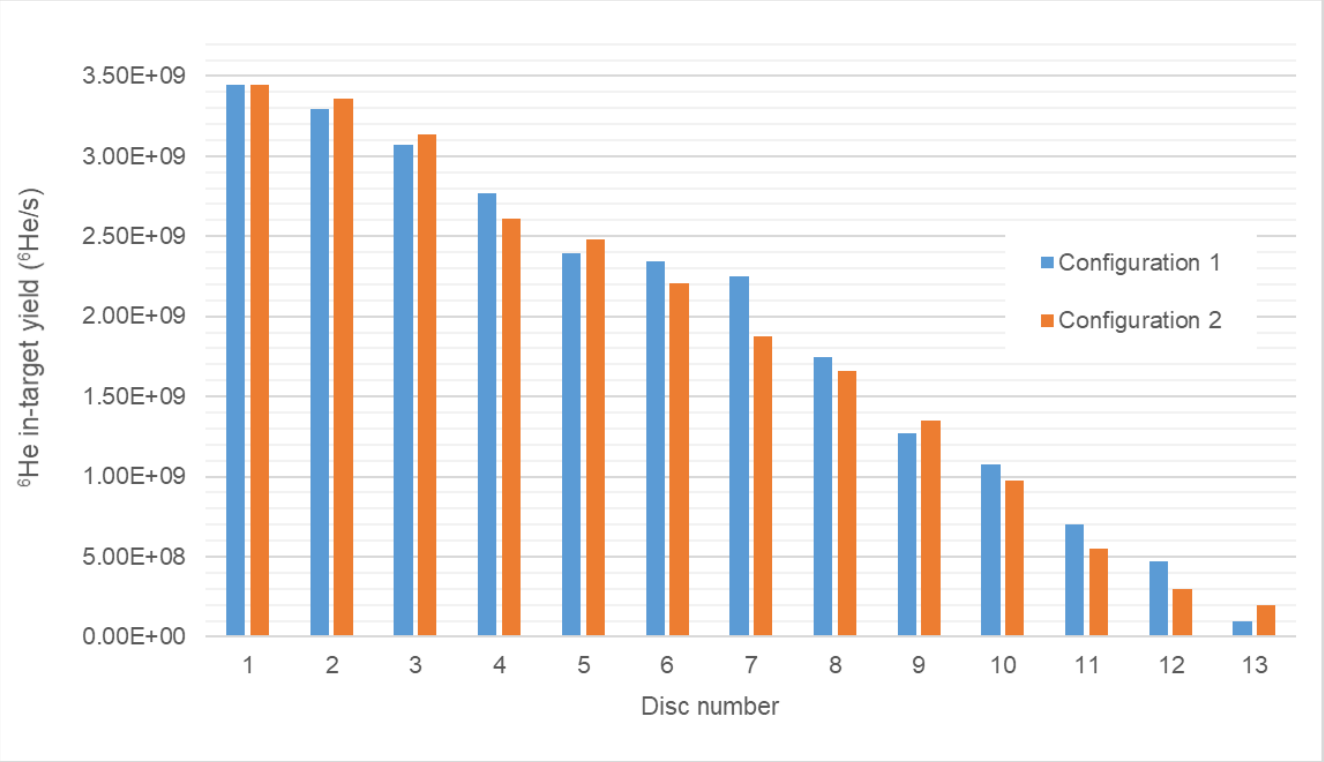

Figure 4-5: In-target ^{6}He yield comparison between configuration 1 and 2, per graphite target disc.

The placement of target discs and associated disc spacing for configurations 1 and 2 is shown in table 4-1 below. It should be noted that the position data shown in table 4-1, is presented with the entry of the target canister being the reference point (0 mm).

	Configuration 1				**Configuration 2**			
Disc number	start of disc (di) [mm]	end of disc (df) [mm]	disc thickness (dz) [mm]	disc spacing after (df) [mm]	start of disc (di) [mm]	end of disc (df) [mm]	disc thickness (dz) [mm]	disc spacing after (df) [mm]
1	13.9	15.0	1.1	13.4	13.9	15.0	1.1	11.9
2	28.4	29.5	1.1	13.4	26.9	28.0	1.1	9.9
3	42.9	44.0	1.1	13.4	37.9	39.0	1.1	8.9
4	57.4	58.5	1.1	13.4	47.9	49.0	1.1	9.4
5	71.9	73.0	1.1	13.4	58.4	59.5	1.1	12.4
6	86.4	87.5	1.1	13.4	71.9	73.0	1.1	14.4
7	100.9	102.0	1.1	13.4	87.4	88.5	1.1	15.4
8	115.4	116.5	1.1	13.4	103.9	105.0	1.1	17.4
9	129.9	131.0	1.1	13.4	122.4	123.5	1.1	17.4
10	144.4	145.5	1.1	13.4	140.9	142.0	1.1	16.4
11	158.9	160.0	1.1	13.4	158.4	159.5	1.1	16.9
12	173.4	174.5	1.1	13.4	176.4	177.5	1.1	11.9
13	187.9	189.0	1.1		189.4	190.5	1.1	

Table 4-1: Configuration 1 – Target disc positioning, dimensions and spacing

The proton distribution during operation of target configuration 1 and 2 with the 70 MeV, 200 µA (1.2482 x 10^{15} protons/s) primary proton beam was simulated in FLUKA. The proton distributions for these target configurations are shown in figures 4-6 and 4-7 below.

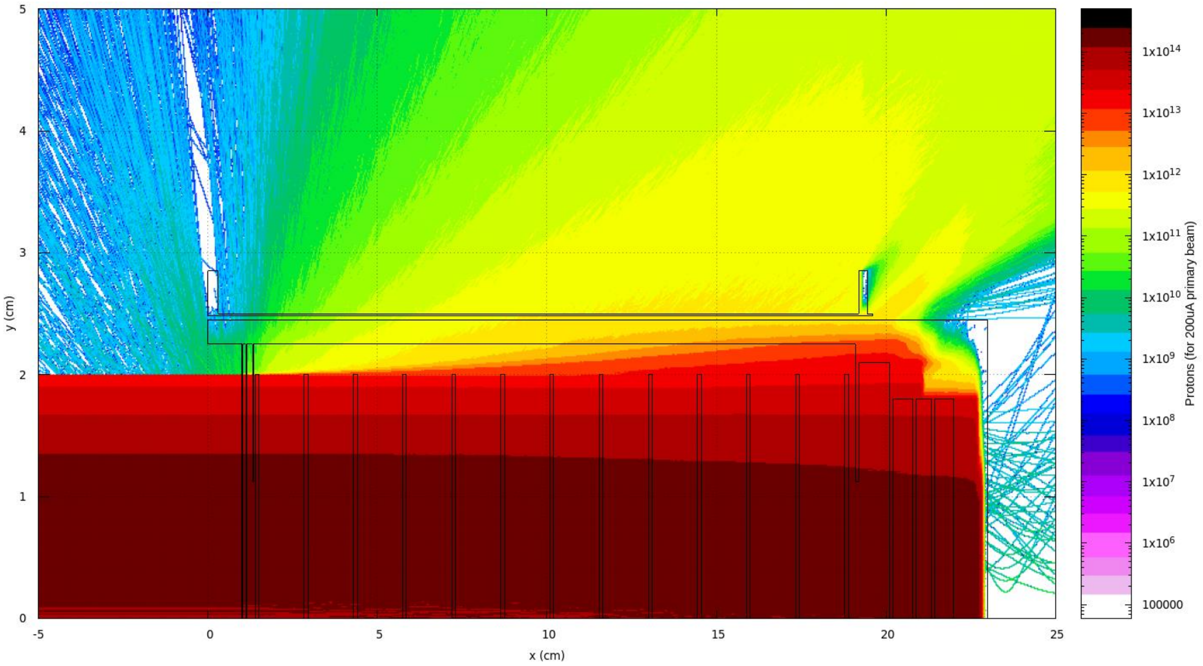

Figure 4-6: Proton distribution within configuration 1.

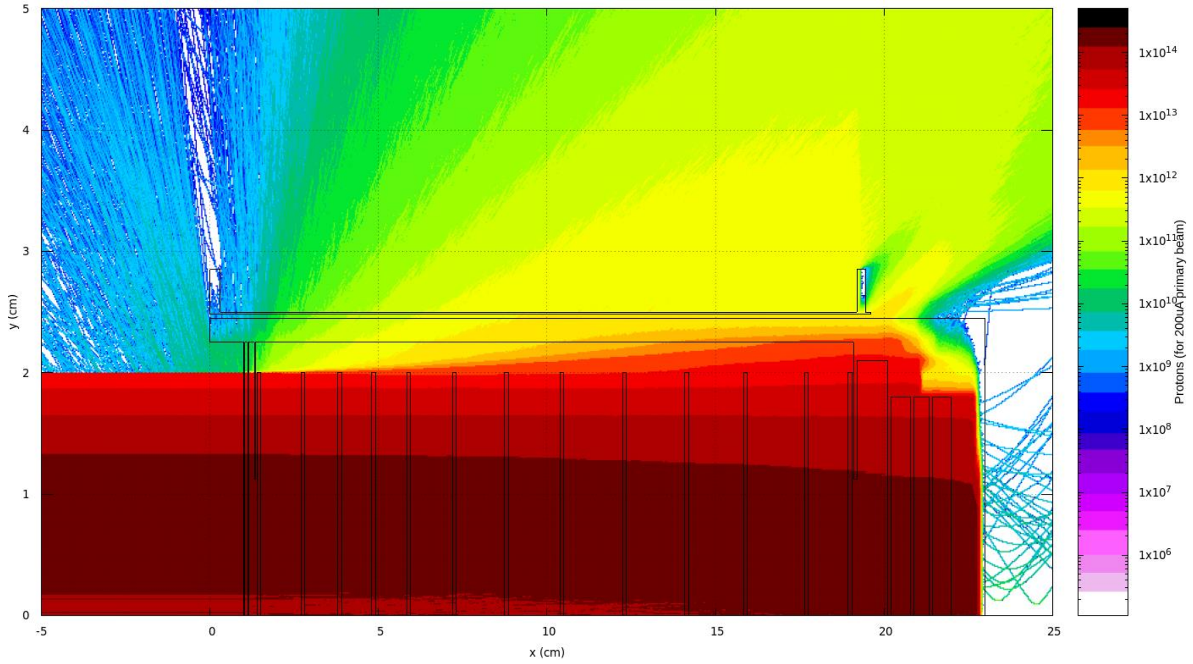

Figure 4-7: Proton distribution within configuration 2.

From figures 4-6 and 4-7 above, it can be seen that the primary beam is well collimated throughout the length of the target system, with minimal beam spreading occurring in the latter half of the target system. Furthermore, it can be seen that the proton beam is stopped within the target system (at the beam dump) in both configuration 1 and 2, which is an important operational safety requirement to be met.

Since lower energy protons would deposit more energy into a target disc, due to higher residence time within the target material, it was decided to place more discs closer to the front of the target where the proton energy is highest, as was done in configuration 2, as opposed to the even spacing used in configuration 1. Additonally, by applying the disc spacing of configuration 2, it was expected that the larger spacing between the discs in the latter half of the target system would reduce the disc and beam dump temperatures in this region, as the thermal radiation between the discs in this region would be reduced.

In order to simulate the thermo-mechanical stresses on the target system components, the power deposition results obtained from FLUKA were coupled to ANSYS as input loads, allowing for simulation of target system component temperatures and mechanical stresses during operation. It should be noted that all ANSYS simulations of the target system were conducted with a 2500 W load from the external heater applied to the outside of the target system canister, which assists in the pre-heating (conditioning) of the target system and subsequent control/maintenance of optimal temperature. Following the detailed discussion regarding the material properties and simulation inputs for graphite in Chapter 3, the following operational safety limits, listed in table 4-2 below, were adopted during the ANSYS thermo-mechanical analysis.

Material	Parameter	Maximum Value	Unit
Graphite (C)	Max. Temperature	2300	°C
	Max. Von-Mises Stress	200	MPa

Table 4-2: Graphite operational temperature and mechanical stress limits.

ANSYS thermal simulation results for configuration 2 are presented in figures 4-8 and 4-9, below. From figure 4-8, it can be seen, as expected, that the temperatures of the discs increase as the primary proton beam moves through the target system, as a result of more energy being deposited in the target material as the primary beam slows down, due to the proton residence time within the material being longer at lower velocities. The maximum temperature experienced on the target discs, specifically discs 4 to 13, is ~ 2267 °C (SMX), which is below the thermal limit set for graphite of 2300 °C, and thus presents no operational concerns. However, from figure 4-9 it can be seen that the maximum temperature in the beam dump is found to be ~ 3042 °C (SMX), which is well above the operational temperature limit for graphite (2300 °C). Therefore, due to the temperatures noted in the beam dump, this target configuration could not be declared fit for use, as the beam dump would be subjected to material degradation at these temperatures.

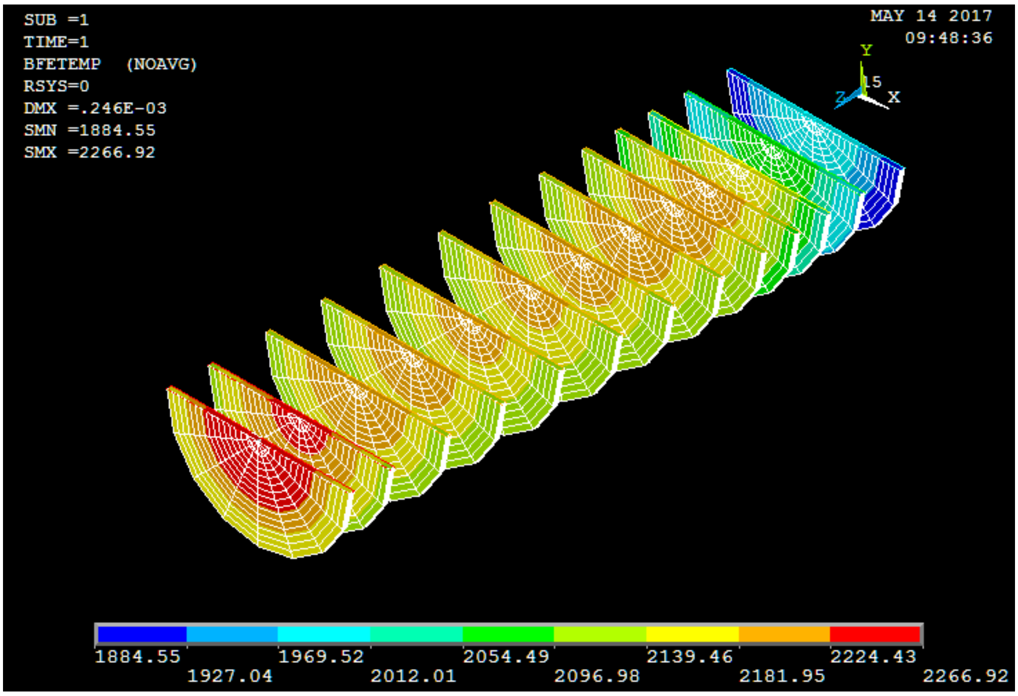

Figure 4-8: Configuration 2 – target discs thermal results.

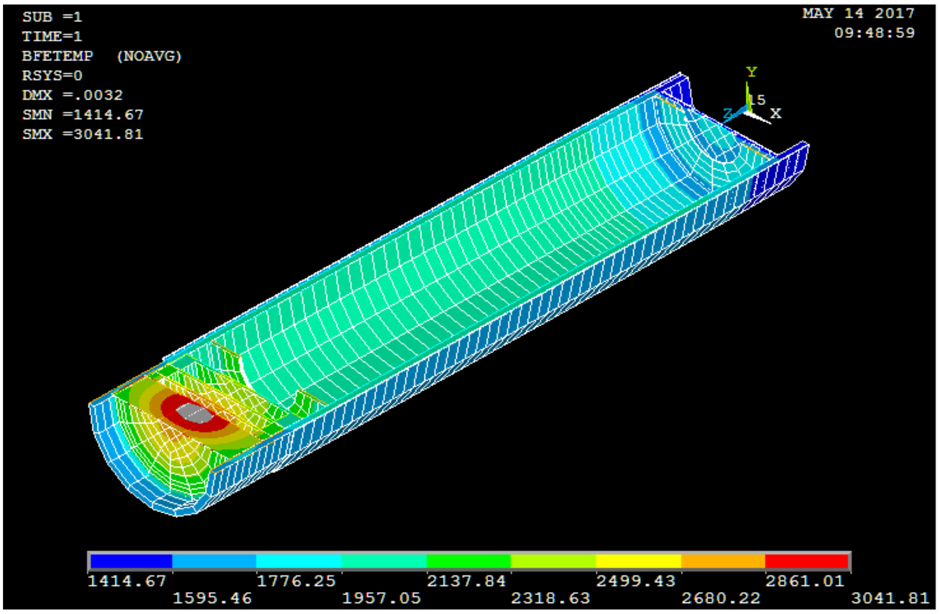

Figure 4-9: Configuration 2 – target canister and beam dump thermal results.

The mechanical stress (Von misses stress) analysis results for configuration 2, shown in figures 4-10 and 4-11 below, indicated a maximum VM stress value of 4.65 MPa on the discs and 23.40 MPa on the beam dump. The target discs, beam dump and system components are thus well within the mechanical stress limit for graphite of 200 MPa. It is noted, as expected, that the stresses in all discs increase radially from the center to the outer edges of the discs. This observation could be attributed to the induced thermal stress placed upon the discs as they experience an increasing temperature gradient during operation, while being restrained at their edges by the disc restraints on the interior of the target system canister.

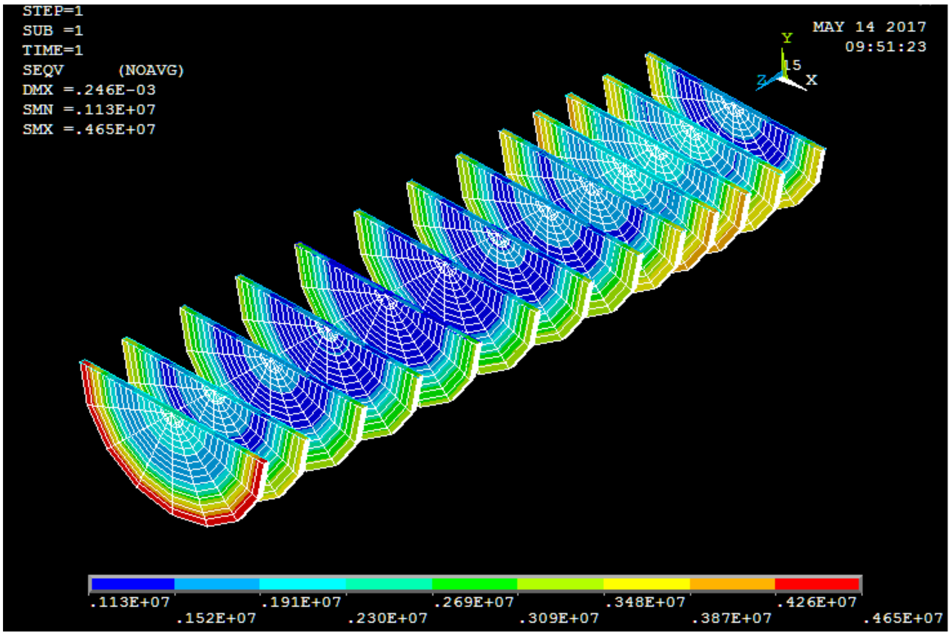

Figure 4-10: Configuration 2 – target discs VM stress results.

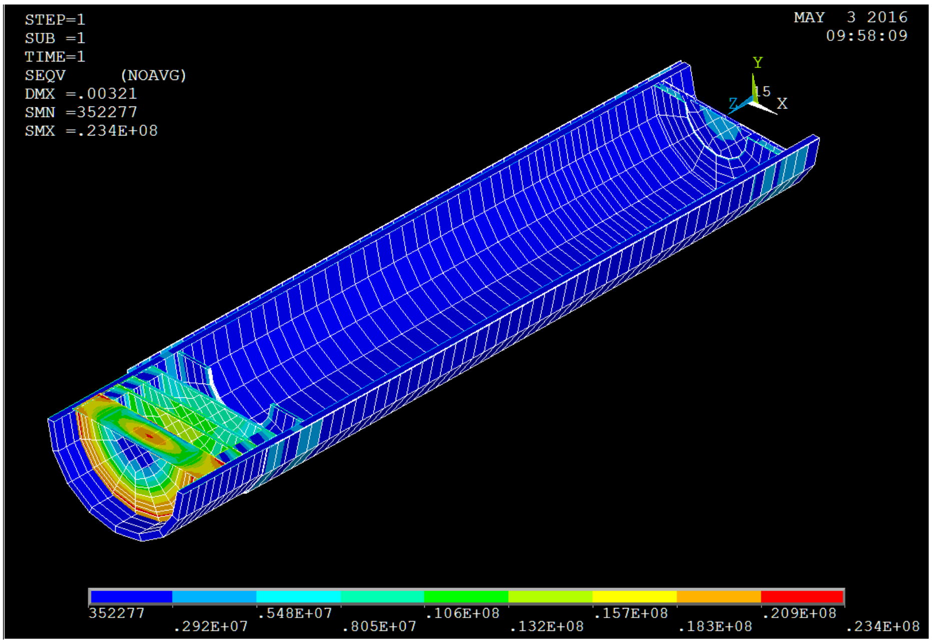

Figure 4-11: Configuration 2 – target canister and beam dump VM stress results.

In an attempt to reduce the beam dump temperatures noted in the ANSYS simulations of configuration 2, a redesign was proposed. This redesign entailed the use of 13 target discs of varying thicknesses, with the thicker discs being placed at the target system entry, where the proton energy is highest, as well as the last disc prior to the beam dump, in order to reduce the thermal load on the beam dump. This redesigned target is hereafter referred to as configuration 3. The disc positions and thickness of configurations 2 and 3 are provided in table 4-3 below, with the target system entry being the reference point (0 mm).

	Configuration 2				**Configuration 3**			
Disc number	start of disc (di) [mm]	end of disc (df) [mm]	disc thickness (dz) [mm]	disc spacing after (df) [mm]	start of disc (di) [mm]	end of disc (df) [mm]	disc thickness (dz) [mm]	disc spacing after (df) [mm]
1	13.9	15.0	1.1	11.9	13.9	15.3	1.4	11.6
2	26.9	28.0	1.1	9.9	26.9	28.1	1.2	9.8
3	37.9	39.0	1.1	8.9	37.9	38.9	1.0	9.0
4	47.9	49.0	1.1	9.4	47.9	48.8	0.9	9.6
5	58.4	59.5	1.1	12.4	58.4	59.3	0.9	12.6
6	71.9	73.0	1.1	14.4	71.9	72.8	0.9	14.6
7	87.4	88.5	1.1	15.4	87.4	88.3	0.9	15.6
8	103.9	105.0	1.1	17.4	103.9	104.8	0.9	17.6
9	122.4	123.5	1.1	17.4	122.4	123.3	0.9	17.6
10	140.9	142.0	1.1	16.4	140.9	141.8	0.9	16.6
11	158.4	159.5	1.1	16.9	158.4	159.3	0.9	17.1
12	176.4	177.5	1.1	11.9	176.4	177.3	0.9	12.1
13	189.4	190.5	1.1		189.4	190.6	1.2	

Table 4-3: Configuration 2 & 3 – Target disc positioning, dimensions and spacing.

The FLUKA simulated total ^{6}He yield obtained from configuration 3, was found to be ~ **2.30 x 10^{10} ^{6}He/s** for a 70 MeV, 200 µA primary proton beam. An approximate reduction of 5% in ^{6}He yield was thus noted from configuration 2 to 3, indicating the effect of reducing the effective graphite target disc length from 14.3 mm in configuration 2 to 12.9 mm in configuration 3.

It is expected that by lowering the temperature of the last disc in the array (disc 13) the beam dump temperature could be reduced as a result of lower thermal radiation from disc 13 to the entry of the beam dump. A method of reducing the temperature of disc 13, is to ensure lower power deposition (lower temperature) in the preceding disc 12, by reducing the disc thickness. Target discs power deposition results obtained from FLUKA, for configuration 2 and 3 are provided in figure 4-12. From figure 4-12, it can be seen that disc 12 in configuration 3 has significantly lower power deposition as opposed to configuration 2. Although the total power deposited in the target array is marginally higher for configuration 2 (5.82 kW) as compared to configuration 3 (5.16 kW), the reduced thermal radiation coming from disc 12 in configuration 3, is expected to result in a lower disc 13 temperature and therefore lower beam dump temperature.

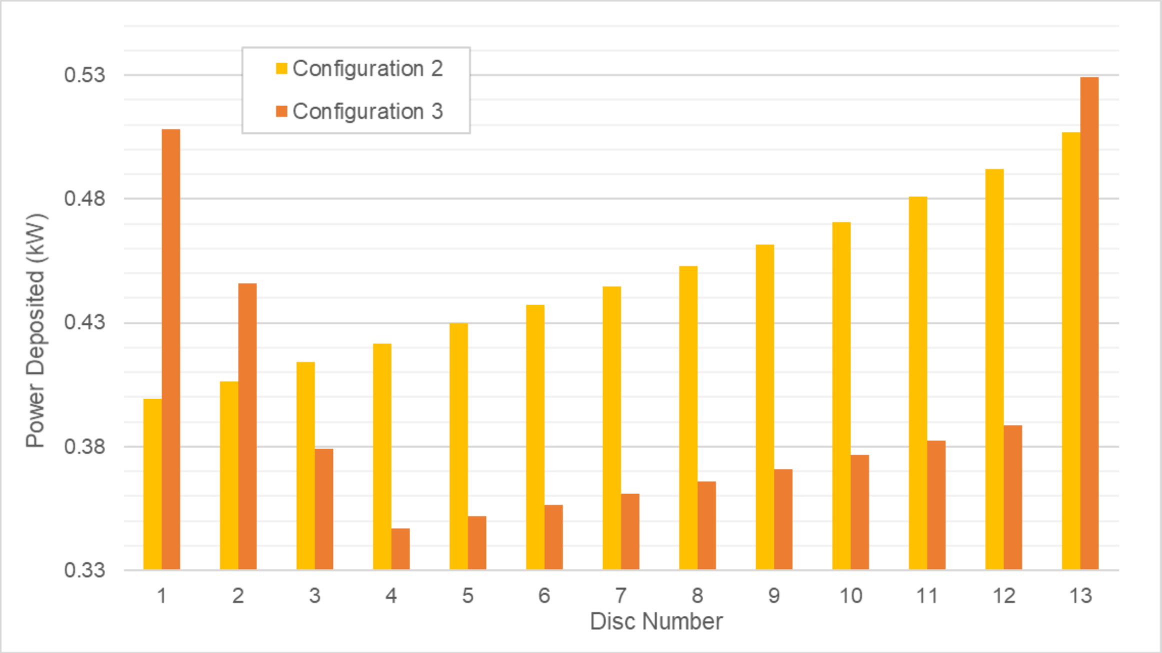

Figure 4-12: Configuration 2 and 3 - Target discs power deposition.

The ANSYS thermal analysis results for the redesigned target (configuration 3) are shown in figures 4-13 and 4-14 below. From figure 4-13, it is noted that the highest/maximum temperature occurs on target disc 13 with a temperature of ~ 2200 °C (SMX), which is a 47 °C reduction from the maximum temperature observed in configuration 2. The beam dump temperature in configuration 3 was found to be ~ 2873 °C (SMX), as shown in figure 4-14 below, which is a 47 °C reduction from the highest beam dump temperature observed in configuration 2. Although this reduction represents a significant improvement, the beam dump temperature is still significantly above the graphite temperature limit of 2300 °C and therefore renders configuration 3 unfit for purpose.

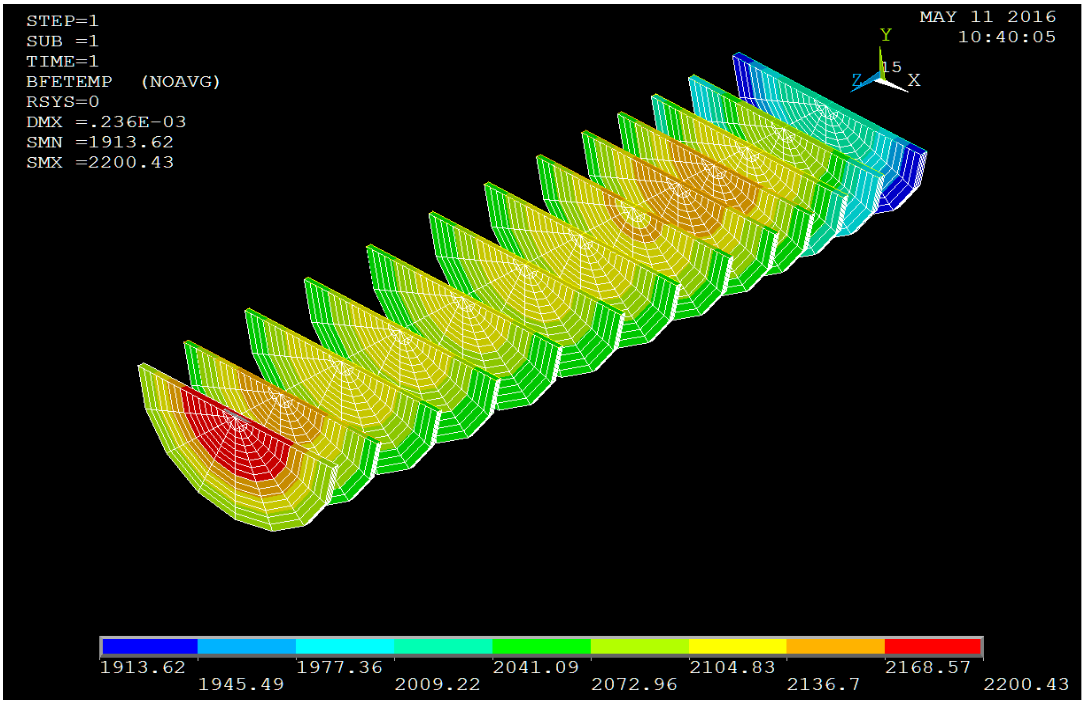

Figure 4-13: Configuration 3 – target discs thermal results.

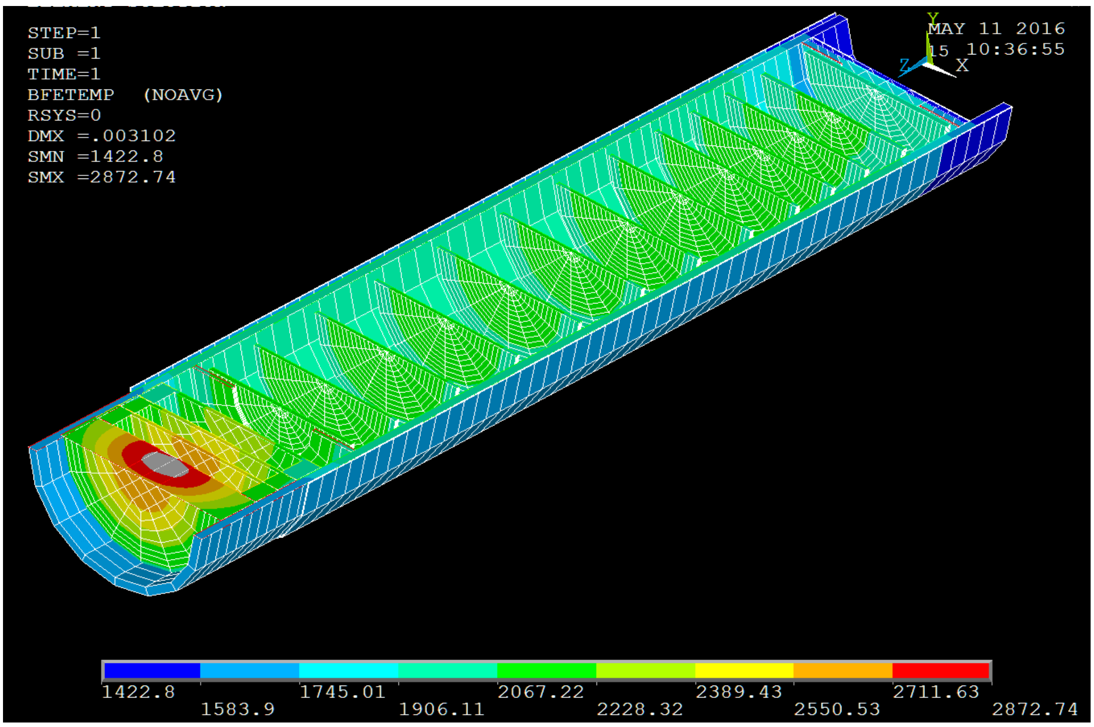

Figure 4-14: Configuration 3 – target canister and beam dump thermal results.

For completeness, the ANSYS VM stress analysis results for configuration 3 is shown in figures 4-15 and 4-16 below. No significant changes in VM stress from configuration 2 were noted, with the maximum VM stress on the discs and beam dump being 4.6 MPa and 25 MPa, respectively, which is still well below the 200 MPa mechanical VM stress limit for graphite.

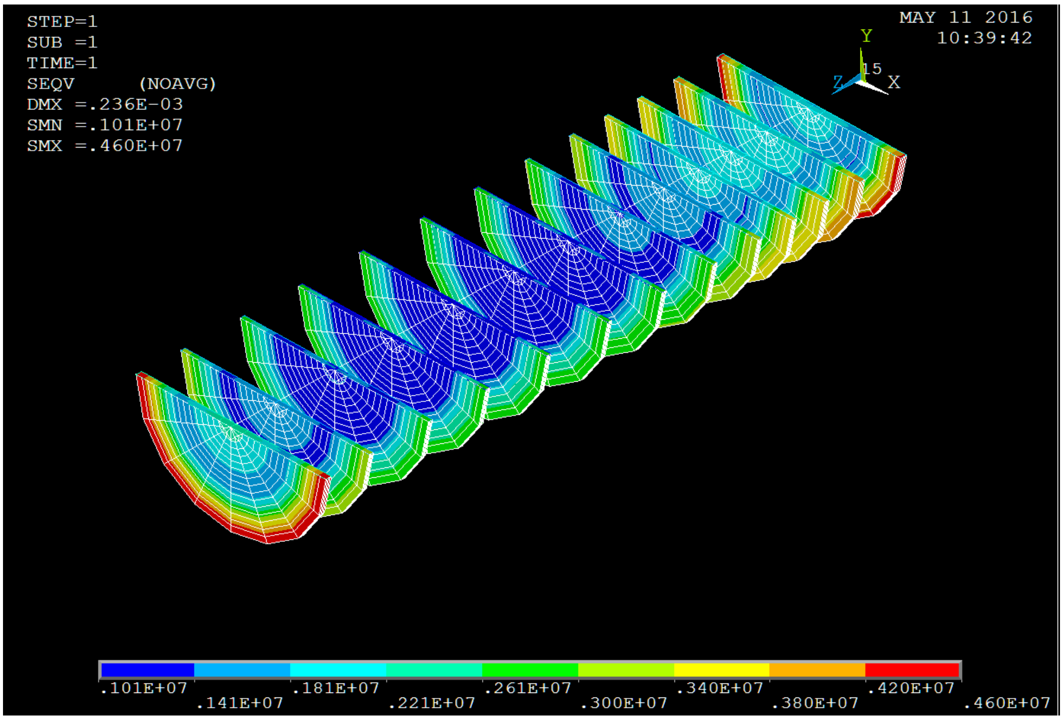

Figure 4-15: Configuration 3 – target discs VM stress results.

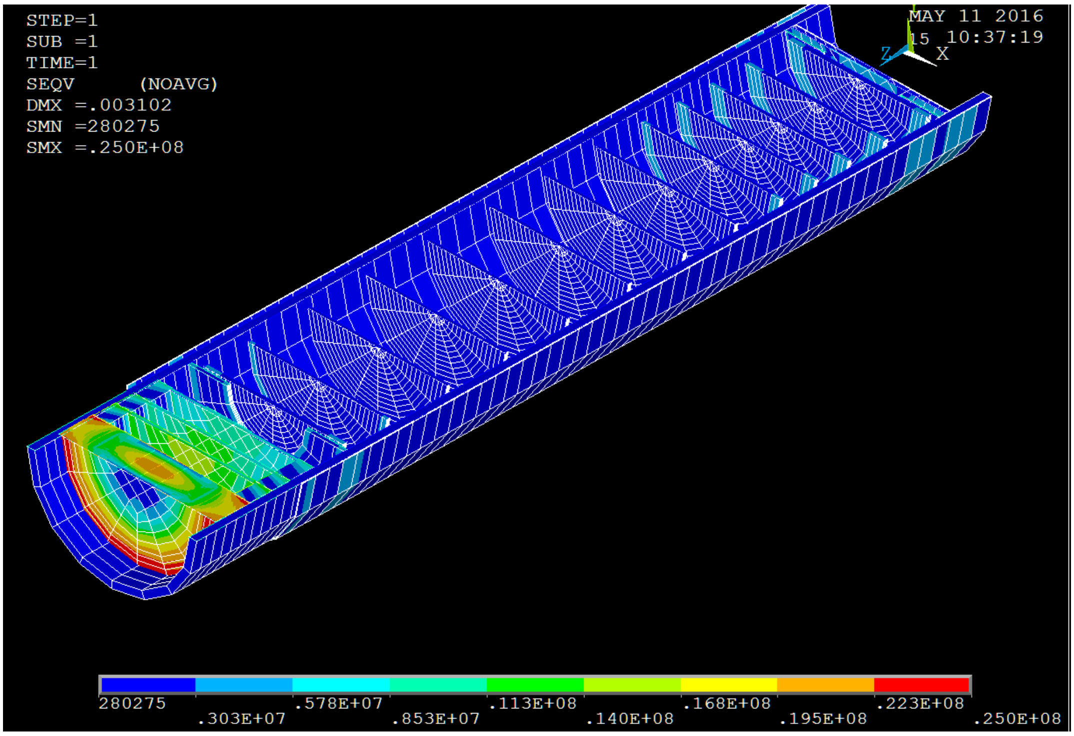

Figure 4-16: Configuration 3 – target canister and beam dump VM stress results.

The target canister is to be placed within a larger vacuum chamber, which serves as an external source of cooling for the hot target canister. This vacuum chamber has been design and tested in the SPES project, details of which are documented in work conducted by A. Monetti [Mon17]. The vacuum chamber is constructed from aluminium, due to its significantly low neutron activation and consists of three main components, namely the cylindrical bucket/chamber, integrated water cooling circuit and a secondary beam dump. These components provide the following functions:

- Drawing and maintaining high vacuum conditions throughout the target system.
- Heat removal (via thermal radiation) from the target canister by means of water cooling loops, constructed from copper tubes.
- Allows for a secondary beam dump, named the chamber beam dump, as a secondary safety barrier, in the event of target beam dump failure.

As a result of the high vacuum (low pressure) environment and high temperature of the target canister during operation, the heat/power deposited in the target canister can be removed mainly via thermal radiation, and directed to the external heat sink constituted by the water cooling circuit in the vacuum chamber. The heat removal process is thus as follows: (1) the discs radiate heat to the target canister, (2) target canister transfers the heat to the vacuum chamber walls and (3) the heat is removed from the vacuum chamber through the integrated water cooling circuit.

A SPES vacuum chamber design has shown no operability concerns for target canister surface temperatures up to 1800 °C, with the vacuum chamber not exceeding 90 °C during testing. In order to adopt the SPES vacuum chamber design with minimal design changes, it is envisaged to maintain the internal target canister temperature below 1800 °C. However, from figures 4-9 and 4-14 it can be seen that the internal target canister temperatures for these designs are between 1900 and 2000°C, and thus design changes to the SPES vacuum chamber would be required to accommodate the higher temperature.

The results presented in this section, for target system configurations 1, 2 and 3 are summarised in table 4-4 below. These results indicate that although no operability concerns regarding mechanical stress limits for discs and beam dumps are noted, the beam dump temperatures of all target configurations were significantly above the thermal limit of graphite. Thus, these target configurations were deemed unfit for purpose and would require additional optimisation or operation at reduced primary beam energy and/or current, in order to be feasible.

Config. no.	Target Disk Material	Beam Dump Material	No. of Target Disks	Disc thickness (mm)	Disc spacing	Effective beam dump length (mm)	6He Yield (nuclei/s) for 200 µA [+/- 5% error]	Max. Disc Temp (°C)	Max. Dump Temp (°C)	Max. Disc VM Stress (Mpa)	Max. Dump VM Stress (Mpa)
1	Graphite	Graphite	13	1.1	Even spacing of 13 mm	13	2.49E+10	No simulation	No simulation	No simulation	No simulation
2	Graphite	Graphite	13	1.1	Optimal spacing	13	2.41E+10	2267	3042	4.65	23.4
3	Graphite	Graphite	13	Varying	Optimal spacing	13	2.30E+10	2200	2873	4.6	25

Table 4-4: Results summary of graphite target system configurations. ‘Green cells’ – within thermal/mechanical limit, ‘Red cells’ – exceeds thermal/mechanical limit.

Nevertheless, the simulations conducted on these graphite targets provided confidence in the simulation codes (FLUKA and ANSYS) and methods employed in the target optimisation process and will serve as a reference point for further RIB target designs.

4.2. Moving from C to B_4C

From the outset of this research work, it was well known that boron carbide (B_4C) was a more beneficial target material as opposed to graphite, as a result of its higher ^{6}He yield, which was verified by preliminary FLUKA simulations of the proton-boron carbide interaction. On completion of the graphite target design and optimisation, the 13 disc optimally spaced graphite target system (configuration 2) was adapted by simply replacing the 13 1.1 mm graphite discs with 13 1.0 mm boron carbide discs. The results of this adaption showed an order of magnitude increase of in-target ^{6}He yield (**2.65×10^{11} ^{6}He/s**) (simulated in FLUKA) and improved thermal results (simulated in ANSYS). However, although the thermal results, specifically that of the beam dump, were an improvement on the previous graphite target results, it was still not within the thermal limits of the beam dump. The thermal results of this preliminary, un-optimised boron carbide target design are provided in figure 4-17 below, in which it is evident that the graphite beam dump temperatures (~ 2526 °C) were still above the graphite thermal limit of 2300 °C.

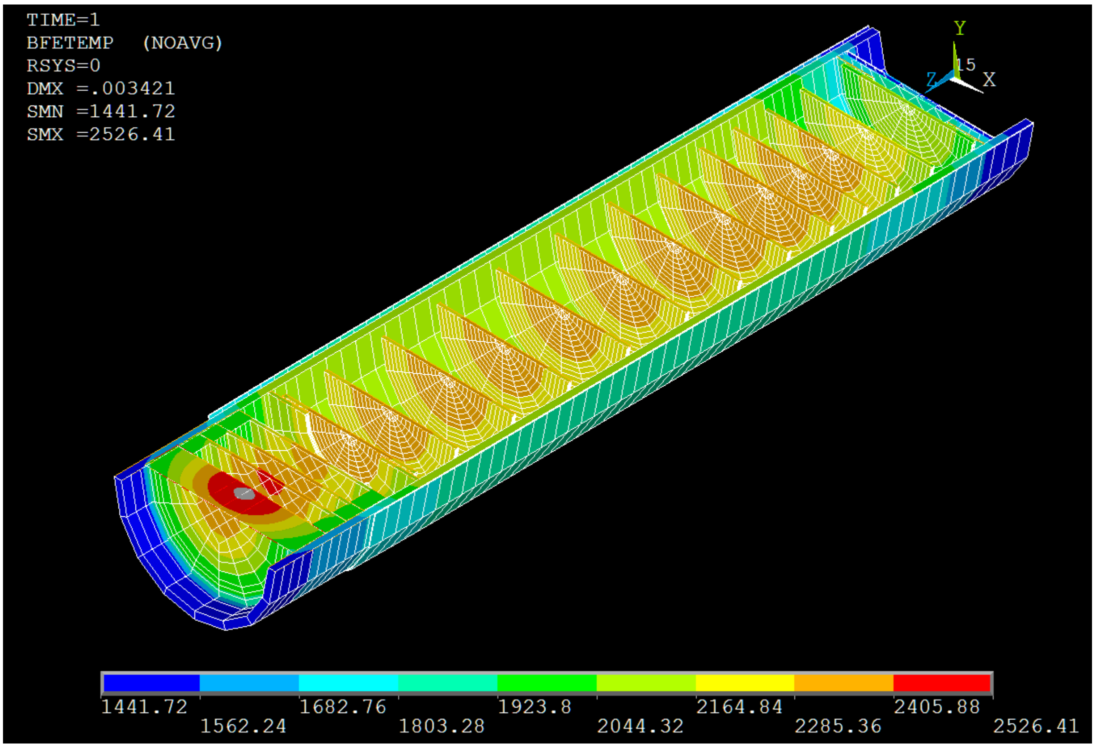

Figure 4-17: Preliminary, un-optimised B_4C target thermal results (13 x 1.0mm B_4C discs).

Hereafter, various target optimisation studies/simulations were conducted by applying the same methodology used for the design and optimisation of the graphite targets in the preceding section. The boron carbide target design and optimisation is covered in complete detail in the section to follow.

4.3. Boron Carbide Targets

The following section presents the optimisation process, design considerations and simulation results obtained during the design of an optimised Boron Carbide target system.

4.3.1 Boron Carbide Targets - Design and optimisation

Similar to the starting point in the methodology employed for the graphite target design (as discussed in section 4.1), information regarding the ^{6}He production reaction(s) from the proton-target interaction and stopping power of boron carbide is required to initiate the target dimensioning process (i.e. number of discs and disc thickness).

Preliminary FLUKA simulations indicated that the use of B_4C as the target material yielded ^{6}He at a factor of 10 greater than that of graphite target system configurations with the same dimensions. As previously discussed in section 4.1, the ^{6}He production mechanism from graphite is posited to proceed via the reaction, ^{12}C(p,α3p)^{6}He. This reaction mechanism is thus expected to be present in B_4C as well, due to its 20 % carbon content. Additionally, the second ^{6}He production mechanism comes from the boron (*natural boron contains 19.9% ^{10}B and 80.1% ^{11}B*) [Sup09] component of the B_4C material, and is postulated to be driven mainly by the ^{11}B(p,α2p)^{6}He reaction. However, it should be noted that this reaction cross section still requires experimental measurement and could not be found for reference in literature sources or reaction cross section databases.

Since no experimentally measured cross section data for the ^{11}B(p,x)^{6}He reaction could be found, a FLUKA simulation (using the PEANUT model) of the ^{nat}B(p,x)^{6}He reaction cross section was employed as a ‘best estimate’ during the optimisation of the B_4C target system. The simulation was conducted using a thin natural boron (^{nat}B) target with $\rho = 2.37$ g/cm^3 impinged by a proton beam at various energies in the range of 5 – 80 MeV. The results obtained from this FLUKA simulation are shown in figure 4-18 below, and indicates that the ^{nat}B(p,x)^{6}He reaction cross section is favored at proton energies in the range of 50 – 70 MeV.

The stopping power and the projected proton range in B_4C, shown in figure 4-19 below, was obtained using SRIM [Zie10], by specifying the B_4C material as having a density of 2.5 g/cm^3, 80% natural boron and 20% carbon. The application/use of these values are discussed in Chapter 3, and was used for all FLUKA and ANSYS simulations to follow.

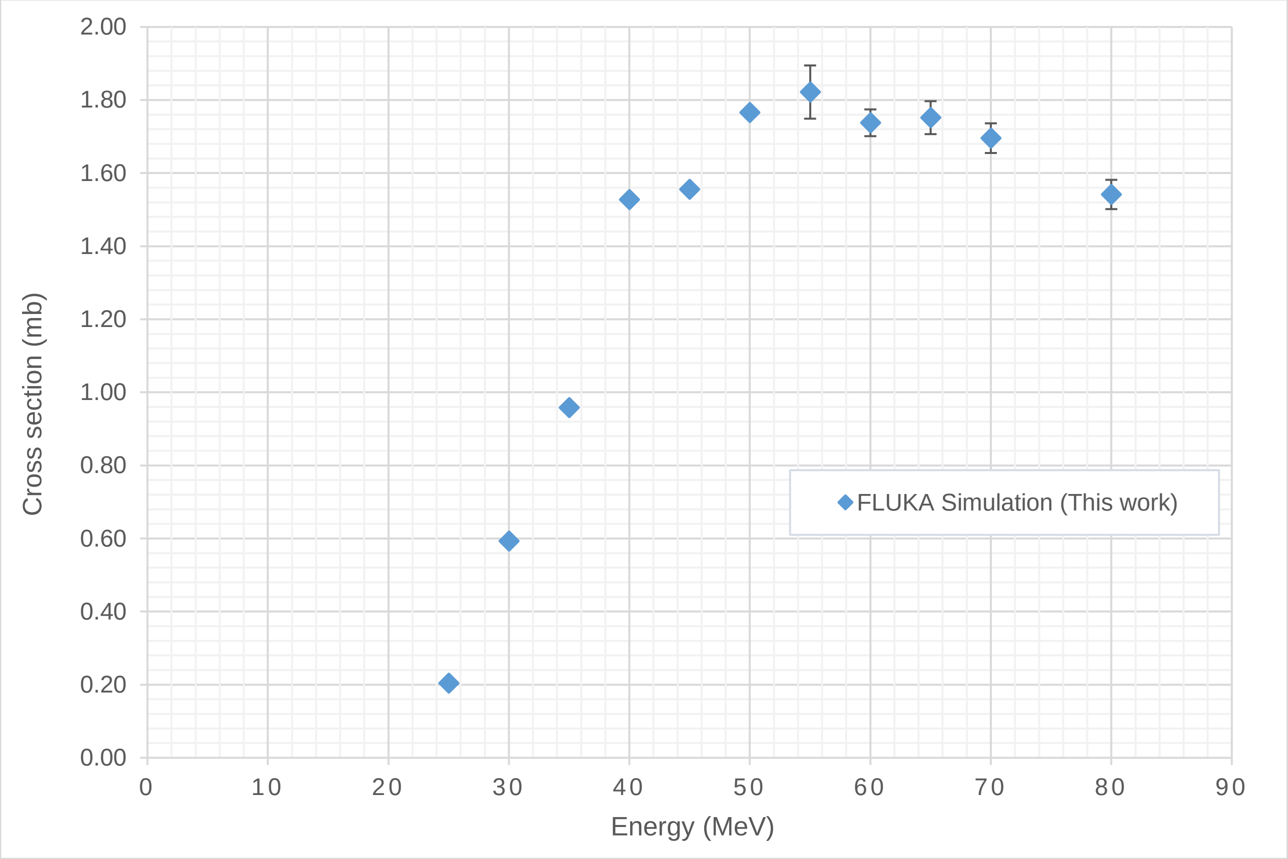

Figure 4-18: Cross section or the ${}^{nat}B(p,x){}^{6}He$ reaction as simulated in FLUKA. Note: Error bars smaller than data points.

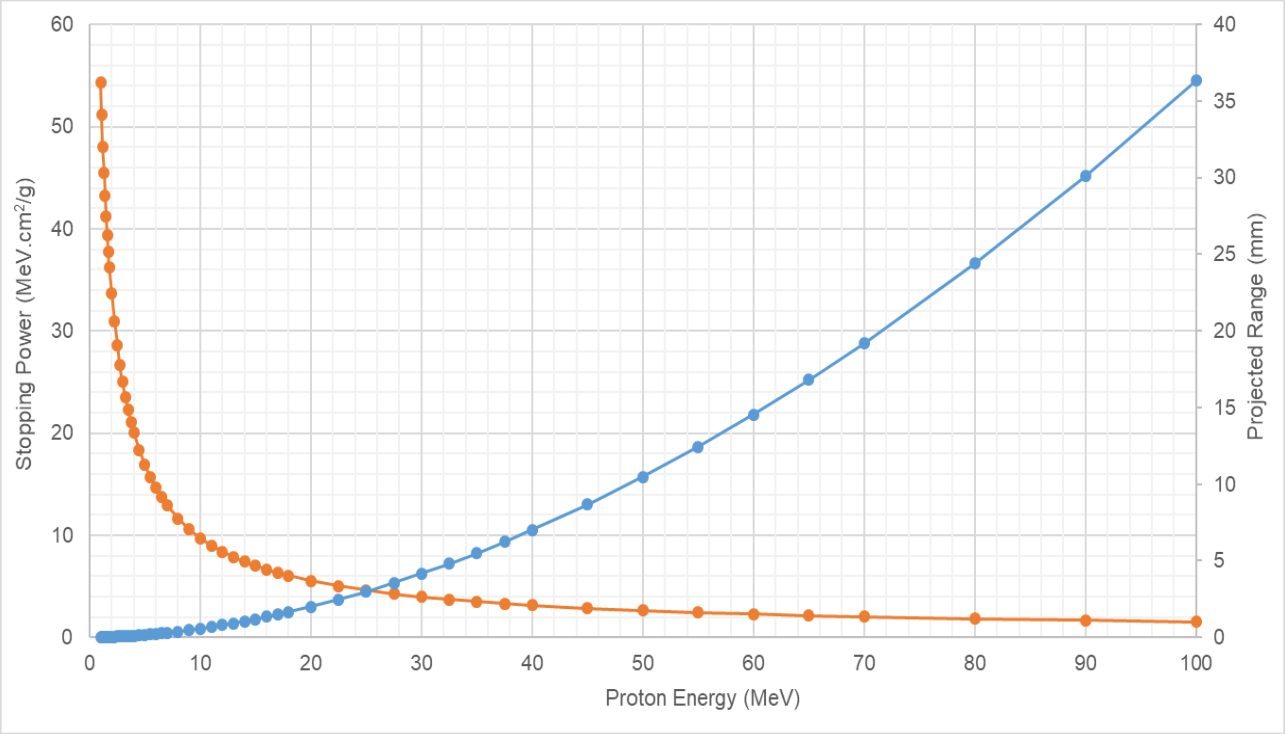

Figure 4-19: Stopping power and proton range in boron carbide. Extracted/calculated using SRIM [Zie10].

From figure 4-19 above, it can be seen that the effective length of B_4C ($\rho = 2.5$ g/cm^3) required to stop 70 MeV protons is 19.2 mm. However, since the graphite beam dump (as well as the graphite screens and windows) will be retained from the previous graphite target design, it was envisioned to have the highest power deposition at the end of the proton range delivered into the beam dump. This design consideration was to ensure that the temperatures on the B_4C target discs are kept as low as possible. As shown in figure 4-19, the stopping power of B_4C starts increasing exponentially below the 25 MeV proton energy mark, and thus protons with energies lower than 25 MeV would ideally need to be delivered to the graphite beam dump.

As discussed and shown in section 4.2, replacing the graphite target discs in the optimally spaced graphite target with 1.0 mm B_4C target discs resulted in an order of magnitude higher ^{6}He yield and a ~ 500 °C reduction in beam dump temperature. In an attempt to reduce the beam dump temperatures further, it was decided to extend the target canister from 230 mm to 236.7 mm, with the beam dump configuration remaining as per the previous design, thus dump 1,2,3 and 4 having thicknesses of 1,1,1 and 10 mm, respectively. This target configuration is hereafter referred to as configuration 4. In addition to the extension of the target canister, the number of target discs was increased from 13 to 15 with a uniform disc spacing of 12.1 mm between the 15 target discs, as shown in table 4-5 below.

Configuration 4				
Disc number	start of disc (di) [mm]	end of disc (df) [mm]	disc thickness (dz) [mm]	disc spacing after (df) [mm]
1	13.9	14.8	0.9	12.1
2	26.9	27.8	0.9	12.1
3	39.9	40.8	0.9	12.1
4	52.9	53.8	0.9	12.1
5	65.9	66.8	0.9	12.1
6	78.9	79.8	0.9	12.1
7	91.9	92.8	0.9	12.1
8	104.9	105.8	0.9	12.1
9	117.9	118.8	0.9	12.1
10	130.9	131.8	0.9	12.1
11	143.9	144.8	0.9	12.1
12	156.9	157.8	0.9	12.1
13	169.9	170.8	0.9	12.1
14	182.9	183.8	0.9	12.1
15	195.9	196.8	0.9	12.1

Table 4-5: Configuration 4 – Target disc positioning, dimensions and spacing.

It was expected that increasing the number of target discs would result in an increase in the in-target ^{6}He yield, however, increasing the number of target discs in combination with the target canister extension would increase the ^{6}He release time from the target canister to the extraction line. In order to counter this expected increase in release time, the discs thickness of the 15 B_4C discs was reduced to 0.9 mm. The reduction in disc thickness results in an effective B_4C length of 13.5 mm, which is only 0.5 mm longer than the effective B_4C length in the previous simulated 13 1.0 mm B_4C disc target of 13 mm. As a result, the predicted increase ^{6}He yield was expected to be marginal.

FLUKA simulation of this target provided a ^{6}He yield of **2.72 x 10^{11} ^{6}He/s** for the 70 MeV, 200 μA primary proton beam. As expected, the ^{6}He yield was a marginal improvement (2.64 % increase) from the 13 1.0 mm B_4C discs target (with optimal graphite target spacing), due to the minor (0.5 mm) increase in effective B_4C length.

Following the detailed discussion regarding the material properties and simulation inputs for graphite and boron carbide (B_4C) in Chapter 3, the following operational safety limits, listed in table 4-6 below, were adopted during the ANSYS thermo-mechanical analysis. It should be noted however, that the thermal limit value of 2400 °C for B_4C under vacuum conditions could be considered conservative. Information sourced from B_4C manufacturers, with specific reference to *Kurt J. Lesker Company*© and Ted Pella. Inc© [Ted14], have quoted the sublimation (melting) point of their manufactured B_4C to be between 2450 and 2650 °C at vacuum conditions. Considering the lowest point of this quoted range, 2450 °C, the assumed conservative thermal limit of 2400 °C has additional safety margin. However, due to the lack of definitive thermal limit values (sublimation point) for B_4C discs at vacuum conditions and the variables which would be introduced during manufacturing of the B_4C discs, such as manufacturing method/process and impurities, the thermal limits of the proposed B_4C discs would need to be experimentally verified in the future, at the RIB production target operating conditions

Material	Parameter	Maximum Value	Unit
Graphite (C)	Max. Temperature	2300	°C
	Max. Von-Mises Stress	200	MPa
Boron Carbide (B_4C)	Max. Temperature	2400	°C
	Max. Von-Mises Stress	260	MPa

Table 4-6: Graphite and Boron Carbide operational temperature and mechanical stress limits.

The ANSYS thermal analysis results for configuration 4 are shown in figure 4-20 and 4-21 below. From figure 4-20, it is noted that the maximum temperature produced in the target discs is ~ 2398 °C (SMX), which is only 2 °C below the temperature threshold for B_4C, too close to be considered safe for operation. However, from figure 4-21, it is noted that the maximum temperature produced in the beam dump is ~ 2668 °C (SMX), which is 142 °C higher than that of the previously simulated 13, 1.0 mm B_4C discs target and thus significantly above the thermal limit of graphite, rendering this target unfit for operation.

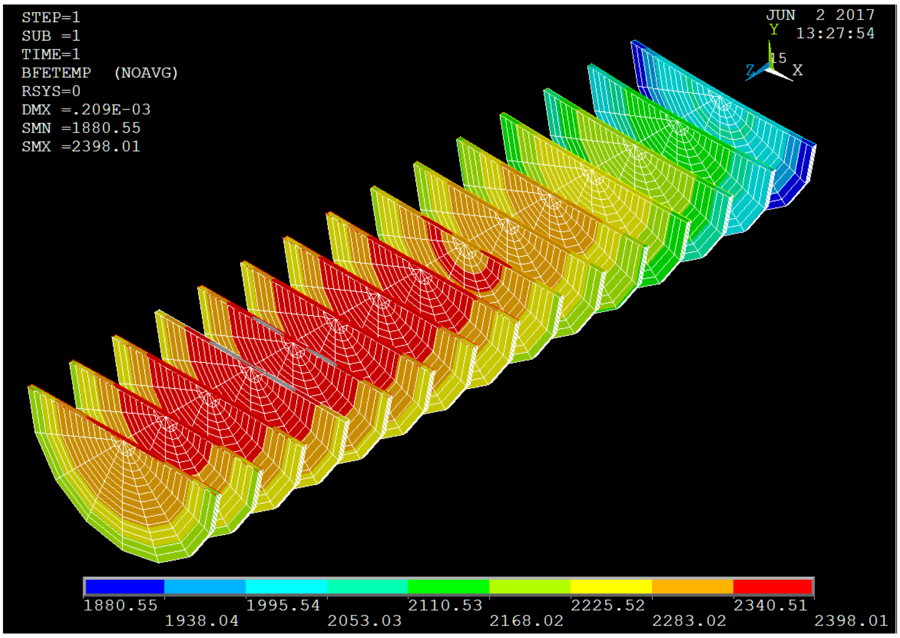

Figure 4-20: Configuration 4 – target discs thermal results.

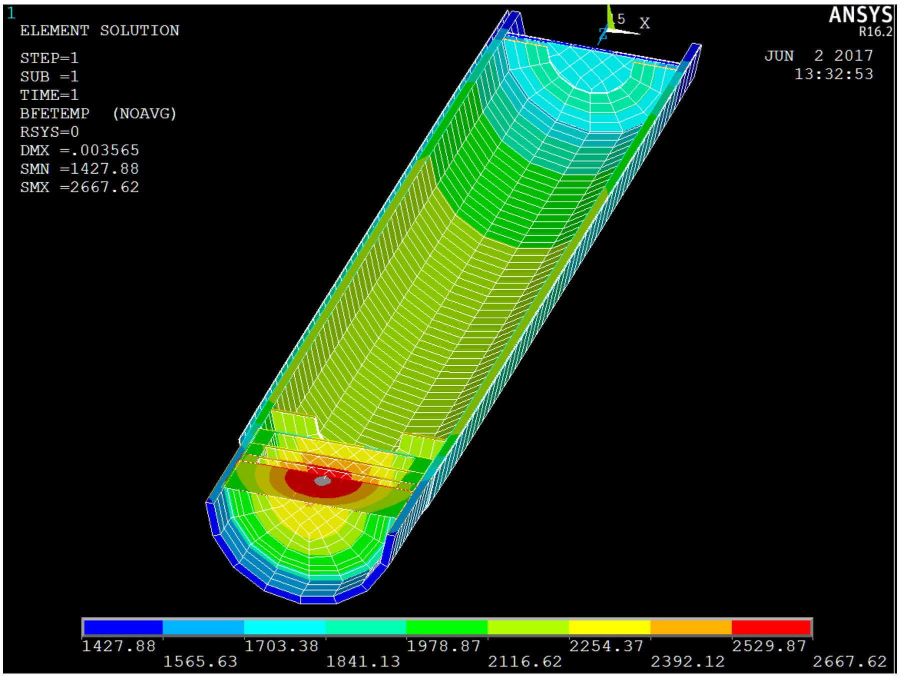

Figure 4-21: Configuration 4 – target canister and beam dump thermal results.

To gain a sense of the mechanical stresses exerted on the components of configuration 4, VM stress analysis was conducted in ANSYS with the results provided in figures 4-22 and 4-23 below. From these figures it can be seen that the maximum VM stress on the B_4C target discs and graphite beam dump is 165 MPa and 20.5 MPa, respectively, which are within the mechanical stress limits for these respective materials.

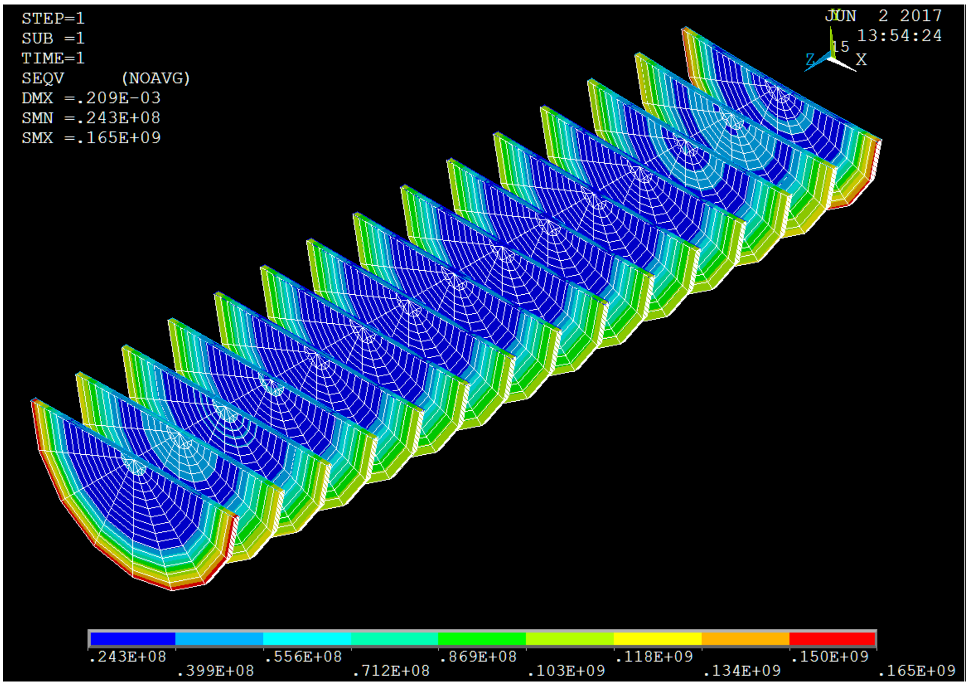

Figure 4-22: Configuration 4 – target discs VM stress results.

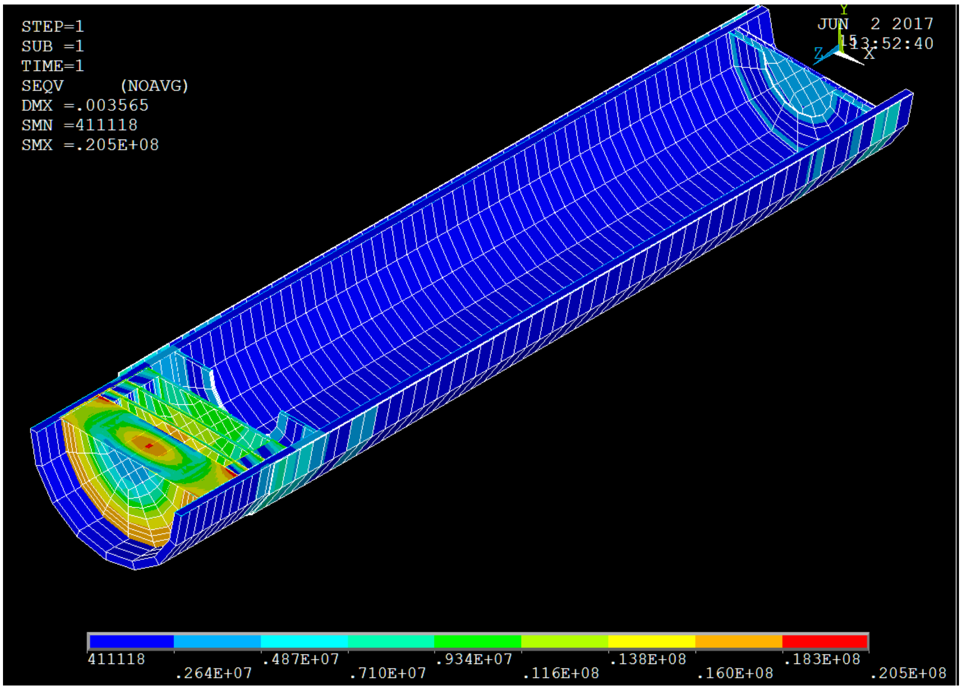

Figure 4-23: Configuration 4 – target canister and beam dump VM stress results.

From the configuration 4 target design and associated simulation results, in which no success was achieved in reducing the beam dump temperatures, the following design considerations were made:

- Increasing the effective graphite beam dump thickness, by extending the length of the last dump (beam dump 4) from 10 mm to 20 mm, as this should allow for greater energy dissipation due to the increased beam dump volume
- Revising the target discs spacing by reducing the spacing between the first 5 discs and increasing the spacing between the last 5 discs. This decision was based on the thermal results shown in figure 4-22 above, in which it can be seen that the highest temperatures are on the last half of the 15 disc array (discs 8 to 14), with the lowest temperatures being on the first 3 discs in disc array.

The disc positioning of the redesigned 15 B_4C target disc of 0.9 mm thickness with revised/optimised spacing and extended beam dump, hereafter referred to as configuration 5, is shown in table 4-7 below.

Configuration 5				
Disc number	start of disc (di) [mm]	end of disc (df) [mm]	disc thickness (dz) [mm]	disc spacing after (df) [mm]
1	13.9	14.8	0.9	10.1
2	24.9	25.8	0.9	10.1
3	35.9	36.8	0.9	10.1
4	46.9	47.8	0.9	11.1
5	58.9	59.8	0.9	11.1
6	70.9	71.8	0.9	11.1
7	82.9	83.8	0.9	12.1
8	95.9	96.8	0.9	12.1
9	108.9	109.8	0.9	13.1
10	122.9	123.8	0.9	15.1
11	138.9	139.8	0.9	15.1
12	154.9	155.8	0.9	13.1
13	168.9	169.8	0.9	13.1
14	182.9	183.8	0.9	12.1
15	195.9	196.8	0.9	

Table 4-7: Configuration 5 – Target disc positioning, dimensions and spacing.

FLUKA simulation of configuration 5 provided an in-target ^{6}He yield of **2.85 x 10^{11} ^{6}He/s** for the 70 MeV, 200 µA primary proton beam. Although the effective B_4C length of configuration 5 and 4 are the same, a 4.8 % increase in ^{6}He yield was obtained with the application of the revised/optimised spacing (hereafter referred to as Rev.1 spacing) in configuration 5. This increase, albeit marginal, can be attributed to the ${}^{nat}B(p,x){}^{6}He$ reaction cross section being higher at the higher proton energies at the front end of the target system, as previous shown in figure 4-18.

The ANSYS thermal analysis results for configuration 5 are shown in figures 4-24, 4-25 and 4-26 below. From figure 4-24, it is noted that the maximum temperature produced in the B_4C target discs is ~ 2355 °C (SMX), which is a ~ 43 °C reduction from the maximum target discs temperature in configuration 4. This temperature reduction (improvement) can thus be concluded to be due to the revised target disc spacing applied in configuration 5. Furthermore, this target disc temperature is below the B_4C thermal limit of 2400 °C, and thus presents no operational concerns with regards to disc temperature.

Thermal analysis results of the beam dump can be seen in figures 4-25 and 4-26 below, with a maximum temperature of ~ 2406 °C (SMX) observed in the beam dump array (beam dump 1,2,3 and 4), which is a significant improvement/reduction from the configuration 4 beam dump temperatures (~ 261 °C reduction). Although this beam dump temperature is still above the thermal limit of graphite, it indicates that increasing the beam dump thickness is an appropriate design change for reduction in beam dump temperatures.

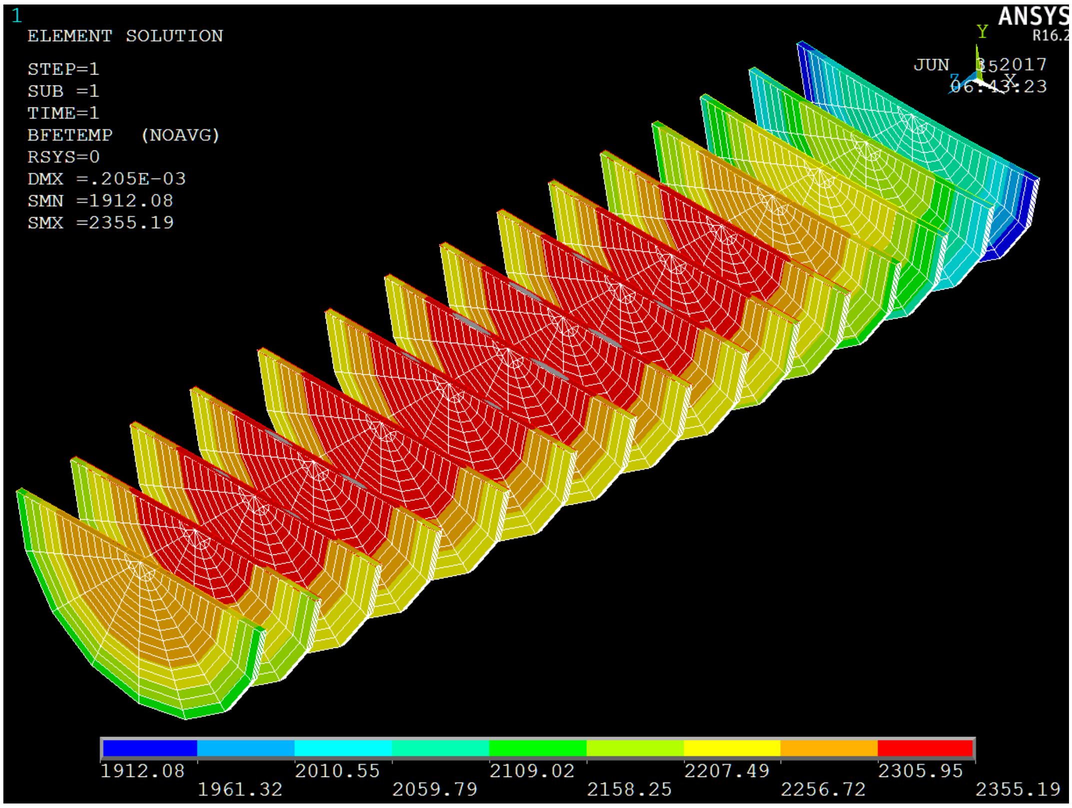

Figure 4-24: Configuration 5 – target discs thermal results.

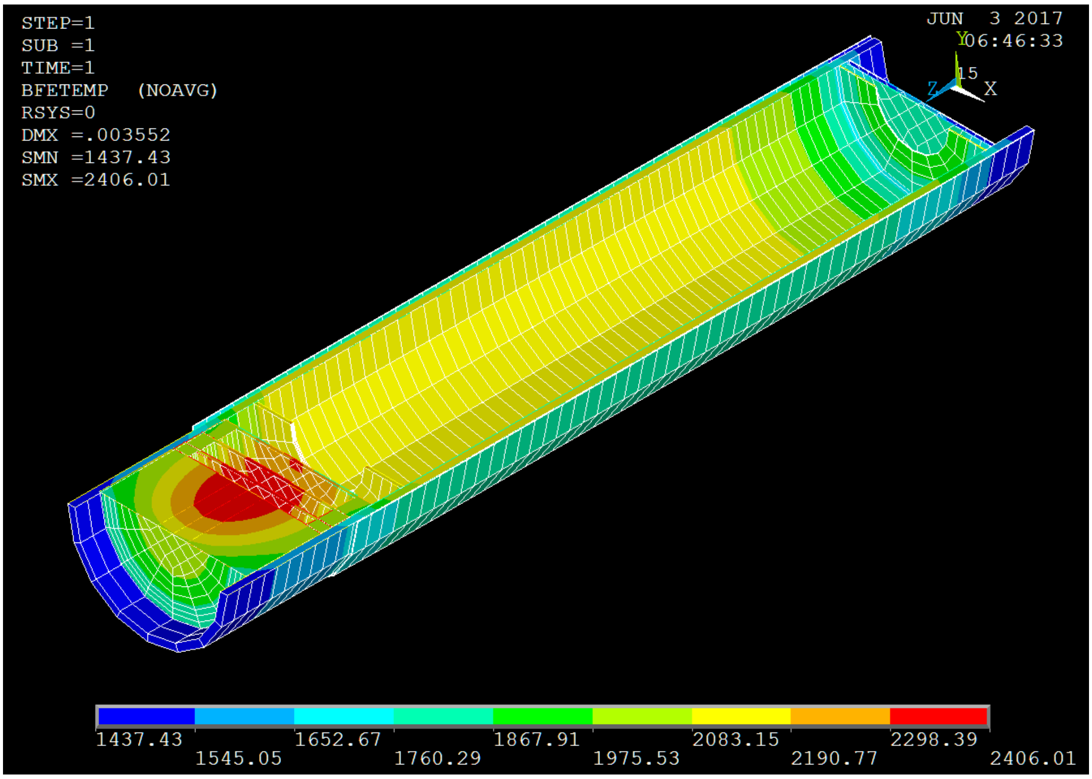

Figure 4-25: Configuration 5 – target canister and beam dump thermal results.

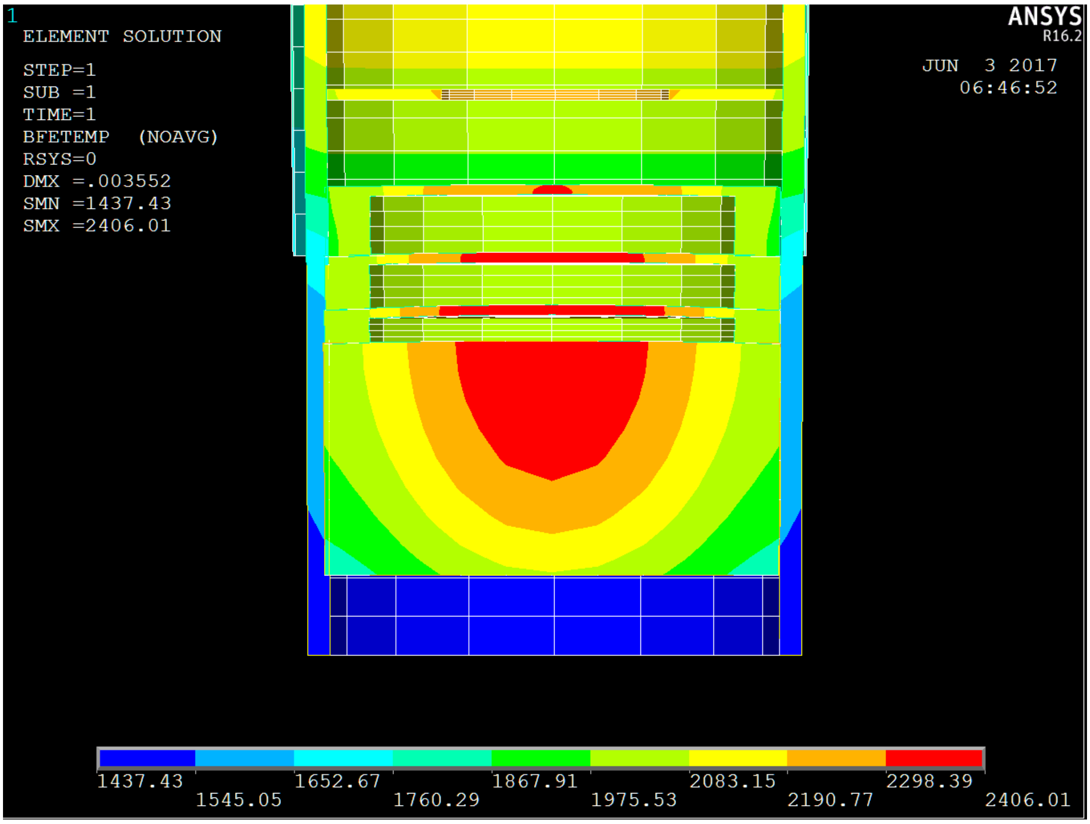

Figure 4-26: Configuration 5 – beam dump thermal results (top view).

The mechanical stress (VM stress) analysis results for configuration 5 is shown in figures 4-27 and 4-28 below. From figure 4-27 below, a maximum VM stress value of 164 MPa (SMX) was found on the B_4C target discs, with the highest VM stress being experienced by disc 1 and 15 (first and last). As expected, this result is similar to that of configuration 4, since configuration 4 and 5 share the same B_4C target discs dimensions and spacing. Similarly to configuration 4, the target discs present no operational concerns in terms of VM stress, as the maximum values are well below the mechanical limit of B_4C (260 MPa).

Mechanical analysis of the beam dump, shown in figure 4-28, indicates a maximum VM stress of 16.2 MPa, a slight reduction from configuration 4, which can be attributed to the increased length of beam dump 4 causing a reduction in thermally induced mechanical stress. There are thus no operational concerns related to the mechanical stresses in the dump beam as the maximum VM stress values observed are well below the mechanical limit of graphite (200 MPa).

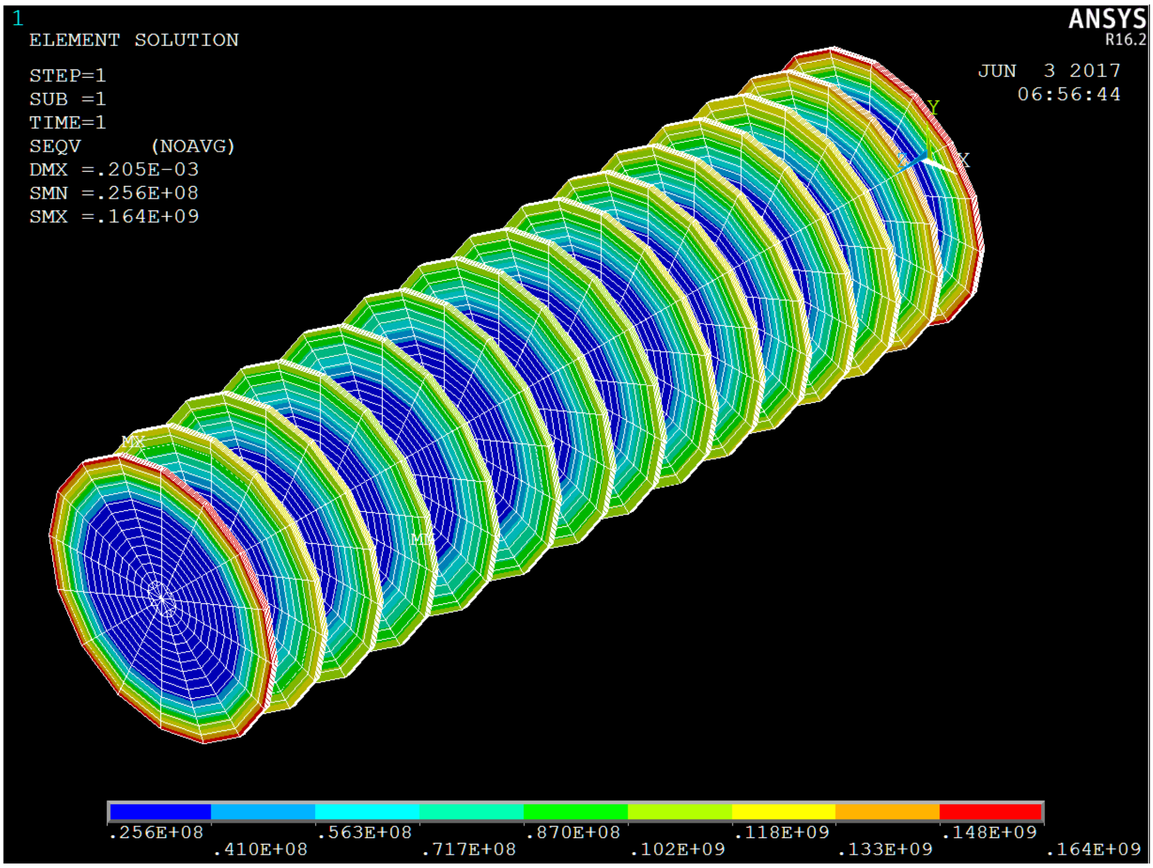

Figure 4-27: Configuration 5 – target discs VM stress results.

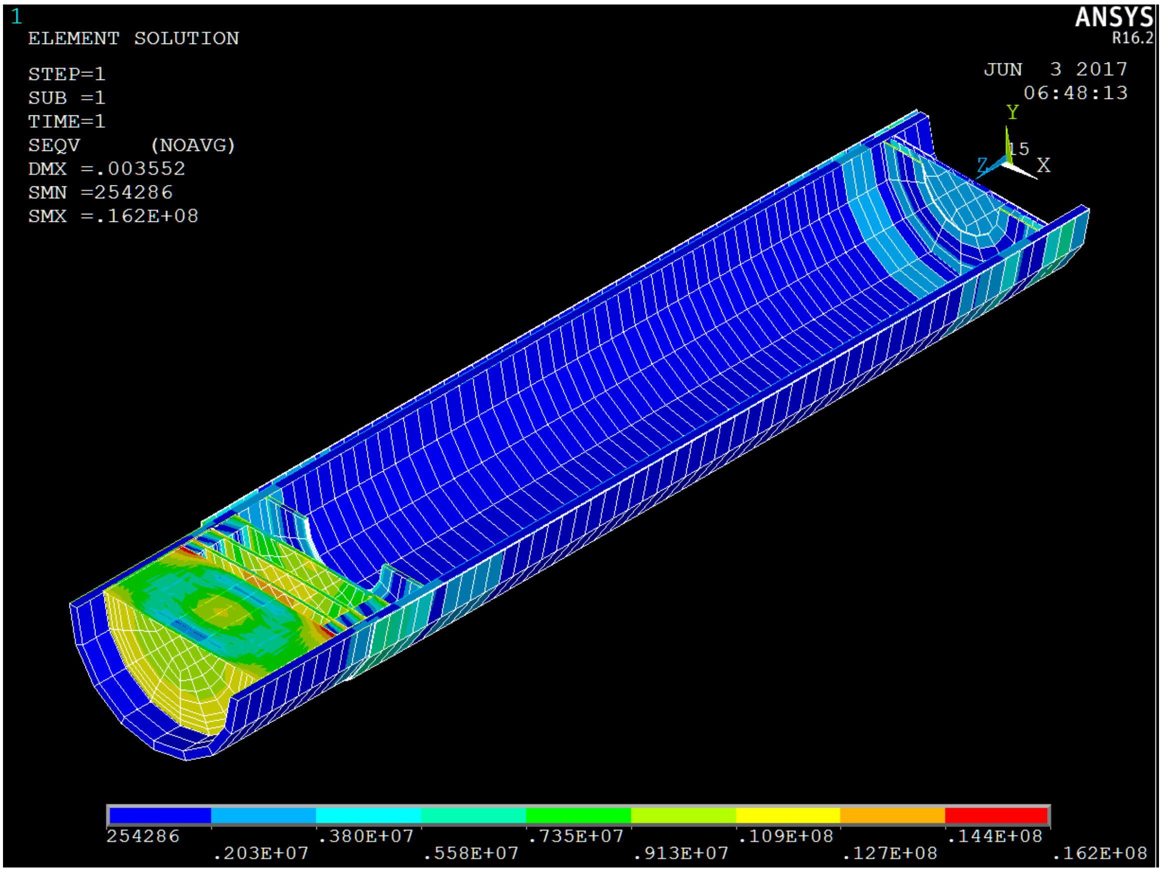

Figure 4-28: Configuration 5 – target canister and beam dump VM stress results.

Resulting from the reduction/improvement in beam dump temperature noted in configuration 5, as a result of the increase in length of beam dump 4, configuration 6 was proposed, in which a further increase in the length of beam dump 4 was employed. In configuration 6, beam dump 4 is extended by an additional 10 mm resulting in a beam dump 4 length of 30 mm. The target canister would therefore also require an extension of 10 mm, resulting in a total target canister length of 256.7 mm.

Additionally, consideration has to be given to beam dumps 1, 2 and 3, as these beam dumps were also shown to be above the graphite thermal limit of 2300 °C. In order to reduce the temperatures in beam dump 1, 2 and 3, their thicknesses/lengths were reduced from 1.0 mm to 0.8 mm. The optimised Rev.1 spacing as applied in configuration 5 was employed for configuration 6. Figure 4-29 below, graphically illustrates configuration 6 as simulated in FLUKA and ANSYS. A complete description of the configuration 6 target dimensions is provided in appendix E.

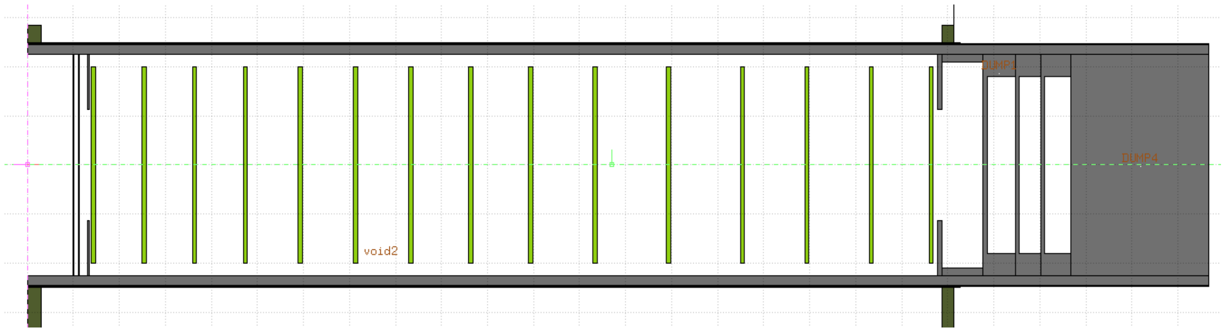

Figure 4-29: Configuration 6 target system design. Grey – graphite, Green – boron carbide.

Configuration 6 FLUKA simulation results provided an in-target ^{6}He yield of **2.85 x 10^{11} ^{6}He/s** for the 70 MeV, 200 µA primary proton beam, the same as that of configuration 5, which is expected since the B_4C target configurations are the same. Figure 4-30 below, provides FLUKA simulated in-target yield rates of all nuclei produced by the configuration 6 target system.

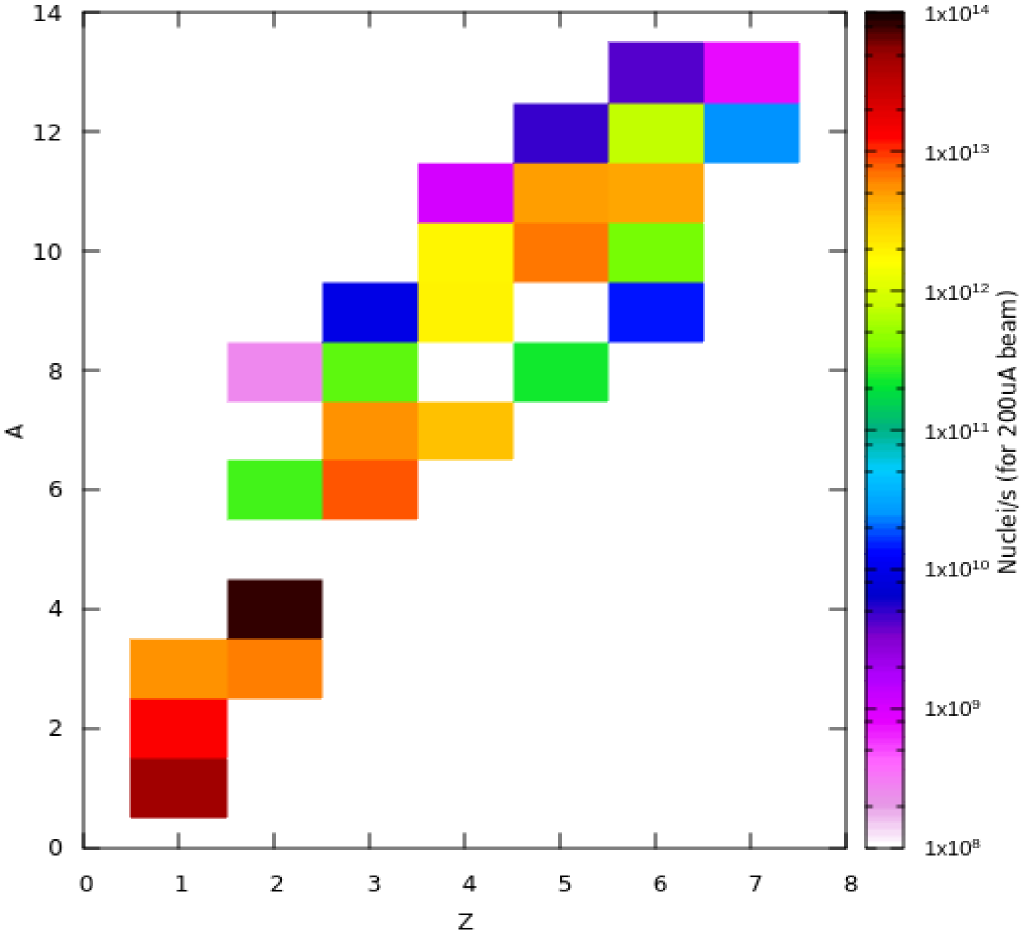

Figure 4-30: Configuration 6 – FLUKA simulation results depicting the in-target yield rates of all nuclides produced during target system operation.

The distribution of both protons and neutrons during operation of the configuration 6 target was investigated through FLUKA simulations of the 70 MeV, 200 µA (1.2482 x 10^{15} protons/s) primary proton beam impinging the target system. The results of these simulations are shown in figures 4-31 and 4-32 below. From figure 4-31, providing the simulated proton distribution during operation, the main factor to be confirmed is that the incoming proton beam is completely stopped within the beam dump. From this figure, it can be seen that the incoming proton beam is stopped completely in the 30 mm thick beam dump 4.

The simulated neutron distribution during operation is shown in figure 4-32. As expected, neutrons do 'leak' through the sides of the target chamber and into the RIB target vault, as a result of the isotropic nature of the distribution coupled with the low shielding capability of the target canister. The dose rates and safety factors associated with the leakage of protons and neutrons from the target chamber are accounted for in separate, on-going iThemba LABS RIB vault design studies, which would assess the shielding requirements for operation of this proposed target system.

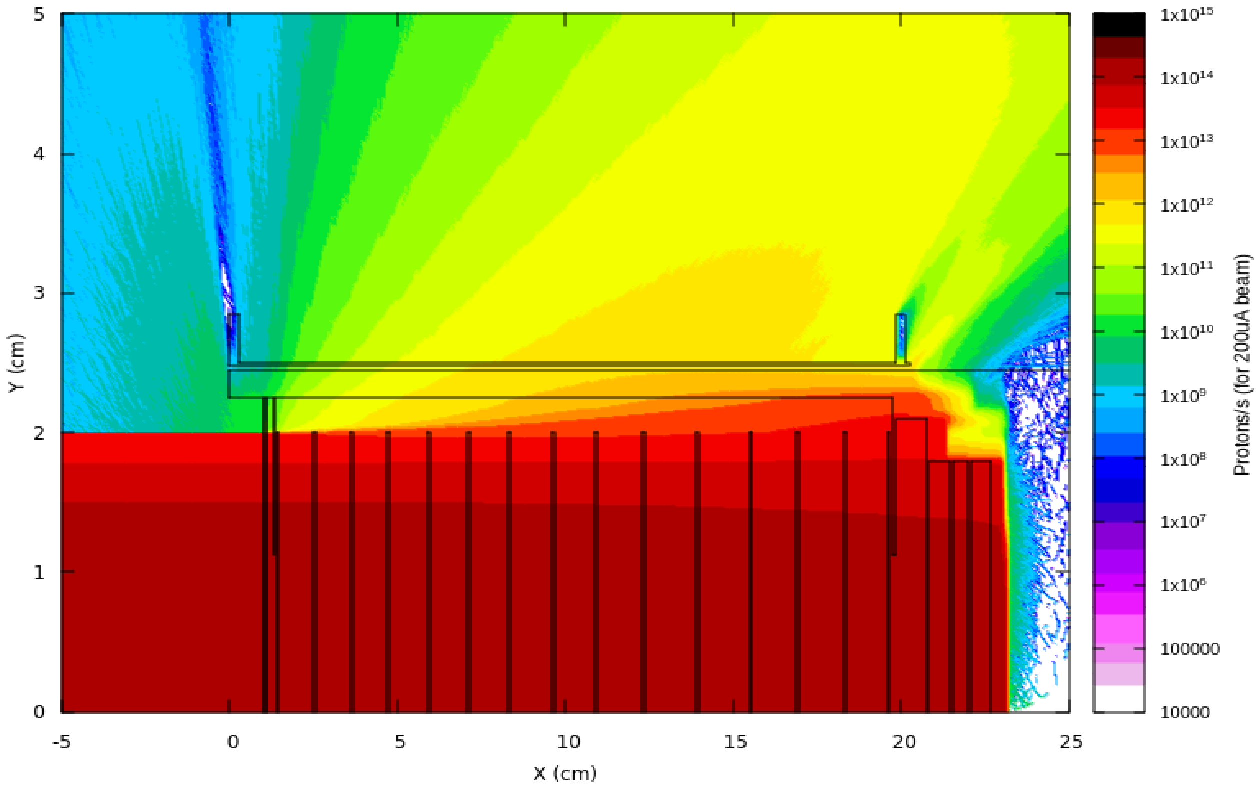

Figure 4-31: Proton distribution within configuration 6.

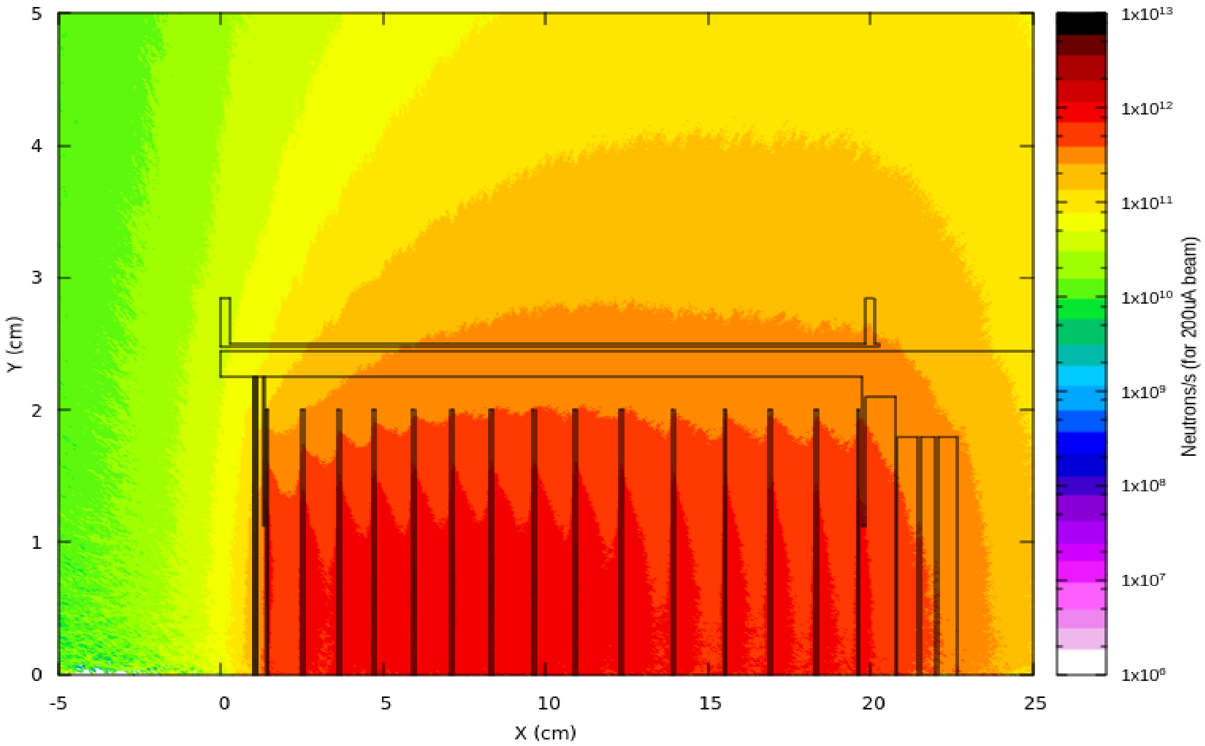

Figure 4-32: Neutron distribution within configuration 6.

The ANSYS thermal analysis results for configuration 6 are shown in figure 4-33, 4-34 and 4-35 below. From figure 4-33, it is noted that the maximum temperature produced in the B_4C target discs is ~ 2356 °C (SMX), which is essentially the same as that of configuration 5 since the B_4C target disc arrays are the same in both configurations. The B_4C target disc temperature is thus below the B_4C thermal limit of 2400 °C, and presents no operational concerns with regards to disc temperature. Another aspect to be considered is that of minimum average target disc temperature, as the target discs should be kept at an elevated temperature in order to ensure efficient release of ^{6}He from the target material matrix. From figure 4-33, the lowest temperature of ~ 1926 °C (SMN) is found on the outer edge of disc 1, with the center of this disc having a temperature of ~ 2100 °C. All discs thus have an average temperature in excess of 2000 °C. Although the ^{6}He release efficiency from the target material has not been evaluated in this research work, it is assumed that temperatures in excess of 2000 °C are sufficient for the efficient release of ^{6}He from the target material.

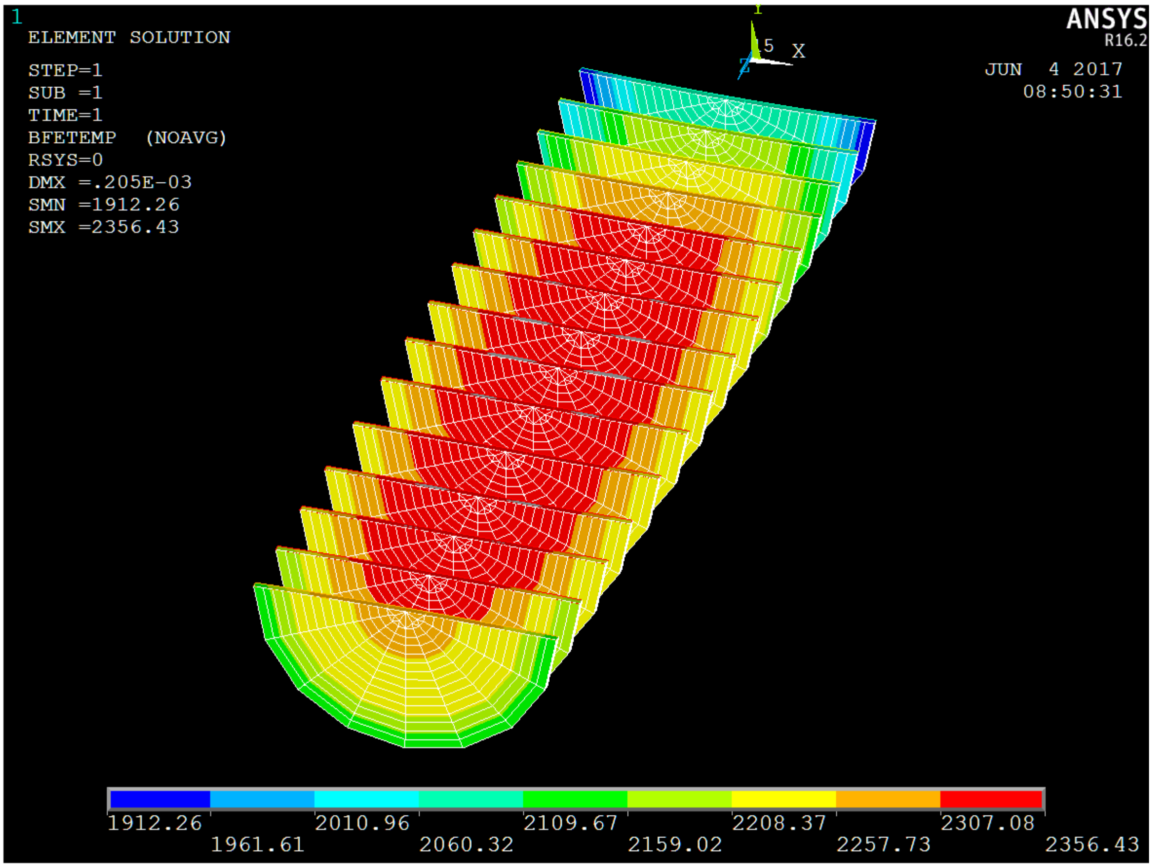

Figure 4-33: Configuration 6 – target discs thermal results.

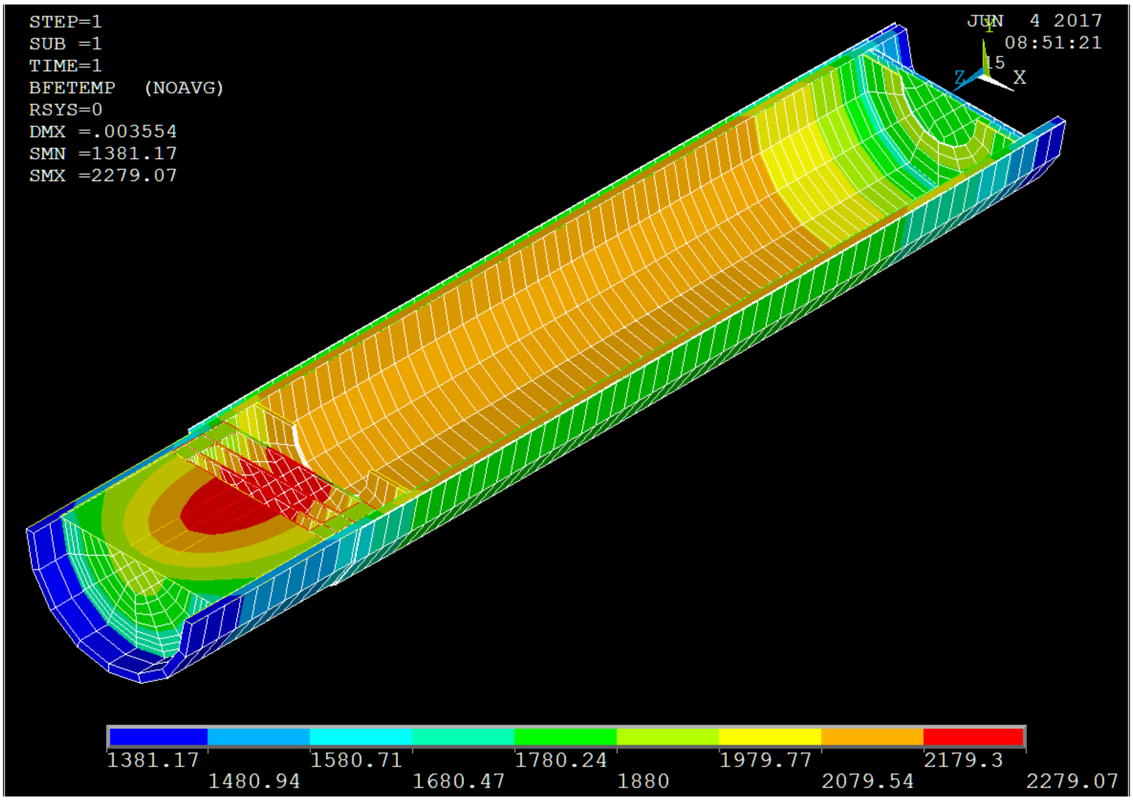

Figure 4-34: Configuration 6 – target canister and beam dump thermal results.

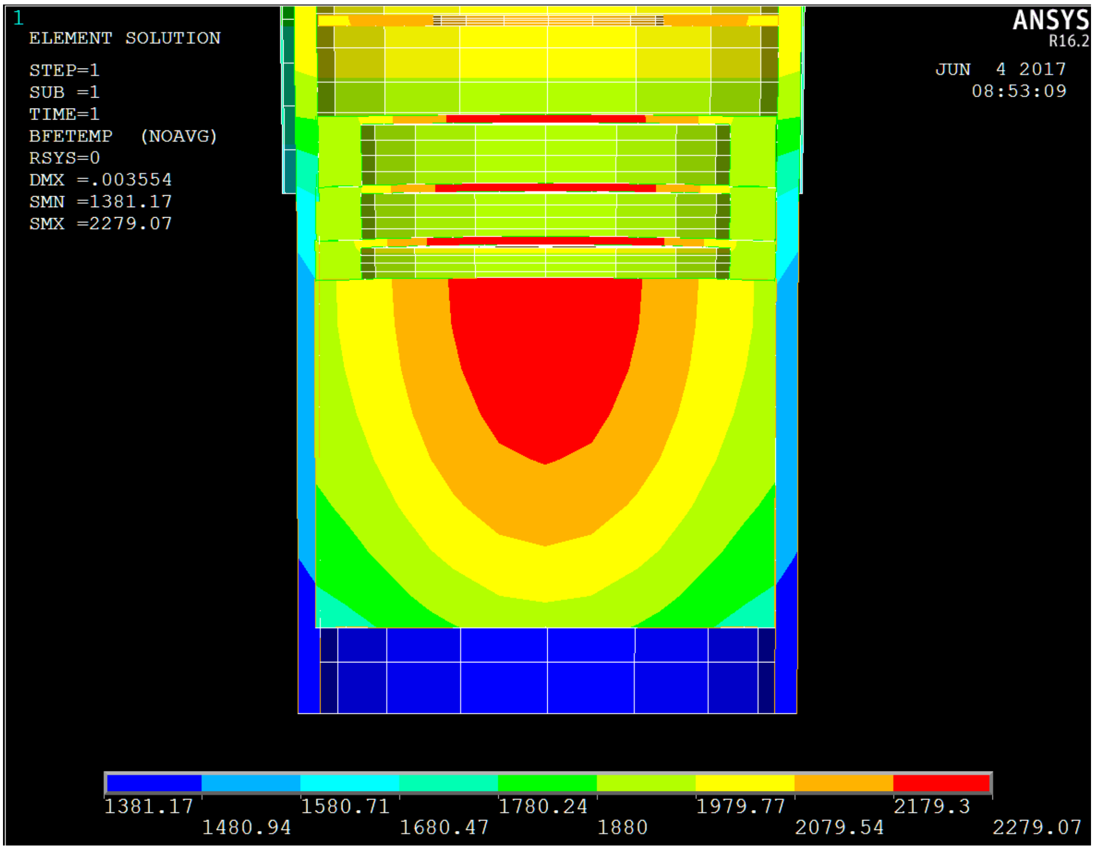

Figure 4-35: Configuration 6 – beam dump thermal results (top view).

Thermal analysis results of the configuration 6 beam dump array can be seen in figures 4-34 and 4-35 above, with a maximum temperature of ~ 2279 °C (SMX) observed in the beam dump (beam dump 1,2,3 and 4), which is a significant improvement/reduction from the configuration 5, but more importantly, it is below the thermal limit of graphite (2300 °C). Although this operating temperature is close to the thermal limit of graphite, the beam dump could be considered safe to operate under the proposed experimental conditions. Furthermore, the interior of the target canister as shown in figure 4-34, has an approximate temperature range of 1950 to 2150 °C, which is considered ideal for the transport/release of ^{6}He from the interior volume of target system to the transfer line, prior to the ^{6}He undergoing post acceleration processes.

As previously mentioned, SPES vacuum chamber has shown no operability concerns for target canister surface temperatures up to 1800 °C, As can be seen in figures 4-34 and 4-35 above, configuration 6 has a maximum target canister surface temperature of ~ 1800 °C. The SPES vacuum chamber design could thus be adopted for the iThemba LABS target system, with little to no design changes required.

Additional reduction in beam dump temperature could be sought by further extending the beam dump length. This additional extension was not covered in this research work, following configuration 6 meeting the operational acceptance requirements. However, further evaluations/studies were conducted to quantify the impact of reducing the beam current, with the expectation that the decrease in power deposition using these reduced beam currents would result in greater safety margins (lower operating temperatures) for both the B_4C discs and graphite beam dump. Although the greater safety margins would come at the expense of ^{6}He production rates, it is a significant factor to consider for a sustainable, safe RIB target system operation. These evaluations considered beam current reductions of 10% (180 μA) and 25% (150 μA), from an initial design beam current of 200 μA. Figure 4-36 below, provides comparative resultant disc and beam dump temperatures at varying beam currents.

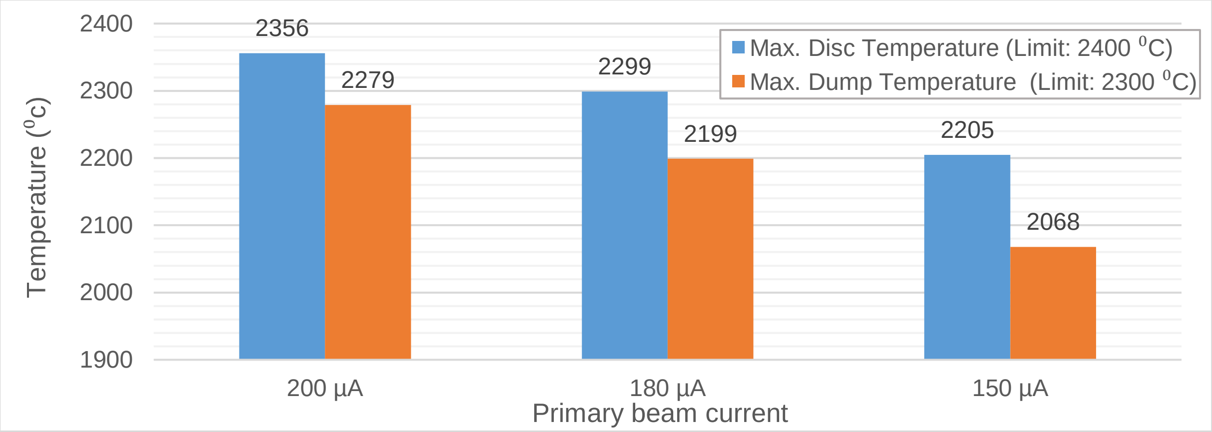

Figure 4-36: Primary beam current evaluation for beam currents of 200, 180 and 150 μA, at an energy of 70 MeV.

The beam current evaluation, shown in figure 4-36 above, indicates a reduction of ~ 57 ⁰ C in target disc temperature, when reducing the primary beam current from 200 μA to 180 μA, and a further 94 ⁰C reduction from a beam current of 180 μA to 150 μA. Therefore, a 10 % beam current reduction provides an additional 2% operational safety margin on the B_4C target discs, resulting in a net safety margin of 4%. Reducing the beam current even further, to 150 μA, doubles the safety margin to 8%.

Similarly, as expected, notable reductions in the temperature of the beam dump were observed, with a temperature reduction of 80 ⁰C noted when reducing the beam current from 200 μA to 180 μA, and a further 131 ⁰C drop from 180 μA to 150 μA. The original estimated safety margin for the beam dump at 200 μA was calculated to be rather tight, at approximately 0.9%. The beam current reductions show significantly higher safety margins of 4.4% and 10.1%, for beam currents of 180 μA and 150 μA, respectively.

The impact of these beam current reductions on the production rate of ^{6}He is provided in table 4-8 below. It should be noted, as previously stated in this chapter, that all simulated FLUKA ^{6}He in-target yield results are presented with an average error of ± 30 %. The decision between operating at higher ^{6}He production rates with lower safety margins, or reduced ^{6}He production rates with higher safety margins, is to be assessed in the future by the RIB target system operators.

Beam Current (μA)	^{6}He yield (nuclei/s)
200	2.85×10^{11}
180	2.56×10^{11}
150	2.14×10^{11}

Table 4-8: In-target ^{6}He yield rates by varying primary beam currents at an energy of 70 MeV.

Additionally, the possibility of reducing the target's tantalum heater power /current in order to reduce the operating temperature of the target materials, was considered. As discussed in previous sections of this research work, an outer cylindrical tantalum heater is attached to the target canister, to provide external heating power by means of resistive heating during the conditioning phase (purification of the target at high temperature prior to impingement by the primary beam) of the target. All target systems previously discussed in this chapter were simulated with an external heating power of 2500 W. An evaluation of the impact of reducing the external heating power was conducted by reducing the beam power from 2500 W to 1500 W, and thereafter 500 W, shown in figure 4-37 below.

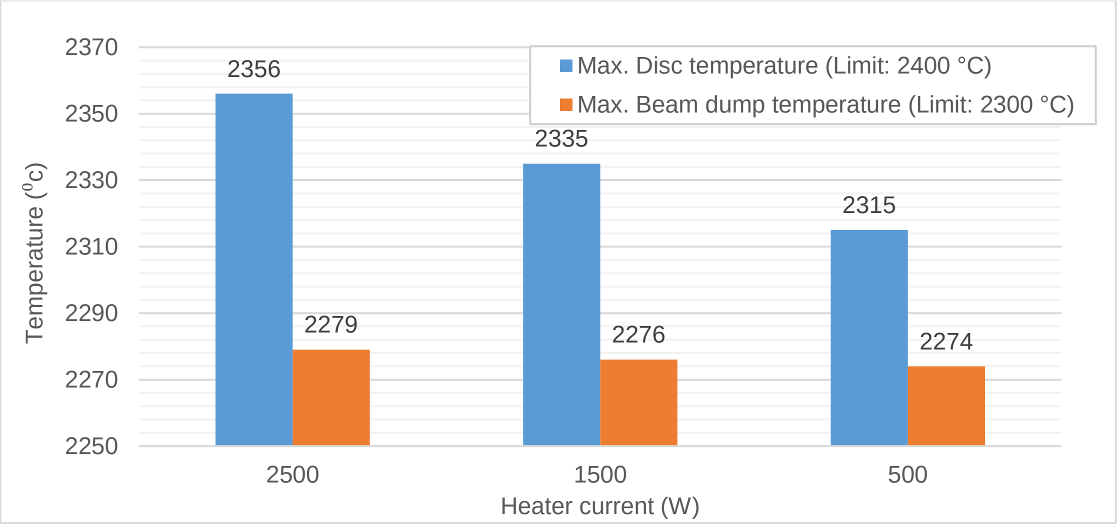

Figure 4-37: External heater power evaluation using configuration 6.

From figure 4-37 above, it is noted that the reduction in external heater power has a minor impact on the B_4C target disc temperature and furthermore, an insignificant impact of the beam dump temperature. Reducing the heater power from 2000 W to 500 W, results in a 41 ^oC temperature drop on the target discs and a 5 ^oC drop in the beam dump temperature. A combination of beam current and heater power reduction could be considered, however, it should be noted that reducing the heater power results in a lower target canister interior wall temperature (approximately 20 – 40 ^oC reduction), which could adversely affect the release efficiency of ^6He from the target system. In addition, reducing the heater power could hamper the effectiveness of the conditioning phase during target system startup.

The mechanical stress (Von misses stress) analysis results for configuration 6 are shown in figures 4-38, 4-39 and 4-40. From figure 4-38 below, a maximum VM stress value of 160 MPa (SMX) was found on the target discs, with the highest VM stress being experience by disc 1 and 15 (first and last). As expected, this result is similar to that of configurations 4 and 5, as these configurations share the same B_4C target discs dimensions and spacing. Furthermore, the target discs present no operational concerns in terms of VM stress, as the maximum values are well below the mechanical limit of B_4C (260 MPa). Mechanical analysis of the beam dump, shown in figures 4-39 and 4-40 above, indicates a maximum VM stress of 13.7 MPa, which is a slight reduction from configuration 5, which can be attributed to the increased length of beam dump 4 causing a reduction in thermally induced mechanical stress. There are thus no operational concerns related to the mechanical stresses in the dump beam as the maximum VM stress values observed are well below the mechanical limit of graphite (200 MPa).

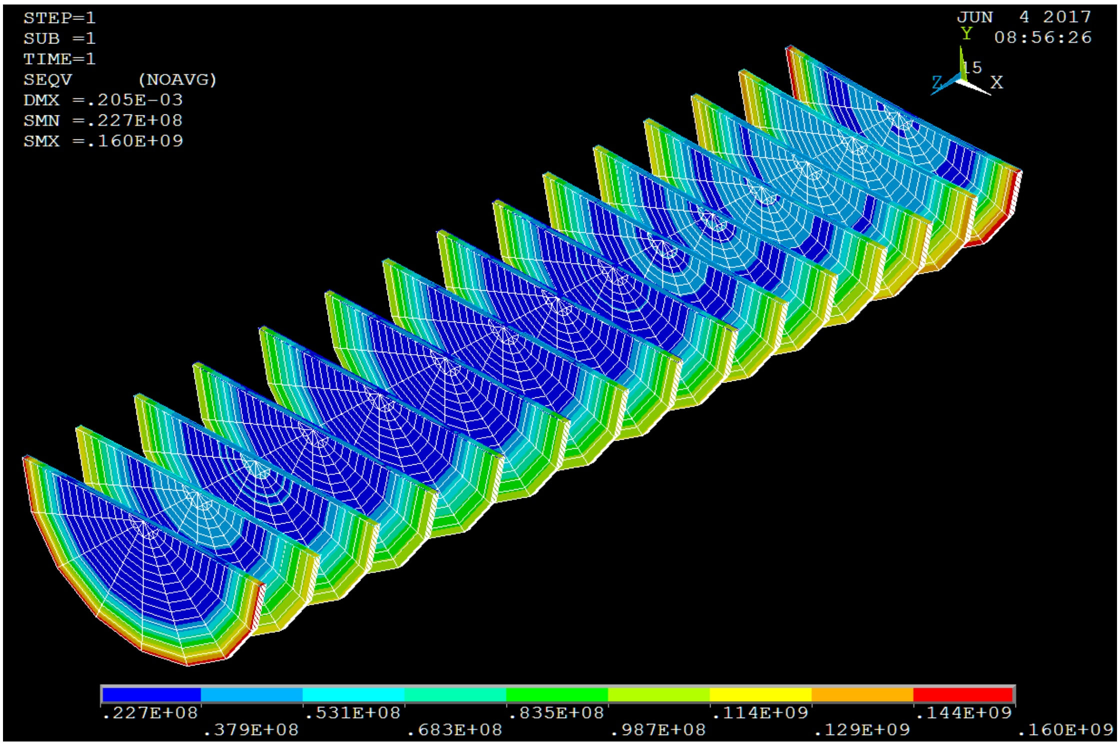

Figure 4-38: Configuration 6 – target discs VM stress results.

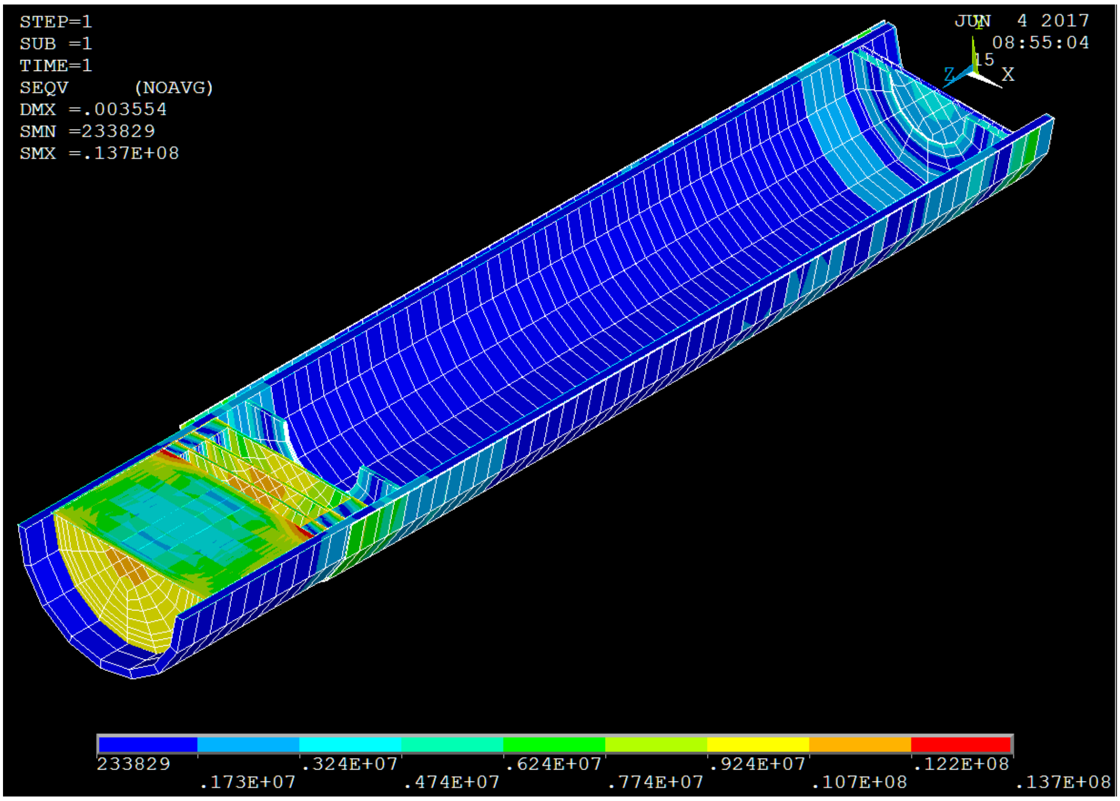

Figure 4-39: Configuration 6 – target canister and beam dump VM stress results.

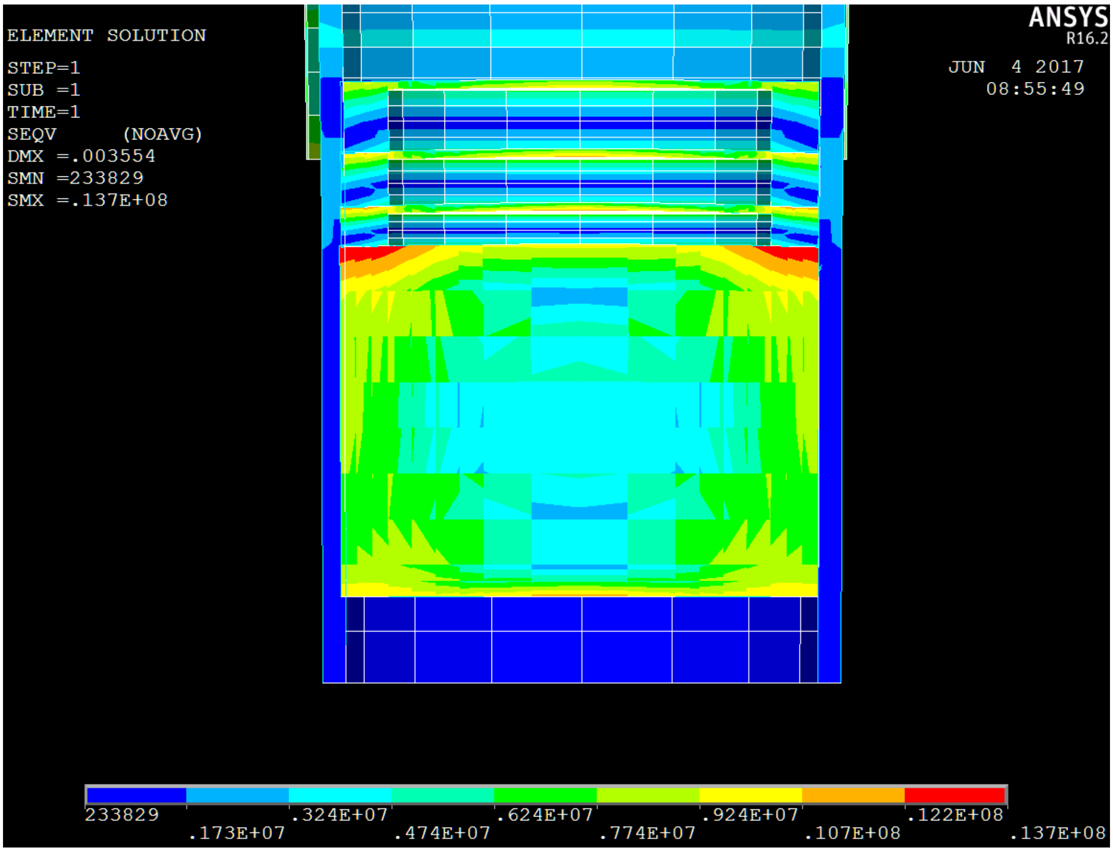

Figure 4-40: Configuration 6 – target canister and beam dump VM stress results (top view).

A summary of in-target ^{6}He yield rates, thermal and mechanical stress values for the three B_4C target systems discussed in this section are presented in table 4-9 below. These results indicate that, although no operability concerns regarding mechanical stress limits for discs and beam dumps are noted in all target configurations, the beam dump temperatures of configuration 4 and 5 were well above the thermal limit of graphite. Configuration 4 and 5 were thus deemed unfit for purpose due to this thermal constraint.

Config. no.	**Target Disk Material**	**Beam Dump Material**	**No. of Target Disks**	**Disc thickness (mm)**	**Disc spacing**	**Effective beam dump length (mm)**	**6He In-target yield (nuclei/s) for 200 µA**	**Max. Disc Temp (°C)**	**Max. Dump Temp (°C)**	**Max. Disc VM Stress (Mpa)**	**Max. Dump VM Stress (Mpa)**
4	Boron Carbide	Graphite	15	0,9	Even spacing of 12,1 mm	13	2,72E+11	2398	2668	165	20,5
5	Boron Carbide	Graphite	15	0,9	Optimal Rev. 1 spacing	23	2,85E+11	2355	2406	164	16,2
6	Boron Carbide	Graphite	15	0,9	Optimal Rev. 1 spacing	32,4	2,85E+11	2356	2279	160	13,7

Table 4-9: Results summary of boron carbide target system configurations. 'Green cells' – within thermal/mechanical limit, 'Red cells' – exceeds thermal/mechanical limit.

Configuration 6, in which 15 B_4C discs of 0.9 mm each, spaced optimally (Rev. 1 spacing) and having an extended beam dump with a total effective length of 32.4 mm, was found to be an acceptable configuration for operational use. Although the safety margins for this target configuration is rather tight, further analysis indicated that reducing the beam current would improve the thermal safety margin, albeit with a reduction in ^{6}He yield. Configuration 6 is thus proposed for application at iThemba LABS.

4.4 Beryllium Oxide two-step target

During this research work, a beryllium oxide target was considered as a possible high yielding ^{6}He production RIB target. Similar research into such a target was proposed and conducted by *Thiollière et al.* [Thi06] in 2006 under the EURISOL (European Isotope Separation Online) Project. Similar to the prototype target proposed and partially investigated in this thesis, the EURISOL ^{6}He production target system employed the two-step ISOL method, in which a neutron convertor is used to convert protons to neutrons through the neutron spallation mechanism, and subsequently having the produced neutrons impinge the target material to produce the required nuclide of interested.

The EURISOL two-step target system (figure 4-41) made use of tungsten (W) as a convertor, surrounded by a beryllium oxide (BeO) envelope. Thus, the proton beam would impinge the W convertor, releasing neutrons which react with BeO to produce ^{6}He, via the ^{9}Be(n,alpha)^{6}He reaction.

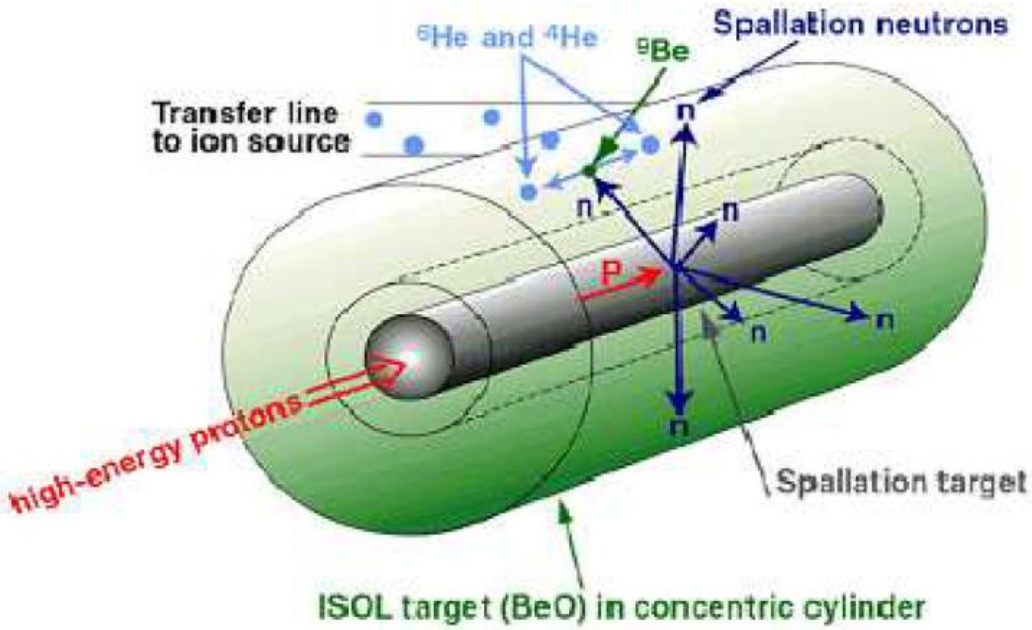

Figure 4-41: EURISOL two-step ^{6}He production target [Thi06].

Using a 1 GeV (100 kW) proton beam, the EURISOL design proposal expects to obtain ^{6}He yields in the region of 10^{13} - 10^{14} ^{6}He/s. However, this target system design has not been completed as of yet.

4.4.1 Two-step RIB target proposal

Using the two-step ISOL methodology, a target of similar nature was conceptualised during this thesis work. The proposed target makes use of a tantalum (Ta) convertor with BeO as the ^{6}He production material. Simulations were conducted using a 70 MeV (14 kW) proton beam, as would be available at iThemba LABS.

Experimental measurements of the ^{9}Be(n,α)^{6}He reaction cross section conducted in various studies, as shown in figure 4-42 below, found the cross section of this reaction peaks at approximately 3 MeV. FLUKA simulations were conducted in order to validate FLUKA against the experimental data, using a thin ^{9}Be target with ρ = 1.85 g/cm^{3} impinged by a neutron beam at various energies in the range of 1 – 15 MeV. The results of the FLUKA simulation is shown in figure 4-42 below, and was found to correlate very well to the experimental data, which is to be expected since FLUKA makes use of a host of validated neutron reaction cross section libraries for neutron energies below 20 MeV. FLUKA was therefore considered applicable for simulations of the proposed two-step BeO target system.

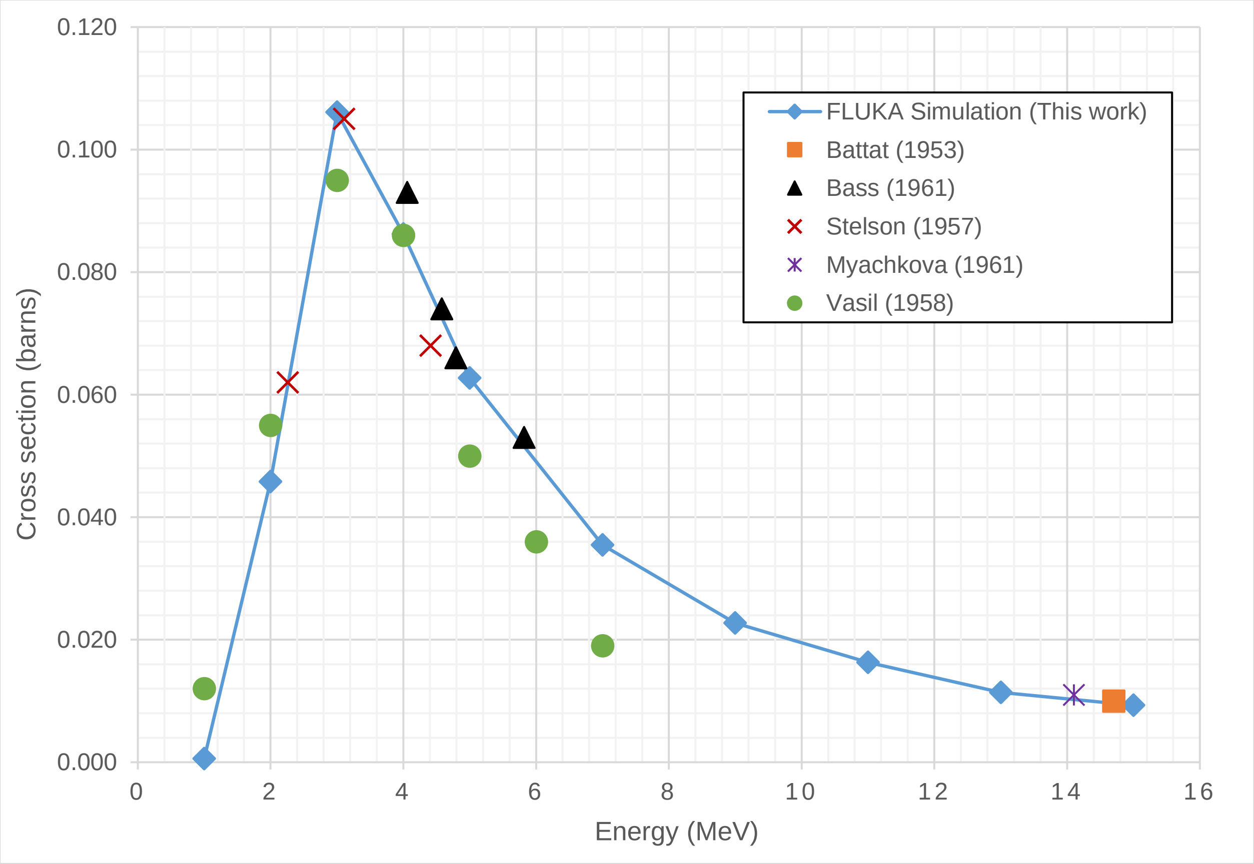

Figure 4-42: FLUKA simulation as well as experimentally obtained cross section data for ^{9}Be(n,alpha)^{6}He reaction [Bas61] [Bat53] [Mya61] [Ste57] [Vas58].

The first step during the conceptualisation of this target was to test and understand the neutron production process occurring within the convertor. A study conducted in 2002 by the Cyclotron and Radioisotope Centre (CYRIC) [Kaw02], in which neutron yields from thick targets (C, Al, Ta, W and Pb) undergoing the (p,xn) reaction were measured at 50 to 70 MeV, was employed for reference. In thier study, the emitted neutrons were measured with the time-of-flight method. The results obtained from this study indicated that Tantalum produced the greatest neutron yield between the tested materials/targets, although marginally so, when compared to W. The neutron spectra produced for a 50 MeV beam impinging on a 3 mm thick Ta target, is shown in figure 4-43 below.

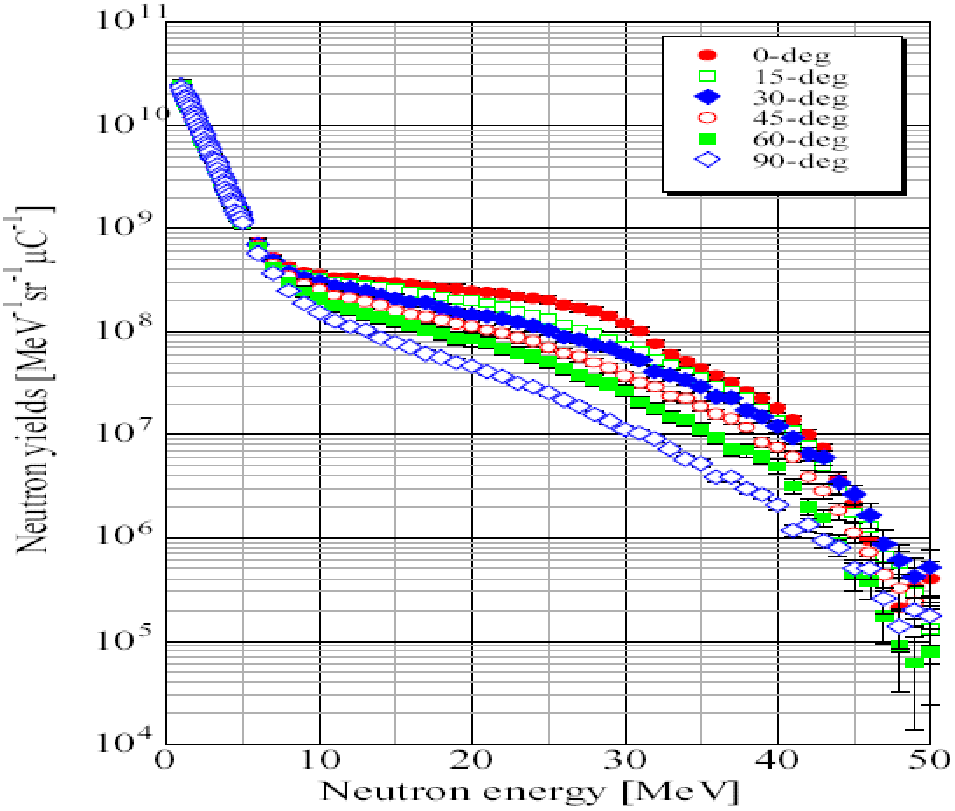

Figure 4-43: Thick target yield for Ta(p,nx) at 50 MeV [Kaw02].

In order to validate FLUKA against the experimental neutron spectra shown in figure 4-43, a simulation was done for a 50 MeV proton beam impinging a 3 mm thick tungsten target, while scoring the neutrons produced at laboratory angles of 0, 15, 30, 45, 60 and 90 degrees. As the beam profile used during experimentation was not stated, a 'pencil' beam profile of 2 mm in radius was assumed. The results obtained from the FLUKA simulation (figure 4-44) were found to be well in agreement with the experimental results, for all laboratory angles.

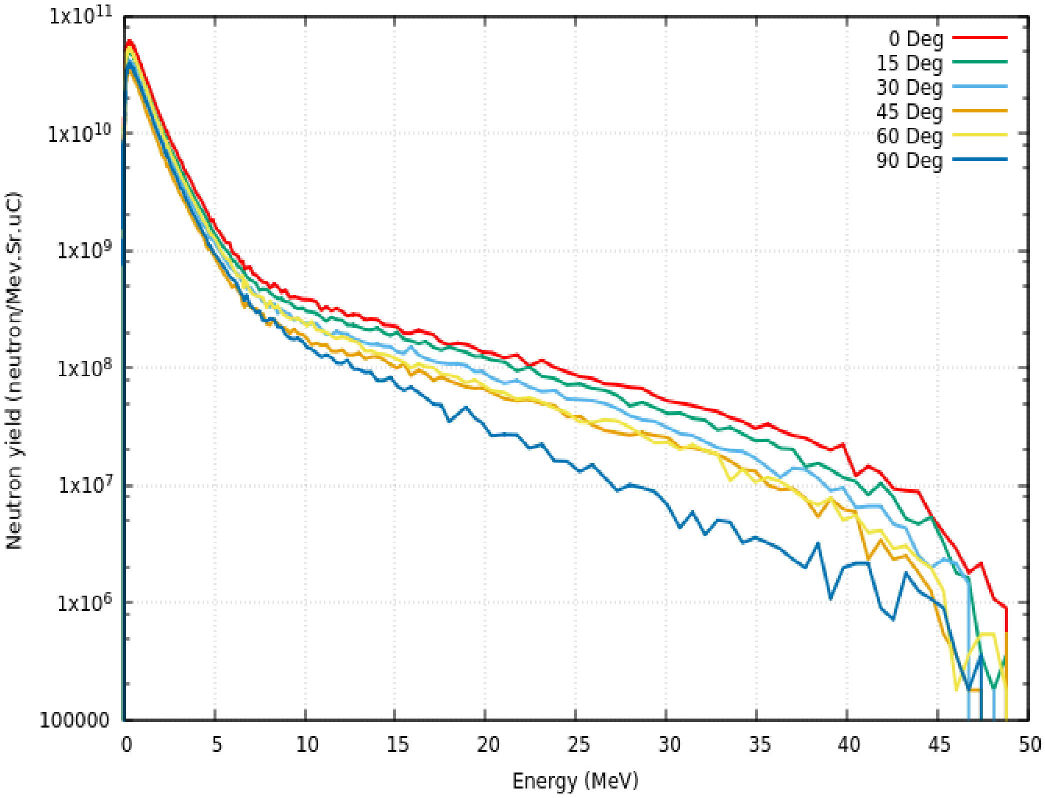

Figure 4-44: FLUKA simulation of neutron yield from Ta(p,nx) at 50 MeV.

From figure 4-44 above, it can be seen that the neutron yield at all scattering angles in the energy range 0 to 5 MeV, is observed to be approximately equal, with the neutron yield decreasing exponentially in this energy range. However, the high yield of 0 – 5 MeV neutrons obtained from the Ta convertor is ideal for driving the $^{9}Be(n,\alpha)^{6}He$ reaction, which has been shown to have a peak reaction cross section at 3 MeV (see figure 4-42).

The challenge hereafter, is designing the target in such a manner, that these low energy neutrons released from the Ta convertor, interact with the BeO material matrix optimally. Due to the isotropic nature of the low energy (< 5 MeV) neutron release, it was envisioned to place the Ta convertor in the center of a larger hollow BeO cyclinder, as shown in figure 4-45 below.

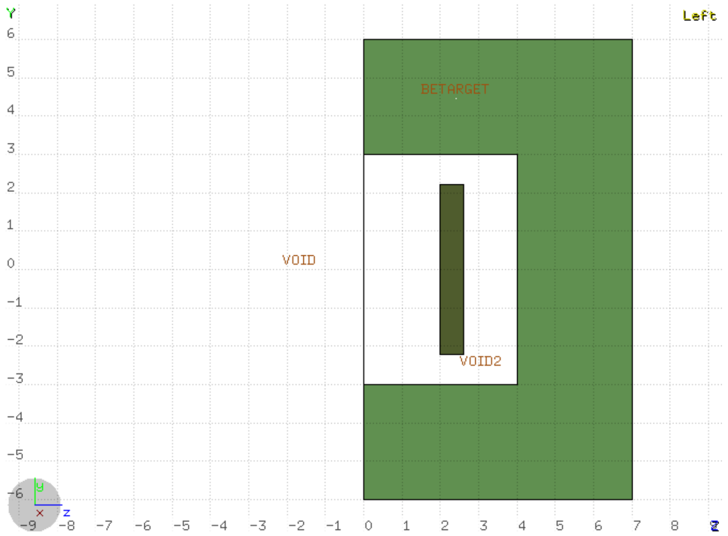

Figure 4-45: Configuration A - Prototype two-step target concept with Ta convertor (dark green) and BeO (lighter green) hollow cylinder.

With reference to the two-step design above; consideration must be given to the stopping distance of the impinging proton beam in the Ta convertor, as the convertor should be designed to bring the beam to a complete stop. A stopping distance simulation was done in FLUKA on Ta targets of increasing thickness, and it was found that the 70 MeV proton beam would be stopped at an approximate depth of 0.58 cm. Furthermore, as expected, the increasing Ta convertor thickness corresponds to an increase in neutron yield, but is seen to not increase appreciably above 0.4 cm as shown in figure 4-46 below.

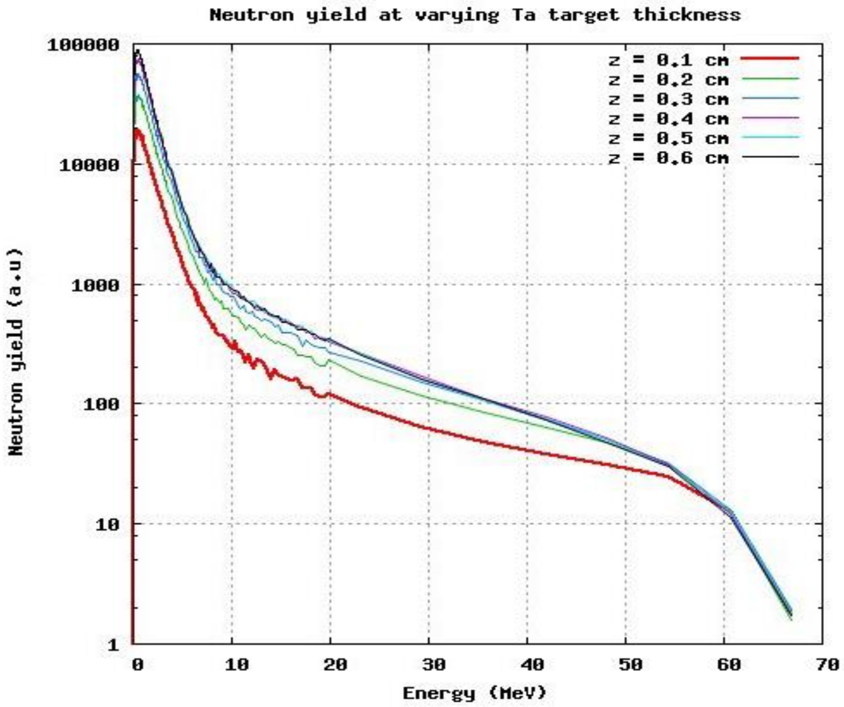

Figure 4-46: Neutron yields (arbitrary units) at varying Ta convertor thicknesses.

Figure 4-47 below, provides 2D illustrations of the neutron profiles at different Ta convertor thicknesses, simulated in FLUKA.

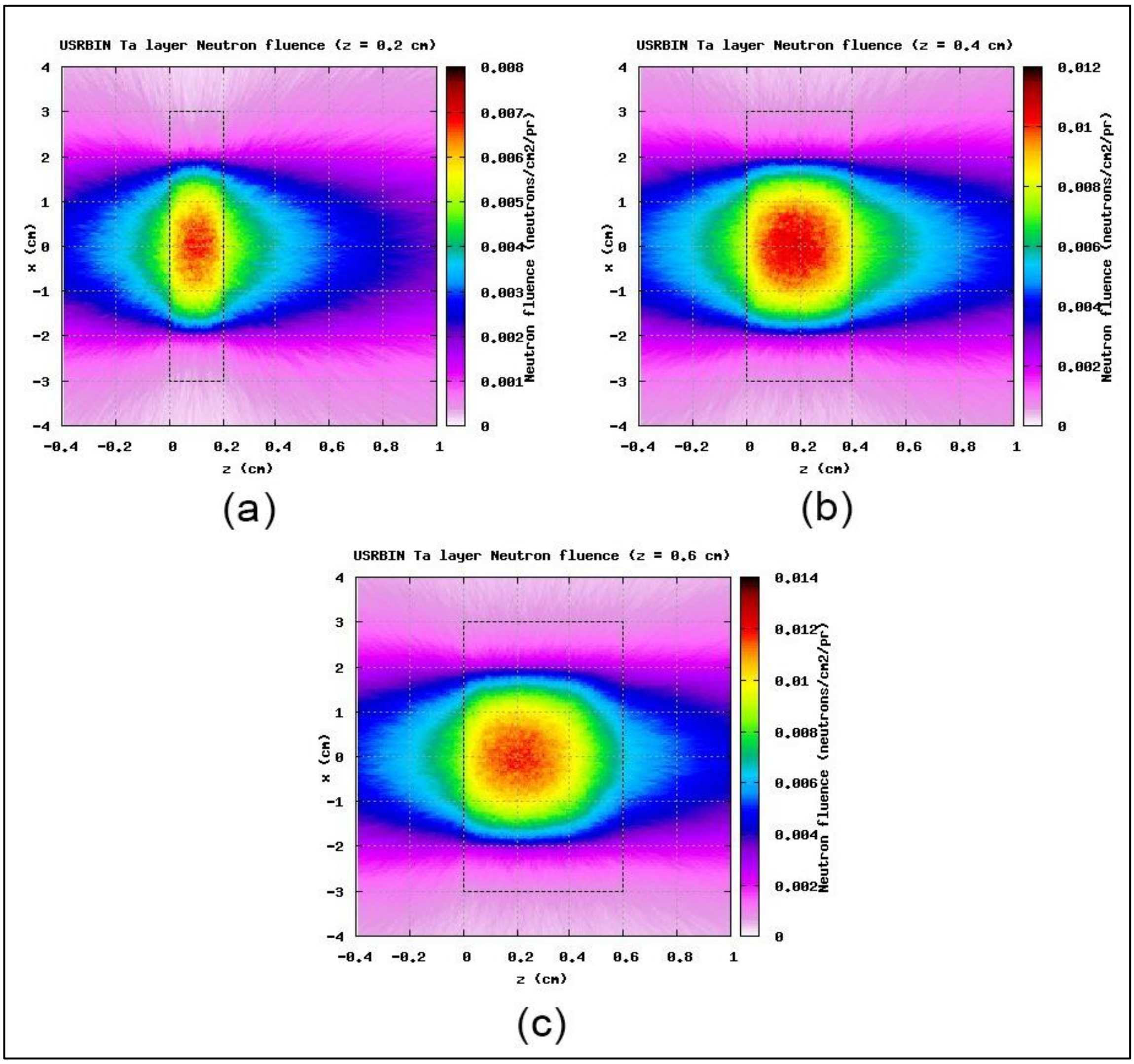

Figure 4-47: Neutron release profiles at varying Ta convertor thicknesses – (a) 0.2 cm, (b) 0.4 cm and (c) 0.6 cm.

Following the stopping distance evaluation, a Ta convertor thickness of 0.6 cm and radius of 2.25 cm was initially selected for the prototype two-step target design. The convertor is placed in the center of a hollow BeO cylinder, with an inner and outer radius of 3 cm and 6 cm, respectively and base thickness of 3 cm (refer to figure 4-45).

A FLUKA simulation of a 70 MeV, 200 μA proton beam impinging the convertor and subsequent scoring of the residual nuclei, showed an in-target ^{6}He yield rate of 3.72 x 10^{11} ^{6}He/s, for the target system depicted above (denoted Configuration A – figure 4-45). Hereafter, various target configurations (some with two Ta convertors) were simulated in an effort to examine and optimize the in-target ^{6}He yield rate. Illustrations of two of these target designs are shown in figures 4-48 and figure 4-49 below.

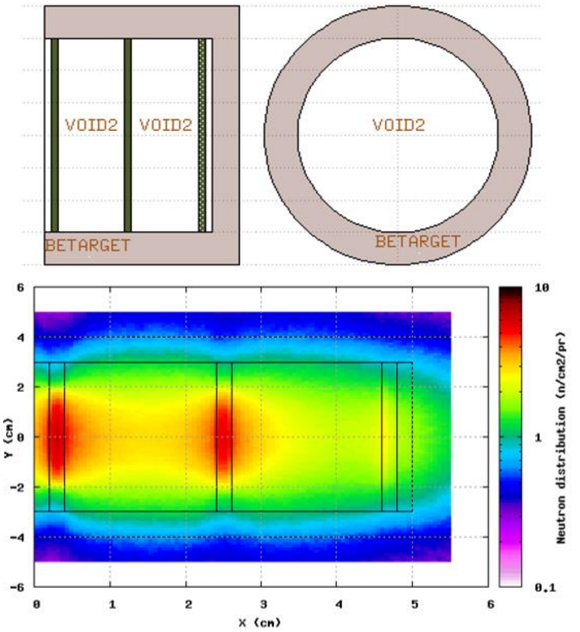

Figure 4-48: Configuration B – Three Ta convertors of 0.2 cm each (green) and BeO hollow target cylinder with 1 cm wall and 1 cm base thickness (grey). Top Left – target side view, top right – target front view, bottom – config. 2 neutron distribution.

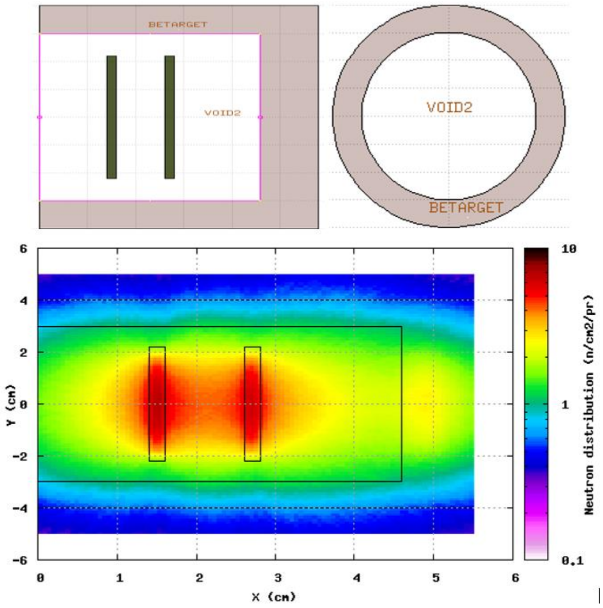

Figure 4-49: Configuration C – Two Ta convertors of 0.2 cm each (green) and BeO hollow target cylinder with 1 cm wall and 1.4 cm base thickness (grey). Left - side view, right - front view.

These target configurations provided yield rates as shown in table 4-10 below, all in the order of 10^{11} ^{6}He/s.

Target System	**^{6}He yield (nuclei/s)**
Configuration A	3.72×10^{11}
Configuration B	5.84×10^{11}
Configuration C	8.70×10^{11}

Table 4-10: ^{6}He yield rate simulation results of 70 MeV, 200 μA proton beam impinging target configurations A, B and C.

No further investigation and/or optimisation work was conducted on two-step target systems of this type as a result of insufficient information related to the thermal and mechanical properties of BeO from both commercial and literature sources. Future research work on this type of target system could be promising.

4.5 iThemba LABS RIB Target benchmarking

As discussed in Chapter 1, there are a number of facilities around the world which have used, currently make use of or plan to construct ^{6}He production facilities. Technical details of these facilities and their predicted/operational ^{6}He yield rates, are presented in table 4-11 below.

Facility	**Country**	**Primary Beam**	**Primary Beam Power (kW)**	**Target Type**	**Target Material**	**6He In-target Yield (6He/s)**	**Status**	**Ref.**
Past								
Louvain-la-Neuve	Belgium	Proton	9	Direct	LiF	1.2×10^6	Closed	[Loi96]
Operational								
TRIUMF-ISAC	Canada	Proton	32.5	Direct	SiC	5.0×10^7	Operational	[TRI18]
GANIL-SPIRAL1	France	Carbon-13	2.5	Direct	C	2.0×10^8	Operational	[GAN16]
Proposed (Future)								
CERN-ISOLDE (EURISOL)	Switzerland	Proton	100	Two-step	(W)-BeO	$\sim 2.8 \times 10^{13}$	Simulated	[Thi06]
GANIL-SPIRAL2	France	Deutron	200	Two-step	(C)-BeO	$\sim 4.0 \times 10^{11}$	Simulated	[Sai10]
SOREQ-SARAF	Israel	Deutron	80	Two-step	(Li)-BeO	$\sim 2.0 \times 10^{13}$	Simulated	[Sai10]
Proposed for Ithemba LABS								
Ithemba LABS	South Africa	Proton	14	Direct	B4C	$\sim 10^{11}$	Simulated	This work
Ithemba LABS	South Africa	Proton	14	Two-Step	(Ta)-BeO	$\sim 10^{11}$	Simulated	This work

Table 4-11: ^{6}He yield rates predicted/obtained at various international research facilities.

From table 4-11 above, it is notable that the predicted ^{6}He yield rates for both the optimised B_4C (configuration 6) target and un-optimised two-step Ta-BeO target, presented in this work, is well within range (if not better, in the case of operational facilities) of other international facilities. Assuming a post-acceleration efficiency of 1%, iThemba LABS would be capable of providing ^{6}He beams at a sufficient intensity (> 10^9 ^{6}He/s) for nuclear physics research.

CHAPTER 5: CONCLUSIONS AND RECOMMENDATIONS

The research work presented in this thesis aimed to develop and optimize an RIB target for the production of ^{6}He. This aim was successfully met with a complete target design, in which boron carbide is used as the target material. This design, as well as the preceding designs conducted during the target optimisation, covered both the physics and engineering aspects, and showed significant ^{6}He yields obtainable with the available primary beam at iThemba LABS, with the final design (configuration 6) remaining within the engineered thermal and mechanical limits of the RIB target system materials. Target configuration 6 is therefore suggested for operational use, consisting of 15 B_4C discs of 0.9 mm thickness, optimally spaced, with a 32.4 mm graphite beam dump, producing ^{6}He yields in the region of 10^{11} ^{6}He/s. This ^{6}He yield is considered 'usable', as the final re-accelerated beam after undergoing extraction efficiency losses, could be expected to be in the region of 10^8 - 10^9 ^{6}He/s.

However, due to the lack of precise data related to the characteristics and performance of boron carbide at high temperature and high vacuum, inherent errors are expected in the final thermo-mechanical results. Since a conservative approach was taken during the optimisation process, it cannot be ascertained whether these inherent errors would tend to be 'beneficial' or 'detrimental' in nature. In order to resolve these uncertainties/inherent errors, the following recommendations are made for future research:

- Conduct a complete evaluation of the thermal and mechanical properties of boron carbide at high temperature (> 2000ºC) and high vacuum (10^{-4} Pa).
- Investigate the effects of impurities in the boron carbide matrix and develop limiting impurity criteria or preferred manufacturing technique.
- Investigate the diffusion/release of ^{6}He from the B_4C material matrix.
- Conduct experimental measurements of the $^{11}B(p,x)^6He$ reaction cross section.

The prototype beryllium oxide (BeO) target proposed in this thesis, showed a similar ^{6}He yield as compared to that of the boron carbide target. The ^{6}He yields obtained from the various BeO targets test were all in the range of 10^{11} ^{6}He/s, before undergoing any target optimisation process. It is thus suspected that two-step targets using a Ta convertor and BeO as the target material, could be further optimised to attain ^{6}He yields in excess of 10^{12} ^{6}He/s (using the same beam conditions). However, no thermo-mechanical analysis could be conducted on these BeO targets due to the lack of information in the literature and commercial space, as it relates to the thermal and mechanical properties of BeO.

A BeO RIB production target (direct or two-step) is recommended for future research, and would encompass the following sub-components of research in order to be successfully analysed/investigated:

- Conduct an analysis comparing direct and two-step RIB production target systems, with BeO as the target material.
- Investigation of the thermal and mechanical properties of BeO at high temperature (> 2000^{o}C) and high vacuum (10^{-4} Pa).
- Since beryllium is known to be toxic [AST17], a safety analysis is to be conducted covering the potential risks of using BeO in an RIB target system.
- Conduct a complete thermo-mechanical analysis of the BeO RIB production target.
- Investigate/consider the use of BeO powder, which could provide better ^{6}He production and release as well as greater thermo-mechanical characteristics.

REFERENCES

[Abb16] Abbott BP, Abbott R, Abbott TD, Abernathy MR, Acernese F, Ackley K, et al. Observation of Gravitational Waves from a Binary Black Hole Merger. Phys Rev Lett. 2016 Feb 12; 116(6):061102.

[Ait17] Aithal, S., Ravindra, H.J. Textbook of Engineering Physics [Internet]. Zenodo; 2017 [cited 2019 May 19]. Available from: https://zenodo.org/record/243407

[Al04] Al-Khalili J. An Introduction to Halo Nuclei. In: Al-Khalili J, Roeckl E, editors. The Euroschool Lectures on Physics with Exotic Beams, Vol I [Internet]. Berlin, Heidelberg: Springer Berlin Heidelberg; 2004 [cited 2019 May 19]. p. 77–112. Available from: http://link.springer.com/10.1007/978-3-540-44490-9_3

[And05] Anderson TL. Fracture mechanics: fundamentals and applications. 3rd ed. Boca Raton, FL: Taylor & Francis; 2005. 621 p.

[ANS15] ANSYS Academic Research Mechanical. ANSYS Release 16.2 [Internet]. ANSYS; 2015. Available from: ww.ansys.com

[Ask11] Askeland DR, Fulay PP, Wright WJ. The science and engineering of materials. 6th ed. [SI ed.]. Stamford, CT: Cengage Learning; 2011. 921 p.

[AST17] ATSDR. Beryllium (Be) Toxicity: Patient Education Care Instruction Sheet | ATSDR - Environmental Medicine & Environmental Health Education - CSEM [Internet]. [cited 2017 Nov 25]. Available from: https://www.atsdr.cdc.gov/csem/csem.asp?csem=5&po=15

[Azo01] AZoM. Properties: Boron Carbide (B4C) - Properties and Information about Boron Carbide [Internet]. AZoM.com. 2001 [cited 2017 Sep 27]. Available from: https://www.azom.com/properties.aspx?ArticleID=75

[Bae10] Baetens R, Jelle BP, Thue JV, Tenpierik MJ, Grynning S, Uvsløkk S, et al. Vacuum insulation panels for building applications: A review and beyond. Energy and Buildings. 2010 Feb; 42(2):147–72.

[Bar18] Bark RA, Barnard AH, Conradie JL, de Villiers JG, van Schalkwyk PA. The South African isotope facility project. In Stellenbosch, South Africa; 2018 [cited 2019 May 19]. p. 030021. Available from: http://aip.scitation.org/doi/abs/10.1063/1.5035538

[Bar13] Bark RA, Cornell JC. A radioactive ion beam facility at iThemba LABS. iThemba Laboratory, Cape Town, South Africa, Internal Report, RIB-PUB-03. 2013;

[Bar01] Barkanov E. Introduction to the finite element method. Institute of Materials and Structures Faculty of Civil Engineering Riga Technical University. 2001; 1–70.

[Bas61] Bass R, Bonner TW, Haenni HP. Cross section for the Be9 (n, α) He6 reaction.

Nuclear Physics. 1961 Feb; 23:122–30.

[Bat53] Battat ME, Ribe FL. Formation of He 6 by 14-Mev Neutron Bombardment of Li and Be. Phys Rev. 1953 Jan 1; 89(1):80–3.

[Bec11] Beck C, Papka P, Zafra AS i, Thummerer S, Azaiez F, Bednarczyk P, et al. Clusters in Light Nuclei. Acta Phys Pol B. 2011; 42(3):747.

[Ber04] Bertulani CA, Danielewicz P. Introduction to nuclear reactions. Bristol ; Philadelphia: Institute of Physics; 2004. 515 p. (Graduate student series in physics).

[Bha05] Bhavikatti SS. Finite element analysis. New Delhi: New Age International (P) Ltd., Publishers; 2005.

[Bia08] Biasetto L, Manzolaro M, Andrighetto A. Emissivity measurements of opaque gray bodies up to 2000 °C by a dual-frequency pyrometer. Eur Phys J A. 2008 Nov; 38(2):167–71.

[Blu13] Blumenfeld Y, Nilsson T, Van Duppen P. Facilities and methods for radioactive ion beam production. Phys Scr. 2013 Jan 1; T152:014023.

[Bos11] Boschini MJ, Consolandi C, Gervasi M, Giani S, Grandi D, Ivanchenko V, et al. Nuclear and Non-Ionizing Energy-Loss for Coulomb Scattered Particles from Low Energy up to Relativistic Regime in Space Radiation Environment. In: Cosmic Rays for Particle and Astroparticle Physics [Internet]. Villa Olmo, Como, Italy: World Scientific; 2011 [cited 2019 May 19]. p. 9–23. Available from: http://www.worldscientific.com/doi/abs/10.1142/9789814329033_0002

[Bou86] Bourgoyne AT, editor. Applied drilling engineering. Richardson, TX: Society of Petroleum Engineers; 1986. 502 p. (SPE textbook series).

[Bro86] Bronitsky G, Hamer R. Experiments in Ceramic Technology: The Effects of Various Tempering Materials on Impact and Thermal-Shock Resistance. American Antiquity. 1986 Jan; 51(01):89–101.

[Bro16] Brookhaven National Laboratory. BNL | NSRL User Guide [Internet]. 2016 [cited 2017 Nov 10]. Available from: https://www.bnl.gov/nsrl/userguide/bragg-curves-and-peaks.php

[Bro96] Broome T. High power targets for spallation sources. In: Proc EPAC96. Sitges, Spain; 1996. p. 267.

[Cal12] Callister WD, Rethwisch DG. Fundamentals of materials science and engineering: an integrated approach. 4th ed. Hoboken, N.J: Wiley; 2012. 910 p.

[Car75] Carter LL, Cashwell ED. Particle-transport simulation with the Monte Carlo method [Internet]. 1975 Jan [cited 2019 May 19] p. TID--26607, 4167844. Report No.: TID--26607, 4167844. Available from:

http://www.osti.gov/servlets/purl/4167844-hO0xdX/

[Cha07] Chautard F, Berthe C, Colombe A, David L, Dolegieviez P, Jacquot B, et al. Status report on GANIL-SPIRAL1. In Giardini-Naxos, Italy; 2007 [cited 2018 Nov 19]. p. 99–104. Available from: http://hal.in2p3.fr/in2p3-00340151

[Che12] Cherry SR, Sorenson JA, Phelps ME. Physics in nuclear medicine. 4th ed. Philadelphia: Elsevier/Saunders; 2012. 523 p.

[Cle97] Cleveland J. Thermophysical properties of materials for water cooled reactors. International Atomic Energy Agency Report IAEATECDOC. 1997; 949:77.

[Con16] Conradie J, Andrighetto A, Anthony L, Azaiez F, Baard S, Bark R, et al. A Radioactive Ion Beam and Isotope Production Facility for iThemba LABS. In: 25th Russian Particle Accelerator Conf (RuPAC'16), St Petersburg, Russia, November 21-25, 2016. St. Petersburg, Russia: JACOW, Geneva, Switzerland; 2017. p. 78–82.

[Coo57] Cook CW, Fowler WA, Lauritsen CC, Lauritsen T. B 12, C 12, and the Red Giants. Physical Review. 1957; 107(2):508.

[Cor13] Corradetti S. Study and development of high release refractory materials for the SPES project [Internet] [Ph.D. thesis]. [Padua, Italy]: Padua University; 2013 [cited 2018 May 19]. Available from: http://paduaresearch.cab.unipd.it/5412/

[Cso01] Csoto A, Oberhummer H, Schlattl H. Fine-tuning the basic forces of nature through the triple-alpha process in red giant stars. Nuclear Physics A. 2001 May; 688(1–2):560–2.

[Cve02] Cverna F. ASM Ready Reference: Thermal properties of metals. ASM International; 2002. 564 p.

[Dav70] Davids CN, Laumer H, Austin SM. Production of the Light Elements Lithium, Beryllium, and Boron by Proton Spallation of C 12. Phys Rev C. 1970 Jan 1; 1(1):270–5.

[deA14] de Angelis G, Prete G, Andrighetto A, Manzolaro M, Corradetti S, Scarpa D, et al. The SPES radioactive ion beam project of INFN. J Phys: Conf Ser. 2014 Jul; 527:012029.

[deA16] de Angelis G, Prete G, Andrigetto A, Manzolaro M, Corradetti S, Scarpa D, et al. The SPES radioactive ion beam project of LNL: status and perspectives. Andreev A, Arsenyev N, Ershov S, Sargsyan V, Vdovin A, editors. EPJ Web of Conferences. 2016; 107:01001.

[Dim08] Dimitrijevic M, Posarac M, Jancic-Heinemman R, Majstorovic J, Volkov-Husovic T, Matovic B. Thermal shock resistance of ceramic fibre composites characterized by non-destructive methods. PAC. 2008; 2(2):115–9.

[Dom11] Domnich V, Reynaud S, Haber RA, Chhowalla M. Boron Carbide: Structure, Properties, and Stability under Stress. J Am Ceram Soc. 2011 Nov; 94(11):3605–28.

[Dow12] Dowling NE. Mechanical behavior of materials: engineering methods for deformation, fracture, and fatigue. 4th ed. Boston: Pearson; 2013. 936 p.

[Ebr12] Ebran J-P, Khan E, Nikšić T, Vretenar D. How atomic nuclei cluster. Nature. 2012 Jul;487(7407):341–4.

[Ego16] Egoriti L, Boeckx S, Ghys L, Houngbo D, Popescu L. Analytical model for release calculations in solid thin-foils ISOL targets. Nuclear Instruments and Methods in Physics Research Section A: Accelerators, Spectrometers, Detectors and Associated Equipment. 2016 Oct; 832:202–7.

[Ekl16] Eklund A. Hot and Cold Isostatic Pressing of Ceramics | 2016-05-02 | Ceramic Industry [Internet]. 2016 [cited 2017 Nov 12]. Available from: https://www.ceramicindustry.com/articles/95484-hot-and-cold-isostatic-pressing-of-ceramics

[Epe13] Epelbaum E, Krebs H, Lähde TA, Lee D, Meißner U-G. Dependence of the triple-alpha process on the fundamental constants of nature. Eur Phys J A. 2013 Jul; 49(7):82.

[Eur18] Eurisol. Eurisol [Internet]. 2018 [cited 2018 Sep 1]. Available from: http://www.eurisol.org/

[Fas94] Fassò A, Ferrari A, Ranft J, Sala PR. Nuclear models in FLUKA for interactions in the intermediate energy range. In: Proceedings of Specialists' Meeting on Intermediate Energy Nuclear Data: Models and Codes. Issy les Moulineaux, France; 1994. p. 271.

[Fas03] Fasso' A, Ferrari A, Roesler S, Ranft J, Sala PR, Battistoni G, et al. The FLUKA code: present applications and future developments. In: arXiv: physics/0306162 [Internet]. La Jolla, USA; 2003 [cited 2019 May 19]. p. 8. Available from: http://arxiv.org/abs/physics/0306162

[Fer05] Ferrari A, Fassò A, Ranft J, Sala PR. FLUKA: A multi-particle transport code (program version 2005). 2005 [cited 2019 May 19]; Available from: http://cds.cern.ch/record/898301

[For99] Forkel-Wirth D. Exploring solid state physics properties with radioactive isotopes. Rep Prog Phys. 1999 Jan; 62(4):527–597.

[Fre10] Freer M. Clusters in nuclei. Scholarpedia. 2010;5(6):9652

[Fri81] Friedlander G, editor. Nuclear and radiochemistry. 3. ed. New York: Wiley; 1981. 684 p. (A Wiley-Interscience publication).

[FRIB12] FRIB Users Organization. FRIB: Opening New Frontiers in Nuclear Science-

Moving Forward with the Long Range Plan [Internet]. 2012 [cited 2018 Nov 12]. Available from: https://frib.msu.edu/_files/pdfs/frib_opening_new_frontiers_in_nuclear_science.pdf

[GAN16] GANIL - Grand Accélérateur National d'Ions Lourd. Chartbeams [Internet]. GANIL Facilities - Available Beams. 2016 [cited 2019 Jan 22]. Available from: http://u.ganil-spiral2.eu/chartbeams/

[Gar16] Garcia FH. Calculation of rates for radioactive isotope beam production at TRIUMF [Internet] [PhD Thesis]. [Burnaby, Canada]: Simon Fraser University; 2016 [cited 2019 May 19]. Available from: http://summit.sfu.ca/item/16881

[Gel01] Gelletly W. Radioactive Ion Beams: A New Window on Atomic Nuclei. Proceedings of the American Philosophical Society. 2001; 145(4):519–54.

[Gra09] GrafTech. Grade ATJ^{TM} Graphite [Internet]. GrafTech International; 2009 [cited 2017 Oct 1]. Available from: http://nstx.pppl.gov/DragNDrop/Working_Groups/PFCR/materials/20090908%20Grade-ATJ-Isomolded-Graphite.pdf

[Hai02] Haines J. Graphite Sublimation Tests for the Muon Collider/Neutrino Factory Target Development Program [Internet]. 2002 Mar [cited 2019 May 19] p. ORNL/TM-2002/27, 814540. Report No.: ORNL/TM-2002/27, 814540. Available from: http://www.osti.gov/servlets/purl/814540/

[Han87] Hansen PG, Jonson B. The Neutron Halo of Extremely Neutron-Rich Nuclei. EPL. 1987 Aug; 4(4):409–414.

[Har04] Harakeh M, Äystö J. Perspectives for nuclear-physics research in Europe – CERN Courier [Internet]. 2004 [cited 2017 Jan 18]. Available from: https://cerncourier.com/perspectives-for-nuclear-physics-research-in-europe/

[Huy11] Huyse M, Raabe R. Radioactive ion beam physics at the cyclotron research centre Louvain-la-Neuve. J Phys G: Nucl Part Phys. 2011 Jan; 38(2):024001.

[Jan07] Janka H, Langanke K, Marek A, Martinezpinedo G, Muller B. Theory of core-collapse supernovae. Physics Reports. 2007 Apr; 442(1–6):38–74.

[Jen04] Jensen AS, Riisager K, Fedorov DV, Garrido E. Structure and reactions of quantum halos. Rev Mod Phys. 2004 Feb 5; 76(1):215–61.

[Jon09] Jong I-C, Springer W. Teaching Von Mises Stress: From Principal Axes To Nonprincipal Axes. In 2009 [cited 2019 May 19]. p 14.1159.1-14.1159.9. Available from: https://peer.asee.org/teaching-von-mises-stress-from-principal-axes-to-nonprincipal-axes

[Kam92] Kaminaga F, Sato S, Okamoto Y. Evaluation of Gap Heat Transfer between Boron Carbide Pellet and Cladding in Control Rod of FBR. Journal of Nuclear Science and Technology. 1992 Feb; 29(2):121–30.

[Kaw02] Kawata N, Baba M, Aoki T, Hagiwara M, Itoga T, Hirabayashi N, et al. Measurements of Differential Thick Target yield for C, Al, Ta, W, P (pxn) reactions at 50 and 70 MeV. In: Proceedings of the 2002 Symposium on Nuclear Data. Tokyo, Japan: T. Ohsawa and T. Fukhori; 2002. p. 160.

[Kne12] Knecht A, Hong R, Zumwalt DW, Delbridge BG, García A, Müller P, et al. Precision Measurement of the He 6 Half-Life and the Weak Axial Current in Nuclei. Phys Rev Lett. 2012 Mar 23; 108(12):122502.

[Kös03] Köster U. Intense radioactive-ion beams produced with the ISOL method. In: Äystö J, Dendooven P, Jokinen A, Leino M, editors. Exotic Nuclei and Atomic Masses. Springer Berlin Heidelberg; 2003. p. 437–45.

[Kra88] Krane KS. Introductory Nuclear Physics. Wiley; 1988. 845 p.

[Krá10] Krása A. Spallation Reaction Physics. Manuscript for the Lecture “Neutron Sources for ADS” [Internet]. Czech Technical University, Prague; 2010 [cited 2017 Feb 11]. Available from: https://pdfs.semanticscholar.org/ba08/30dcab221b45ca5bcc3cfa8ae82558d624e7.pdf

[Kur17] Kurt J. Lesker Company. Boron Carbide (B4C) Pieces Evaporation Materials [Internet]. 2017 [cited 2017 Sep 27]. Available from: https://www.lesker.com/newweb/deposition_materials/depositionmaterials_evaporationmaterials_1.cfm?pgid=bor2

[Lax14] Laxdal RE, Morton AC, Schaffer P. Radioactive Ion Beams and Radiopharmaceuticals. Reviews of Accelerator Science and Technology. 2014 Apr; 6:37–57.

[Lee92] Lee S, Mazurowski J, Ramseyer G, Dowben PA. Characterization of boron carbide thin films fabricated by plasma enhanced chemical vapor deposition from boranes. Journal of Applied Physics. 1992 Nov 15; 72(10):4925–33.

[Lei13] Lienhard JH. A Heat Transfer Textbook. 4th ed. Dover Publications; 2013. 770 p.

[Loi96] Loiselet M, Goffaux H, Daras T, Breyne D, Postiau N, Berger G, et al. Production and Acceleration of Radioactive Beams at Louvain-la-Neuve. In: 14th International Conference on Cyclotrons and Their Applications (CYCLOTRONS 95). Cape Town, South Africa; 1996. p. 629–33.

[Lu98] Lu TJ, Fleck NA. The thermal shock resistance of solids. Acta Materialia. 1998 Aug; 46(13):4755–68.

[Lu13]	Lu Z-T, Mueller P, Drake GWF, Nörtershäuser W, Pieper SC, Yan Z-C. Colloquium: Laser probing of neutron-rich nuclei in light atoms. Rev Mod Phys. 2013 Oct 2; 85(4):1383–400.
[Lun04]	Lunney D. ISOLDE goes on the trail of superlatives – CERN Courier [Internet]. 2004 [cited 2017 Nov 1]. Available from: https://cerncourier.com/isolde-goes-on-the-trail-of-superlatives/
[Mal13]	Malou Z, Mohamed H, Bouaouadja N, Chevalier J, Fantozzi G. Thermal shock resistance of a soda lime glass. Ceramics Silikaty. 2013 Mar 1; 57(1):39–44.
[Mar70]	Marlowe MO. Elastic properties of three grades of fine grained graphite at 2000 °C [Internet]. Nucleonics Laboratory, General Electric; 1970 [cited 2018 Sep 20]. Report No.: CR-66933 for NASA. Available from: https://ntrs.nasa.gov/archive/nasa/casi.ntrs.nasa.gov/19700032783.pdf
[Mar01]	Marqués FM, Labiche M, Orr NA, Angélique JC, Axelsson L, Benoit B, et al. Three-body correlations in Borromean halo nuclei. Phys Rev C. 2001 Nov 5; 64(6):061301.
[Mic07]	Michaux A, Sauder C, Camus G, Pailler R. Young's modulus, thermal expansion coefficient and fracture behavior of selected Si–B–C based carbides in the 20–1200°C temperature range as derived from the behavior of carbon fiber reinforced microcomposites. Journal of the European Ceramic Society. 2007 Jan; 27(12):3551–60.
[Moa99]	Moaveni S. Finite element analysis: theory and application with ANSYS. Upper Saddle River, N.J: Prentice Hall; 1999. 527 p.
[Mon05]	Mongelli ST, Maiorino JR, Anéfalos S, Deppman A, Carluccio T. Spallation physics and the ADS target design. Braz J Phys. 2005 Sep; 35(3b):894–7.
[Mon15]	Monetti A, Andrighetto A, Petrovich C, Manzolaro M, Corradetti S, Scarpa D, et al. The RIB production target for the SPES project. Eur Phys J A. 2015 Oct; 51(10):128.
[Mon16]	Monetti A, Bark RA, Andrighetto A, Beukes P, Conradie JL, Corradetti S, et al. On-line test using multi-foil SiC target at iThemba LABS. Eur Phys J A. 2016 Jun; 52(6):168.
[Mon17]	Monetti A. Design and development of the target-ion source system for the SPES project [Internet] [Ph.D. thesis]. [Padua, Italy]: Padua University; 2017. Available from: http://paduaresearch.cab.unipd.it/10361/
[Meu07]	Mueller P, Sulai IA, Villari ACC, Alcántara-Núñez JA, Alves-Condé R, Bailey K, et al. Nuclear Charge Radius of He 8. Phys Rev Lett. 2007 Dec 21; 99(25):252501.
[Mya61]	Myachkova SA, Perelygin VP. Interaction of 14.1-MeV neutrons with Be-9.

Soviet Physics JETP. 1961; 13(5):876–80.

[Nav17] Nave R. Radioactive Half-Life [Internet]. 2017 [cited 2017 Nov 9]. Available from: http://hyperphysics.phy-astr.gsu.edu/hbase/Nuclear/halfli2.html

[Nik09] Nikishkov GP. Introduction to the finite element method. Lecture Notes - University of Aizu. [Internet]. Aizu, Japan; 2009. Available from: http://citeseerx.ist.psu.edu/viewdoc/download?doi=10.1.1.521.9293&rep=rep1&type=pdf

[Nuc17] Nuclear Power. Bragg Curve and Bragg Peak [Internet]. Nuclear Power. [cited 2017 Nov 10]. Available from: https://www.nuclear-power.net/nuclear-power/reactor-physics/interaction-radiation-matter/interaction-heavy-charged-particles/bragg-curve-bragg-peak/

[Ols93] Olsen DK. The production of accelerated radioactive ion beams [Internet]. Oak Ridge National Lab.; 1993 [cited 2019 May 19]. Report No.: CONF-9305293--2. Available from: http://inis.iaea.org/Search/search.aspx?orig_q=RN:25029435

[Pan17] Panadyne. Panadyne Boron Carbide [Internet]. 2017 [cited 2017 Oct 31]. Available from: http://www.panadyne.com/pdf/panadyne_boron_carbide.pdf

[Pfü12] Pfützner M, Karny M, Grigorenko LV, Riisager K. Radioactive decays at limits of nuclear stability. Rev Mod Phys. 2012 Apr 30; 84(2):567–619.

[Ray08] Raychaudhuri S. Introduction to Monte Carlo Simulation. In: Proceedings of the 40th Conference on Winter Simulation [Internet]. Winter Simulation Conference; 2008 [cited 2019 May 19]. p. 91–100. (WSC ’08). Available from: http://dl.acm.org/citation.cfm?id=1516744.1516768

[Ros14] Rossetto F. Study of radioactive beams production among the SPES accelerator [Internet] [MSc Thesis]. [Padua, Italy]: Padua University; 2014. Available from: http://tesi.cab.unipd.it/46496/

[Roy08] Roylance D. Mechanical properties of materials [Internet]. Massachusetts Institute of Technology; 2008 [cited 2017 Oct 20]. Available from: http://web.mit.edu/course/3/3.225/book.pdf

[Rub16] Rubinstein RY, Kroese DP. Simulation and the Monte Carlo Method [Internet]. Hoboken, NJ, USA: John Wiley & Sons, Inc.; 2016 [cited 2019 May 19]. (Wiley Series in Probability and Statistics). Available from: http://doi.wiley.com/10.1002/9781118631980

[Sai10] Saint-Laurent M-G, Pichard A, Lhersonneau G, de Oliveira Santos F, Pellemoine F, Delahaye P, et al. Comparison Of Expected Yields For Light Radioactive Beams At SPIRAL-1 And 2. In: AIP Conference Proceedings

[Internet]. Sochi, Russia; 2010 [cited 2018 Nov 19]. p. 482–91. Available from: http://aip.scitation.org/doi/abs/10.1063/1.3431456

[San05] Santana-Leitner M. A Monte Carlo code to optimize the production of radioactive ion beams by the ISOL technique [Internet] [Ph.D. thesis]. [CERN, Geneva, Switzerland]: Universitat Politècnica de Catalunya; 2005 [cited 2018 Jul 7]. Available from: http://cds.cern.ch/record/905537/files/thesis-2005-039.pdf

[Sel93] Seltzer S. Stopping-Powers and Range Tables for Electrons, Protons, and Helium Ions, NIST Standard Reference Database 124 [Internet]. National Institute of Standards and Technology; 1993 [cited 2018 Jul 11]. Available from: http://www.nist.gov/pml/data/star/index.cfm

[She01] Sheppard RG, Mathes DM, Bray DJ. Properties and characteristics of graphite for industrial applications. Poco Graphite. 2001 Jan 1; 5–7.

[Sie71] Siegel R, Howell JR. Thermal radiation heat transfer. Vol. 3. New York: McGraw-Hill; 1971. 814 p.

[Sil07] Silberberg MS. Principles of general chemistry. Boston: McGraw-Hill Higher Education; 2007. 792 p.

[Sin01] Singleton J. Band theory and electronic properties of solids. Oxford ; New York: Oxford University Press; 2001. 222 p. (Oxford master series in condensed matter physics; vol. 2).

[Ste57] Stelson PH, Campbell EC. Cross Section for the Be 9 (n,α) He 6 Reaction. Phys Rev. 1957 Jun 15; 106(6):1252–5.

[Sto11] Stolarski TA, Nakasone Y, Yoshimoto S. Engineering analysis with ANSYS software. 1st ed. Amsterdam ; Boston: Butterworth-Heinemann; 2011. 456 p.

[Sto12] Stora T, Noah E, Hodak R, Hirsh TY, Hass M, Kumar V, et al. A high intensity ^{6}He beam for the β-beam neutrino oscillation facility. EPL. 2012 May 1; 98(3):32001.

[Str04] Stracener DW, Alton GD, Auble RL, Beene JR, Mueller PE, Bilheux JC. Targets used in the production of radioactive ion beams at the HRIBF. Nuclear Instruments and Methods in Physics Research Section A: Accelerators, Spectrometers, Detectors and Associated Equipment. 2004 Mar; 521(1):126–35.

[Sun88] Sun CT, Yoon KJ. Mechanical properties of graphite/epoxy composites at various temperatures [Internet]. Composite Materials Laboratory: Purdue University; 1988. Report No.: HTMIAC-9. Available from: https://apps.dtic.mil/dtic/tr/fulltext/u2/a199311.pdf

[Sup09] Suplee C. Atomic Weights and Isotopic Compositions with Relative Atomic

Masses [Internet]. NIST. 2009 [cited 2018 Jul 30]. Available from: https://www.nist.gov/pml/atomic-weights-and-isotopic-compositions-relative-atomic-masses

[Sur10] Suri AK, Subramanian C, Sonber JK, Murthy TSRC. Synthesis and consolidation of boron carbide: a review. International Materials Reviews. 2010 Jan; 55(1):4–40.

[Tan85a] Tanihata I, Hamagaki H, Hashimoto O, Nagamiya S, Shida Y, Yoshikawa N, et al. Measurements of interaction cross sections and radii of He isotopes. Physics Letters B. 1985 Oct; 160(6):380–4.

[Tan85b] Tanihata I, Hamagaki H, Hashimoto O, Shida Y, Yoshikawa N, Sugimoto K, et al. Measurements of Interaction Cross Sections and Nuclear Radii in the Light p -Shell Region. Phys Rev Lett. 1985 Dec 9; 55(24):2676–9.

[Tan96] Tanihata I. Neutron halo nuclei. J Phys G: Nucl Part Phys. 1996 Feb 1; 22(2):157–98.

[Tar14] Tarbert CM, Watts DP, Glazier DI, Aguar P, Ahrens J, Annand JRM, et al. Neutron Skin of Pb 208 from Coherent Pion Photoproduction. Phys Rev Lett. 2014 Jun 18; 112(24):242502.

[Tay78] Taylor RE, Groot H. Thermophysical Properties of POCO Graphite [Internet]. Properties Research Laboratory: Purdue University; 1978. Report No.: AFOSR-TR 78-1375. Available from: https://academic.csuohio.edu/duffy_s/temp/DoE%20CAES%20Program/Stress%20and%20Strain/1972%20Poco%20Graphite%20Thermal%20Properties%20ADA060419.pdf

[Ted14] Ted Pella Inc. Vacuum Deposition Techniques and Tables [Internet]. Ted Pella Inc.; 2014 [cited 2017 Sep 27]. Available from: https://www.tedpella.com/pdfs_html/Vacuum-Deposition-Techniques-and-Tables.pdf

[Thi00] Thieberger P. MUC-0186 Upper Limits for Sublimation Losses from Hot Carbon Targets in Vacuum and in Gasses - Semantic Scholar [Internet]. Brookhaven National Laboratory; 2000 [cited 2017 May 19]. Available from: /paper/MUC-0186-Upper-Limits-for-Sublimation-Losses-from-Thieberger-Brookhaven/b0665d30bbe936450d46cc0f938392a885421101

[Thi06] Thiolliere N, C David J, Blideanu V, Doré D, Rapp B, Ridikas D. Optimization of 6 He production using W or Ta converter surrounded by BeO target assembly [Internet]. Gif-sur-Yvette, France: CAE Saclay; 2006 Oct. Available from: https://www.researchgate.net/publication/268004396_Optimization_of_6_He_ production_using_W_or_Ta_converter_surrounded_by_BeO_target_assembly

[Tou77] Touloukian Y.S., Kirby R.K., Taylor E.R., Lee T.Y.R. Thermophysical Properties of Matter - the TPRC Data Series. Volume 13. Thermal Expansion - Nonmetallic Solids. Thermophysical and Electronic Properties Information Center: Purdue University; 1977 p. 1689. Report No.: AD-A-129116/0/XAB.

[TRI18] TRIUMF. ISAC Yield Database | TRIUMF : Canada's National Laboratory for Particle and Nuclear Physics [Internet]. ISAC Yield Database. 2018 [cited 2019 Jan 16]. Available from: https://mis.triumf.ca/science/planning/yield/beam

[Van06] Van Duppen P. Isotope Separation On Line and Post Acceleration. In: Al-Khalili J, Roeckl E, editors. The Euroschool Lectures on Physics with Exotic Beams, Vol II [Internet]. Berlin, Heidelberg: Springer Berlin Heidelberg; 2006 [cited 2019 May 19]. p. 37–77. (Lecture Notes in Physics; vol. 2). Available from: https://doi.org/10.1007/3-540-33787-3_2

[Vas58] Vasilev SS, Komarov VV, Popova AM. An Investigation of (N,ALPHA) and (N,T) Reactions on BE-9. Доклады Академии наук. 1958; 119(5):914–7.

[Won98] Wong SSM. Introductory nuclear physics. 2nd ed. New York: J. Wiley; 1998. 460 p.

[Woo85] Wood C, Zoltan A, Emin D, Gray PE. Thermal Conductivity Behavior of Boron Carbides. In: Ashworth T, Smith DR, editors. Thermal Conductivity 18 [Internet]. Boston, MA: Springer US; 1985 [cited 2019 May 19]. p. 139–48. Available from: https://doi.org/10.1007/978-1-4684-4916-7_15

[Wür16] Würl M. Towards Offline PET Monitoring at a Cyclotron-Based Proton Therapy Facility Experiments and Monte Carlo Simulations [Internet]. Wiesbaden: Springer Fachmedien Wiesbaden, Imprint: Springer Spektrum; 2016 [cited 2019 May 19]. Available from: https://doi.org/10.1007/978-3-658-13168-5

[XRD17] XRD Graphite. Iso-Molded Graphite Suppliers_XRD Graphite Manufacturing Co.,Ltd [Internet]. ISO-Molded Graphite. 2017 [cited 2017 Nov 12]. Available from: http://www.xrdcarbon.com/materials/iso-molded_graphite/

[Yos16] Yost DC, Kanai Y. Electronic stopping for protons and α particles from first-principles electron dynamics: The case of silicon carbide. Phys Rev B. 2016 Sep 6; 94(11):115107.

[Zha01] Zhang Y, Liu Y, Bhowmick D, Alton GD. Design and characterization of high power targets for RIB generation. In: PACS2001 Proceedings of the 2001 Particle Accelerator Conference (Cat No01CH37268) [Internet]. Chicago, IL, USA: IEEE; 2001 [cited 2019 May 19]. p. 1607–9. Available from: http://ieeexplore.ieee.org/document/986763/

[Zie10] Ziegler JF, Ziegler MD, Biersack JP. SRIM – The stopping and range of ions in matter (2010). Nuclear Instruments and Methods in Physics Research Section B: Beam Interactions with Materials and Atoms. 2010 Jun; 268(11–12):1818–23.

APPENDIX A: FLUKA SIMULATION CODE (15 DISCS B_4C TARGET)

```
* ..+....1....+....2....+....3....+....4....+....5....+....6....+...
.7..
TITLE
FLUKA Simulation of optimised 15 disk B4C target
* Energy threshold for protons, otherwise they stop too early
PART-THR      -1.E-5    PROTON                             0.0
PHYSICS           3.
* Evaporation with heavy fragmentation must be activated in order to
score residual nuclides
EVAPORAT
* The radiation decay is set to "active". In order to change this
option you can work on this card.
RADDECAY          2.       -1.                 0.0         0
1.
* Define the beam characteristics
BEAM           -0.07                        -1.175    -1.175
1.PROTON
* Define the beam position
BEAMPOS           1.       0.0     -150.
GEOBEGIN
COMBNAME
    0    0
SPH void       0.0 0.0 0.0 100.
SPH void1      0.0 0.0 0.0 300.
* Black body
SPH blkbody    0.0 0.0 0.0 3000.
ZCC tantaout   0.0 0.0 2.5
ZCC tantain    0.0 0.0 2.48
ZCC boxout     0.0 0.0 2.45
ZCC boxin      0.0 0.0 2.25
XYP z0         0.0
XYP zbi        -149.
XYP zbf        -148.
ZCC beamout    0.0 0.0 50.
XYP fine_h     19.6
XYP fine_b     23.
XYP w1_i       1.
XYP w1_f       1.02
XYP w2_i       1.12
XYP w2_f       1.14
ZCC screenin   0.0 0.0 1.125
XYP s1i        1.31
XYP s1f        1.34
ZCC discs      0.0 0.0 2.
XYP di1        1.39
XYP di2        2.49
XYP di3        3.59
XYP di4        4.69
XYP di5        5.89
XYP di6        7.09
```

```
XYP di7        8.29
XYP di8        9.59
XYP di9        10.89
XYP di10       12.29
XYP di11       138.9
XYP di12       15.49
XYP di13       16.89
XYP di14       18.29
XYP di15       195.9
XYP df1        1.48
XYP df2        2.58
XYP df3        3.68
XYP df4        4.78
XYP df5        5.98
XYP df6        7.18
XYP df7        8.38
XYP df8        9.68
XYP df9        10.98
XYP df10       12.38
XYP df11       13.98
XYP df12       15.58
XYP df13       16.98
XYP df14       18.38
XYP df15       19.68
XYP s2i        19.77
XYP s2f        19.87
XYP disti      19.87
XYP distf      20.77
ZCC distin     0.0 0.0 2.1
XYP dumpi1     20.77
XYP dumpi2     21.47
XYP dumpi3     22.02
XYP dumpi4     22.67
XYP dumpf1     20.85
XYP dumpf2     21.55
XYP dumpf3     22.10
XYP dumpf4     25.67
ZCC dumpin     0.0 0.0 1.8
ZCC dumpcc1    0.0 0.0 1.2
ZCC dumpcc2    0.0 0.0 2.5
!@what.1=25.67+6.187
XYP dumpcp1    31.857
!@what.1=25.67+6.187+3
XYP dumpcp2    34.857
!@what.1=25.67+6.187+4
XYP dumpcp3    35.857
XZP guat1      15.6
XZP guat2      15.8
YCC guain1     10. 0.0 0.7
YCC guaout1    10. 0.0 1.
XYP zwf1       0.3
XZP wingyf     -6.4
!@what.3=5.7/2
ZCC rmaxris    0.0 0.0 2.85
YZP wingi      2.
YZP winge      -2.
```

```
XZP y0         0.0
XYP zwi2       19.2
XYP zwf2       19.45
XYP clai1      -0.95
XYP claf1      0.0
XYP clai2      .3
!@what.1=-0.95+2.3
XYP claf2      1.3499999999999999
YZP clxi       +6.5
!@what.1=+6.5-9.35
YZP clxf       -2.8499999999999996
YCC punte1     0.2 4.5 0.9
XZP clzi       -4.5
XZP clzf       -7.
XYP clpi1      17.95
!@what.1=17.95+1.25
XYP clpf1      19.2
!@what.1=17.95+1.5
XYP clpi2      19.45
!@what.1=17.95+2.6
XYP clpf2      20.55
YCC punte2     19.325 4.5 0.9
YCC punti1     0.2 4.5 0.55
YCC punti2     19.325 4.5 0.55
XZP puntiy     -3.5
XZP puntfy     -17.43
XZP basei      -9.5
XZP basef      -13.
YCC rbase      10. 0.0 18.
YCC dciy       10. 0.0 16.
YCC dcey       10. 0.0 18.
ZCC dcpi       0.0 0.0 3.
ZCC dcpe       0.0 0.0 3.5
XYP canpi      -148.
ZCC dcpci      0.0 0.0 27.5
ZCC dcpce      0.0 0.0 3.
XYP zcanpc1    35.947
XYP zcanpc2    37.697
XZP ytestai    13.35
ZCC dflangia   0.0 0.0 5.675
XZP testaf     16.1
YCC dtesta     10. 0.0 19.5
* FINE BODIES
XYP FINE_GEO   0.0
END
* Black hole
BLKBODY      5 |+blkbody -void1
               |+beamout-discs+zbf-zbi
* Tantalium region
TANTA        5 |+fine_h -z0 +tantaout -tantain
* Box
BOX          5 |+fine_b -z0 +boxout -boxin
* Window1
WIN1         5 |+w1_f -w1_i +boxin
* Window2
WIN2         5 |+w2_f -w2_i +boxin
```

```
* Screen1
SCREEN1       5 |+s1f -s1i +boxin-screenin
* DISC1
DISCTOT       5 |+df1-di1+discs
                |+df2-di2+discs
                |+df3-di3+discs
                |+df4-di4+discs
                |+df5-di5+discs
                |+df6-di6+discs
                |+df7-di7+discs
                |+df8-di8+discs
                |+df9-di9+discs
                |+df10-di10+discs
                |+df11-di11+discs
                |+df12-di12+discs
                |+df13-di13+discs
                |+df14-di14+discs
                |+df15-di15+discs
#if 0
* DISC1
DISC1         5 |+df1-di1+discs
#endif
#if 0
* DISC2
DISC2         5 |+df2-di2+discs
#endif
#if 0
* DISC3
DISC3         5 |+df3-di3+discs
#endif
#if 0
* DISC4
DISC4         5 |+df4-di4+discs
#endif
#if 0
* DISC5
DISC5         5 |+df5-di5+discs
#endif
#if 0
* DISC6
DISC6         5 |+df6-di6+discs
#endif
#if 0
* DISC7
DISC7         5 |+df7-di7+discs
#endif
#if 0
* DISC8
DISC8         5 |+df8-di8+discs
#endif
#if 0
* DISC9
DISC9         5 |+df9-di9+discs
#endif
#if 0
* DISC10
```

```
DISC10       5 |+df10-di10+discs
#endif
#if 0
* DISC11
DISC11       5 |+df11-di11+discs
#endif
#if 0
* DISC12
DISC12       5 |+df12-di12+discs
#endif
#if 0
* DISC13
DISC13       5 |+df13-di13+discs
#endif
#if 0
* DISC14
DISC14       5 |+df14-di14+discs
#endif
#if 0
* DISC15
DISC15       5 |+df15-di15+discs
#endif
* Screen2
SCREEN2      5 |+s2f -s2i +boxin-screenin
* Distanziatore
DISTA        5 |+distf -disti +boxin -distin
* Dump1
DUMP1        5 |+dumpf1 -dumpi1 +dumpin
               |+dumpi2 -dumpi1 +boxin -dumpin
* Dump2
DUMP2        5 |+dumpf2 -dumpi2 +dumpin
               |+dumpi3 -dumpi2 +boxin -dumpin
* Dump3
DUMP3        5 |+dumpf3 -dumpi3 +dumpin
               |+dumpi4 -dumpi3 +boxin -dumpin
* Dump4
DUMP4        5 |+dumpf4 -dumpi4 +boxin
DUMPCAM      5 |+dumpcp2 -dumpcp1 +dumpcc2
               |+dumpcp3 -dumpcp2 +dumpcc1
* Guarnizione Teflon
GUATE        5 |+guat2-guat1-guain1+guaout1
Voidext      5 +void1 +zbi -void
               | +void1 +canpi -zbi -beamout
               | +void1 -void -dcpe -zbf
               | +void1 +dcpe -void-z0
#if 0
Void         5 +void +zbi
               | +void -zbi +zbf -beamout
               | +void -zbi +zbf +discs
               | +void +z0 -zbf
               | +void +fine_h -z0 -tantaout +guat1
               | +void +fine_h -z0 -guat2
               | +guat2-guat1+guain1
               | +void +fine_h -z0 +guat2-guat1-guaout1
               | +void +fine_h -z0 +tantain -boxout
               | +boxin -z0 +w1_i
```

```
               | +boxin -w1_f +w2_i
               | +boxin +s1i -w2_f
               | +screenin +s1f -s1i
               | +boxin +di1 -s1f
               | +boxin -di1 +s2i -discs
               | di2 -df1 +discs
               | di2 -df1 +discs
               | di3 -df2 +discs
               | di4 -df3 +discs
               | di5 -df4 +discs
               | di6 -df5 +discs
               | di7 -df6 +discs
               | di8 -df7 +discs
               | di9 -df8 +discs
               | di10 -df9 +discs
               | di11 -df10 +discs
               | di12 -df11 +discs
               | di13 -df12 +discs
               | di14 -df13 +discs
               | di15 -df14 +discs
               | s2i -df15 +discs
               | +screenin +s2f -s2i
               | +distf -disti +distin
               | +dumpi2 -dumpf1 +dumpin
               | +dumpi3 -dumpf2 +dumpin
               | +dumpi4 -dumpf3 +dumpin
               | +void -fine_h +fine_b -boxout
               | +void +dumpcp1 -fine_b
               | +void +dumpcp2 -dumpcp1 -dumpcc2
               | +void +dumpcp3 -dumpcp2 -dumpcc1
               | +void -dumpcp3
#endif
#if 0
Void_BACKUP   5 |+void-(beamout-discs+zbf-zbi)-(+fine_h -z0
+tantaout -tantain)-(+fine_b -z0 +boxout -boxin)
               -(+fine_b -z0 +boxout -boxin)-(+w1_f -w1_i +boxin)-
(+w2_f -w2_i +boxin)-( +s1f -s1i +boxin-screenin)
               -(+df1-di1+discs)-(+df2-di2+discs)-(+df3-di3+discs) -
(+df4-di4+discs)-(+df5-di5+discs)
               -(+df6-di6+discs)-(+df7-di7+discs)-(+df8-di8+discs)-
(+df9-di9+discs)-(+df10-di10+discs)
               -(+df11-di11+discs)-(+df12-di12+discs)-(+df13-
di13+discs)-(+df14-di14+discs)-(+df15-di15+discs)
               -( +s2f -s2i +boxin-screenin)-( +distf -disti +boxin
-distin)
               -( |+dumpf1 -dumpi1 +dumpin |+dumpi2 -dumpi1 +boxin -
dumpin)
               -( |+dumpf2 -dumpi2 +dumpin |+dumpi3 -dumpi2 +boxin -
dumpin)
               -( |+dumpf3 -dumpi3 +dumpin |+dumpi4 -dumpi3 +boxin -
dumpin)
               -(+dumpf4 -dumpi4 +boxin)
               -(|+dumpcp2 -dumpcp1 +dumpcc2 |+dumpcp3 -dumpcp2
+dumpcc1)
               -(+guat2-guat1-guain1+guaout1)
#endif
```

```
#if 0
Void_prova   5 |+void-(beamout-discs+zbf-zbi)-(+fine_h -z0 +tantaout
-tantain)-(+fine_b -z0 +boxout -boxin)
               -(+fine_b -z0 +boxout -boxin)-(+w1_f -w1_i +boxin)-
(+w2_f -w2_i +boxin)-( +s1f -s1i +boxin-screenin)
               -(+df1-di1+discs)-(+df2-di2+discs)-(+df3-di3+discs) -
(+df4-di4+discs)-(+df5-di5+discs)
               -(+df6-di6+discs)-(+df7-di7+discs)-(+df8-di8+discs)-
(+df9-di9+discs)-(+df10-di10+discs)
               -(+df11-di11+discs)-(+df12-di12+discs)-(+df13-
di13+discs)-(+df14-di14+discs)-(+df15-di15+discs)
               -( +s2f -s2i +boxin-screenin)-( +distf -disti +boxin
-distin)
               -( |+dumpf1 -dumpi1 +dumpin |+dumpi2 -dumpi1 +boxin -
dumpin)
               -( |+dumpf2 -dumpi2 +dumpin |+dumpi3 -dumpi2 +boxin -
dumpin)
               -( |+dumpf3 -dumpi3 +dumpin |+dumpi4 -dumpi3 +boxin -
dumpin)
               -(+dumpf4 -dumpi4 +boxin)
#endif
wing1        5 +zwf1 +rmaxris -tantaout -z0
               | +zwf1 +wingi -z0 -rmaxris -winge -wingyf +y0
wing2        5 +zwf2 +rmaxris -tantaout -zwi2
               | +zwf2 -wingyf +wingi -rmaxris -winge +y0 -zwi2
clampa1      5 +clxi -clai1 +claf1 -clxf -punte1 +clzi -clzf
clampa2      5 +claf2 +clxi +clzi -clai2 -clxf -punte1 -clzf
clampp1      5 +clxi +clzi +clpf1 -clxf -clzf -clpi1 -punte2
clampp2      5 +clxi +clzi +clpf2 -clxf -clzf -clpi2 -punte2
puntale1     5 +punte1 +puntiy -puntfy
puntale2     5 +punte2 +puntiy -puntfy
Base_cam     5 +basei +rbase -basef -punte1 -punte2
cilindro     5 +dcey +ytestai -dciy -dcpe -basei
               | +dflangia +zcanpc2 -zcanpc1
               | +dcpe +zcanpc1 -dciy -dcpi-z0
               | +dcey +dcpe -dciy -dcpce
canprot      5 +dcpe -dcey -dcpi -canpi +z0
testa        5 +testaf +dtesta -guaout1 -ytestai
               | +guat1 +guaout1 -guain1 -ytestai
ARIA         5 +void -dflangia -dtesta
               | +void +dtesta -testaf
               | +void +basef +dtesta -punte1 -punte2
               | +void +dflangia -dcpe -dtesta +zcanpc1
               | +ytestai +dtesta -basef -rbase -dcpe
               | +void +dflangia -zcanpc2
               | +guaout1 +testaf -guat2
               | +void +punte1 +puntfy
               | +void +puntfy +punte2
#if 0
void         5 +zbf +discs -zbi
               | +dcpi -zbf -dciy +z0
               | +clai1 +dciy +ytestai -basei
               | +dciy +ytestai -clai1 -clxi -basei
               | +clzf +dciy -zbf -clai1 -basei -dcpi -punte1 -
punte2
```

```
               | +z0 +clxi +clpf2 +dciy +ytestai -zbf -rmaxris -
clai1 -punte1 -clzi -clzf -punte2 -basei -dcpi
               | +wingyf +zwf2 +clxi -s2f -clxf -clzf -punte2
               | +zwf1 +clxi +clzi -z0 -wingi -punte1 -clzf
               | +zwf1 +wingi +winge +clxi +clzi -z0 -clxf -punte1 -
clzf
               | +zwf2 +clxi +ytestai -s2f -wingyf -rmaxris -wingi -
clzf -punte2
               | +winge +zwf2 +clzi -s2f -clxf -clzf
               | +punte1 +ytestai -puntiy
               | +punte2 -puntiy +ytestai
               | +clxf +clzi +dciy -clzf
               | +z0 +dcpi -clai1
               | +clxi +clzi +clpi1 -claf2 -clxf -clzf
               | +clxi +clpf2 -rmaxris -wingi -clai1 -punte1 -punte2
-clzi +ytestai
               | +zwf1 +wingyf +clxi -z0 -clxf -punte1 -clzf
               | +winge +dciy +ytestai -rmaxris -clzi -z0
               | +boxin +w1_i -z0
               | +tantain +fine_b -boxout -z0
               | +s2f +rmaxris -tantaout -zwf1
               | +wingi +dciy +ytestai -z0 -rmaxris -winge -y0
               | +s2f +wingi -zwf1 -rmaxris -winge -clzi +ytestai
               | +boxin +w2_i -w1_f
               | +boxin +s1i -w2_f
               | +screenin +s1f -s1i
               | +boxin +di1 -s1f
               | +boxin +s2i -discs -di1
               | +discs +di2 -df1
               | +discs +di3 -df2
               | +discs +di4 -df3
               | +discs +di5 -df4
               | +discs +di6 -df5
               | +discs +di7 -df6
               | +discs +di8 -df7
               | +discs +di9 -df8
               | +discs +di10 -df9
               | +discs +di11 -df10
               | +discs +di12 -df11
               | +discs +di13 -df12
               | +discs +di14 -df13
               | +discs +di15 -df14
               | +discs +s2i -df15
               | +screenin +s2f -s2i
               | +distf +distin -s2f
               | +dumpi2 +dumpin -dumpf1
               | +dumpi3 +dumpin -dumpf2
               | +dumpi4 +dumpin -dumpf3
               | +clxi +dciy -s2f -wingyf -rmaxris -winge -zwf2 -
clzi -clzf -punte2 +ytestai
               | +rmaxris +dciy -tantaout -zwf2
               | +tantaout +fine_b -tantain -fine_h
               | +tantaout +dciy -fine_b
               | +clxi +clzi +dciy -clxf -clzf -clpf2
               | +dumpcp1 +dcpi -dciy -zbf
               | +dcpi +zcanpc1 -tantaout -dumpcp1
```

```
               | +tantaout +zcanpc1 -dumpcc1 -dumpcp2
               | +dumpcc1 +zcanpc1 -dumpcp3
               | +guat2 +guain1 -ytestai
#endif
void1        5 +zbf +discs -zbi
               | +dcpi -zbf -dciy +z0
               | +clai1 +dciy +ytestai -basei
               | +dciy +ytestai -clai1 -clxi -basei
               | +clzf +dciy -zbf -clai1 -basei -dcpi -punte1 -
punte2
               | +z0 +clxi +clpf2 +dciy +ytestai -zbf -rmaxris -
clai1 -punte1 -clzi -clzf -punte2 -basei -dcpi
               | +wingyf +zwf2 +clxi -s2f -clxf -clzf -punte2
               | +zwf1 +clxi +clzi -z0 -wingi -punte1 -clzf
               | +zwf1 +wingi +winge +clxi +clzi -z0 -clxf -punte1 -
clzf
               | +zwf2 +clxi +ytestai -s2f -wingyf -rmaxris -wingi -
clzf -punte2
               | +winge +zwf2 +clzi -s2f -clxf -clzf
               | +punte1 +ytestai -puntiy
               | +punte2 -puntiy +ytestai
               | +clxf +clzi +dciy -clzf
               | +z0 +dcpi -clai1
               | +clxi +clzi +clpi1 -claf2 -clxf -clzf
               | +clxi +zwf2 -rmaxris -wingi -clai1 -punte1 -punte2
-clzi +ytestai
               | +zwf1 +wingyf +clxi -z0 -clxf -punte1 -clzf
               | +winge +dciy +ytestai -rmaxris -clzi -z0
               | +boxin +w1_i -z0
               | +tantain +fine_b -boxout -z0
               | +s2f +rmaxris -tantaout -zwf1
               | +wingi +zwf2 +dciy +ytestai -z0 -rmaxris -winge -y0
               | +s2f +wingi +y0 -zwf1 -rmaxris -winge -clzi
void2        5 +boxin +w2_i -w1_f
               | +boxin +s1i -w2_f
               | +screenin +s1f -s1i
               | +boxin +di1 -s1f
               | +boxin +s2i -discs -di1
               | +discs +di2 -df1
               | +discs +di3 -df2
               | +discs +di4 -df3
               | +discs +di5 -df4
               | +discs +di6 -df5
               | +discs +di7 -df6
               | +discs +di8 -df7
               | +discs +di9 -df8
               | +discs +di10 -df9
               | +discs +di11 -df10
               | +discs +di12 -df11
               | +discs +di13 -df12
               | +discs +di14 -df13
               | +discs +di15 -df14
               | +discs +s2i -df15
               | +screenin +s2f -s2i
               | +distf +distin -s2f
               | +dumpi2 +dumpin -dumpf1
```

```
               | +dumpi3 +dumpin -dumpf2
               | +dumpi4 +dumpin -dumpf3
               | +clxi +dciy -s2f -wingyf -rmaxris -winge -zwf2 -
clzi -clzf -punte2 +ytestai
               | +rmaxris +dciy -tantaout -zwf2
               | +tantaout +fine_b -tantain -fine_h
               | +tantaout +dciy -fine_b
               | +clxi +clzi +dciy -clxf -clzf -clpf2
               | +dcpi +zcanpc1 -tantaout -dumpcp1
               | +tantaout +zcanpc1 -dumpcc1 -dumpcp2
               | +dumpcc1 +zcanpc1 -dumpcp3
               | +guat2 +guain1 -ytestai
               | +dumpcp1 +dcpi -dciy -z0
END
GEOEND           20.       20.       30.      -20.      -20.        -
10.DEBUG
GEOEND           10.       10.       20.
&
MATERIAL                             4.2
UC4
MATERIAL                            3.05
SiC
MATERIAL          6.    12.011      1.76
GRAPHITE
MATERIAL         92.  238.0289     18.95
238.URANIUM
MATERIAL         14.   28.0855      2.33
SI
COMPOUND          1.   URANIUM        4.    CARBON
UC4
COMPOUND          1.        SI        1.    CARBON
SiC
MATERIAL          9.            0.001696
FLUORINE
MATERIAL         29.    63.548    8.9659
COPPER
* Teflon
* Chemical              F    F
* Formula               |    |
*                  ---- C -- C ----
*                       |    |
*                       F    F
MATERIAL                             2.2
Teflon
COMPOUND          2.    CARBON        4.  FLUORINE
Teflon
MATERIAL         13.              2.6989
ALUMINUM
MATERIAL          5.                2.34
BORON
* Boron carbide B4_C
*
MATERIAL                            2.52
B4C
COMPOUND    -0.78261     BORON  -0.21739    CARBON
B4C
```

```
ASSIGNMA    BLCKHOLE   BLKBODY
ASSIGNMA      VACUUM   Voidext
ASSIGNMA    TANTALUM     TANTA
ASSIGNMA      COPPER  puntale1
ASSIGNMA      COPPER  puntale2
ASSIGNMA      COPPER   clampa1
ASSIGNMA      COPPER   clampp1
ASSIGNMA      COPPER   clampa2
ASSIGNMA      COPPER   clampp2
ASSIGNMA         B4C   DISCTOT
ASSIGNMA    GRAPHITE       BOX   SCREEN1
ASSIGNMA    GRAPHITE   SCREEN2   DUMPCAM
ASSIGNMA      Teflon     GUATE
ASSIGNMA    TANTALUM     wing1
ASSIGNMA    TANTALUM     wing2
ASSIGNMA    ALUMINUM  Base_cam
ASSIGNMA    ALUMINUM  cilindro
ASSIGNMA    ALUMINUM   canprot
ASSIGNMA    ALUMINUM     testa
ASSIGNMA         AIR      ARIA
ASSIGNMA      VACUUM     void1
ASSIGNMA      VACUUM     void2
LOW-MAT      URANIUM       92.      238.      296.
238-U
LOW-MAT     GRAPHITE        6.       -3.      296.
CARBON
LOW-MAT           SI       14.       -2.      296.
SILICON
*USRBIN           11.    ENERGY      -21.       2.5       0.0
5.5TANTA
*USRBIN          2.48       0.0     -11.4        1.       64.
169. &
USRBIN           11.    ENERGY      -21.      2.45       0.0
23.BOX
USRBIN          2.25       0.0       0.0        1.       64.
230. &
USRBIN           11.    ENERGY      -21.      2.25       0.0
1.02WIN1
USRBIN           0.0       0.0        1.      225.       64.
1. &
USRBIN           11.    ENERGY      -21.      2.25       0.0
1.14WIN2
USRBIN           0.0       0.0      1.12      225.       64.
1. &
USRBIN           11.    ENERGY      -21.      2.25       0.0
1.34SCREEN1
USRBIN          1.12       0.0      1.31      113.       64.
1. &
USRBIN           11.    ENERGY      -21.        2.       0.0
1.48DISC1
USRBIN           0.0       0.0      1.39      200.       64.
1. &
USRBIN           11.    ENERGY      -21.        2.       0.0
2.68DISC2
USRBIN           0.0       0.0      2.59      200.       64.
1. &
```

```
USRBIN           11.    ENERGY      -21.        2.       0.0
3.88DISC3
USRBIN           0.0       0.0      3.79      200.       64.
1. &
USRBIN           11.    ENERGY      -21.        2.       0.0
5.08DISC4
USRBIN           0.0       0.0      4.99      200.       64.
1. &
USRBIN           11.    ENERGY      -21.        2.       0.0
6.38DISC5
USRBIN           0.0       0.0      6.29      200.       64.
1. &
USRBIN           11.    ENERGY      -21.        2.       0.0
7.68DISC6
USRBIN           0.0       0.0      7.59      200.       64.
1. &
USRBIN           11.    ENERGY      -21.        2.       0.0
8.98DISC7
USRBIN           0.0       0.0      8.89      200.       64.
1. &
USRBIN           11.    ENERGY      -21.        2.       0.0
10.33DISC8
USRBIN           0.0       0.0     10.24      200.       64.
1. &
USRBIN           11.    ENERGY      -21.        2.       0.0
11.83DISC9
USRBIN           0.0       0.0     11.74      200.       64.
1. &
USRBIN           11.    ENERGY      -21.        2.       0.0
13.23DISC10
USRBIN           0.0       0.0     13.14      200.       64.
1. &
USRBIN           11.    ENERGY      -21.        2.       0.0
14.53DISC11
USRBIN           0.0       0.0     14.44      200.       64.
1. &
USRBIN           11.    ENERGY      -21.        2.       0.0
15.73DISC12
USRBIN           0.0       0.0     15.64      200.       64.
1. &
USRBIN           11.    ENERGY      -21.        2.       0.0
16.83DISC13
USRBIN           0.0       0.0     16.74      200.       64.
1. &
USRBIN           11.    ENERGY      -21.        2.       0.0
17.93DISC14
USRBIN           0.0       0.0     17.84      200.       64.
1. &
USRBIN           11.    ENERGY      -21.        2.       0.0
19.03DISC15
USRBIN           0.0       0.0     18.94      200.       64.
1. &
USRBIN           11.    ENERGY      -21.      2.25       0.0
19.2SCREEN2
USRBIN          1.12       0.0      19.1      113.       64.
1. &
```

```
USRBIN           11.    ENERGY      -21.      2.25       0.0
20.1DISTA
USRBIN           2.1       0.0      19.2        1.       64.
90. &
*USRBIN           11.    ENERGY      -21.      22.5       0.0
23.EXT_DUMP
*USRBIN           1.8       0.0      20.1        1.       64.
90. &
USRBIN           11.    ENERGY      -21.       1.8       0.0
20.2DUMP1
USRBIN           0.0       0.0      20.1      180.       64.
1. &
USRBIN           11.    ENERGY      -21.       1.8       0.0
20.9DUMP2
USRBIN           0.0       0.0      20.8      180.       64.
1. &
USRBIN           11.    ENERGY      -21.       1.8       0.0
21.45DUMP3
USRBIN           0.0       0.0     21.35      180.       64.
1. &
USRBIN           11.    ENERGY      -21.       1.8       0.0
23.DUMP4
USRBIN           0.0       0.0       22.      180.       64.
1. &
*USRBIN           11.    PROTON      -21.       2.5       0.0
32.187DUMPCAM_F
*USRBIN           0.0       0.0    29.187        5.        1.
1. &
*USRBIN           11.    PROTON      -22.        5.       0.0
25.DUMPCAM1
*USRBIN           0.0       0.0       -5.      100.        1.
300. &
RESNUCLE          3.      -23.                       DISCTOT
ISOT_PRO
USRBIN           11.   NEUTRON      -27.        5.       0.0
25.N_DIST
USRBIN           0.0       0.0       -5.      500.        1.
600. &
USRBIN           11.    PROTON      -28.        5.       0.0
25.P_DIST
USRBIN           0.0       0.0       -5.      500.        1.
600. &
USRBDX           11.   NEUTRON      -24.      ARIA   Voidext
NEUTRON_Y1
USRBDX           70.       0.0       70.
&
USRBDX           11.   NEUTRON      -24.     void1   Voidext
NEUTRON_Y2
USRBDX           70.       0.0       70.
&
*USRBIN           10.    DOSE-EQ     -25.       0.5       0.5
400.N_EN_DOSE
*USRBIN          -0.5      -0.5     -400.        1.        1.
800. &
*USRBIN           10.    DOSE-EQ     -25.      400.      400.
400.G_EN_DOSE
```

```
*USRBIN         -400.     -400.     -400.      100.      100.
100. &
*AUXSCORE      USRBIN   NEUTRON           N_EN_DOSE
*AUXSCORE      USRBIN    PHOTON           G_EN_DOSE
*USRBIN           12.      DOSE      -26.
N_DAMAGE
*USRBIN         GUATE
&
*USRBIN           12.      DOSE      -26.
G_DAMAGE
*USRBIN         GUATE
&
*AUXSCORE      USRBIN   NEUTRON            N_DAMAGE
*AUXSCORE      USRBIN    PHOTON            G_DAMAGE
* Set the random number seed
RANDOMIZ          1.1418926680
* Set the number of primary histories to be simulated in the run (>=
1E8 primaries recommended in order to reduce % error)
START            5E8                                     0.0
STOP
```

APPENDIX B: ANSYS ADPL CODE (CONFIGURATION 6)

```
FINISH
/CONFIG,NRES,1000000
/PREP7

ET,1,SOLID70
ET,2,SHELL131
ET,11,SOLID70

pi=3.141592653589793

!---Material properties---
M26Ta.mac
M27W.mac
M28Cu.mac
M29C_ATJ.mac
M23Al5083_X.mac
M32B4C.mac

!PARAMETERS FOR GEOMETRY DEFINITION

!HEATER
ng_h=100
!Geometry
z_h=0
re_heater=50/2
t_heater=0.2
ri_heater=re_heater-t_heater

l_heater=202.7                          !Extended
V_heater=(pi*(re_heater*re_heater-ri_heater*ri_heater)*l_heater)/1e9
!Mesh
n_h_r=1
n_h_c=4
n_h_l=50

!BOX
ng_b=900                                !MUST BE AT LEAST 100 IN THE NUMBER OF FIRST DISC
!Geometry
d_h_b=0
z_b=z_h+d_h_b
to=0.1
re_box=ri_heater-to
```

```
t_box=1
                                        !ri_box=re_box-t_box
ri_box=45/2
l_box=l_heater-d_h_b
V_box=(pi*(re_box*re_box-ri_box*ri_box)*l_box)/1e9
!mesh
n_b_r=2
n_b_c=4
n_b_l=6                                 !The number of the first part only
n_b_ld=4                                !number of divisions between two discs

!DUMP_BOX
ng_dumpbox=300
!geometry
d_b_dumpbox=0
z_dumpbox=z_b+l_box+d_b_dumpbox
re_dumpbox=ri_heater-to

ri_dumpbox=42/2

l_dumpbox=54                            !Extended dumpbox to accomodate 30mm Dump4
V_dumpbox=(pi*(re_dumpbox*re_dumpbox-ri_dumpbox*ri_dumpbox)*l_dumpbox)/1e9
!mesh
n_dumpbox_r=2
n_dumpbox_c=4
n_dumpbox_l=10

!WINDOW1
ng_w1=400
!geometry
d_b_w1=10
z_w1=d_b_w1+z_b
re_w1=ri_box-to
l_w1=0.2
V_w1=(pi*(re_w1**2)*l_w1)/1e9
!mesh
n_w1_re=4
n_w1_c=4
n_w1_l=4

lqi=re_w1/2          !SIDE OF SQUARE INSIDE THE CYRCLE TO IMPROVE MESH QUALITY AND DECREASE
ELEMENTS'NUMBER

!WINDOW2
ng_w2=500
```

```
!geometry
d_w2_w1=1
z_w2=z_w1+l_w1+d_w2_w1
re_w2=ri_box-to
l_w2=0.2
V_w2=(pi*(re_w2**2)*l_w2)/1e9
!mesh as WINDOW1

nddis=8

!factor for convergence of discs
nfatt_d=1
dnd=200
ddd=300

!DISK1
ng_d1=1000
ng_b1=ng_d1+dnd
!geometry
d_w2_d1=2.5
z_d1=z_w2+l_w2+d_w2_d1
!re_d1=ri_box-to
re_d1=40/2
l_d1=0.9
V_d=(pi*re_d1*re_d1*l_d1)/1e9
!mesh
n_d1_r=2*nfatt_d
n_d1_c=4*nfatt_d
n_d1_l=4*nfatt_d

!DISK2
ng_d2=ng_d1+ddd
ng_b2=ng_d2+dnd
!geometry as DISK1
d_d1_d2=11
z_d2=z_d1+d_d1_d2
!mesh as DISK1

!DISK3
ng_d3=ng_d2+ddd
ng_b3=ng_d3+dnd
!geometry as DISK1
d_d2_d3=11
z_d3=z_d2+d_d2_d3
!mesh as DISK1
```

```
!DISK4
ng_d4=ng_d3+ddd
ng_b4=ng_d4+dnd
!geometry as DISK1
d_d3_d4=11
z_d4=z_d3+d_d3_d4
!mesh as DISK1

!DISK5
ng_d5=ng_d4+ddd
ng_b5=ng_d5+dnd
!geometry as DISK1
d_d4_d5=12
z_d5=z_d4+d_d4_d5
!mesh as DISK1

!DISK6
ng_d6=ng_d5+ddd
ng_b6=ng_d6+dnd
!geometry as DISK1
d_d5_d6=12
z_d6=z_d5+d_d5_d6
!mesh as DISK1

!DISK7
ng_d7=ng_d6+ddd
ng_b7=ng_d7+dnd
!geometry as DISK1
d_d6_d7=12
z_d7=z_d6+d_d6_d7
!mesh as DISK1

!DISK8
ng_d8=ng_d7+ddd
ng_b8=ng_d8+dnd
!geometry as DISK1
!d_d7_d8=13
!z_d8=z_d7+l_d1+d_d7_d8
d_d7_d8=13.5
z_d8=z_d7+d_d7_d8
!mesh as DISK1

!DISK9
ng_d9=ng_d8+ddd
```

```
ng_b9=ng_d9+dnd
!geometry as DISK1
d_d8_d9=13
z_d9=z_d8+d_d8_d9
!mesh as DISK1

!DISK10
ng_d10=ng_d9+ddd
ng_b10=ng_d10+dnd
!geometry as DISK1
d_d9_d10=14
z_d10=z_d9+d_d9_d10
!mesh as DISK1

!DISK11
ng_d11=ng_d10+ddd
ng_b11=ng_d11+dnd
!geometry as DISK1
d_d10_d11=16
z_d11=z_d10+d_d10_d11
!mesh as DISK1

!DISK12
ng_d12=ng_d11+ddd
ng_b12=ng_d12+dnd
!geometry as DISK1
d_d11_d12=16
z_d12=z_d11+d_d11_d12
!mesh as DISK1

!DISK13
ng_d13=ng_d12+ddd
ng_b13=ng_d13+dnd
!geometry as DISK1
d_d12_d13=14
z_d13=z_d12+d_d12_d13
!mesh as DISK1

!DISK14
ng_d14=ng_d13+ddd
ng_b14=ng_d14+dnd
!geometry as DISK1
d_d13_d14=14
z_d14=z_d13+d_d13_d14
!mesh as DISK1
```

```
!DISK15
ng_d15=ng_d14+ddd
ng_b15=ng_d15+dnd
!geometry as DISK1
d_d14_d15=13
z_d15=z_d14+d_d14_d15
!mesh as DISK1

!DUMP1
ng_dump1=10000
!geometry
d_dumpbox_dump1=5
z_dump1=z_dumpbox+d_dumpbox_dump1
re_dump1=36/2
l_dump1=0.8
V_dump1=(pi*re_dump1*re_dump1*l_dump1)/1e9
!mesh
n_dump1_r=4
n_dump1_c=4
n_dump1_l=4
n_dump1_rf=2

re_fdump=45/2-to/2
lqd=re_dump1/2

ndisk=15          !NUMBER OF TARGET DISK

z_last_disk=z_d%ndisk%
d_d%ndisk%_d%(ndisk+1)%=z_dumpbox-Z_d%ndisk%+d_dumpbox_dump1
!d_d%ndisk%_d%(ndisk+1)%=z_dumpbox-Z_d%ndisk%-l_d1

!DUMP2
ng_dump2=ng_dump1+100
!geometry
d_dump1_dump2=6
z_dump2=z_dump1+l_dump1+d_dump1_dump2
re_dump2=re_dump1
l_dump2=0.8
V_dump2=(pi*re_dump2*re_dump2*l_dump2)/1e9
!mesh
n_dump2_r=4
n_dump2_c=4
n_dump2_l=4
n_dump2_rf=2
```

```
!DUMP3
ng_dump3=ng_dump1+200
!geometry
d_dump2_dump3=4.5
z_dump3=z_dump2+l_dump2+d_dump2_dump3
re_dump3=re_dump1
l_dump3=0.8
V_dump3=(pi*re_dump3*re_dump3*l_dump3)/1e9
!mesh
n_dump3_r=4
n_dump3_c=4
n_dump3_l=4
n_dump3_rf=2

!DUMP4 (FINAL)
ng_dump4=ng_dump1+300
!geometry
d_dumpboxf_dump4=3
!z_dump4=z_dump3+l_dump3+d_dump3_dump4
l_dump4=30
z_dump4=z_dumpbox+l_dumpbox-d_dumpboxf_dump4-l_dump4
re_dump4=re_dump1
V_dump4=(pi*(re_dump4**2)*l_dump4)/1e9
!mesh
n_dump4_r=4
n_dump4_c=4
n_dump4_l=7

ndump=4                              !NUMBER OF GRAPHITE DUMPS

!-------------------------------
!BEGINNING WITH SOLID COSTRUCION AND MESHING
!-------------------------------

!HEATER
!--------------

MAT,Ta

!geometry
NUMSTR,KP,ng_h
NUMSTR,LINE,ng_h
NUMSTR,AREA,ng_h
NUMSTR,VOLU,ng_h
```

```
K,ng_h,0,0,z_h
K,ng_h+1,ri_heater,0,z_h
K,ng_h+2,0,ri_heater,z_h
K,ng_h+3,-ri_heater,0,z_h
K,ng_h+4,0,-ri_heater,z_h
K,ng_h+5,re_heater,0,z_h
K,ng_h+6,0,re_heater,z_h
K,ng_h+7,-re_heater,0,z_h
K,ng_h+8,0,-re_heater,z_h

LARC,ng_h+1,ng_h+2,ng_h,ri_heater
LARC,ng_h+2,ng_h+3,ng_h,ri_heater
LARC,ng_h+3,ng_h+4,ng_h,ri_heater
LARC,ng_h+4,ng_h+1,ng_h,ri_heater
LARC,ng_h+5,ng_h+6,ng_h,re_heater
LARC,ng_h+6,ng_h+7,ng_h,re_heater
LARC,ng_h+7,ng_h+8,ng_h,re_heater
LARC,ng_h+8,ng_h+5,ng_h,re_heater

L,ng_h+1,ng_h+5
L,ng_h+2,ng_h+6
L,ng_h+3,ng_h+7
L,ng_h+4,ng_h+8

AL,ng_h,ng_h+8,ng_h+4,ng_h+9
AL,ng_h+1,ng_h+9,ng_h+5,ng_h+10
AL,ng_h+2,ng_h+10,ng_h+6,ng_h+11
AL,ng_h+3,ng_h+11,ng_h+7,ng_h+8

!meshing
LSEL,S,LINE,,ng_h,ng_h+3,1
LESIZE,ALL,,,n_h_c
ALLSEL,ALL
LSEL,S,LINE,,ng_h+8,ng_h+11,1
LESIZE,ALL,,,n_h_r
ALLSEL,ALL

MSHAPE,0,2D
MSHKEY,1
!TYPE,4
TYPE,2
AMESH,ng_h,ng_h+3,1

!TYPE,3
TYPE,1
```

```
EXTOPT,ACLEAR,1
EXTOPT,ESIZE,n_h_l
VEXT,ng_h,ng_h+3,1,,,l_heater

!BOX
!--------------

MAT,C_ATJ

!geometry
NUMSTR,KP,ng_b
NUMSTR,LINE,ng_b
NUMSTR,AREA,ng_b
NUMSTR,VOLU,ng_b

K,ng_b,0,0,z_b
K,ng_b+1,ri_box,0,z_b
K,ng_b+2,0,ri_box,z_b
K,ng_b+3,-ri_box,0,z_b
K,ng_b+4,0,-ri_box,z_b
K,ng_b+5,re_box,0,z_b
K,ng_b+6,0,re_box,z_b
K,ng_b+7,-re_box,0,z_b
K,ng_b+8,0,-re_box,z_b

LARC,ng_b+1,ng_b+2,ng_b,ri_box
LARC,ng_b+2,ng_b+3,ng_b,ri_box
LARC,ng_b+3,ng_b+4,ng_b,ri_box
LARC,ng_b+4,ng_b+1,ng_b,ri_box
LARC,ng_b+5,ng_b+6,ng_b,re_box
LARC,ng_b+6,ng_b+7,ng_b,re_box
LARC,ng_b+7,ng_b+8,ng_b,re_box
LARC,ng_b+8,ng_b+5,ng_b,re_box

L,ng_b+1,ng_b+5
L,ng_b+2,ng_b+6
L,ng_b+3,ng_b+7
L,ng_b+4,ng_b+8

AL,ng_b,ng_b+8,ng_b+4,ng_b+9
AL,ng_b+1,ng_b+9,ng_b+5,ng_b+10
AL,ng_b+2,ng_b+10,ng_b+6,ng_b+11
AL,ng_b+3,ng_b+11,ng_b+7,ng_b+8

!MESHING
```

```
LSEL,S,LINE,,ng_b,ng_b+3,1
LESIZE,ALL,,,n_h_c
ALLSEL,ALL
LSEL,S,LINE,,ng_b+8,ng_b+11,1
LESIZE,ALL,,,n_h_r
ALLSEL,ALL

MSHAPE,0,2D
MSHKEY,1
TYPE,2
AMESH,ng_b,ng_b+3,1

TYPE,1
EXTOPT,ACLEAR,1
EXTOPT,ESIZE,n_b_ld
!VEXT,ng_b,ng_b+3,1,,,l_box
l_p_box=d_b_w1+l_w1+d_w2_w1+l_w2+d_w2_d1
V_p_box=(pi*(re_box*re_box-ri_box*ri_box)*l_p_box)/1e9
VEXT,ng_b,ng_b+3,1,,,l_p_box

!WINDOW1
!--------------

MAT,C_ATJ

!geometry
NUMSTR,KP,ng_w1
NUMSTR,LINE,ng_w1
NUMSTR,AREA,ng_w1
NUMSTR,VOLU,ng_w1

K,ng_w1,0,0,z_w1
K,ng_w1+1,re_w1,0,z_w1
K,ng_w1+2,0,re_w1,z_w1
K,ng_w1+3,-re_w1,0,z_w1
K,ng_w1+4,0,-re_w1,z_w1
K,ng_w1+5,lqi,0,z_w1
K,ng_w1+6,0,lqi,z_w1
K,ng_w1+7,-lqi,0,z_w1
K,ng_w1+8,0,-lqi,z_w1

LARC,ng_w1+1,ng_w1+2,ng_w1,re_w1
LARC,ng_w1+2,ng_w1+3,ng_w1,re_w1
LARC,ng_w1+3,ng_w1+4,ng_w1,re_w1
LARC,ng_w1+4,ng_w1+1,ng_w1,re_w1
```

```
L,ng_w1+5,ng_w1+6
L,ng_w1+6,ng_w1+7
L,ng_w1+7,ng_w1+8
L,ng_w1+8,ng_w1+5

L,ng_w1+1,ng_w1+5
L,ng_w1+2,ng_w1+6
L,ng_w1+3,ng_w1+7
L,ng_w1+4,ng_w1+8

AL,ng_w1,ng_w1+8,ng_w1+4,ng_w1+9
AL,ng_w1+1,ng_w1+9,ng_w1+5,ng_w1+10
AL,ng_w1+2,ng_w1+10,ng_w1+6,ng_w1+11
AL,ng_w1+3,ng_w1+11,ng_w1+7,ng_w1+8
AL,ng_w1+4,ng_w1+5,ng_w1+6,ng_w1+7

!meshing
LSEL,S,LINE,,ng_w1,ng_w1+7,1
LESIZE,ALL,,,n_w1_c
ALLSEL,ALL
LSEL,S,LINE,,ng_w1+8,ng_w1+11,1
LESIZE,ALL,,,n_w1_re
ALLSEL,ALL

MSHAPE,0,2D
MSHKEY,1
TYPE,2
AMESH,ng_w1,ng_w1+4,1

TYPE,1
EXTOPT,ACLEAR,1
EXTOPT,ESIZE,n_w1_l
VEXT,ng_w1,ng_w1+4,1,,,l_w1


!WINDOW2
!--------------

MAT,C_ATJ

!geometry
NUMSTR,KP,ng_w2
NUMSTR,LINE,ng_w2
NUMSTR,AREA,ng_w2
NUMSTR,VOLU,ng_w2
```

```
K,ng_w2,0,0,z_w2
K,ng_w2+1,re_w2,0,z_w2
K,ng_w2+2,0,re_w2,z_w2
K,ng_w2+3,-re_w2,0,z_w2
K,ng_w2+4,0,-re_w2,z_w2
K,ng_w2+5,lqi,0,z_w2
K,ng_w2+6,0,lqi,z_w2
K,ng_w2+7,-lqi,0,z_w2
K,ng_w2+8,0,-lqi,z_w2

LARC,ng_w2+1,ng_w2+2,ng_w2,re_w2
LARC,ng_w2+2,ng_w2+3,ng_w2,re_w2
LARC,ng_w2+3,ng_w2+4,ng_w2,re_w2
LARC,ng_w2+4,ng_w2+1,ng_w2,re_w2
L,ng_w2+5,ng_w2+6
L,ng_w2+6,ng_w2+7
L,ng_w2+7,ng_w2+8
L,ng_w2+8,ng_w2+5

L,ng_w2+1,ng_w2+5
L,ng_w2+2,ng_w2+6
L,ng_w2+3,ng_w2+7
L,ng_w2+4,ng_w2+8

AL,ng_w2,ng_w2+8,ng_w2+4,ng_w2+9
AL,ng_w2+1,ng_w2+9,ng_w2+5,ng_w2+10
AL,ng_w2+2,ng_w2+10,ng_w2+6,ng_w2+11
AL,ng_w2+3,ng_w2+11,ng_w2+7,ng_w2+8
AL,ng_w2+4,ng_w2+5,ng_w2+6,ng_w2+7

!meshing
LSEL,S,LINE,,ng_w2,ng_w2+7,1
LESIZE,ALL,,,n_w1_c
ALLSEL,ALL
LSEL,S,LINE,,ng_w2+8,ng_w2+11,1
LESIZE,ALL,,,n_w1_re
ALLSEL,ALL

MSHAPE,0,2D
MSHKEY,1
TYPE,2
AMESH,ng_w2,ng_w2+4,1

TYPE,1
```

```
EXTOPT,ACLEAR,1
EXTOPT,ESIZE,n_w1_l
VEXT,ng_w2,ng_w2+4,1,,,l_w2



!DISK (ALL)
!---------------------

nindisc=1

*DO,i,nindisc,ndisk,1
        MAT,B4C                                 !TARGET DISK MATERIAL - B4C
        !geometry
        NUMSTR,KP,ng_d%i%
        NUMSTR,LINE,ng_d%i%
        NUMSTR,AREA,ng_d%i%+1
        NUMSTR,VOLU,ng_d%i%+1

        K,ng_d%i%,0,0,z_d%i%            !DISK CENTRE
        !central disk
        K,ng_d%i%+1,re_d1/nddis,0,z_d%i%
        K,ng_d%i%+2,0,re_d1/nddis,z_d%i%
        K,ng_d%i%+3,-re_d1/nddis,0,z_d%i%
        K,ng_d%i%+4,0,-re_d1/nddis,z_d%i%
        LARC,ng_d%i%+1,ng_d%i%+2,ng_d%i%,re_d1/nddis
        LARC,ng_d%i%+2,ng_d%i%+3,ng_d%i%,re_d1/nddis
        LARC,ng_d%i%+3,ng_d%i%+4,ng_d%i%,re_d1/nddis
        LARC,ng_d%i%+4,ng_d%i%+1,ng_d%i%,re_d1/nddis
        !AL,ng_d%i%,ng_d%i%+1,ng_d%i%+2,ng_d%i%+3

        *DO,j,1,nddis-1,1
                K,ng_d%i%+1+j*4,re_d1/nddis*(j+1),0,z_d%i%
                K,ng_d%i%+2+j*4,0,re_d1/nddis*(j+1),z_d%i%
                K,ng_d%i%+3+j*4,-re_d1/nddis*(j+1),0,z_d%i%
                K,ng_d%i%+4+j*4,0,-re_d1/nddis*(j+1),z_d%i%
                L,ng_d%i%+1+(j-1)*4,ng_d%i%+1+j*4
                L,ng_d%i%+2+(j-1)*4,ng_d%i%+2+j*4
                L,ng_d%i%+3+(j-1)*4,ng_d%i%+3+j*4
                L,ng_d%i%+4+(j-1)*4,ng_d%i%+4+j*4
                LARC,ng_d%i%+1+j*4,ng_d%i%+2+j*4,ng_d%i%,re_d1/nddis*(j+1)
                LARC,ng_d%i%+2+j*4,ng_d%i%+3+j*4,ng_d%i%,re_d1/nddis*(j+1)
                LARC,ng_d%i%+3+j*4,ng_d%i%+4+j*4,ng_d%i%,re_d1/nddis*(j+1)
                LARC,ng_d%i%+4+j*4,ng_d%i%+1+j*4,ng_d%i%,re_d1/nddis*(j+1)

                AL,ng_d%i%+8*(j-1),ng_d%i%+8*(j-1)+4,ng_d%i%+8*(j-1)+8,ng_d%i%+8*(j-1)+5
```

```
        AL,ng_d%i%+8*(j-1)+1,ng_d%i%+8*(j-1)+5,ng_d%i%+8*(j-1)+9,ng_d%i%+8*(j-1)+6
        AL,ng_d%i%+8*(j-1)+2,ng_d%i%+8*(j-1)+6,ng_d%i%+8*(j-1)+10,ng_d%i%+8*(j-1)+7
        AL,ng_d%i%+8*(j-1)+3,ng_d%i%+8*(j-1)+7,ng_d%i%+8*(j-1)+11,ng_d%i%+8*(j-1)+4
*ENDDO
LSEL,S,LINE,,ng_d%i%+4,ng_d%i%+4+(nddis-2)*8,8
LSEL,A,LINE,,ng_d%i%+5,ng_d%i%+5+(nddis-2)*8,8
LSEL,A,LINE,,ng_d%i%+6,ng_d%i%+6+(nddis-2)*8,8
LSEL,A,LINE,,ng_d%i%+7,ng_d%i%+7+(nddis-2)*8,8
LESIZE,ALL,,,n_d1_r
ALLSEL,ALL
LSEL,S,LINE,,ng_d%i%,ng_d%i%+(nddis-2)*8,8
LSEL,A,LINE,,ng_d%i%+1,ng_d%i%+1+(nddis-2)*8,8
LSEL,A,LINE,,ng_d%i%+2,ng_d%i%+2+(nddis-2)*8,8
LSEL,A,LINE,,ng_d%i%+3,ng_d%i%+3+(nddis-2)*8,8
LESIZE,ALL,,,n_d1_c
ALLSEL,ALL
MSHAPE,0,2D
MSHKEY,1
TYPE,2
AMESH,ng_d%i%+1,ng_d%i%+4*(nddis-1),1

NUMSTR,LINE,ng_d%i%-4
NUMSTR,AREA,ng_d%i%-3
NUMSTR,VOLU,ng_d%i%-3
L,ng_d%i%,ng_d%i%+1
L,ng_d%i%,ng_d%i%+2
L,ng_d%i%,ng_d%i%+3
L,ng_d%i%,ng_d%i%+4
AL,ng_d%i%-4,ng_d%i%-3,ng_d%i%
AL,ng_d%i%-3,ng_d%i%-2,ng_d%i%+1
AL,ng_d%i%-2,ng_d%i%-1,ng_d%i%+2
AL,ng_d%i%-1,ng_d%i%-4,ng_d%i%+3
MSHAPE,1,2D
MSHKEY,0
TYPE,2
ASEL,S,AREA,,ng_d%i%-3,ng_d%i%
AESIZE,ALL,20/nfatt_d
AMESH,ALL
ALLSEL,ALL
EXTOPT,ACLEAR,1
EXTOPT,ESIZE,n_d1_l
TYPE,11
VEXT,ng_d%i%-3,ng_d%i%+4*(nddis-1),1,,,l_d1

!BOX
```

```
        MAT,C_ATJ
        NUMSTR,KP,ng_b%i%
        NUMSTR,LINE,ng_b%i%
        NUMSTR,AREA,ng_b%i%
        NUMSTR,VOLU,ng_b%i%
        *IF,i,EQ,1,THEN
                ASEL,S,AREA,,ng_b%i%-ddd+4
                ASEL,A,AREA,,ng_b%i%-ddd+9
                ASEL,A,AREA,,ng_b%i%-ddd+13
                ASEL,A,AREA,,ng_b%i%-ddd+17
        *ELSE
                ASEL,S,AREA,,ng_b%i%-ddd
                ASEL,A,AREA,,ng_b%i%-ddd+5
                ASEL,A,AREA,,ng_b%i%-ddd+9
                ASEL,A,AREA,,ng_b%i%-ddd+13
        *ENDIF
        EXTOPT,ESIZE,n_b_ld
        TYPE,1
!       VEXT,ALL,,,,,l_d1+d_d%i%_d%(i+1)%
        VEXT,ALL,,,,,d_d%i%_d%(i+1)%
        ALLSEL,ALL
*ENDDO

!DUMP (ALL)
!---------------------

MAT,C_ATJ

*DO,i,1,ndump,1
        !geometry
        NUMSTR,KP,ng_dump%i%
        NUMSTR,LINE,ng_dump%i%
        NUMSTR,AREA,ng_dump%i%
        NUMSTR,VOLU,ng_dump%i%

        K,ng_dump%i%,0,0,z_dump%i%
        K,ng_dump%i%+1,re_dump%i%,0,z_dump%i%
        K,ng_dump%i%+2,0,re_dump%i%,z_dump%i%
        K,ng_dump%i%+3,-re_dump%i%,0,z_dump%i%
        K,ng_dump%i%+4,0,-re_dump%i%,z_dump%i%
        K,ng_dump%i%+5,lqd,0,z_dump%i%
        K,ng_dump%i%+6,0,lqd,z_dump%i%
        K,ng_dump%i%+7,-lqd,0,z_dump%i%
        K,ng_dump%i%+8,0,-lqd,z_dump%i%
```

```
LARC,ng_dump%i%+1,ng_dump%i%+2,ng_dump%i%,re_dump%i%
LARC,ng_dump%i%+2,ng_dump%i%+3,ng_dump%i%,re_dump%i%
LARC,ng_dump%i%+3,ng_dump%i%+4,ng_dump%i%,re_dump%i%
LARC,ng_dump%i%+4,ng_dump%i%+1,ng_dump%i%,re_dump%i%
L,ng_dump%i%+5,ng_dump%i%+6
L,ng_dump%i%+6,ng_dump%i%+7
L,ng_dump%i%+7,ng_dump%i%+8
L,ng_dump%i%+8,ng_dump%i%+5

L,ng_dump%i%+1,ng_dump%i%+5
L,ng_dump%i%+2,ng_dump%i%+6
L,ng_dump%i%+3,ng_dump%i%+7
L,ng_dump%i%+4,ng_dump%i%+8

AL,ng_dump%i%,ng_dump%i%+8,ng_dump%i%+4,ng_dump%i%+9
AL,ng_dump%i%+1,ng_dump%i%+9,ng_dump%i%+5,ng_dump%i%+10
AL,ng_dump%i%+2,ng_dump%i%+10,ng_dump%i%+6,ng_dump%i%+11
AL,ng_dump%i%+3,ng_dump%i%+11,ng_dump%i%+7,ng_dump%i%+8
AL,ng_dump%i%+4,ng_dump%i%+5,ng_dump%i%+6,ng_dump%i%+7

!parte esterno del dump
K,ng_dump%i%+9,re_fdump,0,z_dump%i%
K,ng_dump%i%+10,0,re_fdump,z_dump%i%
K,ng_dump%i%+11,-re_fdump,0,z_dump%i%
K,ng_dump%i%+12,0,-re_fdump,z_dump%i%

L,ng_dump%i%+1,ng_dump%i%+9
L,ng_dump%i%+2,ng_dump%i%+10
L,ng_dump%i%+3,ng_dump%i%+11
L,ng_dump%i%+4,ng_dump%i%+12
LARC,ng_dump%i%+9,ng_dump%i%+10,ng_dump%i%,re_fdump
LARC,ng_dump%i%+10,ng_dump%i%+11,ng_dump%i%,re_fdump
LARC,ng_dump%i%+11,ng_dump%i%+12,ng_dump%i%,re_fdump
LARC,ng_dump%i%+12,ng_dump%i%+9,ng_dump%i%,re_fdump

AL,ng_dump%i%,ng_dump%i%+12,ng_dump%i%+16,ng_dump%i%+13
AL,ng_dump%i%+1,ng_dump%i%+13,ng_dump%i%+17,ng_dump%i%+14
AL,ng_dump%i%+2,ng_dump%i%+14,ng_dump%i%+18,ng_dump%i%+15
AL,ng_dump%i%+3,ng_dump%i%+15,ng_dump%i%+19,ng_dump%i%+12

!meshing
LSEL,S,LINE,,ng_dump%i%,ng_dump%i%+7,1
LESIZE,ALL,,,n_dump%i%_c
ALLSEL,ALL
LSEL,S,LINE,,ng_dump%i%+8,ng_dump%i%+11,1
```

```
		LESIZE,ALL,,,n_dump%i%_r
		ALLSEL,ALL
		LSEL,S,LINE,,ng_dump%i%+12,ng_dump%i%+15,1
		LESIZE,ALL,,,n_dump%i%_rf
		ALLSEL,ALL

		MSHAPE,0,2D
		MSHKEY,1
		TYPE,2
		AMESH,ng_dump%i%,ng_dump%i%+8,1

		TYPE,1
		EXTOPT,ACLEAR,1
		EXTOPT,ESIZE,n_dump%i%_l
		VEXT,ng_dump%i%,ng_dump%i%+8,1,,,l_dump%i%
		*IF,i,LT,ndump,THEN
			ASEL,S,AREA,,ng_dump%i%+26
			ASEL,A,AREA,,ng_dump%i%+30
			ASEL,A,AREA,,ng_dump%i%+33
			ASEL,A,AREA,,ng_dump%i%+36
			VEXT,ALL,,,,,z_dump%i+1%-z_dump%i%-l_dump%i%-to
		*ENDIF
	*ENDDO

	ASEL,S,AREA,,ng_dump%ndump%+9
	ASEL,A,AREA,,ng_dump%ndump%+14
	ASEL,A,AREA,,ng_dump%ndump%+18
	ASEL,A,AREA,,ng_dump%ndump%+22
	ASEL,A,AREA,,ng_dump%ndump%+25
	ASEL,A,AREA,,ng_dump%ndump%+26
	ASEL,A,AREA,,ng_dump%ndump%+30
	ASEL,A,AREA,,ng_dump%ndump%+33
	ASEL,A,AREA,,ng_dump%ndump%+36
	TYPE,1
	EXTOPT,ACLEAR,1
	EXTOPT,ESIZE,2
	!VEXT,ALL,,,,,d_dumpboxf_dump4
	VEXT,ALL,,,,,d_dumpboxf_dump4

	!DUMP BOX
	!--------------

	!geometry
	NUMSTR,KP,ng_dumpbox
	NUMSTR,LINE,ng_dumpbox
```

```
NUMSTR,AREA,ng_dumpbox
NUMSTR,VOLU,ng_dumpbox

ASEL,S,AREA,,ng_b%ndisk%
ASEL,A,AREA,,ng_b%ndisk%+5
ASEL,A,AREA,,ng_b%ndisk%+9
ASEL,A,AREA,,ng_b%ndisk%+13
EXTOPT,ESIZE,n_dumpbox_l
VEXT,ALL,,,,,l_dumpbox-d_dumpbox_dump1
!VCLEAR,ng_dumpbox,ng_dumpbox+3
ALLSEL,ALL

!WPCSYS,0
!NUMSTR,KP,ng_dumpbox+30
!NUMSTR,LINE,ng_dumpbox+30
!NUMSTR,AREA,ng_dumpbox+30
!NUMSTR,VOLU,ng_dumpbox+30
!CYLIND,re_fdump+to/2,re_box,z_dumpbox+d_dumpbox_dump1-to,z_dumpbox+l_dumpbox

!NUMSTR,KP,ng_dumpbox+50
!NUMSTR,LINE,ng_dumpbox+50
!NUMSTR,AREA,ng_dumpbox+50
!NUMSTR,VOLU,ng_dumpbox+50

!VSEL,S,VOLU,,ng_dumpbox,ng_dumpbox+3
!VSEL,A,VOLU,,ng_dumpbox+30,ng_dumpbox+33
!VGLUE,ALL

!MSHAPE,1,3D
!MSHKEY,0
!TYPE,1
!ESIZE,6
!VMESH,ALL

!WINDOW SCREENS
!---------------- start

n_ws=2
MAT,C_ATJ

!WINDOW SREEN1
ng_ws1=700
!geometry
d_ws1_d1=0.5
re_ws1=ri_box-to
```

```
!ri_ws1=re_ws1/2
ri_ws1=22.5/2
l_ws1=0.3
z_ws1=z_d1-l_ws1-d_ws1_d1
V_ws1=pi*(re_ws1**2-ri_ws1**2)*l_ws1/1e9
!mesh
n_ws1_re=4
n_ws1_c=4
n_ws1_l=4

!WINDOW SREEN2
ng_ws2=750
!geometry
d_ws2_d%ndisk%=0.5
z_ws2=z_d%ndisk%+l_d1+d_ws2_d%ndisk%
re_ws2=ri_box-to
!ri_ws2=re_ws2/2
ri_ws2=22.5/2
l_ws2=1
V_ws2=pi*(re_ws2**2-ri_ws2**2)*l_ws2/1e9
!mesh
n_ws2_re=4
n_ws2_c=4
n_ws2_l=4

!WINDOW SREEN
!--------------

MAT,C_ATJ

*DO,i,1,n_ws,1
        !geometry
        NUMSTR,KP,ng_ws%i%
        NUMSTR,LINE,ng_ws%i%
        NUMSTR,AREA,ng_ws%i%
        NUMSTR,VOLU,ng_ws%i%

        K,ng_ws%i%,0,0,z_ws%i%
        K,ng_ws%i%+1,ri_ws%i%,0,z_ws%i%
        K,ng_ws%i%+2,0,ri_ws%i%,z_ws%i%
        K,ng_ws%i%+3,-ri_ws%i%,0,z_ws%i%
        K,ng_ws%i%+4,0,-ri_ws%i%,z_ws%i%
        K,ng_ws%i%+5,re_ws%i%,0,z_ws%i%
        K,ng_ws%i%+6,0,re_ws%i%,z_ws%i%
        K,ng_ws%i%+7,-re_ws%i%,0,z_ws%i%
```

```
        K,ng_ws%i%+8,0,-re_ws%i%,z_ws%i%

        LARC,ng_ws%i%+1,ng_ws%i%+2,ng_ws%i%,ri_ws%i%
        LARC,ng_ws%i%+2,ng_ws%i%+3,ng_ws%i%,ri_ws%i%
        LARC,ng_ws%i%+3,ng_ws%i%+4,ng_ws%i%,ri_ws%i%
        LARC,ng_ws%i%+4,ng_ws%i%+1,ng_ws%i%,ri_ws%i%
        LARC,ng_ws%i%+5,ng_ws%i%+6,ng_ws%i%,re_ws%i%
        LARC,ng_ws%i%+6,ng_ws%i%+7,ng_ws%i%,re_ws%i%
        LARC,ng_ws%i%+7,ng_ws%i%+8,ng_ws%i%,re_ws%i%
        LARC,ng_ws%i%+8,ng_ws%i%+5,ng_ws%i%,re_ws%i%

        L,ng_ws%i%+1,ng_ws%i%+5
        L,ng_ws%i%+2,ng_ws%i%+6
        L,ng_ws%i%+3,ng_ws%i%+7
        L,ng_ws%i%+4,ng_ws%i%+8

        AL,ng_ws%i%,ng_ws%i%+8,ng_ws%i%+4,ng_ws%i%+9
        AL,ng_ws%i%+1,ng_ws%i%+9,ng_ws%i%+5,ng_ws%i%+10
        AL,ng_ws%i%+2,ng_ws%i%+10,ng_ws%i%+6,ng_ws%i%+11
        AL,ng_ws%i%+3,ng_ws%i%+11,ng_ws%i%+7,ng_ws%i%+8

        !meshing
        LSEL,S,LINE,,ng_ws%i%,ng_ws%i%+3,1
        LESIZE,ALL,,,n_ws%i%_c
        ALLSEL,ALL
        LSEL,S,LINE,,ng_ws%i%+8,ng_ws%i%+11,1
        LESIZE,ALL,,,n_ws%i%_re
        ALLSEL,ALL

        MSHAPE,0,2D
        MSHKEY,1
        !TYPE,4
        TYPE,2
        AMESH,ng_ws%i%,ng_ws%i%+3,1

        !TYPE,3
        TYPE,1
        EXTOPT,ACLEAR,1
        EXTOPT,ESIZE,n_ws%i%_l
        VEXT,ng_ws%i%,ng_ws%i%+3,1,,,l_ws%i%
        ALLSEL,ALL
*ENDDO

!----------------------------
! DEFINING CO-ORDINATE SYSTEM
```

```
!----------------------------

WPCSYS
CLOCAL,15,1,0,0,0,0,0,0
CSYS,15

!-------------------
!BOUNDARY CONDITIONS
!-------------------

I_beam=200                !BEAM CURRENT
convP=I_beam/1E6          !Conversion factor to calculate power

!Read in power deposition data on components - obtained from FLUKA
/INPUT,pbox.txt
/INPUT,pw1.txt
/INPUT,pw2.txt
/INPUT,ps1.txt
/INPUT,pdisc1.txt
/INPUT,pdisc2.txt
/INPUT,pdisc3.txt
/INPUT,pdisc4.txt
/INPUT,pdisc5.txt
/INPUT,pdisc6.txt
/INPUT,pdisc7.txt
/INPUT,pdisc8.txt
/INPUT,pdisc9.txt
/INPUT,pdisc10.txt
/INPUT,pdisc11.txt
/INPUT,pdisc12.txt
/INPUT,pdisc13.txt
/INPUT,pdisc14.txt
/INPUT,pdisc15.txt
/INPUT,ps2.txt
!/INPUT,pdista.txt
!/INPUT,pexdump.txt
/INPUT,pdump1.txt
/INPUT,pdump2.txt
/INPUT,pdump3.txt
/INPUT,pdump4.txt

P_h = 1500/V_heater       !HEATERT POWER (Watts/m3)

!--------------------------------------------------------------------!
!Reading in input files
```

```
!-----------------------------------------------------------------------!

VSEL,S,VOLU,,ng_h,ng_h+10
BFV,ALL,HGEN,P_h

VSEL,S,VOLU,,ng_w1,ng_w1+10
BFV,ALL,HGEN,%pw1%

VSEL,S,VOLU,,ng_w2,ng_w2+10
BFV,ALL,HGEN,%pw2%

VSEL,S,VOLU,,ng_d1-3,ng_d1+32
BFV,ALL,HGEN,%pdisc1%

VSEL,S,VOLU,,ng_d2-3,ng_d2+32
BFV,ALL,HGEN,%pdisc2%

VSEL,S,VOLU,,ng_d3-3,ng_d3+32
BFV,ALL,HGEN,%pdisc3%

VSEL,S,VOLU,,ng_d4-3,ng_d4+32
BFV,ALL,HGEN,%pdisc4%

VSEL,S,VOLU,,ng_d5-3,ng_d5+32
BFV,ALL,HGEN,%pdisc5%

VSEL,S,VOLU,,ng_d6-3,ng_d6+32
BFV,ALL,HGEN,%pdisc6%

VSEL,S,VOLU,,ng_d7-3,ng_d7+32
BFV,ALL,HGEN,%pdisc7%

VSEL,S,VOLU,,ng_d8-3,ng_d8+32
BFV,ALL,HGEN,%pdisc8%

VSEL,S,VOLU,,ng_d9-3,ng_d9+32
BFV,ALL,HGEN,%pdisc9%

VSEL,S,VOLU,,ng_d10-3,ng_d10+32
BFV,ALL,HGEN,%pdisc10%

VSEL,S,VOLU,,ng_d11-3,ng_d11+32
BFV,ALL,HGEN,%pdisc11%

VSEL,S,VOLU,,ng_d12-3,ng_d12+32
```

```
BFV,ALL,HGEN,%pdisc12%

VSEL,S,VOLU,,ng_d13-3,ng_d13+32
BFV,ALL,HGEN,%pdisc13%

VSEL,S,VOLU,,ng_d14-3,ng_d14+32
BFV,ALL,HGEN,%pdisc14%

VSEL,S,VOLU,,ng_d15-3,ng_d15+32
BFV,ALL,HGEN,%pdisc15%

VSEL,S,VOLU,,ng_dump1,ng_dump1+182
BFV,ALL,HGEN,%pdump1%

VSEL,S,VOLU,,ng_dump2,ng_dump2+182
BFV,ALL,HGEN,%pdump2%

VSEL,S,VOLU,,ng_dump3,ng_dump3+182
BFV,ALL,HGEN,%pdump3%

VSEL,S,VOLU,,ng_dump4,ng_dump4+182
BFV,ALL,HGEN,%pdump4%

VSEL,S,VOLU,,ng_ws1,ng_ws1+115
BFV,ALL,HGEN,%ps1%

VSEL,S,VOLU,,ng_ws2,ng_ws2+115
BFV,ALL,HGEN,%ps2%

VSEL,S,VOLU,,ng_b,ng_b+3
!*DO,i,1,13
*DO,i,1,15                              !Update for 15 discs
VSEL,A,VOLU,,ng_b%i%,ng_b%i%+3
*ENDDO
VSEL,A,VOLU,,ng_dumpbox,ng_dumpbox+3
BFV,ALL,HGEN,%pbox%

ALLSEL,ALL

CSYS,0
WPCSYS

!--------------------------------
!TOTAL RADIATION
!--------------------------------
```

```
RADOPT,,0.001,0,10000,,0.5
HEMIOPT,100
SPCTEMP,1,50
STEF,5.67e-8
TOFFST,273.15
TUNIF,1500

ALLSEL,ALL

VSEL,R,MAT,,1
ALLSEL,BELOW,VOLU
SFA,ALL,,RDSF,em1,1
ALLSEL,ALL

VSEL,R,MAT,,2
ALLSEL,BELOW,VOLU
SFA,ALL,,RDSF,em2,1
ALLSEL,ALL

VSEL,R,MAT,,Ta
ALLSEL,BELOW,VOLU
SFA,ALL,,RDSF,-Ta,1
ALLSEL,ALL

VSEL,R,MAT,,C_ATJ
ALLSEL,BELOW,VOLU
SFA,ALL,,RDSF,-C_ATJ,1
ALLSEL,ALL

VSEL,R,MAT,,B4C
ALLSEL,BELOW,VOLU
SFA,ALL,,RDSF,-B4C,1
ALLSEL,ALL
ALLSEL,ALL

*GET,nvolu,VOLU,0,COUNT
nn=0
*DO,i,1,nvolu
        nn=vlnext(nn)
        VSEL,ALL
        VSEL,U,VOLU,,nn
        ALLSEL,BELOW,VOLU
        VSEL,S,VOLU,,nn
        ASLV,R
        SFADELE,ALL,,RDSF
```

```
          ALLSEL,ALL
*ENDDO

/INPUT,'APDL_CAMERA','txt',,0,1

!call model geometry
VLSCALE,ALL,,,0.001,0.001,0.001,,0,1
ALLSEL,ALL

!AMBIENTE SOLUTION
/SOLU
SOLCONTROL,ON
ANTYPE,TRANS
AUTOTS,ON
KBC,1
DELTIM,0.001,0.0001,1000
TIME,10000
OUTRES,NSOL,ALL
SAVE,TERM,DB
SOLVE
SAVE,TERM,DB

/INPUT,'APDL_struct','txt',,0,1
```

APPENDIX C: GRAPHITE – ANSYS MATERIAL FILE

```
!---------1----------2----------3----------4----------5----------6---------7----------8

  !-------------------------------------------------------
  !ATJ graphite
  !Composition: isomolded graphite
  !-------------------------------------------------------
  !Version 0.4 (Apr 2017)  by
  !L Davis
  !Nuclear Physics
  !iThemba LABS
  !Cape Town, South Africa
  !e-mail: lancegarthdavis@gmail.com
  !-------------------------------------------------------
  !
  !Ver. 0.1  - 1 Jun 16
  !-------------------------------------------------------

  /prep7

  C_ATJ=29            !Material number in the ANSYS library
  MPDELE,all,C_ATJ

  !------------------------------------------------------
  !ELECTRICAL RESISTIVITY
  !
  !NOTE 1 - Data are taken from: Taylor, R.E. and Groot, H., 1978.
  !Thermophysical Properties of POCO Graphite (No. PRL-153).
  !PURDUE UNIV LAFAYETTE IND PROPERTIES RESEARCH LAB
  !
  !NOTE 2 - values over 2126.9−C are calculated by linear extrapolation.
  !
  !NOTE 3 - 5% error; National Carbon Co.
  !
  !NOTE 4 - the S.I. system of units is used.
  !------------------------------------------------------
  !Temperature table [−C]
  MPTEMP ! erase previous table
  MPTEMP,       1,      27.,     127.,     227.,
  MPTEMP,       4,     327.,     427.,     527.,
  MPTEMP,       7,     627.,     727.,     827.,
  MPTEMP,      10,     927.,    1027.,    1127.,
```

```
MPTEMP,       13,      1227.,      1327.,      1427.,
MPTEMP,       16,      1527.,      1627.,      1727.,
MPTEMP,       19,      1827.,      1927.,      2027.,
MPTEMP,       22,      2127.,
!Electrical resistivity table [ohm m]
MPDATA,RSVX , C_ATJ    ,  1,   1.3430E-04,   1.1750E-04,   1.0670E-04,
MPDATA,RSVX , C_ATJ    ,  4,   9.9650E-05,   9.4800E-05,   9.1400E-05,
MPDATA,RSVX , C_ATJ    ,  7,   8.9650E-05,   8.9200E-05,   8.9150E-05,
MPDATA,RSVX , C_ATJ    , 10,   8.9800E-05,   9.0750E-05,   9.2100E-05,
MPDATA,RSVX , C_ATJ    , 13,   9.3700E-05,   9.5300E-05,   9.7050E-05,
MPDATA,RSVX , C_ATJ    , 16,   9.9000E-05,   1.0110E-04,   1.0330E-04,
MPDATA,RSVX , C_ATJ    , 19,   1.0550E-04,   1.0780E-04,   1.1000E-04,
MPDATA,RSVX , C_ATJ    , 22,   1.1230E-04,

!------------------------------------------------------------------
!THERMAL CONDUCTIVITY
!
!NOTE 1 - Data are taken from: Taylor, R.E. and Groot, H., 1978.
!Thermophysical Properties of POCO Graphite (No. PRL-153).
!PURDUE UNIV LAFAYETTE IND PROPERTIES RESEARCH LAB
!
!NOTE 2 - thermal conductivity is strongly dependent on impurities.
!
!NOTE 3 - 5% error; National Carbon Co.
!
!NOTE 4 - the S.I. system of units is used.
!------------------------------------------------------------------
!Temperature table [−C]
MPTEMP ! erase previous table
MPTEMP,        1,        27.,       127.,       227.,
MPTEMP,        4,       327.,       427.,       527.,
MPTEMP,        7,       627.,       727.,       827.,
MPTEMP,       10,       927.,      1027.,      1127.,
MPTEMP,       13,      1227.,      1327.,      1427.,
MPTEMP,       16,      1527.,      1627.,      1727.,
MPTEMP,       19,      1827.,      1927.,      2027.,
MPTEMP,       22,      2127.,
!Thermal conductivity table [W/m−C]
MPDATA,KXX , C_ATJ    ,  1,   1.0600E+02,   9.9700E+01,   9.2250E+01,
MPDATA,KXX , C_ATJ    ,  4,   8.5750E+01,   7.9800E+01,   7.4650E+01,
MPDATA,KXX , C_ATJ    ,  7,   6.9500E+01,   6.4800E+01,   6.0550E+01,
MPDATA,KXX , C_ATJ    , 10,   5.6800E+01,   5.3250E+01,   5.0150E+01,
MPDATA,KXX , C_ATJ    , 13,   4.7450E+01,   4.5350E+01,   4.3700E+01,
MPDATA,KXX , C_ATJ    , 16,   4.2200E+01,   4.1050E+01,   4.0100E+01,
MPDATA,KXX , C_ATJ    , 19,   3.9300E+01,   3.8700E+01,   3.8200E+01,
```

```
MPDATA,KXX , C_ATJ     , 22,    3.7900E+01,

!------------------------------------------------------------
!EMISSIVITY (hemispherical total emissivity)
!
!NOTE 1 - Data are taken from:
!L. Biasetto, M. Manzolaro, A. Andrighetto Emissivity measurements
!of opaque gray bodies up to 2000−C by a dual-frequency pyrometer (2008)
!
!NOTE 2 - Isotropic graphite 2114 (unpolished)
!
!------------------------------------------------------------
!Temperature table [−C]
MPTEMP ! erase previous table
MPTEMP,           1,         1270,        1380,        1450,
MPTEMP,           4,         1560,        1660,        1775,
MPTEMP,           7,         1870,        1970,
!Emissivity table [-]
MPDATA,EMIS , C_ATJ     ,  1,    0.815,   0.820,   0.825,
MPDATA,EMIS , C_ATJ     ,  4,    0.835,   0.840,   0.845,
MPDATA,EMIS , C_ATJ     ,  7,    0.850,   0.855

!------------------------------------------------------------------
!DENSITY
!
!NOTE 1 - UCAR "Tecnical Data Sheet: 31": Grade ATJ Isomolded Graphite.
!
!NOTE 2 - the S.I. system of units is used.
!------------------------------------------------------------------
!Temperature table [−C]
MPTEMP ! erase previous table
MPTEMP,   1,   20.,
!Density table [kg/m^3]
MPDATA,DENS , C_ATJ  ,  1,   1.76E+03,

!------------------------------------------------------------------
!SPECIFIC HEAT
!
!NOTE 1 - Data are taken from: Taylor, R.E. and Groot, H., 1978.
!Thermophysical Properties of POCO Graphite (No. PRL-153).
!PURDUE UNIV LAFAYETTE IND PROPERTIES RESEARCH LAB
!
!------------------------------------------------------------------
!Temperature table [−C]
```

```
MPTEMP ! erase previous table
MPTEMP,        1,       27.,      127.,      227.,
MPTEMP,        4,      327.,      427.,      527.,
MPTEMP,        7,      627.,      727.,      827.,
MPTEMP,       10,       927.,     1027.,     1127.,
MPTEMP,       13,      1227.,     1327.,     1427.,
MPTEMP,       16,      1527.,     1627.,     1727.,
MPTEMP,       19,      1827.,     1927.,     2027.,
MPTEMP,       22,      2127.,
!Specific heat table [J/kg−C]
MPDATA,C , C_ATJ    ,  1,       702,     955,    1168,
MPDATA,C , C_ATJ    ,  4,      1282,    1520,    1637,
MPDATA,C , C_ATJ    ,  7,      1726,    1797,    1859,
MPDATA,C , C_ATJ    , 10,       1905,    1942,    1975,
MPDATA,C , C_ATJ    , 13,       2002,    2028,    2050,
MPDATA,C , C_ATJ    , 16,       2070,    2087,    2100,
MPDATA,C , C_ATJ    , 19,       2111,    2127,    2140,
MPDATA,C , C_ATJ    , 22,       2155,

!-----------------------------------------------------------------
!COEFFICIENT OF THERMAL EXPANSION
!
!NOTE 1 - Data are taken from:
!Thermophysical Properties of Matter, v13, Y.S. Touloukian, R.K.
!Kirby, R.E. Taylor & T.Y.R. Lee, 1977, IFI/Plenum, NY, NY.
!
!NOTE 2 - Orientation: with grain
!
!NOTE 3 - 10% error; National Carbon Co..
!
!NOTE 4 - the S.I. system of units is used.
!-----------------------------------------------------------------
!Temperature table [−C]
MPTEMP ! erase previous table
MPTEMP,        1,       20.,      127.,      327.,
MPTEMP,        4,      527.,      727.,      927.,
MPTEMP,        7,     1127.,     1327.,     1527.,
MPTEMP,       10,      1727.,     1927.,     2127.,
MPTEMP,       13,      2327.,
!Secant coefficient of thermal expansion [1/−C]
MPDATA,ALPX , C_ATJ    ,  1,   2.2162E-06,  2.4088E-06,  2.9000E-06,
MPDATA,ALPX , C_ATJ    ,  4,   3.3000E-06,  3.7000E-06,  4.0000E-06,
MPDATA,ALPX , C_ATJ    ,  7,   4.3000E-06,  4.6000E-06,  4.9000E-06,
MPDATA,ALPX , C_ATJ    , 10,   5.1000E-06,  5.4000E-06,  5.5000E-06,
```

```
MPDATA,ALPX , C_ATJ     , 13,    5.7000E-06,

!------------------------------------------------------------------------
!ELASTIC MODULUS
!
!NOTE 1 - Data are taken from:
!Marlowe, M.O., 1970. Elastic properties of three grades of fine grained graphite at 2000 C.
!
!NOTE 2 - the S.I. system of units is used.
!------------------------------------------------------------------------
!Temperature table [−C]
MPTEMP ! erase previous table
MPTEMP,           1,          20.,        500.,       1000.,
MPTEMP,           4,        1500.,       2000.,
!Elastic modulus [Pa]
MPDATA,EX , C_ATJ     ,   1,    1.192E+10,  1.252E+10,     1.359E+10,
MPDATA,EX , C_ATJ     ,   4,    1.574E+10,  1.729E+10,

!-----------------------------------------------------------------------
!POISSON'S RATIO
!
!NOTE 1 - No data available:
!Sun, C.T. and Yoon, K.J., 1988.
!Mechanical properties of graphite/epoxy composites at various temperatures
!(No. HTMIAC-9). High temperature materials information analysis center west Lafayette in.
!
!-----------------------------------------------------------------------
!Temperature table [−C]
MPTEMP ! erase previous table
MPTEMP,           1,             20.,
!Poisson's ratio [-]
MPDATA,PRXY , C_ATJ     ,   1,      3.0E-01,
```

APPENDIX D: BORON CARBIDE – ANSYS MATERIAL FILE

```
!---------1----------2----------3----------4----------5----------6---------7----------8

  !--------------------------------------------------------
  !Boron Carbide
  !Composition: Sintered Boron Carbide
  !--------------------------------------------------------
  !Version 0.3 (Jun 2017)  by
  !L Davis
  !Nuclear Physics
  !iThemba LABS
  !Cape Town, South Africa
  !e-mail: lancegarthdavis@gmail.com
  !--------------------------------------------------------
  !
  !Ver. 0.1  - 10 June 16
  !--------------------------------------------------------
  /prep7

  B4C=32          !Material number in the ANSYS library
  MPDELE,all,B4C

  !-------------------------------------------------------
  !ELECTRICAL RESISTIVITY
  !
  ! Lee, S., Mazurowski, J., Ramseyer, G. and Dowben, P.A., 1992. Characterization of boron carbide thin films
  !fabricated by plasma enhanced chemical vapor deposition from boranes. Journal of applied physics, 72(10),
  !pp.4925-4933.
  !NOTE 2 - Data used was for approximately 20% carbon containing boron carbide
  !
  !NOTE 3 - the S.I. system of units is used.
  !
  !-------------------------------------------------------
  !Temperature table [−C]
  MPTEMP ! erase previous table
  MPTEMP,        1,      1023.,      1273.,      1523.,
  MPTEMP,        4,      1773.,      2023.,      2273.,
  MPTEMP,        7,      2523.,      2773.,      3023.,
  MPTEMP,       10,      3273.,      3523.,      3773.,
  !Electrical resistivity table [ohm m]
  MPDATA,RSVX , B4C    ,  1,    1.2500E-05,   1.4286E-05,   1.5385E-05,
  MPDATA,RSVX , B4C    ,  4,    1.5625E-05,   2.2222E-05,   1.0000E-04,
  MPDATA,RSVX , B4C    ,  7,    1.1111E-04,   1.2500E-04,   1.5385E-04,
```

```
MPDATA,RSVX , B4C     , 10,    2.2222E-04,   3.3333E-04,   5.0000E-04,
!-------------------------------------------------------------------
!THERMAL CONDUCTIVITY
!
!NOTE 1 - Data taken from:
!Fischer, H.E., Swartz, E.T., T・kes, P.R.H., Pojl, R.O.: in: Novel Refractory Semiconductors, MRS
!Symp. Proc. Vol. 97, D. Emin, T.L. Aselage, C. Wood ed., Materials Research Soc.: Pittsburgh, 1987,
!p. 69. (and) Wood, C., Zoltan, A., Emin, D.: in: Thermal conductivity, T. Ashworth and D.R. Smith ed., Plenum
!Press: New York, 1985, p. 139
!
!NOTE 2 - thermal conductivity is strongly dependent on impurities.
!
!NOTE 3 - No data above 2000−C obtainable.
!
!NOTE 4 - the S.I. system of units is used.
!-------------------------------------------------------------------
!Temperature table [−C]
MPTEMP ! erase previous table
MPTEMP,           1,          1.,          10.,         100.,
MPTEMP,           4,        200.,          400.,         600.,
MPTEMP,           7,        800.,        1000.,        1500.,
!Thermal conductivity table [W/m−C]
MPDATA,KXX , B4C     ,  1,    8.0000E-03,   5.0000E-01,   9.0000E+00,
MPDATA,KXX , B4C     ,  4,    1.2000E+01,   1.2200E+01,   1.1000E+01,
MPDATA,KXX , B4C     ,  7,    9.0000E+00,   8.0000E+00,   6.5000E+00
!-------------------------------------------------------------
!EMISSIVITY
!
!NOTE 1 - Data taken from:
!Kaminaga, F., Sato, S. and Okamoto, Y., 1992.
!Evaluation of gap heat transfer between boron carbide pellet and cladding in control rod of FBR.
!Journal of Nuclear Science and Technology, 29(2), pp.121-130.
!
!-------------------------------------------------------------
!Temperature table [−C]
MPTEMP ! erase previous table
MPTEMP,           1,          5,        200,        300,
MPTEMP,           4,        400,        500,
!Emissivity table [-]
MPDATA,EMIS , B4C     ,  1,    0.990,   0.890,   0.865,
MPDATA,EMIS , B4C     ,  4,    0.855,   0.860,
!-------------------------------------------------------------------
!DENSITY
!
```

```
!NOTE 1 - Data taken from:
!Gosset, D., Guery, M., Kryger, B.: in: Boron-Rich Solids, Proc. 10th Int. Symp. Boron, Borides and
!Rel. Compounds, Albuquerque, NM 1990 (AIP Conf. Proc. 231), D. Emin, T.L. Aselage, A.C.
!Switendick, B. Morosin, C.L. Beckel ed., American Institute of Physics: New York, 1991, p. 380
!
!NOTE 2 - the S.I. system of units is used.
!------------------------------------------------------------------
!Temperature table [−C]
MPTEMP ! erase previous table
MPTEMP,   1,   25.,
!Density table [kg/m^3]
MPDATA,DENS , B4C  ,  1,   2.52E+03,
!------------------------------------------------------------------
!SPECIFIC HEAT
!
!NOTE 1 - Data taken from:
!Cleveland, J., 1997. Thermophysical properties of materials for water cooled reactors.
!International Atomic Energy Agency Report IAEA-TECDOC-949, 77.
!
!------------------------------------------------------------------
!Temperature table [−C]
MPTEMP ! erase previous table
MPTEMP,          1,           0.,        223.,        723.,
MPTEMP,          4,        1223.,       1723.,       2023.,
MPTEMP,          7,        2423.,
!Specific heat table [J/kg−C]
MPDATA,C , B4C     ,  1,       1050,     1400,     1700,
MPDATA,C , B4C     ,  4,       2020,     2200,     2400,
MPDATA,C , B4C     ,  7,       2450,
!------------------------------------------------------------------
!COEFFICIENT OF THERMAL EXPANSION
!
!NOTE 1 - Data are taken from:
!Michaux, A., Sauder, C., Camus, G. and Pailler, R., 2007.
!Young's modulus, thermal expansion coefficient and fracture behavior of selected Si?B?C based carbides
!in the 20?1200° C temperature range as derived from the behavior of carbon fiber reinforced microcomposites.
!Journal of the European Ceramic Society, 27(12), pp.3551-3560
!
!NOTE 2 - the S.I. system of units is used.
!------------------------------------------------------------------
!Temperature table [−C]
MPTEMP ! erase previous table
MPTEMP,          1,          25.,        200.,        600.,
MPTEMP,          4,        1000.,       1200.,
```

```
!Coefficient of thermal expansion [1/−C]
MPDATA,ALPX , B4C     ,  1,    2.6000E-06,   3.9000E-06,   6.3000E-06,
MPDATA,ALPX , B4C     ,  4,    7.4000E-06,   7.7000E-06,
!--------------------------------------------------------------------------
!ELASTIC/YOUNGS MODULUS
!
!NOTE 1 - Data  taken from:
!Michaux, A., Sauder, C., Camus, G. and Pailler, R., 2007.
!Young's modulus, thermal expansion coefficient and fracture behavior of selected Si?B?C based carbides
!in the 20?1200° C temperature range as derived from the behavior of carbon fiber reinforced microcomposites.
!Journal of the European Ceramic Society, 27(12), pp.3551-3560
!
!NOTE 2 - the S.I. system of units is used.
!--------------------------------------------------------------------------
!Temperature table [−C]
MPTEMP ! erase previous table
MPTEMP,           1,           0.,        200.,        400.,
MPTEMP,           4,         600.,        800.,       1000.,
MPTEMP,           7,        1200.,

!Elastic modulus [Pa]
MPDATA,EX, B4C     ,  1,      448.00E+09,    446.00E+09,  444.00E+09,
MPDATA,EX, B4C     ,  4,      440.00E+09,    420.00E+09,  380.00E+09,
MPDATA,EX, B4C     ,  7,      330.00E+09,
!-------------------------------------------------------------------------
!POISSON'S RATIO
!
!NOTE 1 - No data available:
!To perform thermo-structural analysis a "reasonable" value of 0.2 was used.
!
!-------------------------------------------------------------------------
!Temperature table [−C]
MPTEMP ! erase previous table
MPTEMP,           1,              20.,
!Poisson's ratio [-]
MPDATA,PRXY , B4C     ,   1,      0.2E-01,
```

APPENDIX E: 15 DISCS B_4C TARGET DESIGN DETAILS

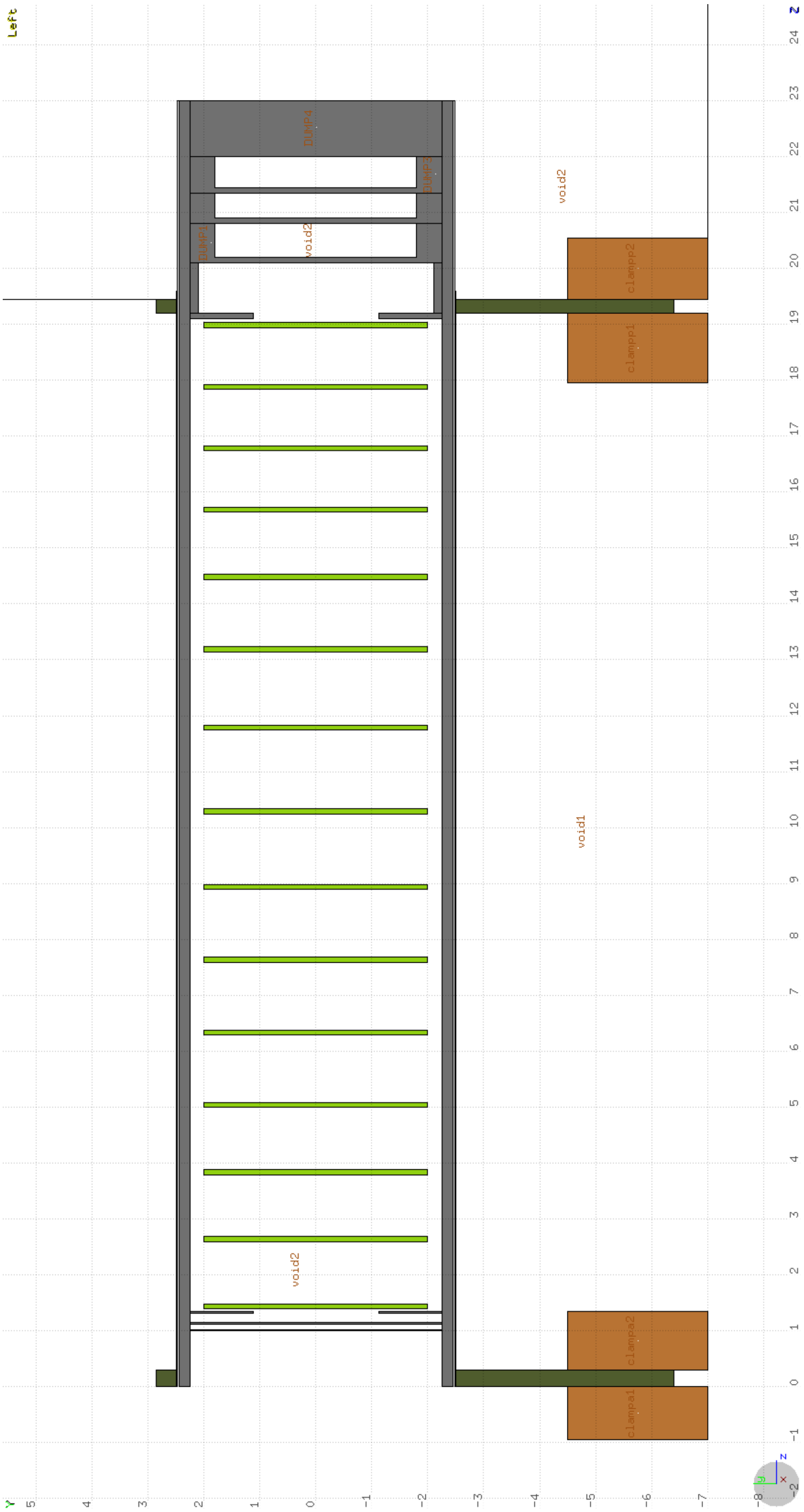

Figure E-A: Configuration 6 target layout.

Component	Material	Start (zi) [mm]	Final (zf) [mm]	Length (∆z) [mm]
Target box	Graphite	0	256,7	256,7
Window 1	Graphite	10	10,2	0,2
Window 2	Graphite	11,2	11,4	0,2
Screen 1	Graphite	13,1	13,4	0,3
Disk 1	Boron Carbide	13,9	14,8	0,9
Disk 2	Boron Carbide	24,9	25,8	0,9
Disk 3	Boron Carbide	35,9	36,8	0,9
Disk 4	Boron Carbide	46,9	47,8	0,9
Disk 5	Boron Carbide	58,9	59,8	0,9
Disk 6	Boron Carbide	70,9	71,8	0,9
Disk 7	Boron Carbide	82,9	83,8	0,9
Disk 8	Boron Carbide	95,9	96,8	0,9
Disk 9	Boron Carbide	108,9	109,8	0,9
Disk 10	Boron Carbide	122,9	123,8	0,9
Disk 11	Boron Carbide	138,9	139,8	0,9
Disk 12	Boron Carbide	154,9	155,8	0,9
Disk 13	Boron Carbide	168,9	169,8	0,9
Disk 14	Boron Carbide	182,9	183,8	0,9
Disk 15	Boron Carbide	195,9	196,8	0,9
Screen 2	Graphite	197,7	198,7	1
Dump 1	Graphite	207,7	208,5	0,8
Dump 2	Graphite	214,7	215,5	0,8
Dump 3	Graphite	220,2	221	0,8
Dump 4	Graphite	226,7	256,7	30

Table E-A: Configuration 6 - Component layout/positioning